Adam Mickiewicz University in Poznań
Faculty of Physics

Ultrasound Study of Magnetic Pickering Emulsions

A dissertation submitted for the degree of Doctor of Philosophy in Physics

By

Bassam Jameel

Supervised by
Prof. dr. hab. Arkadiusz Józefczak
Co-supervised by
Dr. Rafał Bielas

Poznań 2024

Acknowledgments

First, I extend my deepest gratitude to my supervisor, Prof. dr hab. Arkadiusz Józefczak, whose unwavering support has been instrumental throughout my PhD research journey. I am equally indebted to my co-supervisor, Dr. Rafał Bielas, whose expertise and guidance in navigating scientific and technical challenges have significantly enhanced the quality of my research.

I dedicate my PhD thesis to Prof. UAM dr hab. Tomasz Hornowski, whose profound insights into ultrasound scattering theory have been pivotal in resolving complex issues encountered during my research. I express my heartfelt gratitude for his invaluable support.

I am also grateful to all members of the Institute of Experimental Physics of the Slovak Academy of Science, where I had the privilege of spending six months as a visiting scholar. As well, special thanks are due to Yaroslav Harkavyi and Viktoriia Drushliak for their encouragement in pursuing a PhD and for their pleasant company. In addition, I would like to thank all my friends that I met during my stay in Poland; it was never easy without them.

Not least, my deepest appreciation goes to my family for their unwavering support throughout my years of study. To my father, for his kindness and encouragement, and to my mother, for her boundless love and insightful suggestion to pursue studies in Poland. I would also like to thank the Polish National Science Center and the Polish National Agency for Academic Exchange for their financial support during my study.

The author obtained financial resources as part of the financing of a research project from the National Science Centre, project no. 2019/35/O/ST3/00503 (PRELUDIUM BIS): “Ultrasonic study of magnetic Pickering emulsions.”

The Polish National Agency for Academic Exchange (NAWA) also supported the author’s research through the grant no. PPN/STA/2021/1/00033/DEC/1.

Dedicated to Prof. Tomasz Hornowski
(October 22, 1958 – March 7, 2023)

Table of Contents

List of papers constituting the dissertation

I. **Ultrasound study of magnetic and non-magnetic nanoparticles agglomeration in high viscous media**
Jameel, B., Hornowski, T., Bielas, R., and Józefczak, A.
Materials 15 (2022) 3450
IF_{2022} = 3.4 $Ministerial\ points_{2024} = 140$

II. **Ultrasound measurements of particle shells in magnetic Pickering emulsions**
Jameel, B., Bielas, R., and Józefczak, A.
Measurement 220 (2023) 113409
IF_{2022} = 5.6 $Ministerial\ points_{2024} = 200$

III. **Magnetorheological characterization of oil-in-oil magnetic Pickering emulsions**
Jameel, B., Paulovičová, K., Tóthová, J., Rajňák, M., Molčan, M., Bielas, R., and Józefczak, A.
Journal of Magnetism and Magnetic Materials 588 (2023) 171433
IF_{2022} = 2.7 $Ministerial\ points_{2024} = 100$

IV. **Optimization of ultrasound heating with Pickering droplets using core-shell scattering theory**
Jameel, B., Harkavyi, Y., Bielas, R., and Józefczak, A.
Ultrasonics Sonochemistry (2024): *submitted, under review*

V. **Propagation of ultrasonic wave in magnetic Pickering emulsion under DC magnetic field**
Jameel, B., Hornowski, T., Bielas, R., and Józefczak, A.
Journal of Magnetism and Magnetic Materials 542 (2022) 168590
IF_{2022} = 2.7 $Ministerial\ points_{2024} = 100$

VI. **Magnetic pickering emulsions heated in a rotating magnetic field**
Bielas, R., Jameel, B., Skumiel, A., Timko, M., Kopčanský, P., and Józefczak, A.
Journal of Magnetism and Magnetic Materials 563 (2022) 169946
IF_{2022} = 2.7 $Ministerial\ points_{2024} = 100$

Abstract

Emulsions are inherently unstable systems that require emulsifiers to ensure their stability over time, and various types of emulsifiers exist, including surfactants and solid particles. Pickering emulsions refer to emulsion droplets stabilized by solid particles that accumulate at the droplet interface. Stabilizing emulsions with particles having magnetic properties leads to the transfer of these properties to Pickering droplets, making them responsive to external stimuli. However, Pickering emulsion stability depends on several factors, including particle wettability, concentration, size, and shape. Therefore, controlling the formation process is necessary to ensure droplet stability. In the last decades, efforts have been made to improve the formation process to achieve better stability, with reduced possibilities of aggregation, creaming, or sedimentation. Several methods for monitoring and controlling the formation process of Pickering droplets involve microscopy imaging and analytical techniques, with ultrasound spectroscopy emerging as a promising tool for investigating the internal structures of suspensions and emulsions.

The publications constituting this doctoral dissertation regard two main aspects of the study on magnetic Pickering emulsions: their characterization and their possible applications. Ultrasound waves are used to characterize oil-based suspensions and Pickering emulsions to provide valuable information on internal structures, such as particle size and aggregation rate, especially in high-viscosity media. Ultrasound scattering theory, based on the core–shell model, is employed to analyze measurement data from ultrasound attenuation spectroscopy, and the results demonstrate an ultrasound wave's ability to detect the sizes of particle shells around Pickering droplets, which is hard to control using other non-destructive methods. Magnetorheological measurements are also used to characterize oil-based magnetic fluid and magnetic Pickering emulsions, revealing changes in the viscoelastic response of Pickering emulsions prepared by different methods. Moreover, the rheological results show good agreement with ultrasound predictions.

Control over the parameters of fabricated Pickering emulsions, especially the shell thickness and core radius, is significantly important in several industrial and medical applications. Computational approaches coupled with numerical simulations thus provide the opportunity to optimize ultrasound heating using particle-covered droplets of various shell thicknesses and core radii and to control their ultrasound attenuation. Computer simulation results directly illustrate changes in temperature elevation and penetration depth inside agar phantoms doped with Pickering emulsions. Another potential application of tested systems could be magnetic separation, successfully investigated using an ultrasound method under

various gradient magnetic fields. When magnetic fields change over time, magnetic heating occurs, as shown in numerous reports on magnetic suspensions and among the magnetic Pickering emulsions herein.

This PhD dissertation consists of six chapters. Chapter 1 presents the fundamental concepts of Pickering emulsion formation and stability, along with the aspects of characterization and ultrasound scattering theory for two- and three-phase systems. Chapter 2 covers the experimental techniques used in my research related to Pickering emulsion formation methods, ultrasound spectroscopy measurements, magnetorheological measurements, and rotating magnetic field applications. Chapter 3 provides a concise summary of the papers constituting the thesis, describing the final achieved results and their connections with each other. Chapter 4 presents the conclusion of the PhD dissertation, while Chapter 5 contains the literature references and Chapter 6 the papers that constitute the core of the dissertation. The statements about the contributions of the co-authors of the papers are included in Chapter 7.

Abstract in Polish

Emulsje stanowią niestabilny z natury typ układów koloidalnych. Aby zapewnić im długotrwałą stabilność, konieczne jest zastosowanie dodatkowych materiałów zwanych emulgatorami. Do stabilizowania emulsji można wykorzystać zarówno substancje powierzchniowo-czynne (surfaktanty), jak i cząstki stałe. Emulsje stabilizowane przez cząstki stałe obecne na powierzchni kropel fazy rozproszonej nazywane są emulsjami Pickeringa. Jeśli cząstki stabilizujące taką emulsję posiadają własności magnetyczne, wówczas krople Pickeringa także uzyskują te własności, a cały układ staje się podatny na działanie zewnętrznych czynników, takich jak stałe pole magnetyczne. Stopień stabilizacji takich emulsji zależy od wielu parametrów, w tym rozmiaru, kształtu i zwilżalności cząstek, a także ich stężenia w układzie. Aby zapewnić stabilność emulsji Pickeringa konieczna jest zatem ścisła kontrola procesu jej otrzymywania. W ostatnich dekadach podejmowano liczne próby udoskonalenia procedury tworzenia emulsji w taki sposób, aby ograniczyć możliwość agregacji kropel, a także procesów sedymentacji i śmietankowania. Do tego celu wykorzystywano różne metody charakteryzowania emulsji Pickeringa, spośród których spektroskopia ultradźwiękowa pozwala na skuteczną analizę wewnętrznej struktury emulsji oraz zawiesin cząstek.

Prace naukowe wchodzące w skład niniejszej rozprawy doktorskiej dotyczą dwóch głównych aspektów badań magnetycznych emulsji Pickeringa: opisu ich własności oraz możliwych zastosowań. Fale ultradźwiękowe zostały wykorzystane do zbadania zawiesin cząstek oraz emulsji Pickeringa, co pozwoliło na uzyskanie informacji na temat wielkości cząstek i kropel, a także stopnia ich agregacji w ośrodkach o wysokiej lepkości. Jest to istotne ze względu na nieliczne badania w takich ośrodkach. Do analizy danych, pochodzących ze spektroskopii ultradźwiękowej, wykorzystano teorię opisującą rozpraszanie fal ultradźwiękowych, opartą o tak zwany *core-shell model*. Uzyskano dzięki niej informacje na temat grubości powłoki wokół kropel Pickeringa, co jest trudne do osiągnięcia przy pomocy innych nieniszczących metod pomiarowych. Dodatkowo, do dalszego opisu własności cieczy magnetycznych oraz magnetycznych emulsji Pickeringa wykorzystano badania magnetoreologiczne. Wykazały one różnice we własnościach lepkosprężystych badanych emulsji, w zależności od sposobu ich wytworzenia. Wyniki pokryły się z rezultatami badań ultradźwiękowych.

Kontrola parametrów emulsji Pickeringa, w szczególności wielkości kropel i grubości powłoki wokół nich, ma kluczowe znaczenie w zastosowaniach przemysłowych i medycznych. Obliczenia numeryczne w połączeniu z symulacjami komputerowymi pozwoliły na kontrolę i optymalizację efektywności nagrzewania ultradźwiękowego w fantomach z emulsjami, ze

względu na wielkość kropel oraz grubość powłoki wokół nich. Pokazano, że parametry te wpływają na tłumienie fal ultradźwiękowych, co skutkuje rożnym wzrostem temperatury i głębokością wnikania fal ultradźwiękowych. Za pomocą metody ultradźwiękowej zbadano także separację magnetyczną. Przy użyciu rotującego pola magnetycznego zaś scharakteryzowano efektywność nagrzewania magnetycznego w emulsjach Pickeringa.

Niniejsza rozprawa doktorska składa się z sześciu rozdziałów. W rozdziale 1 zaprezentowano podstawowe informacje dotyczące wytwarzania i stabilności emulsji Pickeringa, a także metody opisu ich własności. Przybliżono także wykorzystaną w przedstawianych pracach naukowych teorię rozpraszania fal ultradźwiękowych w ośrodkach dwu- i trójfazowych. Rozdział 2 zawiera opis metod eksperymentalnych wykorzystanych w pracy badawczej, związanych z wytwarzaniem emulsji Pickeringa, pomiarami spektroskopii ultradźwiękowej, pomiarami magnetoreologicznymi oraz zastosowaniem rotującego pola magnetycznego do uzyskania efektu termicznego. Rozdział 3 zawiera zwięzłe podsumowanie prac naukowych wchodzących w skład rozprawy, w tym opis uzyskanych wyników oraz ich wzajemne powiązanie. W rozdziale 4 przedstawiono końcowe wnioski rozprawy doktorskiej, natomiast w rozdziale 5 zestawiono wykorzystaną literaturę. Najważniejszą częścią całej pracy jest rozdział 6, który zawiera zbiór powiązanych tematycznie prac naukowych. W rozdziale 7 przedstawiono oświadczenia współautorów dotyczące wkładu w proces przygotowania i publikacji tychże prac.

List of symbols

Pickering emulsion

ΔG	The energy needed to detach a single particle from a liquid–liquid interface
r_p	Particle radius
γ_{c-d}	Interfacial tension between the continuous phase and dispersed phase
θ_c	Contact angle
r_e	Droplet radius
ρ_p	Particle density
n_e	Droplet number distribution
n_p	Particle number needed to stabilize all emulsion droplets

Magnetic Pickering emulsion

τ_N	Néel relaxation time
τ_0	Time constant
K	Anisotropy constant
V	Volume of a single particle core
k_B	Boltzmann constant
T	Temperature
τ_B	Brownian relaxation time
η	Viscosity
V_h	Hydrodynamic volume

Ultrasound propagation in colloidal system

A	Ultrasound amplitude
A_0	Initial amplitude
x	Propagation distance
t	Time
c	Ultrasound wave velocity
α	Ultrasound wave attenuation coefficient
A_s	Scattered wave amplitude
λ	Wavelength

θ	Scattering angle
A_i	Incident wave amplitude
ρ_{eff}	Effective density
β_{eff}	Effective compressibility

Ultrasound scattering theory

$\alpha_{thermal}$	Thermal attenuation coefficient
$\alpha_{viscous}$	Viscous attenuation coefficient
k_c	Wavenumber of compressional wave
k_T	Wavenumber of thermal wave
k_s	Wavenumber of shear wave
ω	Angular frequency
ρ	Density
C_p	Specific heat
κ	Thermal conductivity
η	Viscosity
φ_0	Potential of incident wave
A_n	Partial scattering amplitude
$j_n(kr)$	Spherical Bessel function
$h_n(kr)$	Spherical Hankel function
P_n	Legendre polynomial
φ_{c1}	Potential of the compressional wave propagating outside the object
φ_{t1}	Potential of the thermal wave propagating outside the object
$A_{\psi 1}$	Potential of the shear wave propagating outside the object
φ_{c2}	Potential of the compressional wave propagating inside the object
φ_{t2}	Potential of the thermal wave propagating inside the object
$A_{\psi 2}$	Potential of the shear wave propagating inside the object
A_n	Partial scattering amplitude of the compressional wave in the outward direction
B_n	Partial scattering amplitude of the thermal wave in the outward direction
C_n	Partial scattering amplitude of the shear wave in the outward direction
$A`_n$	Partial scattering amplitude of the compressional wave in the inward direction
$B`_n$	Partial scattering amplitude of the thermal wave in the inward direction

$C`_n$	Partial scattering amplitude of the shear wave in the inward direction
a_c	Normalized wavenumber of compressional waves in the continuous phase
a_T	Normalized wavenumber of thermal waves in the continuous phase
a_s	Normalized wavenumber of shear waves in the continuous phase
$a_c p$	Normalized wavenumber of compressional waves in the dispersed phase
a_Tp	Normalized wavenumber of thermal waves in the dispersed phase
$a_s P$	Normalized wavenumber of shear waves in the dispersed phase
b	Inner radius
a	Outer radius
x_c	Normalized wavenumber of compressional waves for the outer radius
x_T	Normalized wavenumber of thermal waves for the outer radius
x_s	Normalized wavenumber of shear waves for the outer radius
y_c	Normalized wavenumber of compressional waves for the inner radius
y_T	Normalized wavenumber of thermal waves for the inner radius
y_s	Normalized wavenumber of shear waves for the inner radius
b_c	Thermal factor for compressional waves
b_T	Thermal factor for thermal waves
c_0	Compressional velocity
c_s	Shear velocity
α_L	Thermal expansion coefficient
T	Temperature
$f(\theta)$	Far field scattering amplitude
β	Complex wavenumber of the scattered waves
ϕ	Volume fraction
N	Number of scattering objects

1. Introduction

Emulsions are types of colloidal systems made from two immiscible fluids, with one being dispersed in the other in droplet form. These colloids exhibit the classic behaviors of metastable colloids, i.e., reversible phase transitions due to droplet coalescence and interaction [1]. The most known emulsion system consists of oil droplets dispersed in water or vice versa, and it is widely used across many industries, such as the food industry, as encapsulated bioactive compounds [2]. Simultaneously, there are few reports on non-aqueous emulsions [3] despite their wide variety of possible applications, such as in cosmetics [4] and the pharmaceutical industry [5].

Emulsions are thermodynamically unstable and commonly require the presence of surfactants to improve their stability. These surfactants can be characterized in general as having a molecular structure and an association with the amphipathic group. The type of surfactant needed is determined based on the hydrophilic–lipophilic balance method in the emulsion system [6]. As such, the process of fabricating non-aqueous emulsions is more challenging, as it requires high-molecular-weight surfactants [7], which is why another method of stabilizing emulsion systems via the use of a solid particle is adopted. There are several advantages of using solid particles; for example, their stabilization includes a low concentration of stabilizers, and inversion of the emulsion is much easier by changing the surface properties of the particles [8].

A type of emulsion stabilized by solid particles accumulated on the droplet interface is called Pickering emulsion. In the last decade, the rapid development of materials technology has increased the variety of particles available, rendering Pickering emulsion an interesting technique in different industrial [9] and medical applications [10,11]. Because of this increased scientific interest, determining the stability of Pickering emulsions has become crucial, including the sizes of Pickering droplets and the concentration of particles on the droplet interface. Since the discovery of an emulsion stabilized by solid particles at the beginning of the 20th century by Ramsden and Pickering [1], ongoing research to develop a formation process is still in the improvement stage. Because of the additional third phase (comparison to emulsions having droplets without a particle coating), the characterization process is more challenging.

Several methods enable the characterization of Pickering emulsion properties, and these include small-angle X-rays or neutron scattering [12], dynamic light scattering [13], nuclear magnetic resonance [14,15], focused beam reflectance measurement [16], rheological measurement [17], and microscopy measurement [18], each of which has

limitations, one of the most common of which is the sample preparation requirement before testing. The ultrasound technique is one method having the advantage of being a non-destructive method for testing systems, and it does not require sample preparation. The ultrasound wave is successfully employed for characterizing emulsions and suspensions [19–22], but regardless, few works use ultrasound spectroscopy to characterize and control the formation process and stability of oil-in-water non-magnetic Pickering emulsions [23]. Furthermore, there are essentially no studies yet in the literature on the ultrasound characterization of oil-in-oil magnetic Pickering emulsions. This includes studies involving the calculation of the core radii of Pickering droplets, as well as the shell thickness of particles, which is significantly important in several applications.

This doctoral dissertation presents a study of a theoretical and experimental approach to ultrasound propagation in the colloidal system, including magnetic suspensions and magnetic Pickering emulsions, classified as follows:

1. **Characterization objectives:**

A. Studying the agglomeration rate in high-viscous-magnetic and non-magnetic suspensions.
B. Investigating sizes and stabilities of magnetic Pickering droplets by ultrasound wave.
C. Determining the magnetorheological effect in magnetic emulsion and fluid.

2. **Application objectives:**

D. Optimizing ultrasound heating with magnetic and non-magnetic Pickering emulsion.
E. Studying magnetic separation in magnetic Pickering emulsion using the ultrasound method.
F. Studying the influence of a rotating magnetic field on magnetic Pickering emulsions.

The overall results of the PhD dissertation provide essential information regarding the internal structure of Pickering emulsions, such as their droplet stability, droplet size, and aggregation rate. Furthermore, both theoretical and experimental methodologies for ultrasound wave propagation in colloidal systems were employed as an alternative to, e.g., dynamic light scattering, which is particularly beneficial for characterizing high-concentration and optically opaque systems, such as magnetic Pickering emulsions. The next sections contain a literature survey of the formation and characterization of Pickering emulsions, providing the basis for ultrasound wave measurements and for the implementation of the core–shell model for characterizing colloidal systems.

1.1. Pickering emulsion

An emulsion is a mixture of two (or more) immiscible liquids, that is, one liquid phase is dispersed in another liquid phase in the form of a droplet—commonly referred to as the dispersed phase—that is distributed in a carrier fluid (continuous phase). During the process of emulsion formation, known as emulsification, the free energy of the interface changes due to an increase in the total interfacial area and configurational entropy of the dispersion. As the free energy of the emulsion is higher than that of the system before emulsification, the emulsion droplet becomes thermodynamically unstable without stabilization, one of the results of which is the tendency of the droplets to coalesce over time.

There are diverse ways of reducing the free energy in the system and preventing the coalescence of emulsion droplets. To stabilize emulsions, low-molecular-mass surfactants, surface-active polymers, or solid nano- and microscale particles have been used, all three of which are used to reduce the interfacial tension between the dispersed phase and the continuous phase. The surfactants are characterized as molecular structures, known as amphipathic structures, and they have a hydrophilic head and hydrophobic tail. The surfactant properties can vary with numerous variations in the surfactant structure, such as single-tail or double-tail [24]. However, the concentration of the surfactant impacts the system's stability and the size of the emulsion droplets, where an increased amount of surfactant leads to a decrease in droplet sizes of the emulsion, as small droplets are more favorable for emulsion stability [25].

In opposition to surfactant-based emulsions, Pickering emulsions refer to emulsions stabilized by solid particles. Ramsden [26] and Pickering [27] first investigated this system, which is why the particle-stabilized emulsions are named after them. Despite pioneering works published over 100 years ago, substantial scientific interest in such emulsions has increased in the last decades with the increase in publications. In Pickering emulsions, solid particles attach to the droplet interface and reduce the interfacial tension. Thus, the energy needed to separate the single particle from a liquid–liquid interface can be written as follows [28]:

$$\Delta G = \pi r_p^2 \gamma_{c-d} (1 - |cos\theta_c|)^2, \quad (1)$$

where r_p is the particle radius, γ_{c-d} is the interfacial tension between the continuous phase and dispersed phase, and $|cos\theta_c|$ is the absolute value of the cosine function of the contact

angle, θ_c. In the case of 90° > θ_c, the particles will progress to the continuous phase; otherwise, if 90° < θ_c, the particles will progress to the dispersion phase, as shown in **Figure 1**.

Wettability is a key factor in Pickering emulsion stability, characterized by the contact angle at the liquid–liquid interface, as described by the Young equation [29]. For instance, if the particles are highly wetted by water, they are suitable for oil-in-water emulsion formation; when wetted by oil, however, they are suitable for water-in-oil emulsion [30]. The wettability of the particle may also be affected by the particle size. The different penetrations of particles on the droplet interface increase with a smaller particle size, as shown by the contact angle measurement [31]. The particle diameter, from 100 nm to 220 nm, resulted in contact angles of θ_c = 89.1 and 94.8, respectively.

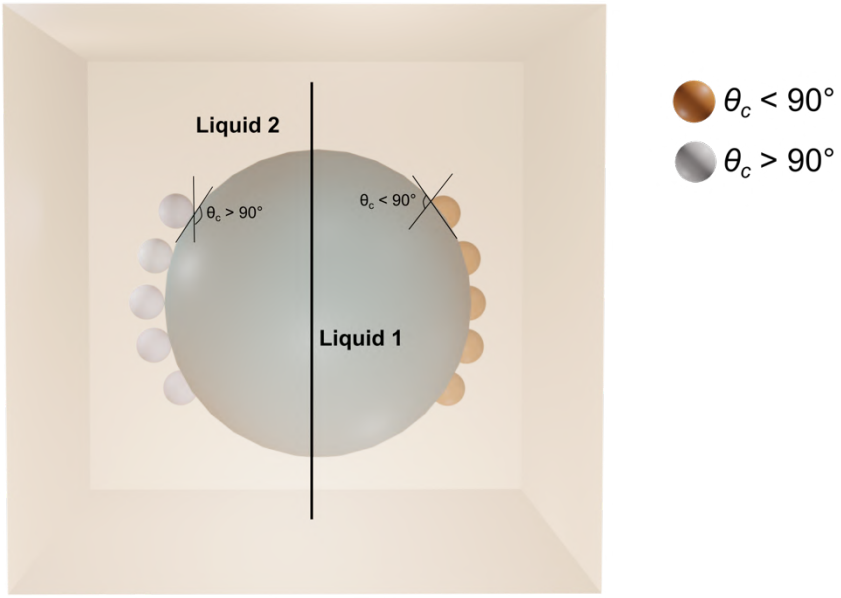

Figure 1 Schematic illustration of the behavior of particles placed at the liquid–liquid interface, depending on their contact angles (θ_c).

Using solid particles to stabilize emulsion droplets has an advantage compared to surfactants. For example, it eliminates skin irritation in cosmetic products that appear due to the surfactant [32], as well as can reduce overall environmental pollution [33]. When emulsion stability is measured using surfactants and solid particles (Pickering emulsion) for aqueous systems, both techniques reduced the interfacial tension between the liquid–liquid interface [34]. However, utilizing the solid particles for a stabilized non-aqueous system has

the advantage of being able to adsorb between the liquid–liquid interface, resulting in higher desorption energies [35].

An oil-in-oil emulsion system was reported for the first time in the 1960s [36,37], having found several applications in material science, such as the formation of polymer nanoparticles [38]. However, there are few reports in the literature related to oil-in-oil Pickering emulsion formation and characterization. For instance, the particle hydrophobicity was determined for oil-in-oil formation for fumed silica particles in a mixture of silicone oil and vegetable oil [3]. In turn, the two stages of fabrication were used to prepare Pickering emulsions and enhance the droplet stability of silicone oil droplets dispersed in castor oil stabilized by polystyrene particles [39], and ultrasound waves were used to follow this formation process in line [40]. The sedimentation rate of emulsion droplets was shown associated with the size of solid particles, and the increase in particle size had a proportional relation to Pickering droplet diameter [41]. The high particle concentration induced more particles adsorbed on the droplet interface, and this led to the oil-in-oil emulsion becoming more stable against coalescence [42].

The mass of stabilizing particles can be calculated from the following equation:

$$m_p = \frac{16}{3}\pi r_p \rho_p r_e^2 n_e, \quad (2)$$

where r_p and r_e are the radius of particles and droplets respectively, ρ_p is the particle density, and n_e is the assumption of the droplet number distribution, where the total number of particles required to stabilize all droplets is $n_p = \frac{4r_e^2 n_e}{r_p^2}$ [42]. The relation indicates the increasing required mass of particles with a higher number of droplets, as well as the droplet radius. The density of packing the particles on the droplet interface was determined to prevent droplet coalescence, which is why, for example, for an oil-in-water emulsion stabilized by poly (lactic-co-glycolic acid), the use of a particle with a radius of 330 nm lowers the interfacial tension compared with 1,150-nm particles [43].

Distinct types of solid particles, including inorganic particles, polymer particles, and food-grade particles, have been found to stabilize emulsion droplets [44]. These include gold [45], silica [46], zinc oxide [47], titanium dioxide [48], and iron oxide [49,50]. In addition, stabilization mechanisms are influenced by the different shapes and structure of the particle, such as ellipsoids, nanotubes, nanofibers, and other irregular shapes [51]. In addition to the shape and size of the particles, particle functionalization affects the long-term stability of emulsions. The compatibility between the oil-in-oil system and solid particle type and

function contributes significantly to the emulsion preparation. For example, the several types of surface groups of silica solid particles show the ability to form oil-to-oil double emulsion. The particles with higher hydrophilic properties (70% SIOH) were used to stabilize rapeseed oil or olive oil–silicone oil, where more hydrophobic particles (20% SIOH) enable the formation of a reversed system [52].

In the next section, iron oxide nanoparticles, serving as inorganic stabilizing particles, are introduced. The discussion encompasses their formation process and recent applications in the formation of colloidal systems.

1.2. Magnetic Pickering emulsion

Among many potential stabilizers, inorganic magnetic nanoparticles play a significant role in fabricating Pickering emulsions due to their variable functionality, biocompatibility, non-toxicity, and suitability for delivery to the body, which are crucial requirements for emulsifiers in biomedical and pharmaceutical applications [53]. Experimental results from Zhou et al. demonstrate that both unmodified and modified magnetic particles effectively stabilize oil-in-water Pickering droplets [49,50], and numerous other reports detail the use of magnetic nanoparticles to stabilize oil droplets dispersed in water [54] and water droplets dispersed in oil [55]. These droplets constitute a type of magneto-responsive colloidal system that can be influenced by external magnetic fields. For instance, magnetophoresis occurred for an oil-in-water monodispersed magnetic Pickering emulsion during the application of a static gradient magnetic field, and the separation velocity was determined in the microscopic scale with different pH levels [56]. The oil-in-water emulsion, stabilized by hydrophobic light-sensitive titanium dioxide ($\mathrm{Ti\ O_2}$) and hydrophilic superparamagnetic iron oxide ($\mathrm{Fe_3O_4}$), was utilized as the microreactor [57], and the magnetic nanoparticles coated with oleic acid were used to stabilize the water-in-oil Pickering emulsion; after that, water is dispersed in the continuous phase to fabricate a water-in-oil-in-water emulsion liquid membrane, which is used to extract the magnetic emulsion and remove wastewater [58].

An important feature of magnetic nanoparticles is their ability to function as heat sources under external time-varying magnetic field applications. The applied external alternating (or rotating) magnetic field leads to heat generation in the targeted system [59], where the heat dissipation of magnetic nanoparticles depends mainly on three mechanisms: the relaxation mechanism, hysteresis mechanism, and eddy current losses, all of which are related to the particle size, as well as other properties, such as the viscosity of the continuous phase. The relaxation mechanisms are classified as either Néel or Brownian [60], where the

former occur due to the magnetic moment reorientation to magnetic field lines, and it can be expressed as:

$$\tau_N = \tau_0 \, exp \left(\frac{KV}{k_B T}\right), \quad (3)$$

where τ_0 is a time constant, *K* is the anisotropy constant, *V* is the volume of the magnetic core, k_B is the Boltzmann constant, and *T* is the temperature.

Meanwhile, Brownian relaxation occurs due to the rotation of all nanoparticles to the magnetic field lines, and the viscosity η and hydrodynamic volume V_h proportionally influence time relaxation as follows:

$$\tau_B = \frac{3\eta V_h}{k_B T}. \quad (4)$$

The hysteresis mechanism is dominant, with a particle size exceeding the single domain size limit for particles (> 100 nm). In larger particles, induction of the eddy current mechanism also exists [61], dominating the particles with a centimeter scale. However, they can be neglected for iron oxide nanoparticles due to the low value of electrical conductivity, as well as the fast relaxation time of the nanoparticles.

Besides use in research on magnetic hyperthermia, magnetic hyperthermia combined with ultrasound thermal treatments is shown to optimize the efficiency of thermal therapy. Magnetic nanoparticle suspensions enhance ultrasound attenuation, as well as act as a source of heat under an external alternative magnetic field. The coupling of magnetic and ultrasound hyperthermia leads to a better performance with lower magnetic nanoparticle concentrations [62]. In the case of Pickering emulsions, control over the magnetic droplet size, as well as the magnetic concentration on the droplet interface, is needed to optimize hyperthermia treatment, as well as capsule formation, as the alternating magnetic field has been used recently for capsule formation via magnetic nanoparticles [63].

There are several challenges of using magnetic nanoparticles as a Pickering emulsion stabilizer, including the particle size and shape, particle–particle interaction, and the aggregation rate in the system. Moreover, the black color of the particle led to difficult optical control of the formation of the Pickering emulsion. Thus, one of the main goals of this thesis is to control the process of forming magnetic Pickering emulsions by characterizing their internal structure. The next section presents the methods available for Pickering emulsion characterization and comparison to ultrasound spectroscopy.

1.3. Characterization of Pickering emulsion properties

Key features must be investigated during the process of preparing Pickering emulsions, such as the contact angle between phases, droplet size distribution, surface charge, and droplet interaction resulting in coalescence or aggregation. The aspects of the characterization of Pickering emulsion are presented in **Figure 2**. The internal structure of the Pickering emulsion is strongly connected to the Pickering droplet properties, and as such, several methods are used to evaluate the process of Pickering emulsion formation and their stability, including experimental methods, such as microscopy imaging and analytical instruments [64,65].

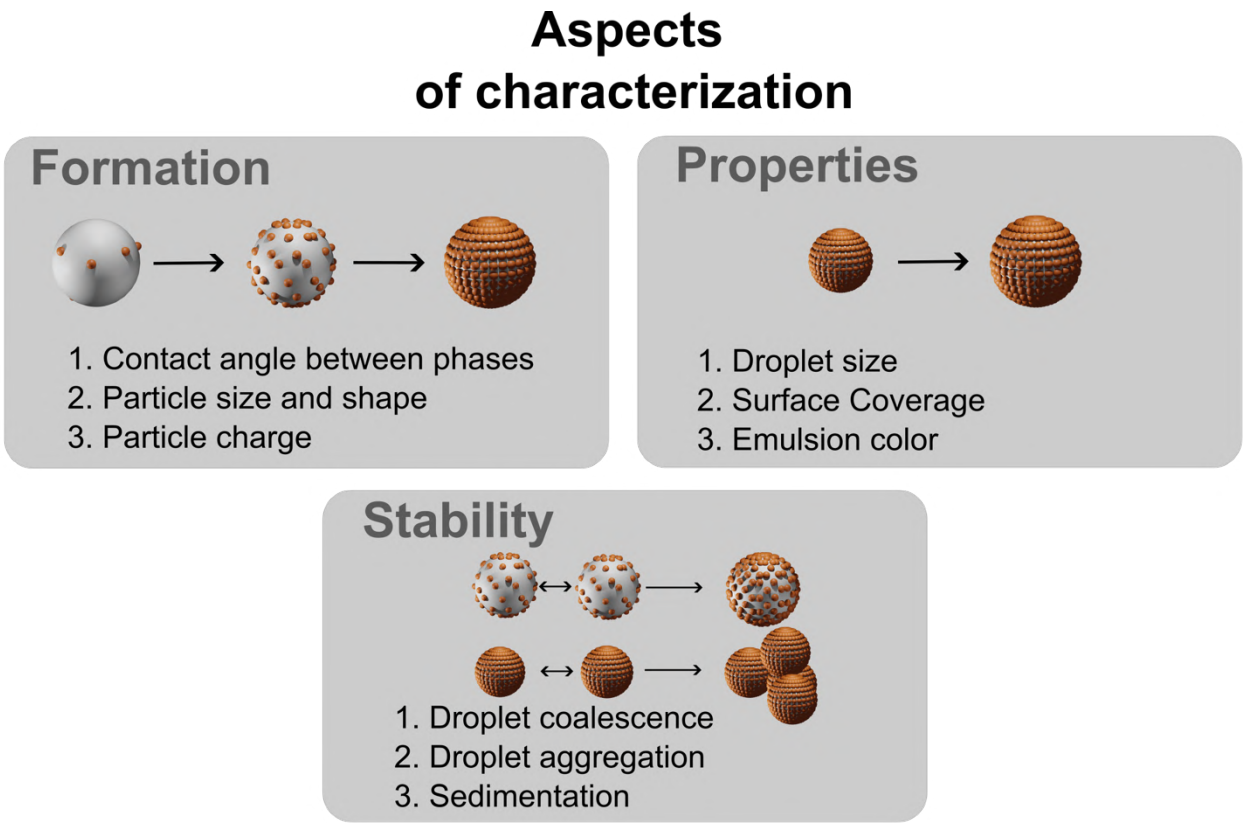

Figure 2 Schematic illustration of the various aspects of Pickering emulsion characterization.

There are several analysis methods combining the measurements with a mathematical model of material characterization, as presented in **Figure 3**, such as analyzing the light-scattering spectra to calculate the particle size distribution. The microscopy method is one of the types of experimental methods used to visualize the fine scale in the system, such as optical microscopy, electron microscopy, and atomic force microscopy. One of the

major limitations of microscopy is sample preparation, which involves altering the real structure of the material [66]. Another disadvantage is that microscopy measurement requires time, and time will vary based on the type of microscopy device. Analytical tools, on the other hand, such as dynamic light scattering, measure the intensity fluctuations of the scattering wave that occur over time. Light scattering leads to a change in particles' relative spatial location due to Brownian motion, and the frequency of these particles depends on their size, where smaller particles move faster than bigger ones. The mathematical model is used to analyze the scattering intensity of the particle size distribution [67,68]. For instance, oil-in-water Pickering emulsion was characterized in this way when using different concentrations of modified silica nanoparticles [69]. However, a major limitation is the requirement of a diluted sample to measure the scattering intensity of dynamic light scattering [67]. Moreover, there are recent results of using small-angle X-ray scattering (SAXS) together with the corresponding core–shell model to characterize nanoflowers [70]. Finally, the scattering model for analyzing the experimental data from SAXS, which characterized the stability of Pickering emulsion, was also used elsewhere [12].

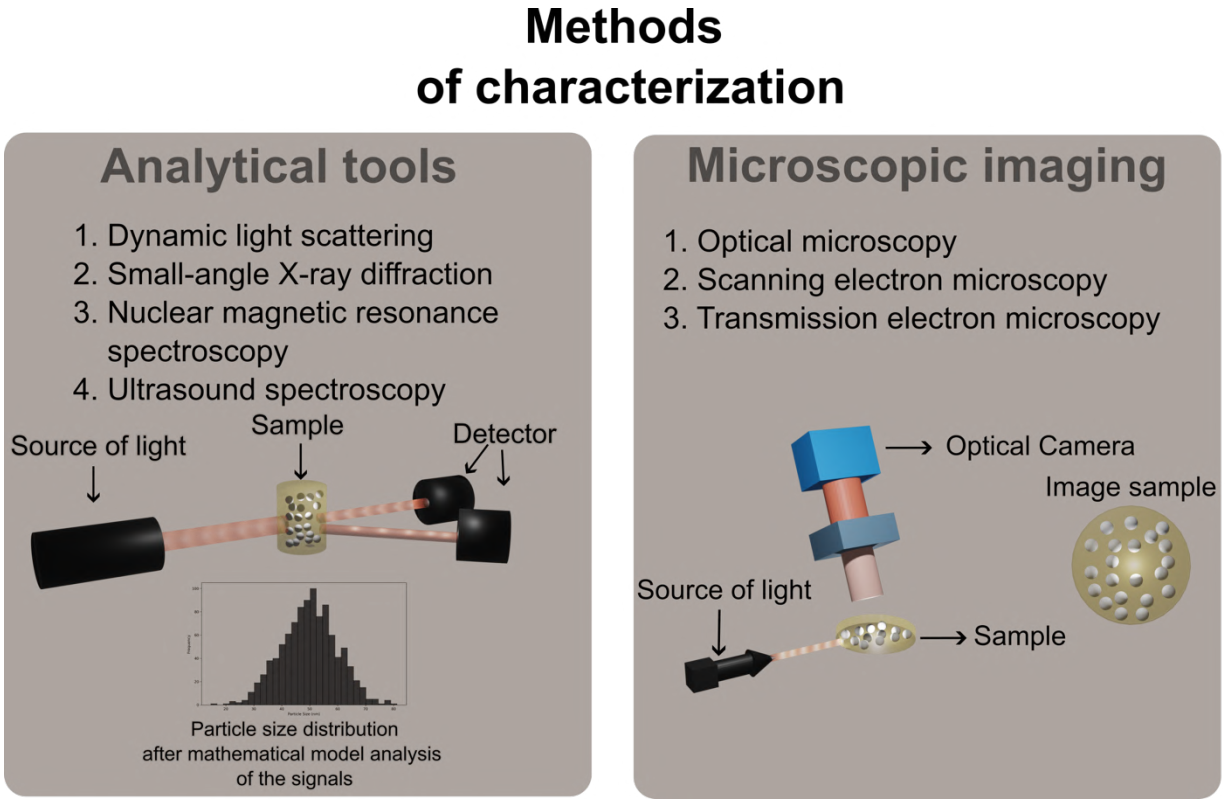

Figure 3 Schematic illustration of the methods of characterizing Pickering emulsions.

Ultrasonic spectroscopy is another promising method of emulsion characterization, as its properties, i.e., ultrasound attenuation and velocity, are primary properties of evaluating the internal structure, including the particle size distribution and concentration. Ultrasonic spectroscopy has a unique and important advantage over many traditional particle size-measuring technologies due to the possibility of the analysis emulsion which is a concentrated and optically opaque mixture without the need for any sample preparation in situ. Further, the determination of the crystallization and melting of the emulsion droplets was investigated by ultrasound wave [71]. However, a major limitation of the ultrasound technique is the requirement of a number of physicochemical properties of each phase to interpret the measurements. A concentration higher than 15% must extend ultrasound scattering theories to consider interactions between particles or droplets. The mathematical model of ultrasound propagation of the emulsion is thus used to convert ultrasound attenuation into information on droplet sizes. In the next section, the mathematical model of the ultrasound scattering theory is discussed in more detail.

1.4. Ultrasound propagation in a colloidal system

Ultrasound spectroscopy is an effective method for the characterization of colloidal systems, such as suspensions and emulsions. This technique has several advantages compared to others, such as the ability to be used in concentrated and optically opaque mixtures. Moreover, ultrasound wave was used to evaluate viscoelastic information in a non-destructive way without sample preparation requirements [72], which could provide information about the solid and liquid transition in materials during the fabrication process.

The energy of ultrasound decreases during propagation in the media due to the influence of different mechanisms. As a result, the waves are attenuated with a distance and the ultrasound amplitude decreases, as presented in the following formula [73]:

$$A = A_0 e^{i(\frac{\omega}{c}x-\omega t)} e^{-\alpha x}, \quad (5)$$

where the A_0 is the initial amplitude, x is the propagation distance, t is the time, c is the wave velocity, and α is the wave attenuation coefficient. The behavior of the wave depends primarily on the medium properties, where compressional ultrasound waves exist in liquid material and shear waves of the mechanical wave exist in more elastic/solid materials [74].

The experimental analysis of ultrasound velocity and attenuation are essential for physical interpretation purposes and material characterization. The many approaches to ultrasound scattering were used to reproduce the ultrasound properties and to analyze the experimental data in specific colloidal systems. The first investigation of the ultrasound scattering theory was in the 19th century [75], when Lord Rayleigh investigated the scattering of light or sound by particles. Rayleigh scattering is thus considered the elastic scattering of a wave by an object particulate much smaller than the wavelength of the incident wave [75]. Another type of scattering (known as Mie scattering) represents wave scattering by objects of a similar or larger size compared to the incident wavelength [76]. The power function law developed by Rayleigh can also be used to predict scattering amplitude, as shown in the following equation:

$$A_s \propto A_i \frac{1+\cos^2\theta}{\lambda^4}, \tag{6}$$

where A_s is the amplitude of the scattered wave for the wavelength λ at angle θ with incident wave amplitude A_i, and it is reversely proportional to the λ^4. Rayleigh used the partial wave expansion analysis of the sound wave scattered with particles, and the zero-order term of the amplitude was related to the compressibility contrast between the two phases (particle and medium). The first term was related to the density contrast between phases. In the zero term, the particle acts as a monopole radiator, whereas in the first term, it behaves as a dipole radiator.

Urick first developed the theoretical model for calculating sound attenuation, and the applicability of this calculation was examined by measurement of sand and kaolin suspension through the pulse–reflection method [77]. Moreover, Urick provided a simple method of determining the compressibility of a particle and liquid suspensions by measuring the sound velocity and density of both phases [78]. The weighted average was used to determine the effective density ρ_{eff} and effective compressibility β_{eff} related to the ultrasound velocity from the so-called Wood's equation:

$$c = \sqrt{\frac{1}{\rho_{eff}\beta_{eff}}}. \tag{7}$$

The velocity and attenuation of the emulsion were calculated based on the complex wavenumber expression by Urick and Ament [79]. Meanwhile, the novel theoretical development of the ultrasound scattering theory was attributable to Epstein, Carhart, Allegra,

and Hawley (ECAH) [80,81]. The ECAH theory describes the compressional ultrasound wave scattered by suspended spherical objects in the continuous phase and propagating toward an infinite distance. The theory was successfully used to characterize various colloidal systems, such as suspension [82] and emulsion [83]. The theory can also be used along with the measurement of the ultrasound pulses in emulsions and suspensions to obtain the characteristics of the medium, i.e., particle size, volume concentration, phase transition, particle interaction, particle compressibility, and creaming and sedimentation [73].

The further improved ultrasound scattering theory, including multiple scattering effects (described by Lloyd and Berry [84] and Waterman and Truell [85]) has been utilized for a wide range of concentrations for particle size determination [86]. Typographical errors in the original ECAH theory were further corrected by Challis et al. [22], and the boundary equations were implemented in matrix form. In addition, the complex wavenumber modification enabled the reproduction of the properties of polydisperse emulsions or suspensions using ultrasound data, which was also developed by Challis et al. [21,22], leading to an increase in characterization precision. Recently, viscoelastic ECAH theory has studied particle elasticity, demonstrating the ability to examine the mechanical properties of particles dispersed in a carrier fluid [20].

The suspensions of coated particles known as core–shell objects (encapsulated particles) are also studied by ultrasound scattering theory. The modification of the ECAH model with an additional shell phase was performed by Anson and Chivers in the ‘90s [87]. This model (known also as the core–shell model) can successfully calculate ultrasound properties in system, where classical ECAH was unable to or limited in investigating the system. The core–shell model was used by Hipp et al. [88] to simulate the influence of both thermal and shear waves on neighboring particles [89], and the Anson and Chivers model was recently successfully implemented to investigate the stability of droplets stabilized by solid particles [23]. One of the objectives of this thesis was to implement the core–shell model to investigate the acoustic properties of magnetic Pickering emulsions, depending on their formation process.

1.4.1. The Epstein–Carhart and Allegra–Hawley theory

The ECAH ultrasound scattering theory describes acoustic wave interactions with single spherical particles, where the wave scatters at the particle interface and propagates toward an infinity distance, such that the receiver is located at the infinity point to receive plane waves after scattering, as shown in **Figure 4**. In this section, the ECAH model is presented in detail.

The first work by Sewell et al. investigated the sound absorption of spheres dispersed as a fog [90]. After that, Epstein et al. modified the theory and calculated the influence of the densities between the dispersed phase and the continuous phase, which was correlated to the resulting viscous attenuation. After that, Epstein and Carhart [80] investigated a partial wave analysis of ultrasound scattering by fluid-suspended into a fluid continuous phase. The calculation included the thermal transport effect and shear effects of compressional wave propagation in liquid suspended in the liquid continuous phase. The total wave attenuation depends on the thermal, as well as on the viscous mechanism of attenuation, as shown in the following equation [21]:

$$\alpha = \alpha_{thermal} + \alpha_{viscous}. \quad (8)$$

Thermal attenuation is related to the heat cycles for heating to cooling during ultrasound pressure changes from higher to lower pressure, known as pressure–temperature coupling, which depends on the thermal contrast between phases. The thermal wave is generated as monopole radiation from the object, contributing to wave propagation and the penetration depth of the thermal wave depends on the thermal properties [86]. Viscous attenuation is related to the particle oscillating to the continuous phase during ultrasound wave propagation. The shear wave is generated around the spherical object as dipole radiation due to the object's movement, and this effect depends on the object's density and continuous phase viscosity, potentially making a lesser contribution to overall wave propagation in the case of the highly viscous continuous liquid phase. Further, the dipolar mode dominates with solid particles, i.e., suspensions, while the monopole mode dominates with liquid droplets, i.e., emulsions [91].

The theoretical calculation assumes the elastic droplets are dispersed in the continuous phase at a low concentration to avoid interactions between thermal and viscous waves. As well, the spherical object should be smaller than the wavelength. Allegra and Hawley [81] extended the theoretical calculation by introducing the influence of solid- and

liquid-dispersed particles in scattering theory. The partial wave analysis was used to calculate scattering coefficients for the dispersed object in the continuous phase.

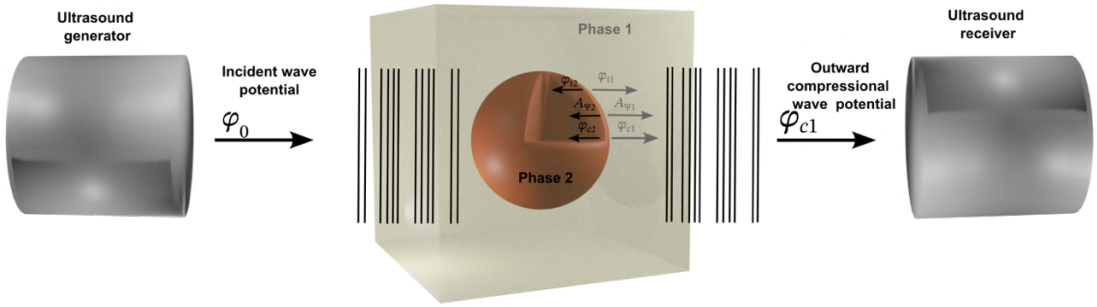

Figure 4 Schematic illustration of the compressional incident wave scattered by a spherical object suspended in the liquid phase, resulting in inward and outward propagation of the compressional, thermal, and shear waves.

The ultrasound scattering model based on Epstein and Carhart [80], Allegra, and Hawley's [81] calculations is a common formulation for modeling the scattering of the compressional wave by single particles. The model describes the scattering of the compressional incident wave by a single solid or liquid spherical object into thermal, shear, and compression waves.

Wave equations can be obtained from the conservation laws of mass, momentum, and energy and written as three ordinary differential equations, which can be solved separately to get the three wave potentials, as follows [81]:

$$(\nabla^2 + k_c^2)\varphi_c = 0, \quad (9a)$$

$$(\nabla^2 + k_T^2)\varphi_t = 0, \quad (9b)$$

$$(\nabla^2 + k_s^2)A_\Psi = 0, \quad (9c)$$

where φ_c, φ_t, and A_Ψ are the potentials of the compressional, thermal, and shear waves, respectively, and k_c, k_T, and k_s are the wavenumbers of the compressional, thermal, and shear waves, respectively, represented as follows:

$$k_c = \frac{\omega}{c} + i\alpha, \quad (10a)$$

$$k_T = (1+i)\left(\frac{\omega\rho C_p}{2\kappa}\right)^{\frac{1}{2}}, \quad (10b)$$

$$k_s = (1+i)\left(\frac{\omega\rho}{2\eta}\right)^{\frac{1}{2}}, \quad (10c)$$

where ω, c, α, ρ, C_p, κ, and η represent the angular frequency, ultrasound velocity, ultrasound attenuation, density, specific heat, thermal conductivity, and viscosity, respectively. In the case of a solid phase, $\eta = \frac{\mu}{-i\omega}$, where μ is the shear modulus.

Partial wave analysis is used to define the wave potential in both the continuous and dispersed phases, and the potential of incident wave can be described in the following equation:

$$\varphi_0 = \sum_{n=0}^{\infty} i^n (2n+1) j_n(k_{c1}r) P_n(cos\Theta), \quad (11)$$

where φ_0 is the incident wave potential, $j_n(k_{c1}r)$ the spherical Bessel function representing the inward wave, and P_n the Legendre polynomial representing the angular distribution of the field with several orders of *n*. Based on this, the monopole effect is related to *n* = 0, the dipole effect to *n* = 1, and the quadripole effect to *n* = 2 [21]. Moreover, the analysis with the spherical coordinators (*r, θ, z*) is used. Here, θ represents an angle toward the propagation direction, *z.*

As presented schematically in **Figure 4**, φ_{c1}, φ_{t1}, and $A_{\Psi 1}$ represent the potentials of the compressional, thermal, and shear wave propagating outside the scattering object, respectively:

$$\varphi_{c1} = \sum_{n=0}^{\infty} i^n (2n+1) A_n h_n(k_{c1}r) P_n(cos\Theta), \quad (12a)$$
$$\varphi_{t1} = \sum_{n=0}^{\infty} i^n (2n+1) B_n h_n(k_{T1}r) P_n(cos\Theta), \quad (12b)$$
$$A_{\Psi 1} = \sum_{n=0}^{\infty} i^n (2n+1) C_n h_n(k_{s1}r) p_n^1(cos\Theta), \quad (12c)$$

where $h_n(k_{c1}r)$ is the spherical Hankel function, which is the third kind of Bessel function used to represent wave propagation in the forward direction. The argument $k_{c1}r$ is the compressional wave number multiplied by the object radius, and A_n, B_n, and C_n are the partial scattering amplitudes of the compressional, thermal, and shear wave outward direction, respectively. Further, the φ_{c2}, φ_{t2}, and $A_{\Psi 2}$ represent the potential of compressional, thermal, and shear waves transmitted to propagate within the spherical object:

$$\varphi_{c2} = \sum_{n=0}^{\infty} i^n (2n+1) A`_n j_n(k_{c2}r) P_n(cos\Theta), \quad (13a)$$
$$\varphi_{t2} = \sum_{n=0}^{\infty} i^n (2n+1) B`_n j_n(k_{T2}r) P_n(cos\Theta), \quad (13b)$$
$$A_{\Psi 2} = \sum_{n=0}^{\infty} i^n (2n+1) C`_n h_n(k_{s2}r) P_n^1(cos\Theta), \quad (13c)$$

where $j_n(k_{c2}r)$ is the spherical Bessel function representing the wave propagation inside, and the argument $k_{c2}r$ is the wavenumber multiplied by radius. In addition, $A`_n$, $B`_n$, and $C`_n$represent the amplitudes of the transmitted wave propagating within the object.

These six wave potential equations (**Equation 12-13**) can be obtained by applying the six boundary condition equations to the spherical object interface. The boundary equation is applied to each partial wave order independently, whereas in Challis et al. [22], the six-boundary equation is implemented in matrix form with six unknown parameters:

$$[d] \begin{bmatrix} A_n \\ B_n \\ C_n \\ A`_n \\ B`_n \\ C`_n \end{bmatrix} = - \begin{bmatrix} -ac\ j'[ac] \\ -j[ac] \\ -XX\ ((as^2-2ac^2)j[ac] - 2ac^2\ j''[ac]) \\ -XX(ac\ j'[ac]-j[ac]\ ) \\ -bc\ j[ac] \\ -\kappa\ ac\ bc\ j'[ac] \end{bmatrix}, \quad (14)$$

where [*d*] represents the six boundary equations of the radial velocity, radial pressure, tangential velocity, tangential pressure, temperature, and heat flux, as derived by Epstein and Carhart [80] and Allegra and Hawley [81]:

$$[d] = \begin{bmatrix} d_{11} & d_{12} & d_{13} & d_{14} & d_{15} & d_{16} \\ d_{21} & d_{22} & d_{23} & d_{24} & d_{25} & d_{26} \\ d_{31} & d_{32} & d_{33} & d_{34} & d_{35} & d_{36} \\ d_{41} & d_{42} & d_{43} & d_{44} & d_{45} & d_{46} \\ d_{51} & d_{52} & d_{53} & d_{54} & d_{55} & d_{56} \\ d_{61} & d_{62} & d_{63} & d_{64} & d_{65} & d_{66} \end{bmatrix}. \quad (15)$$

The column vector on the left-hand side of **Equation 14** represents the value of the unknown partial amplitude of the wave propagation outward of the compressional (A_n) thermal (B_n), and shear waves (C_n), as well as inward of the compressional ($A`_n$), thermal ($B`_n$), and shear waves ($C`_n$). Meanwhile, the right-hand side of the matrix in **Equation 14** represents the value of the incident field.

The 6×6 matrix elements in **Equation 15** are summarized in **Appendix A** in the form they were used in the Wolfram Mathematica 13.2 software. In the matrix equations listed there, *c*, *T*, and *s* refer to the compressional, thermal, and shear waves, respectively. Based on these, a_c, a_T, and a_s refer to the wavenumber, normalized in the continuous phase of the compressional, thermal, and shear waves, respectively:

$$a_c = k_c r, \quad (16a)$$
$$a_T = k_T r, \quad (16b)$$
$$a_s = k_s r. \quad (16c)$$

In turn, $a_c p$, $a_T p$, and $a_s p$ refer to the normalized wavenumber according to the wavenumber of the dispersed phase for the compressional, thermal, and shear waves, respectively.

The generalized Allegra and Hawley model, which calculates the partial scattering amplitude of either liquid or solid dispersion, refers to so-called wild-card variables represented in the Challis et al. version of the ECAH model as [22]:

$$XX = \eta, \quad (17a)$$
$$XXp = \frac{\mu}{-(i\omega)}, \quad (17b)$$

where η is the shear viscosity and μ is the shear modulus. These wild cards can be determined depending on the material properties of the analyzed system using either solid or viscous terms.

1.4.2. Core–shell model

In the previous section, the description of ultrasound wave scattering by either solid or liquid was presented based on the ECAH theory. However, an ultrasound scattering theory modification, including the third phase, is calculated by Anson and Chivers [87] as a so-called core–shell model. This alternative approach involves calculating the acoustic properties of particles with additional surface modifications dispersed in the continuous phase, as presented in **Figure 5**. The thermal and shear effect are included in the model developed by Anson and Chivers, similar to the ECAH model, and the incident compressional wave is transmitted to a particle covered with a shell. The thermal and shear waves are then produced at both interfaces, in addition to scattered compressional waves.

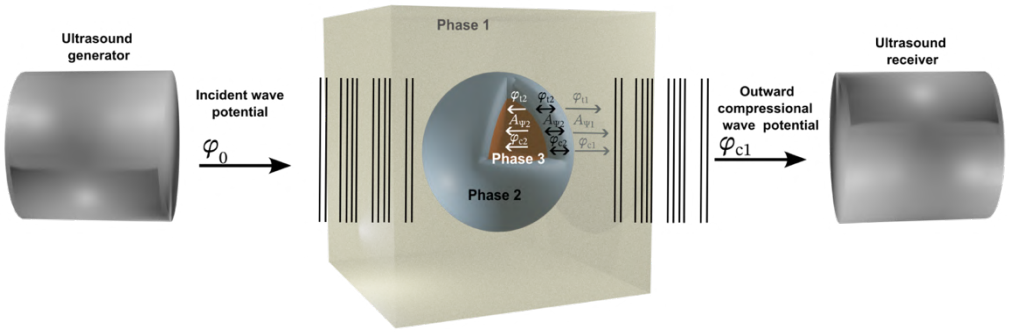

Figure 5 Schematic illustration of the incident compressional wave scattered by a spherical core–shell object, resulting in inward and outward propagation of the compressional, thermal, and shear waves in the presence of the shell layer.

Similar to the ECAH theory, there are three types of waves generated after the incident wave is transmitted to the core–shell object, represented by three wave potentials: compressional, thermal, and shear. These waves travel outward in the shell-continuous phase (phase 2-1) interface and the continuous phase (phase 1), and they travel inward in the core–shell (phase 2-3) interface and core (phase 3), as shown schematically in **Figure 5**.

Further, partial wave analysis can be used to obtain the wave potential, such that the incident compressional wave is represented by:

$$\varphi_0 = \sum_{n=0}^{\infty} i^n (2n+1) j_n(k_{c1}r) P_n(cos\Theta), \quad (18)$$

where j_n is the Bessel spherical function of the order *n*. The potentials of scattered waves in the continuous phase are given in the order of the compressional, thermal, and shear modes, respectively, similar to the ECAH model in **Equation 12**:

$$\varphi_{c1} = \sum_{n=0}^{\infty} i^n (2n+1) A_n h_n(k_{c1}r) P_n(cos\Theta), \quad (19a)$$
$$\varphi_{t1} = \sum_{n=0}^{\infty} i^n (2n+1) B_n h_n(k_{T1}r) P_n(cos\Theta), \quad (19b)$$
$$A_{\Psi 1} = \sum_{n=0}^{\infty} i^n (2n+1) C_n h_n(k_{s1}r) P_n^1(cos\Theta), \quad (19c)$$

where φ_{c1} is the potential of the scattering wave for the compressional wave in the continuous phase, A_n is the partial scattering amplitude in the continuous phase, h_n is the Hankel function, $k_{c1}r$ is the complex wave number multiplied by the object radius, P_n is the Legendre polynomials of the order *n*, and Θ is the scattering angle, similar to that presented in the previous section. Similarly, the potential of the thermal and shear waves was calculated by considering the thermal and shear wavenumbers k_{T1} and k_{s1}. Therefore, φ_{t1} is related to the potential of the thermal wave, and B_n is related to the partial amplitude of the thermal

wave. In turn, $A_{\Psi 1}$ is related to the potential of the shear wave in the continuous phase, and C_n is related to the partial wave amplitude of the shear wave.

The wave scattered outward (the boundary between the droplet shell and continuous phase) and inward (the boundary between the droplet shell and core), and it can be expressed as the following equations for the compressional, thermal, and shear waves, respectively:

$$\varphi_{c2} = \sum_{n=0}^{\infty} i^n (2n+1)[D_n j_n(k_{c2}r) + G_n h_n(k_{c2}r)]P_n(cos\Theta), \quad (20a)$$

$$\varphi_{t2} = \sum_{n=0}^{\infty} i^n (2n+1)[E_n j_n(k_{T2}r) + H_n h_n(k_{T2}r)]P_n(cos\Theta), \quad (20b)$$

$$A_{\Psi 2} = \sum_{n=0}^{\infty} i^n (2n+1)[F_n j_n(k_{s2}r) + I_n h_n(k_{s2}r)]P_n^1(cos\Theta), \quad (20c)$$

where D_n, E_n, and F_n are the partial wave amplitudes of the inward of the three potential waves, and G_n, H_n, and I_n are the partial wave amplitudes for the three modes of the outward wave.

In the core, the wave potentials are written similar to those in the continuous phase, but the outward propagating waves (represented by the Hankel function h_n) are replaced with the Bessel function, similar to in ECAH model in **Equation 13**:

$$\varphi_{c3} = \sum_{n=0}^{\infty} i^n (2n+1) J_n j_n(k_{c3}r)P_n(cos\Theta), \quad (21a)$$

$$\varphi_{t3} = \sum_{n=0}^{\infty} i^n (2n+1) K_n j_n(k_{t3}r)P_n(cos\Theta), \quad (21b)$$

$$A_{\Psi 3} = \sum_{n=0}^{\infty} i^n (2n+1) L_n j_n(k_{s3}r)P_n^1(cos\Theta), \quad (21c)$$

where J_n, K_n, and L_n are the partial wave amplitudes of the inward of the three potential compressional, thermal, and shear waves, respectively.

In the core–shell model, two sets of boundary equations are used in the calculation. The first is the boundary equation between the shell (phase 2) and the core (phase 3), and the second boundary equation is between the shell (phase 2) and the continuous phase (phase 1), similar to the equation used in the ECAH theory. The two boundaries in the calculation resulted in 12 boundary equations and 12 unknown coefficients, the former of which were formatted as a 12×12 matrix equation, as follows:

$$[M1]\begin{bmatrix} A_n \\ B_n \\ C_n \\ D_n \\ E_n \\ F_n \\ G_n \\ H_n \\ I_n \\ J_n \\ K_n \\ L_n \end{bmatrix} = \begin{bmatrix} C_1 \\ C_2 \\ C_3 \\ C_4 \\ C_5 \\ C_6 \\ 0 \\ 0 \\ 0 \\ 0 \\ 0 \\ 0 \end{bmatrix}. \quad (22)$$

The left-hand side of **Equation 22** includes the multiplication of 12 unknown parameters A_n, B_n, C_n, D_n, E_n, F_n, G_n, H_n, I_n, J_n, K_n, and L_n by [M1] representing the boundary equations for scattered and transmitted wave. The equation elements of the [M1] matrix in **Equation 22** are presented in **Appendix B** in the form they were used in the Wolfram Mathematica 13.2 software. In **Equation 23**, the first three columns represent the wave propagation outward in the continuous phase, and the last three columns are related to the inward wave propagation inside the core material. Columns four through nine are related to the inward and outward wave propagations in the shell material, and in some cases, the thermal effect can be neglected in the calculation that leads to a decreased number of matrix elements. The elements columns related to the thermal properties of the system are the second column, which represents the outward propagation of the thermal wave in the continuous phase, the column number eleven represent the inward thermal wave in the core phase, and the fifth and eighth columns are related to the inward and outward thermal wave propagations for the shell material. This modification can be used to reduce the complexity of the calculation in the case of using a system in which the viscous effect dominates compared to the thermal effect. The same technique can simplify the matrix to neglect the shear wave in the case of the thermal wave's contribution by removing the matrix element related to the shear effect:

Wave propagating in an outward direction (continuous phase)

Wave propagating in outward and inward direction (shell phase)

Wave propagating in an inward direction (core phase)

$$[M1] = \begin{bmatrix} m_{11} & m_{12} & m_{13} & m_{14} & m_{15} & m_{16} & m_{17} & m_{18} & m_{19} & 0 & 0 & 0 \\ m_{21} & m_{22} & m_{23} & m_{24} & m_{25} & m_{26} & m_{27} & m_{28} & m_{29} & 0 & 0 & 0 \\ m_{31} & m_{23} & m_{23} & m_{34} & m_{35} & 0 & m_{37} & m_{38} & 0 & 0 & 0 & 0 \\ m_{41} & m_{24} & m_{23} & m_{44} & m_{45} & 0 & m_{47} & m_{48} & 0 & 0 & 0 & 0 \\ m_{51} & m_{25} & m_{23} & m_{54} & m_{55} & m_{56} & m_{57} & m_{58} & m_{59} & 0 & 0 & 0 \\ m_{61} & m_{26} & m_{23} & m_{64} & m_{65} & m_{66} & m_{67} & m_{68} & m_{69} & 0 & 0 & 0 \\ 0 & 0 & 0 & m_{74} & m_{75} & m_{76} & m_{77} & m_{78} & m_{79} & m_{7,10} & m_{7,11} & m_{7,12} \\ 0 & 0 & 0 & m_{84} & m_{85} & m_{86} & m_{87} & m_{88} & m_{89} & m_{8,10} & m_{8,11} & m_{8,12} \\ 0 & 0 & 0 & m_{94} & m_{95} & 0 & m_{97} & m_{98} & m_{99} & m_{9,10} & m_{9,11} & 0 \\ 0 & 0 & 0 & m_{10,4} & m_{10,5} & 0 & m_{10,7} & m_{10,8} & m_{10,9} & m_{10,10} & m_{10,11} & 0 \\ 0 & 0 & 0 & m_{11,4} & m_{11,5} & m_{11,6} & m_{11,7} & m_{11,8} & m_{11,9} & m_{11,10} & m_{11,11} & m_{11,12} \\ 0 & 0 & 0 & m_{12,4} & m_{12,5} & m_{12,6} & m_{12,7} & m_{12,8} & m_{12,9} & m_{12,10} & m_{12,11} & m_{12,12} \end{bmatrix}. \quad (23)$$

In the 12 boundary equations, two radii are utilized: the inner radius (*b*) and the outer radius (*a*). Therefore, the normalized wave numbers of the compressional, thermal, and shear waves were used for each phase based on these radii, as in the following equations:

$$x_c = k_c a, \quad (24a)$$
$$x_T = k_T a, \quad (24b)$$
$$x_S = k_s a, \quad (24c)$$

$$y_c = k_c b, \quad (25a)$$
$$y_T = k_T b, \quad (25b)$$
$$y_s = k_s b. \quad (25c)$$

In the case of the matrix element for thermal mode, the thermal factors are needed and are referred to in the boundary equation as b_c and b_T. In the solid phase, they can be presented as in following equations:

$$b_c = \frac{-\gamma}{c_0^2 \alpha_L}[\omega^2 - (\frac{c_0^2}{\gamma} + \frac{4\mu}{3\rho})k_c^2], \quad (26a)$$
$$b_T = \frac{-\gamma}{c_0^2 \alpha_L}[\omega^2 - (\frac{c_0^2}{\gamma} + \frac{4\mu}{3\rho})k_T^2], \quad (26b)$$

where b_c depends on the compressional wavenumber k_c and b_T depends on the thermal wave number k_T. The same thermal factors also exist in the liquid phase with the conversion of the shear modulus: $\mu = -i\omega\eta$. In addition, γ is the heat capacity ratio $\gamma = 1 + \frac{c^2\alpha_L^2 T}{C_p}$, where C_p is the specific heat, α_L is the thermal expansion coefficient, and *T* is the temperature in kelvins. As well, c_0 is the compressional velocity $c_0 = \sqrt{c - \frac{4}{3}c_s}$, and c_s is the shear velocity.

In the liquid phase, the thermal factor can be described using the following equations:

$$b_c = \frac{-\gamma}{c^2\alpha_L}[\omega^2 - (\frac{c^2}{\gamma} - \frac{4i\omega\eta}{3\rho})k_c^2], \quad (27a)$$

$$b_T = \frac{-\gamma}{c^2\alpha_L}[\omega^2 - (\frac{c^2}{\gamma} - \frac{4i\omega\eta}{3\rho})k_T^2]. \quad (27b)$$

The main objective of the boundary equation calculation is to determine the partial scattering amplitude A_n. The coefficient A_n is required in the calculation of attenuation and velocity of the compressional wave, which could be used in analysis of the experimental results.

1.4.3. Complex wavenumbers of two- and three-phase systems

The acoustic wave is scattered from the objects that are randomly distributed in the system, and the scattering amplitude in the far field of the scatterer depends on the angle related to the axis. In the effective wavenumber calculation, it is necessary to calculate the partial compressional wave amplitudes for both two- and three-phase systems:

$$f(\theta) = \frac{1}{ik_c}\sum_{n=0}^{\infty}(2n+1)A_nP_n(cos\Theta), \quad (28)$$

where $f(\theta)$ is the far field scattering amplitude, and A_n is the partial scattering amplitude calculated for either the ECAH or the core–shell model [22]. Waterman and Truell calculated the forward and backward scattering of the wave by individual objects [85], as follows:

$$\left(\frac{\beta}{k_c}\right)^2 = 1 + \frac{4\pi N}{k_c^2}f(0) + \frac{4\pi^2N^2}{k_c^4}[f^2(0) - f^2(\pi)]. \quad (29)$$

The forward scattering wave, including just monopole scattering $f(0) = f(\pi)$, was derived by Foldy et al. [92]:

$$\left(\frac{\beta}{k_c}\right)^2 = 1 + \frac{4\pi N}{k_c^2} f(0), \tag{30}$$

where:

$$f(0) = \frac{1}{ik_c}\sum_{n=0}^{\infty}(2n+1)A_n, \tag{31a}$$

$$f(\pi) = \frac{1}{ik_c}\sum_{n=0}^{\infty}(-1)^n(2n+1)A_n. \tag{31b}$$

After substituting **Equations 31a** and **31b** into **Equation 29**, the effective wave number equation can be finally developed as:

$$\beta = \sqrt{k_c^2 - \frac{3i\phi}{(k_c^3)(r^3)}(A_0 + 3A_1 + 5A_2)}. \tag{32}$$

Here, $\beta = \frac{\omega}{c_{system}} + i\alpha_{system}$ is the complex wavenumber of the scattered wave, ϕ is the volume fraction of the dispersed phase $\phi = \frac{4}{3}\pi r^3 N$, N is the number of objects (dispersed phase) distributed in the continuous phase, and r the radii of the object. In the case of the core–shell model, *r = a*, where *a* is the outer radius of the core–shell object. The scattering coefficient A_n is obtained by solving the matrix equation above.

An additional modification of the wave number equation was performed by Challis et al. [22], which incorporates the polydispersity of the system:

$$\beta = \sqrt{k_c^2 - \sum_{j=1}^{J}\frac{3i\phi_j}{k_c^3 r_j^3}(A_{0j} + 3A_{1j} + 5A_{2j})}, \tag{33}$$

where *j* represents the change in the radius of the particles based on the histogram distribution. In addition, the partial scattering amplitude A_{nj} is also calculated with different values of *j*.

The ultrasound scattering theory, developed by Epstein and Carhart [80] and Allegra and Hawley [81], offers the ability to calculate the partial scattering amplitude of the compressional wave in the continuous phase after scattering via a spherical suspension object. This model finds application in the examination of both solid suspensions and liquid

emulsion droplets, including thermal effects. Moreover, Anson and Chivers [87] enhance the ECAH theory by considering the influence of a third phase, an additional layer surrounding the core. Consequently, this PhD study is devoted to utilizing the ultrasound scattering theory to predict ultrasound attenuation in a suspensions and a magnetic Pickering emulsions.

Employing solid particles to stabilize emulsion droplets presents a promising approach to oil-in-oil emulsions. Nevertheless, effective control of the formation of solid particles on the droplet interface profoundly impacts the system's stability efficiency. Emulsion characterization encompasses several crucial techniques, including microscopy imaging and analysis methods, such as dynamic light scattering and X-ray diffraction. In this PhD research, ultrasound spectroscopy was selected as the experimental technique for characterizing the formation process and internal structure due to its unique capability to investigate concentrated systems without requiring sample preparation.

2. Experimental techniques

The experimental section of this dissertation describes the methods of the fabrication of magnetic Pickering emulsions, the measurement of ultrasound waves, magnetorheological tests, and the application of rotating magnetic fields to magnetic Pickering emulsions as they were used in the papers constituting this thesis.

2.1. Fabrication of magnetic Pickering emulsions

As mentioned in sections 1.1 and 1.2, this research focused on investigating oil-in-oil emulsions, and in the case of magnetic Pickering emulsions, important factors must be investigated to improve the formation process, such as the number of particles on the droplet interface and droplet size distribution. Several factors make the oil-in-oil system an attractive choice, including the high viscosity of the continuous phase, providing long-term stability against sedimentation, especially during measurements. In addition, the oil polarity of the oil-in-oil system helps to utilize the direct current (DC) electric field to enhance droplet stabilization by solid particles [39,40].

In the experiments, castor oil (MA 220-1, MERLIN, Spain), a natural oil produced from the castor seed plant, known as Ricinus communis, represented the continuous phase of the oil-in-oil emulsion [93]. The unique chemical structure and renewable properties of castor oil have led to its use in various industrial applications, such as the chemical industry [94], as well as in medical applications as a drug delivery vehicle for nonpolar drugs [95,96]. Silicone oil (Rhodosil Oils 47V 50, VWR Chemicals, USA) represented the dispersed phase of the oil-in-oil emulsion, which is the hydrophobic polymeric liquid that constitutes silicon–oxygen bonds [97]. The density match between castor oil and silicone oil provided better stability compared to, for instance, water-in-oil systems. Long-term stability is further crucial for accurately characterizing emulsions through optical and ultrasound measurements. Although oil-in-oil emulsions have not been extensively studied in the literature compared to oil-in-water or water-in-oil emulsions, it was presented recently that the nanoparticle functionality influences silicone droplet stability in castor oil. Meanwhile, stabilizers with hydrophilic properties showed better stability due to proper wettability, measured according to the contact angle between phases [98].

In this dissertation, iron oxide (iron [II, III] oxide) hydrophilic nanoparticles, purchased in powder form from Sigma-Aldrich Co. (St. Louis, MO, USA, product no. 310069), were

utilized as stabilizers for silicone oil droplets dispersed in castor oil. Ultrasound homogenization is a popular method for fabricating emulsions in bulk quantities; therefore, the first method of fabricating magnetic Pickering emulsions involved ultrasound homogenization of all substances, including the stabilizing particles and oils, using the ultrasound homogenizer Sonopuls HD 3100 (Bandelin, Germany) at a working frequency of 20 kHz, as illustrated in **Figure 6a**.

Taking ultrasound homogenization as a basic approach, additional strategies could be employed to enhance droplet stability and increase the number of particles on the droplet interface. Several factors may also prevent droplets from being fully covered, such as a lower particle concentration compared to the dispersed oil, known as a limited coalescence regime, or variations in particle shape and surface functionality. An external DC electric field was applied to promote coalescence of partially stable droplets (prepared via ultrasound homogenization), as depicted in **Figure 6b**, and interactions between droplets under a DC electric field occur in liquids of low conductivity subjected to an electrical potential difference, resulting in free charges on the droplet interface.

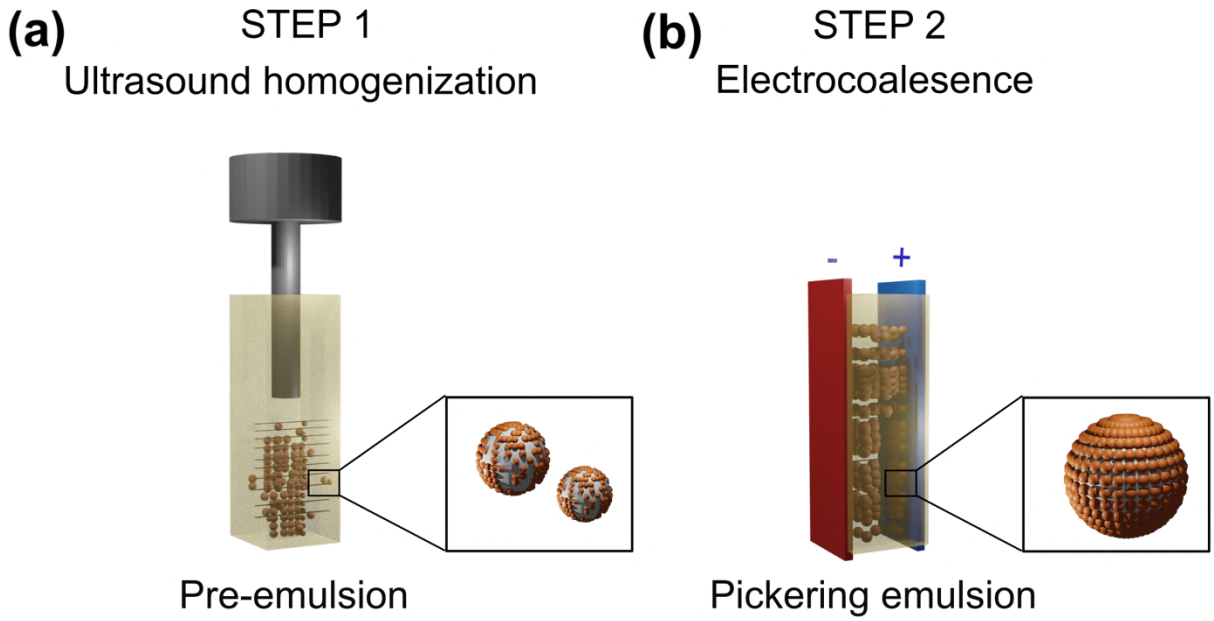

Figure 6 Scheme of the two-step fabrication of magnetic Pickering emulsions: (a) ultrasound homogenization and (b) electrocoalesence under a direct current (DC) electric field.

In addition to using magnetic particles for stabilizing Pickering emulsions, a non-magnetic material was tested in suspensions investigated using ultrasound spectroscopy. The silica particles from Sigma-Aldrich Co. (St. Louis, MO, USA, product no. 637246) were

dispersed in castor oil in one of the experiments, and silica particles were chosen, as they exhibit unique properties, including high chemical stability, biocompatibility, and targeted and controlled release [99].

2.2. Ultrasonic measurements

The ultrasound system consisted of two ultrasound piezoelectric broadband transducers—a transmitter and a receiver (OLYMPUS, USA)—driven by an ultrasound generator (OPBOX 2.1 from OPTEL, Poland, with UT probe adapter, model AD-1T, version RC-1N50). In all experiments, the technique based on the transmission method was used to measure the ultrasound attenuation in the system. A broadband ultrasonic signal was transmitted through water to the sample cell and subsequently detected by the receiver, with the signal recorded at a sample frequency of 100 MHz. The ultrasonic waveform changed with the internal structure, such as the object size, sedimentation, and aggregation. As the ultrasound properties in the sample are temperature-dependent, all measurements were conducted at a temperature of 25 ± 0.2°C using a thermostat setup, and the ultrasonic wave propagated through the water and the sample, as shown in **Figure 7**. The system was designed using the AutoCAD software and printed using a 3D printer, which enabled adjustments specific to experimental scenarios. The sample cell for suspensions and emulsions used in the experiments was the standard polystyrene sample cell used for spectroscopic measurements (45mm×10 mm×10mm).

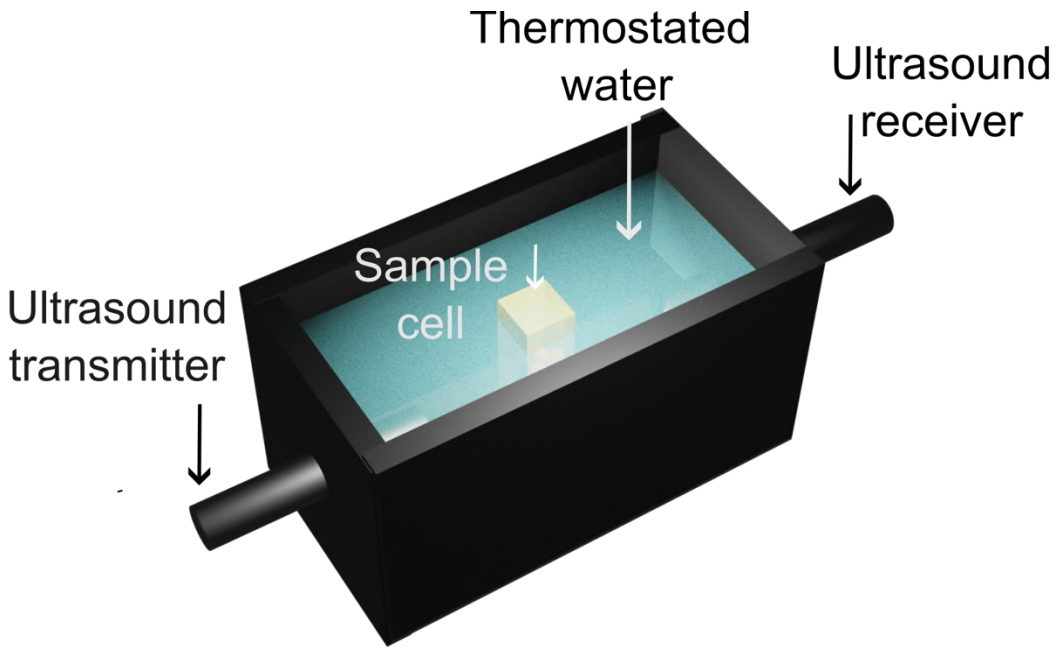

Figure 7 Scheme of the ultrasound measurement system consisting of two piezoelectric broadband transducers immersed in thermostated sample cell at temperature of 25°C.

The ultrasound attenuation coefficient in the frequency function was calculated using the well-known formula (reference method) [100,101], as follows:

$$\alpha(f) = \alpha(f)_{ref} + \frac{1}{d}\ln\frac{|F_1(f)|}{|F_2(f)|}, \qquad (34)$$

where $\alpha(f)$ is the ultrasound attenuation coefficient in Np/m, and $\alpha(f)_{ref} = 6.4 \cdot f^{1.56}$ is the attenuation spectra of the carrier fluid (castor oil), treated as the reference medium and f is expressed in MHz. The expression for $\alpha(f)_{ref}$ was determined in another experiment for pure castor oil when silicone oil was used as the reference medium, and d is the acoustic path inside the sample cell (10 mm). Further, $|F_1(f)|$ is the absolute value of the fast Fourier transform (FFT) for the pulse recorded in the castor oil, and $|F_2(f)|$ is the FFT absolute value of the pulse recorded in the systems, such as suspensions or emulsions.

The processing of ultrasound signals was achieved by determining the pulse position, filtering the noise, and applying the Hamming window to mitigate spectral leakage. After, the FFT algorithm was applied to convert the signal from the time domain to the frequency domain.

2.3. Rheological measurements

The ultrasound technique is not the only one used to characterize suspensions and emulsions; it can also be used together with rheological measurements to characterize the internal structure and stability of colloidal systems, as the viscosity contribution is important in both techniques [102]. Magnetorheological measurements represent a branch of rheology that characterizes the flow behavior of magnetic materials under an external magnetic field. Such materials are often referred to as smart materials due to their capacity to alter their physical properties when subjected to the application of an external magnetic field [103,104].

During a six-month stay at the Institute of Experimental Physics of the Slovak Academy of Science in Kosice as a part of a NAWA grant, the rheological properties of magnetic systems were studied using a magnetorheological system with a twin gap rheometer, provided by Anton Paar (MCR 502, Austria), with a dedicated magnetorheological cell (MRD170/1T) and a measuring system (PP20/MRD/TI). The magnetic field was generated by applying an electrical current to a coil located below the sample cell plate, and the magnetic field was uniform and oriented perpendicularly to the measuring system gap between the plates, the distance of which was constant (1 mm) in all measurements, and the volume of the sample placed between the plates was 0.3 ml. The temperature of the sample cell was maintained during the measurements at ~25°C, though a thermocouple sensor (GMH 3230, Germany) was utilized to monitor the temperature of the systems during the measurement. Finally, a teslameter (FH 54, Germany) was utilized to measure the magnetic field strength, where the magnetic flux density gradually increased linearly over time from 0 mT to 212 mT.

2.4. Rotating magnetic field measurements

As mentioned in section 1.2, the magnetic suspension and emulsion can be used a source of heating under an alternating-magnetic-fields application [63,105]. Although the use of alternating magnetic fields is common, a rotating magnetic field is another possible method of heat generation, potentially with a higher output [106,107].

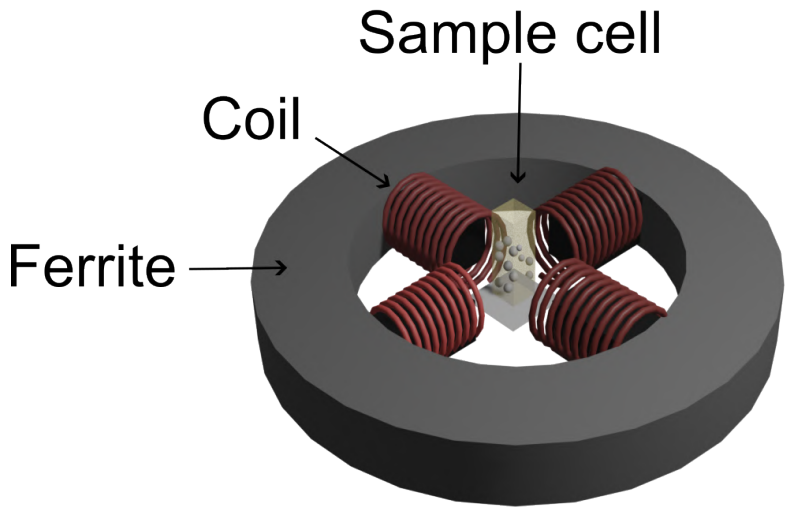

Figure 8 Scheme of the four-coil setup for the generation of a rotating magnetic field.

In the experiments, the rotating magnetic field was produced by a magnetic circuit containing four separate magnetic fluxes shifted in space by an angle of 90°. As shown in **Figure 8**, the system used a closed magnetic circuit containing a ferrite torus with ferrite cores. Further, the amplitude of the magnetic field intensity was measured with a probe (measuring coil) inserted into the center of the magnetic system, and the range of magnetic field strength used was from 5.8 kA/m to 15.7 kA/m.

3. Summary of publications

The previous chapters introduced basic information regarding Pickering emulsions and the use of magnetic nanoparticles as stabilizers, and several system characterizations were presented, including the thorough explanation of ultrasound scattering theory for two- and three-phase systems used in calculations, and ultrasound spectroscopy experiments. Now, this chapter covers the link between papers that constitute the thesis: **[Scientific Papers I–VI]**. The first three papers cover the characterization of an oil-based magnetic suspension system, magnetic Pickering emulsion by ultrasound attenuation spectroscopy **[Scientific Paper I–II]**, and magnetorheological measurements **[Scientific Paper III]**, whereas the latter three papers **[Scientific Paper IV–VI]** cover the application aspects of the research on magnetic Pickering droplets concerning optimizing and investigating ultrasound heating, magnetic separation, and magnetic heating.

[Scientific Paper I]: "Ultrasound study of magnetic and non-magnetic nanoparticle agglomeration in high viscous media"

Ultrasound attenuation spectroscopy has been widely used in material characterization, including in such colloidal systems as suspensions or emulsions, demonstrating the capability to detect volume fraction, compressibility, and particle size distribution via a non-destructive method without requiring sample preparation, making it suitable for low-cost measurements in optically opaque mixtures. Both magnetic and non-magnetic suspensions have found applications in various industrial and medical contexts. Hence, understanding nanoparticle properties, such as size and tendency for aggregation, is crucial to their application-specific determination.

In this paper, ultrasound scattering theory based on the ECAH model, along with ultrasound attenuation measurements, enables the measurement of particle size for magnetite and silica nanoparticles dispersed in a highly viscous medium (castor oil). The distinct physical properties of silica and magnetite particles significantly influence ultrasound attenuation values experimentally and theoretically due to differing movements and heat exchanges between the carrier fluid and suspension particles, phenomena included in the ECAH model description. Upon comparison with electron microscopy images, the results indicate a higher tendency for aggregation in magnetic nanoparticles compared to silica nanoparticles, with an aggregation tendency proportional to the particle concentration.

The ultrasound results provide insights into the actual particle sizes in situ without necessitating sample preparation, and this finding lays the groundwork for the further exploration of more complex systems, such as Pickering emulsions.

The results presented in the paper can be summarized as follows:

1. The change in the ultrasound attenuation value correlates to the particle size distribution, concentration, and aggregation rate.
2. Silica nanoparticles exhibit a lower tendency for agglomeration compared to magnetic nanoparticles due to the lower possibility of particle–particle interaction.
3. The ultrasound attenuation results indicate a higher rate of agglomeration, with a higher particle concentration.
4. The results show the potential application of the ultrasound method for monitoring aggregation in systems, as well as for characterizing solid particles intended for stabilizing Pickering droplets.

[Scientific Paper II]: "Ultrasound measurements of particle shells in magnetic Pickering emulsions"

Ultrasound attenuation spectroscopy, as demonstrated in **[Scientific Paper I]**, offers the possibility of calculating the sizes of particles dispersed in an oil suspension using the ECAH model. However, in the case of Pickering emulsions, the calculation of ultrasound attenuation requires an extension of the ECAH model to account for the presence of a third phase of particles on the droplet interface.

The theoretical data obtained from the core–shell model proposed by Anson and Chivers are utilized to investigate the droplet radius and shell thickness of magnetic Pickering emulsions. The theoretical calculation demonstrates the sensitivity of ultrasound attenuation to different shell thicknesses, highlighting the necessity of use of this extended model to control the stability of Pickering droplets. Two fabrication methods are tested using the core–shell model. The one-stage method for emulsion preparation employs ultrasound homogenization individually. Furthermore, ultrasound homogenization followed by a DC electric field is used to enhance droplet stability. The internal structure of magnetic Pickering emulsions is influenced by the concentration of the dispersed phase and the fabrication method.

The results show a notable change in the outer radius of Pickering emulsions with varying particle concentrations, and higher concentrations of magnetic nanoparticles result in smaller outer radii of Pickering droplets, with aggregated magnetic nanoparticles on the

droplet interface. Furthermore, droplet coalescence due to the application of a DC electric field leads to a relatively thicker particle shell on the droplet interface.

The results presented in the paper can be summarized as follows:

1. A higher volume ratio of magnetic nanoparticles to silicone oil leads to a higher aggregation rate of particles on the droplet interface, resulting in an almost ten-fold thicker shell compared to a lower volume ratio.
2. The application of a DC electric field results in a higher shell thickness of Pickering droplets that were also larger due to electrocoalesence events.
3. Ultrasound attenuation can be an efficient alternative method for characterizing three-phase systems, such as Pickering emulsions, without a sample preparation requirement.
4. Ultrasound attenuation analyzed based on the core–shell model is suggested as a promising predictor for characterizing particle shell properties that could be crucial for drug release and magnetic separation processes.

[Scientific Paper III]: "Magnetorheological characterization of oil-in-oil magnetic Pickering emulsions"

Rheological measurements are an important method of characterizing the flow behavior of emulsions and suspension systems. For this reason, it is used to investigate the internal structure and stability of oil-in-oil magnetic Pickering emulsions and can be compared with the outcomes of the ultrasound spectroscopy results in **[Scientific Paper II]**.

The shear viscosity and dynamic yield stress as functions of the shear rate and magnetic field are measured for partially and fully stable magnetic Pickering emulsions, where magnetorheological measurements reflect changes in the internal structure under magnetic field application. The emulsion fabricated using ultrasound and an additional DC electric field application exhibits a higher dynamic yield stress compared to the one-stage fabrication method. Furthermore, the results indicate different magnitudes of the magnetoviscous effect between partial and stable emulsions, which is correlated with changes in the sizes of Pickering droplets and the shell thickness on the droplet interface.

The results presented in the paper can be summarized as follows:

1. The fully stable emulsion demonstrates a viscoelastic behavior with a strong solid-like structure compared to the partly stable emulsion. This is attributed to the higher

number of particles on the droplet interface, leading to stronger droplet interaction under a homogeneous magnetic field.

2. The initial flow of the emulsion, determined by the dynamic yield point, is higher for fully covered droplets compared to partially covered droplets.
3. The results of the magnetorheological measurements can be used in conjunction with ultrasound to control the formation process of magnetic Pickering emulsion.

[Scientific Paper IV]: "Optimization of ultrasound heating with Pickering droplets using core–shell scattering theory"

Ultrasound hyperthermia is a medical treatment accomplished by the absorption of wave energy into heat. Several factors influence ultrasound-induced heating, including the intensity of ultrasound waves, frequency, and thermal and acoustic material properties. The effectiveness of ultrasound can thus be enhanced using sonosensitizers, additional materials that significantly attenuate ultrasound waves and dissipate energy in the form of heat.

In this research, Pickering droplets are modeled to be stabilized by magnetite and silica nanoparticles, serving as candidates for sonosensitization in an agar phantom. A computational approach based on ultrasound scattering theory, shown to be efficient in Pickering emulsion characterization in **[Scientific Paper II]**, is utilized to calculate ultrasound attenuation and velocity in agar phantoms with inclusions doped with Pickering droplets. Furthermore, numerical simulations of pure agar phantoms and agar phantoms incorporating spherical inclusions are conducted to compute heat generation based on a bioheat transfer model.

In the pure agar phantom simulations, the results indicate that temperature elevation and penetration depth vary with different frequencies ranging from 1 MHz to 10 MHz. Subsequently, magnetic Pickering droplets with varying core radii and shell thicknesses are dispersed in spherical inclusions with a diameter of 10 mm immersed inside the cylindrical agar phantom. It is observed that temperature rise and penetration depth change significantly with different core radii while maintaining a constant shell thickness. Nanodroplets with a radius below 400 nm exhibit higher temperature elevations compared to microdroplets, and spherical inclusions doped with non-magnetic Pickering droplets (stabilized with silica nanoparticles) yield lower temperature elevations compared to magnetic Pickering droplets, attributed to differences in physical droplet properties.

The results presented in the paper can be summarized as follows:

1. The temperature increase depends on the ultrasound frequency, as well as on the thermal and acoustic properties of the agar phantom doped with sonosensitizers.
2. The optimization of ultrasound heating can be achieved by changing the core radius and shell thickness of Pickering droplets.
3. Controlling the internal structure and size of the sonosensitizer can help improve the heat elevation, as well as the penetration depth.
4. The non-focused ultrasound wave propagation in the agar phantom doped with Pickering droplets of the proper size can enable similar localized heating effects to be obtained for use in the focused ultrasound devices.

[Scientific Paper V]: "Propagation of ultrasonic wave in magnetic Pickering emulsion under DC magnetic field"

One of the unique features of Pickering emulsions stabilized by magnetic nanoparticles is their ability to respond to an external magnetic field. The gradual migration of magnetic droplets under the influence of a static gradient magnetic field is known as the phenomenon of magnetophoresis, and it can be used in industrial applications.

In this paper, the magnetic separation of an oil-in-oil magnetic Pickering emulsion is investigated under different intensities of the magnetic field and concentrations of magnetic particles. The low-gradient magnetic field, produced by permanent magnets, is positioned outside the sample cell, as illustrated in **Figure 9**. Ultrasound attenuation as a function of frequency provides information about the movement of magnetic Pickering droplets from regions of lower to those of higher magnetic field intensity. In addition, ultrasound attenuation exhibits a significant difference after the application of a magnetic field due to magnetophoresis. The velocity of magnetophoresis increases with a higher shell thickness and aggregation rate in the system, owing to the magnetophoretic force that pushes the Pickering droplets to a high region of magnetic field intensity. The purification and velocity of Pickering droplet movement can be controlled by combining the ultrasound attenuation value after magnetic field application with the reference oil attenuation.

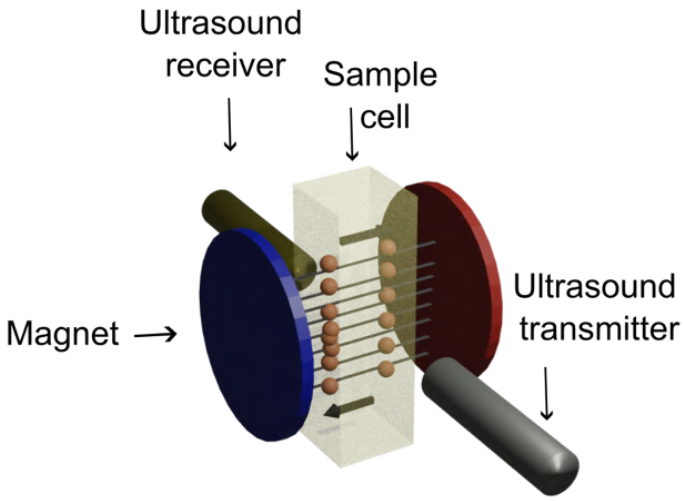

Figure 9 Schematic illustration of the experimental setup for magnetic separation under a static low-gradient magnetic field controlled by the ultrasound method.

The results presented in the paper can be summarized as follows:

1. The magnetic field intensity and internal structure of the Pickering emulsion, including its size and aggregation, influence the magnetic separation in the system directly.
2. A higher intensity or larger droplet radius correlates with an increased magnetophoretic force.
3. The experimental results suggest that magnetic separation time and purification can be controlled based on the reference value of the carrier fluid through ultrasound attenuation.

[Scientific Paper VI]: "Magnetic pickering emulsions heated in a rotating magnetic field"

Pickering emulsions stabilized by magnetic nanoparticles can serve as a source of heat when subjected to an alternating magnetic field. In addition, rotating magnetic fields can be efficiently employed for magnetic heating purposes. The temperature elevation within a magnetic Pickering emulsion finds application in magnetic hyperthermia, whereas in an alternative magnetic field, oscillation leads to delays in the relaxation of the magnetic moment, resulting in temperature elevation, as described in Section 1.2. However, in a rotating magnetic field, the particles can be rotating rather than oscillating, and the friction between particles leads to a temperature elevation. In the case of large objects, such as magnetic Pickering emulsions, the movement of the domain walls was the cause of the temperature elevation in the rotating magnetic field.

In this paper, the efficiency of magnetic heating is investigated using a rotating magnetic field, and the performance of the rotating magnetic field is compared with that of an alternating magnetic field for both magnetic suspensions and magnetic Pickering emulsions. The experimental results indicate that a higher temperature elevation is achieved with a rotating magnetic field for both magnetic suspensions and emulsions, and the responsible mechanism of heating is hysteresis loss. Magnetic heating can be optimized by controlling the internal structure of suspensions and emulsions, such as the aggregation and shell thickness of the Pickering emulsion, as presented in **[Scientific Papers I and II]**.

The results presented in the paper can be summarized as follows:

1. The rotating magnetic field is proven to achieve a temperature elevation higher than via the common method of an alternating magnetic field.
2. The study shows the ability to use a relatively low concentration of magnetic materials to induce a temperature increase sufficient for hyperthermia therapy applications.
3. The slight changes in shape of the stabilizing magnetic particles and their size influence the heating effect.
4. The experimental results indicate that a low concentration of magnetic nanoparticles is enough to obtain the required temperature elevation, which is important in biomedical application.

4. Conclusions

Within my PhD project, I began my investigation by characterizing the internal structures of both magnetic and non-magnetic suspensions using the ECAH model, and the results yielded valuable insights into particle interactions within high-viscosity carrier fluids. However, the ECAH model's utility appeared limited for Pickering emulsions due to an additional layer with distinct properties on the droplet interface, necessitating additional boundary conditions for an accurate calculation. Consequently, the core–shell model was employed to compute ultrasound scattering waves by core–shell objects, which facilitated the determination of the core size and shell thickness of Pickering droplets across various volume fractions and fabrication methods. In addition, magnetorheological measurements revealed changes in the viscoelastic properties of the emulsion related to the shell thickness and aggregation rate, which were measured by ultrasound spectroscopy.

Based on these characterizations, further research into the formation process is needed to enhance droplet stability, ensure proper encapsulation, and mitigate aggregation within the system. This is particularly crucial, as computer simulations indicate varying temperature elevations with changes in the size of Pickering droplets, as well as in their particle shell thicknesses, which could be altered by optimizing fabrication routes when different particle stabilizers are used.

This PhD research identifies ultrasound waves as a promising tool to control the formation process and detect the aggregation in both suspensions and Pickering emulsions, and they can be used in the future to enhance the fabrication process, offering a substantial contribution to the application of Pickering emulsions in the medical and industrial fields.

5. References

1. Bibette, J.; Calderon, F.L.; Poulin, P. Emulsions: Basic Principles. *Rep. Prog. Phys.* **1999**, *62*, 969–1033, doi:10.1088/0034-4885/62/6/203.
2. Zhu, Q.; Pan, Y.; Jia, X.; Li, J.; Zhang, M.; Yin, L. Review on the Stability Mechanism and Application of Water-in-Oil Emulsions Encapsulating Various Additives. *Compr. Rev. Food Sci. Food Saf.* **2019**, *18*, 1660–1675, doi:10.1111/1541-4337.12482.
3. Binks, B.P.; Tyowua, A.T. Oil-in-Oil Emulsions Stabilised Solely by Solid Particles. *Soft Matter* **2016**, *12*, 876–887, doi:10.1039/C5SM02438B.
4. Nonomura, Y.; Sugawara, T.; Kashimoto, A.; Fukuda, K.; Hotta, H.; Tsujii, K. Self-Assembly of Surface-Active Powder at the Interfaces of Selective Liquids. 1: Multiple Structural Polymorphism. *Langmuir* **2002**, *18*, 10163–10167, doi:10.1021/la020511u.
5. Atanase, L.I.; Riess, G. Block Copolymer Stabilized Nonaqueous Biocompatible Sub-Micron Emulsions for Topical Applications. *Int. J. Pharm.* **2013**, *448*, 339–345, doi:10.1016/j.ijpharm.2013.03.051.
6. Dingcong, W. A Study of Identifying the Emulsion Type of Surfactant: Volume Balance Value. *J. Colloid Interface Sci.* **2002**, *247*, 389–396, doi:10.1006/jcis.2001.8152.
7. Crespy, D.; Landfester, K. Making Dry Fertile: A Practical Tour of Non-Aqueous Emulsions and Miniemulsions, Their Preparation and Some Applications. *Soft Matter* **2011**, *7*, 11054, doi:10.1039/c1sm06156a.
8. Sjöblom, J.; Stenius, P.; Simon, S.; Grimes, B.A. Emulsion Stabilization. In *Encyclopedia of Colloid and Interface Science*; Tadros, T., Ed.; Springer Berlin Heidelberg: Berlin, Heidelberg, 2013; pp. 415–454 ISBN 978-3-642-20664-1.
9. Fu, L.; Ma, Q.; Liao, K.; An, J.; Bai, J.; He, Y. Application of Pickering Emulsion in Oil Drilling and Production. *Nanotechnol. Rev.* **2021**, *11*, 26–39, doi:10.1515/ntrev-2022-0003.
10. Pan, J.; Chen, J.; Wang, X.; Wang, Y.; Fan, J. Pickering Emulsion: From Controllable Fabrication to Biomedical Application. *Interdiscip. Med.* **2023**, *1*, e20230014, doi:10.1002/INMD.20230014.
11. Wu, J.; Ma, G. Recent Studies of Pickering Emulsions: Particles Make the Difference. *Small* **2016**, *12*, 4633–4648, doi:10.1002/smll.201600877.
12. Larson-Smith, K.; Jackson, A.; Pozzo, D.C. Small Angle Scattering Model for Pickering Emulsions and Raspberry Particles. *J. Colloid Interface Sci.* **2010**, *343*, 36–41, doi:10.1016/j.jcis.2009.11.033.
13. Wu, B.; Li, Y.; Li, Y.; Li, H.; Ji, S.; Xia, Q. Pickering Emulsions-Chitosan Hydrogel Beads Carrier System for Loading of Resveratrol: Formulation Approach and Characterization Studies. *React. Funct. Polym.* **2021**, *169*, 105074, doi:10.1016/j.reactfunctpolym.2021.105074.
14. Pawlik, A.; Kurukji, D.; Norton, I.; Spyropoulos, F. Food-Grade Pickering Emulsions Stabilised with Solid Lipid Particles. *Food Funct.* **2016**, *7*, 2712–2721, doi:10.1039/C6FO00238B.
15. Gestranius, M.; Stenius, P.; Kontturi, E.; Sjöblom, J.; Tammelin, T. Phase Behaviour and Droplet Size of Oil-in-Water Pickering Emulsions Stabilised with Plant-Derived Nanocellulosic Materials. *Colloids Surf. Physicochem. Eng. Asp.* **2017**, *519*, 60–70, doi:10.1016/j.colsurfa.2016.04.025.

16. Schümann, H.; Khatibi, M.; Tutkun, M.; H. Pettersen, B.; Yang, Z.; Nydal, O.J. Droplet Size Measurements in Oil–Water Dispersions: A Comparison Study Using FBRM and PVM. *J. Dispers. Sci. Technol.* **2015**, *36*, 1432–1443, doi:10.1080/01932691.2014.989569.
17. Chen, J.; Vogel, R.; Werner, S.; Heinrich, G.; Clausse, D.; Dutschk, V. Influence of the Particle Type on the Rheological Behavior of Pickering Emulsions. *Colloids Surf. Physicochem. Eng. Asp.* **2011**, *382*, 238–245, doi:10.1016/j.colsurfa.2011.02.003.
18. Yang, H.; Su, Z.; Meng, X.; Zhang, X.; Kennedy, J.F.; Liu, B. Fabrication and Characterization of Pickering Emulsion Stabilized by Soy Protein Isolate-Chitosan Nanoparticles. *Carbohydr. Polym.* **2020**, *247*, 116712, doi:10.1016/j.carbpol.2020.116712.
19. Silva, C.A.M.; Saraiva, S.V.; Bonetti, D.; Higuti, R.T.; Cunha, R.L.; Pereira, L.O.V.; Silva, F.V.; Fileti, A.M.F. Measurements of Bimodal Droplet Size Distribution of Emulsions Using Ultrasonic Spectroscopy in the Long and Intermediate Wavelength Regimes. *Chem. Eng. Sci.* **2022**, *252*, 117274, doi:10.1016/j.ces.2021.117274.
20. Tsuji, K.; Nakanishi, H.; Norisuye, T. Viscoelastic ECAH: Scattering Analysis of Spherical Particles in Suspension with Viscoelasticity. *Ultrasonics* **2021**, *115*, 106463, doi:10.1016/j.ultras.2021.106463.
21. Challis, R.E.; Povey, M.J.W.; Mather, M.L.; Holmes, A.K. Ultrasound Techniques for Characterizing Colloidal Dispersions. *Rep. Prog. Phys.* **2005**, *68*, 1541–1637, doi:10.1088/0034-4885/68/7/R01.
22. Challis, R.E.; Tebbutt, J.S.; Holmes, A.K. Equivalence between Three Scattering Formulations for Ultrasonic Wave Propagation in Particulate Mixtures. *J. Phys. Appl. Phys.* **1998**, *31*, 3481–3497, doi:10.1088/0022-3727/31/24/012.
23. Kanamori, C.; Nguyen, T.T.; Tsuji, K.; Nakanishi, H.; Tran-Cong-Miyata, Q.; Norisuye, T. Interfacial Structures of Particle-Stabilized Emulsions Examined by Ultrasonic Scattering Analysis with a Core–Shell Model. *Ultrasonics* **2021**, *116*, 106510, doi:10.1016/j.ultras.2021.106510.
24. Wang, Z.; Li, Y.; Guo, Y.; Zhang, H. Investigations of Interfacial Properties of Surfactants with Different Structures at the Oil/Water Interface Using Dissipative Particle Dynamics. *J. Dispers. Sci. Technol.* **2013**, *34*, 1020–1028, doi:10.1080/01932691.2012.731637.
25. Guha, I.F.; Anand, S.; Varanasi, K.K. Creating Nanoscale Emulsions Using Condensation. *Nat. Commun.* **2017**, *8*, 1371, doi:10.1038/s41467-017-01420-8.
26. Ramsden Separation of Solids in the Surface-Layers of Solutions and 'Suspensions' (Observations on Surface-Membranes, Bubbles, Emulsions, and Mechanical Coagulation).—Preliminary Account. *Proc. R. Soc. Lond.* **1904**, *72*, 156–164, doi:10.1098/rspl.1903.0034.
27. Pickering, S.U. CXCVI.—Emulsions. *J Chem Soc Trans* **1907**, *91*, 2001–2021, doi:10.1039/CT9079102001.
28. Binks, B.P., Horozov, T.S. *Colloidal Particles at Liquid Interfaces*; Eds.; 1st ed: Cambridge University Press, 2006; ISBN 978-0-521-84846-6.
29. Binks, B.P. Particles as Surfactants—Similarities and Differences. *Curr. Opin. Colloid Interface Sci.* **2002**, *7*, 21–41, doi:10.1016/S1359-0294(02)00008-0.
30. Berton-Carabin, C.C.; Schroën, K. Pickering Emulsions for Food Applications: Background, Trends, and Challenges. *Annu. Rev. Food Sci. Technol.* **2015**, *6*, 263–297, doi:10.1146/annurev-food-081114-110822.

31. Ge, S.; Xiong, L.; Li, M.; Liu, J.; Yang, J.; Chang, R.; Liang, C.; Sun, Q. Characterizations of Pickering Emulsions Stabilized by Starch Nanoparticles: Influence of Starch Variety and Particle Size. *Food Chem.* **2017**, *234*, 339–347, doi:10.1016/j.foodchem.2017.04.150.
32. Marto, J.; Ascenso, A.; Simoes, S.; Almeida, A.J.; Ribeiro, H.M. Pickering Emulsions: Challenges and Opportunities in Topical Delivery. *Expert Opin. Drug Deliv.* **2016**, *13*, 1093–1107, doi:10.1080/17425247.2016.1182489.
33. Cserháti, T.; Forgács, E.; Oros, G. Biological Activity and Environmental Impact of Anionic Surfactants. *Environ. Int.* **2002**, *28*, 337–348, doi:10.1016/S0160-4120(02)00032-6.
34. Dekker, R.I.; Velandia, S.F.; Kibbelaar, H.V.M.; Morcy, A.; Sadtler, V.; Roques-Carmes, T.; Groenewold, J.; Kegel, W.K.; Velikov, K.P.; Bonn, D. Is There a Difference between Surfactant-Stabilised and Pickering Emulsions? *Soft Matter* **2023**, *19*, 1941–1951, doi:10.1039/D2SM01375D.
35. Zia, A.; Pentzer, E.; Thickett, S.; Kempe, K. Advances and Opportunities of Oil-in-Oil Emulsions. *ACS Appl. Mater. Interfaces* **2020**, *12*, 38845–38861, doi:10.1021/acsami.0c07993.
36. Hamill, R.D.; Olson, F.A.; Petersen, R.V. Some Interfacial Properties of a Nonaqueous Emulsion. *J. Pharm. Sci.* **1965**, *54*, 537–540, doi:10.1002/jps.2600540408.
37. Hamill, R.D.; Petersen, R.V. Effect of Surfactant Concentration on the Interfacial Viscosity of a Nonaqueous System. *J. Pharm. Sci.* **1966**, *55*, 1274–1277, doi:10.1002/jps.2600551121.
38. Klapper, M.; Nenov, S.; Haschick, R.; Müller, K.; Müllen, K. Oil-in-Oil Emulsions: A Unique Tool for the Formation of Polymer Nanoparticles. *Acc. Chem. Res.* **2008**, *41*, 1190–1201, doi:10.1021/ar8001206.
39. Rozynek, Z.; Bielas, R.; Józefczak, A. Efficient Formation of Oil-in-Oil Pickering Emulsions with Narrow Size Distributions by Using Electric Fields. *Soft Matter* **2018**, *14*, 5140–5149, doi:10.1039/C8SM00671G.
40. Bielas, R.; Rozynek, Z.; Hornowski, T.; Józefczak, A. Ultrasound Control of Oil-in-Oil Pickering Emulsions Preparation. *J. Phys. Appl. Phys.* **2020**, *53*, 085301, doi:10.1088/1361-6463/ab58a7.
41. Binks, B.P.; Lumsdon, S.O. Pickering Emulsions Stabilized by Monodisperse Latex Particles: Effects of Particle Size. *Langmuir* **2001**, *17*, 4540–4547, doi:10.1021/la0103822.
42. Nan, F.; Wu, J.; Qi, F.; Liu, Y.; Ngai, T.; Ma, G. Uniform Chitosan-Coated Alginate Particles as Emulsifiers for Preparation of Stable Pickering Emulsions with Stimulus Dependence. *Colloids Surf. Physicochem. Eng. Asp.* **2014**, *456*, 246–252, doi:10.1016/j.colsurfa.2014.05.017.
43. Qi, F.; Wu, J.; Sun, G.; Nan, F.; Ngai, T.; Ma, G. Systematic Studies of Pickering Emulsions Stabilized by Uniform-Sized PLGA Particles: Preparation and Stabilization Mechanism. *J Mater Chem B* **2014**, *2*, 7605–7611, doi:10.1039/C4TB01165A.
44. Jiang, H.; Sheng, Y.; Ngai, T. Pickering Emulsions: Versatility of Colloidal Particles and Recent Applications. *Curr. Opin. Colloid Interface Sci.* **2020**, *49*, 1–15, doi:10.1016/j.cocis.2020.04.010.
45. Larson-Smith, K.; Pozzo, D.C. Pickering Emulsions Stabilized by Nanoparticle Surfactants. *Langmuir* **2012**, *28*, 11725–11732, doi:10.1021/la301896c.

46. Binks, B.P.; Whitby, C.P. Nanoparticle Silica-Stabilised Oil-in-Water Emulsions: Improving Emulsion Stability. *Colloids Surf. Physicochem. Eng. Asp.* **2005**, *253*, 105–115, doi:10.1016/j.colsurfa.2004.10.116.
47. Chen, W.; Liu, X.; Liu, Y.; Kim, H.-I. Synthesis of Microcapsules with Polystyrene/ZnO Hybrid Shell by Pickering Emulsion Polymerization. *Colloid Polym. Sci.* **2010**, *288*, 1393–1399, doi:10.1007/s00396-010-2277-8.
48. Chen, T.; Colver, P.J.; Bon, S.A.F. Organic–Inorganic Hybrid Hollow Spheres Prepared from TiO_2 -Stabilized Pickering Emulsion Polymerization. *Adv. Mater.* **2007**, *19*, 2286–2289, doi:10.1002/adma.200602447.
49. Zhou, J.; Qiao, X.; Binks, B.P.; Sun, K.; Bai, M.; Li, Y.; Liu, Y. Magnetic Pickering Emulsions Stabilized by Fe_3O_4 Nanoparticles. *Langmuir* **2011**, *27*, 3308–3316, doi:10.1021/la1036844.
50. Zhou, J.; Wang, L.; Qiao, X.; Binks, B.P.; Sun, K. Pickering Emulsions Stabilized by Surface-Modified Fe_3O_4 Nanoparticles. *J. Colloid Interface Sci.* **2012**, *367*, 213–224, doi:10.1016/j.jcis.2011.11.001.
51. Li, W.; Jiao, B.; Li, S.; Faisal, S.; Shi, A.; Fu, W.; Chen, Y.; Wang, Q. Recent Advances on Pickering Emulsions Stabilized by Diverse Edible Particles: Stability Mechanism and Applications. *Front. Nutr.* **2022**, *9*, 864943, doi:10.3389/fnut.2022.864943.
52. Tyowua, A.T.; Yiase, S.G.; Binks, B.P. Double Oil-in-Oil-in-Oil Emulsions Stabilised Solely by Particles. *J. Colloid Interface Sci.* **2017**, *488*, 127–134, doi:10.1016/j.jcis.2016.10.089.
53. Harman, C.L.G.; Patel, M.A.; Guldin, S.; Davies, G.-L. Recent Developments in Pickering Emulsions for Biomedical Applications. *Curr. Opin. Colloid Interface Sci.* **2019**, *39*, 173–189, doi:10.1016/j.cocis.2019.01.017.
54. Yang, H.; Wang, S.; Zhang, W.; Wu, J.; Yang, S.; Yu, D.; Wu, X.; Sun, Y.; Wang, J. Rapid Demulsification of Pickering Emulsions Triggered by Controllable Magnetic Field. *Sci. Rep.* **2020**, *10*, 16565, doi:10.1038/s41598-020-73551-w.
55. Jalili Darbandi Sofla, M.; Norouzi-Apourvari, S.; Schaffie, M. The Effect of Magnetic Field on Stability of Conventional and Pickering Water-in-Crude Oil Emulsions Stabilized with Fumed Silica and Iron Oxide Nanoparticles. *J. Mol. Liq.* **2020**, *314*, 113629, doi:10.1016/j.molliq.2020.113629.
56. Tham, F.K.; Ng, W.M.; Leong, S.S.; Yeap, S.P.; Low, S.C.; Lee, H.L.; Lim, J. Magnetophoresis of Magnetic Pickering Emulsions Under Low Field Gradient: Macroscopic and Microscopic Motion. *Langmuir* **2021**, *37*, 1811–1822, doi:10.1021/acs.langmuir.0c03153.
57. Xie, C.-Y.; Meng, S.-X.; Xue, L.-H.; Bai, R.-X.; Yang, X.; Wang, Y.; Qiu, Z.-P.; Binks, B.P.; Guo, T.; Meng, T. Light and Magnetic Dual-Responsive Pickering Emulsion Micro-Reactors. *Langmuir* **2017**, *33*, 14139–14148, doi:10.1021/acs.langmuir.7b03642.
58. Lin, Z.; Zhang, Z.; Li, Y.; Deng, Y. Magnetic Nano-Fe3O4 Stabilized Pickering Emulsion Liquid Membrane for Selective Extraction and Separation. *Chem. Eng. J.* **2016**, *288*, 305–311, doi:10.1016/j.cej.2015.11.109.
59. Thiesen, B.; Jordan, A. Clinical Applications of Magnetic Nanoparticles for Hyperthermia. *Int. J. Hyperthermia* **2008**, *24*, 467–474, doi:10.1080/02656730802104757.
60. Wang, X.; Gu, H.; Yang, Z. The Heating Effect of Magnetic Fluids in an Alternating Magnetic Field. *J. Magn. Magn. Mater.* **2005**, *293*, 334–340, doi:10.1016/j.jmmm.2005.02.028.

61. Deatsch, A.E.; Evans, B.A. Heating Efficiency in Magnetic Nanoparticle Hyperthermia. *J. Magn. Magn. Mater.* **2014**, *354*, 163–172, doi:10.1016/j.jmmm.2013.11.006.
62. Kaczmarek, K.; Hornowski, T.; Antal, I.; Timko, M.; Józefczak, A. Magneto-Ultrasonic Heating with Nanoparticles. *J. Magn. Magn. Mater.* **2019**, *474*, 400–405, doi:10.1016/j.jmmm.2018.11.062.
63. Bielas, R.; Surdeko, D.; Kaczmarek, K.; Józefczak, A. The Potential of Magnetic Heating for Fabricating Pickering-Emulsion-Based Capsules. *Colloids Surf. B Biointerfaces* **2020**, *192*, 111070, doi:10.1016/j.colsurfb.2020.111070.
64. Low, L.E.; Siva, S.P.; Ho, Y.K.; Chan, E.S.; Tey, B.T. Recent Advances of Characterization Techniques for the Formation, Physical Properties and Stability of Pickering Emulsion. *Adv. Colloid Interface Sci.* **2020**, *277*, 102117, doi:10.1016/j.cis.2020.102117.
65. Mcclements, D.J. Critical Review of Techniques and Methodologies for Characterization of Emulsion Stability. *Crit. Rev. Food Sci. Nutr.* **2007**, *47*, 611–649, doi:10.1080/10408390701289292.
66. Aguilera, M.; Stanley, D.W. *Microstructural Principles of Food Processing and Engineering*; Springer Science & Business Media, 1999
67. Balcaen, M.; De Neve, L.; Dewettinck, K.; Van Der Meeren, P. Effect of Dilution on Particle Size Analysis of w/o Emulsions by Dynamic Light Scattering. *J. Dispers. Sci. Technol.* **2021**, *42*, 869–879, doi:10.1080/01932691.2020.1712216.
68. Kaszuba, M.; McKnight, D.; Connah, M.T.; McNeil-Watson, F.K.; Nobbmann, U. Measuring Sub Nanometre Sizes Using Dynamic Light Scattering. *J. Nanoparticle Res.* **2008**, *10*, 823–829, doi:10.1007/s11051-007-9317-4.
69. Sadeghpour, A.; Pirolt, F.; Glatter, O. Submicrometer-Sized Pickering Emulsions Stabilized by Silica Nanoparticles with Adsorbed Oleic Acid. *Langmuir* **2013**, *29*, 6004–6012, doi:10.1021/la4008685.
70. Patel, H.; Upadhyay, R.V.; Parekh, K.; Reis, D.; Oliveira, C.L.P.; Figueiredo Neto, A.M. Optimized Mn0.5Zn0.5Fe2O4 Nanoflowers Based Magnetic Fluids for Potential Biomedical Applications. *J. Magn. Magn. Mater.* **2024**, *590*, 171656, doi:10.1016/j.jmmm.2023.171656.
71. McClements, D.J.; Povey, M.J.W.; Dickinson, E. Absorption and Velocity Dispersion Due to Crystallization and Melting of Emulsion Droplets. *Ultrasonics* **1993**, *31*, 433–437, doi:10.1016/0041-624X(93)90052-2.
72. Norisuye, T. Structures and Dynamics of Microparticles in Suspension Studied Using Ultrasound Scattering Techniques. *Polym. Int.* **2017**, *66*, 175–186, doi:10.1002/pi.5100.
73. McClements, D.J. Ultrasonic Characterisation of Emulsions and Suspensions. *Adv. Colloid Interface Sci.* **1991**, *37*, 33–72, doi:10.1016/0001-8686(91)80038-L.
74. Povey, M.J.W. Ultrasound Particle Sizing: A Review. *Particuology* **2013**, *11*, 135–147, doi:10.1016/j.partic.2012.05.010.
75. Strutt, J.; Rayleigh, B. Theory of Sound. **1877**.
76. Horvath, H. Gustav Mie and the Scattering and Absorption of Light by Particles: Historic Developments and Basics. *J. Quant. Spectrosc. Radiat. Transf.* **2009**, *110*, 787–799.
77. Urick, R.J. The Absorption of Sound in Suspensions of Irregular Particles. *J. Acoust. Soc. Am.* **1948**, *20*, 283–289, doi:10.1121/1.1906373.

78. Urick, R.J. A Sound Velocity Method for Determining the Compressibility of Finely Divided Substances. *J. Appl. Phys.* **1947**, *18*, 983–987, doi:10.1063/1.1697584.
79. Urick, R.J.; Ament, W.S. The Propagation of Sound in Composite Media. *J. Acoust. Soc. Am.* **1949**, *21*, 115–119, doi:10.1121/1.1906474.
80. Epstein, P.S.; Carhart, R.R. The Absorption of Sound in Suspensions and Emulsions. I. Water Fog in Air. *J. Acoust. Soc. Am.* **1953**, *25*, 553–565, doi:10.1121/1.1907107.
81. Allegra, J.R.; Hawley, S.A. Attenuation of Sound in Suspensions and Emulsions: Theory and Experiments. *J. Acoust. Soc. Am.* **1972**, *51*, 1545–1564, doi:10.1121/1.1912999.
82. Tajika, K.; Norisuye, T. Particle Elastic Modulus Analysis of Waterborne Polyurethane Nanoparticles by Ultrasound Scattering Method. *Jpn. J. Appl. Phys.* **2024**, doi:10.35848/1347-4065/ad22bb.
83. Saraiva, S.V.; Silva, C.A.M.; Bonetti, D.; Fileti, A.M.F.; Silva, E.F.V. Coupling of Support Vector Machine and Acoustic Models to Characterize the Droplet Size Distribution of Emulsions Using Ultrasonic Techniques. In *Computer Aided Chemical Engineering*; Elsevier, 2023; Vol. 52, pp. 1745–1752 ISBN 978-0-443-15274-0.
84. Lloyd, P.; Berry, M. Wave Propagation through an Assembly of Spheres: IV. Relations between Different Multiple Scattering Theories. *Proc. Phys. Soc.* **1967**, *91*, 678.
85. Waterman, P.C.; Truell, R. Multiple Scattering of Waves. *J. Math. Phys.* **1961**, *2*, 512–537.
86. McClements, D.J.; Povey, M.J.W. Scattering of Ultrasound by Emulsions. *J. Phys. Appl. Phys.* **1989**, *22*, 38–47, doi:10.1088/0022-3727/22/1/006.
87. Anson, L.W.; Chivers, R.C. Ultrasonic Scattering from Spherical Shells Including Viscous and Thermal Effects. *J. Acoust. Soc. Am.* **1993**, *93*, 1687–1699, doi:10.1121/1.406734.
88. Hipp, A.K.; Storti, G.; Morbidelli, M. Acoustic Characterization of Concentrated Suspensions and Emulsions. 1. Model Analysis. *Langmuir* **2002**, *18*, 391–404, doi:10.1021/la015538c.
89. Challis, R.E.; Pinfield, V.J. Ultrasonic Wave Propagation in Concentrated Slurries – The Modelling Problem. *Ultrasonics* **2014**, *54*, 1737–1744, doi:10.1016/j.ultras.2014.04.003.
90. Sewell, C. VII. The Extinction of Sound in a Viscous Atmosphere by Small Obstacles of Cylindrical and Spherical Form. *Philos. Trans. R. Soc. Lond. Ser. Contain. Pap. Math. Phys. Character* **1911**, *210*, 239–270.
91. Okura, S.; Tsuji, K.; Norisuye, T. Transition from Liquid Droplet to Solid Particle Investigated by Ultrasonic Spectroscopy. *Ultrasonics* **2023**, *128*, 106879, doi:10.1016/j.ultras.2022.106879.
92. Foldy, L.L. The Multiple Scattering of Waves. I. General Theory of Isotropic Scattering by Randomly Distributed Scatterers. *Phys. Rev.* **1945**, *67*, 107–119, doi:10.1103/PhysRev.67.107.
93. Mubofu, E.B. Castor Oil as a Potential Renewable Resource for the Production of Functional Materials. *Sustain. Chem. Process.* **2016**, *4*, 11, doi:10.1186/s40508-016-0055-8.
94. Ogunniyi, D. Castor Oil: A Vital Industrial Raw Material. *Bioresour. Technol.* **2006**, *97*, 1086–1091, doi:10.1016/j.biortech.2005.03.028.
95. Gelderblom, H.; Verweij, J.; Nooter, K.; Sparreboom, A. Cremophor EL: The Drawbacks and Advantages of Vehicle Selection for Drug Formulation. *Eur. J. Cancer* **2001**, *37*, 1590–1598, doi:10.1016/S0959-8049(01)00171-X.

96. Gradishar, W.J.; Tjulandin, S.; Davidson, N.; Shaw, H.; Desai, N.; Bhar, P.; Hawkins, M.; O'Shaughnessy, J. Phase III Trial of Nanoparticle Albumin-Bound Paclitaxel Compared with Polyethylated Castor Oil–Based Paclitaxel in Women with Breast Cancer. *J. Clin. Oncol.* **2005**, *23*, 7794–7803.
97. Russo, A.; Morescalchi, F.; Donati, S.; Gambicorti, E.; Azzolini, C.; Costagliola, C.; Semeraro, F. Heavy and Standard Silicone Oil: Intraocular Inflammation. *Int. Ophthalmol.* **2018**, *38*, 855–867, doi:10.1007/s10792-017-0489-3.
98. Do Amaral, L.F.M.; Aires, G.S.; Wypych, F.; De Freitas, R.A. Oil-in-Oil Pickering Emulsions Stabilized by Shigaite-like Layered Double Hydroxide Particles. *Appl. Clay Sci.* **2023**, *238*, 106947, doi:10.1016/j.clay.2023.106947.
99. Kakoty, V.; K.C., S.; Pandey, M.; Dubey, S.K.; Kesharwani, P.; Taliyan, R. Biological Toxicity of Nanoparticles. In *Nanoparticle Therapeutics*; Elsevier, 2022; pp. 603–628 ISBN 978-0-12-820757-4.
100. Liang, S.; Lashkari, B.; Choi, S.S.S.; Ntziachristos, V.; Mandelis, A. The Application of Frequency-Domain Photoacoustics to Temperature-Dependent Measurements of the Grüneisen Parameter in Lipids. *Photoacoustics* **2018**, *11*, 56–64, doi:10.1016/j.pacs.2018.07.005.
101. Treeby, B.E.; Cox, B.T.; Zhang, E.Z.; Patch, S.K.; Beard, P.C. Measurement of Broadband Temperature-Dependent Ultrasonic Attenuation and Dispersion Using Photoacoustics. *IEEE Trans. Ultrason. Ferroelectr. Freq. Control* **2009**, *56*, 1666–1676, doi:10.1109/TUFFC.2009.1231.
102. Bélicard, N.; Niémet-Mabiala, M.J.; Tourvieille, J.-N.; Lidon, P. Acoustic Monitoring of the Gelation of a Colloidal Suspension. *Rheol. Acta* **2023**, *62*, 71–89, doi:10.1007/s00397-022-01381-w.
103. Qiao, X.; Bai, M.; Tao, K.; Gong, X.; Gu, R.; Watanabe, H.; Sun, K.; Wu, J.; Kang, X. Magnetorheological Behavior of Polyethyene Glycol-Coated Fe3O4 Ferrofluids. *Nihon Reoroji Gakkaishi* **2010**, *38*, 23–30, doi:10.1678/rheology.38.23.
104. Qiao, X.; Zhou, J.; Binks, B.P.; Gong, X.; Sun, K. Magnetorheological Behavior of Pickering Emulsions Stabilized by Surface-Modified Fe3O4 Nanoparticles. *Colloids Surf. Physicochem. Eng. Asp.* **2012**, *412*, 20–28, doi:10.1016/j.colsurfa.2012.06.026.
105. Bielas, R.; Jameel, B.; Józefczak, A. Monitoring of Pickering Emulsion Stability during Magnetic Heating Using Ultrasound Measurements. *Measurement* **2021**, *178*, 109431, doi:10.1016/j.measurement.2021.109431.
106. Skumiel, A. A New Way to Generate a Rotating Magnetic Field in the High Frequency Range. *J. Magn. Magn. Mater.* **2022**, *541*, 168529, doi:10.1016/j.jmmm.2021.168529.
107. Wojciechowski, R.M.; Skumiel, A.; Kurzawa, M.; Demenko, A. Design, Application and Investigation of the System for Generation of Fast Changing, Rotating Magnetic Field Causing Hyperthermic Effect in Magnetic Liquids. *Measurement* **2022**, *194*, 111020, doi:10.1016/j.measurement.2022.111020.

6. Papers constituting the dissertation

[Scientific Paper I]

Ultrasound study of magnetic and non-magnetic nanoparticles agglomeration in high viscous media

Jameel, B., Hornowski, T., Bielas, R., and Józefczak, A.

Materials 15 (2022) 3450

materials

MDPI

Article

Ultrasound Study of Magnetic and Non-Magnetic Nanoparticle Agglomeration in High Viscous Media

Bassam Jameel, Tomasz Hornowski, Rafał Bielas and Arkadiusz Józefczak *

Chair of Acoustics, Faculty of Physics, Adam Mickiewicz University, Uniwersytetu Poznańskiego 2, 61-614 Poznań, Poland; basjam@amu.edu.pl (B.J.); hornaku@amu.edu.pl (T.H.); rafal.bielas@amu.edu.pl (R.B.)
* Correspondence: arkadiusz.jozefczak@amu.edu.pl

Abstract: Ultrasound attenuation spectroscopy has found wide application in the study of colloidal dispersions such as emulsions or suspensions. The main advantage of this technique is that it can be applied to relatively high concentration systems without sample preparation. In particular, the use of Epstein-Carhart-Allegra-Hawley's (ECAH) ultrasound scattering theory, along with experimental data of ultrasound velocity or attenuation, provide the method of estimation for the particle or droplet size from nanometers to millimeters. In this study, suspensions of magnetite and silica nanoparticles in high viscous media (i.e., castor oil) were characterized by ultrasound spectroscopy. Both theoretical and experimental results showed a significant difference in ultrasound attenuation coefficients between the suspensions of magnetite and silica nanoparticles. The fitting of theoretical model to experimental ultrasound spectra was used to determine the real size of objects suspended in a high viscous medium that differed from the size distributions provided by electron microscopy imaging. The ultrasound spectroscopy technique demonstrated a greater tendency of magnetic particles toward agglomeration when compared with silica particles whose sizes were obtained from the combination of experimental and theoretical ultrasonic data and were more consistent with the electron microscopy images.

Keywords: magnetic nanoparticles; silica nanoparticles; suspension; ultrasound spectroscopy; ultrasound scattering theory

Citation: Jameel, B.; Hornowski, T.; Bielas, R.; Józefczak, A. Ultrasound Study of Magnetic and Non-Magnetic Nanoparticle Agglomeration in High Viscous Media. *Materials* **2022**, *15*, 3450. https://doi.org/10.3390/ma15103450

Academic Editors: Erick Ogam and Zine El Abiddine Fellah

Received: 28 March 2022
Accepted: 8 May 2022
Published: 11 May 2022

1. Introduction

In the last few decades, nanoparticles (NPs) of different origins have been used in numerous industrial and biomedical applications. The small size of magnetic NPs combined with the possibility of surface modification [1,2] gave them the ability, among others, to carry other compounds and deliver them in the site of interest. The additional feature is that the shape of magnetic NPs is not limited to spheres, but can be extended to the forms of wires, tubes, and disks [3]. One of the most often proposed applications of magnetic NPs is using them to heat the medium when exposed to an oscillating or a rotating magnetic field [4–7]. Additionally, magnetic NPs can be guided to the target location by applying a static magnetic field [8] that makes them attractive for many applications, such as separation techniques for water purification [9], bioseparation [10], and magnetic resonance imaging [11].

Another application is to utilize magnetic NPs as stabilizers in so-called Pickering emulsions, in which solid particles accumulate on the surfaces of droplets. The use of magnetic NPs can alter emulsion properties in response to external magnetic fields. Magnetic separation is then possible when a low gradient magnetic field is used [12]. Moreover, magnetic Pickering droplets can work as a source of heat under the application of an alternating magnetic field [13]. However, knowledge of the particles' properties, especially their sizes, is crucial in the preparation of Pickering emulsions. The behavior of particles suspended in a carrier liquid, especially their tendency toward agglomeration, is also of

significance. Among the various experimental techniques, ultrasonic spectroscopy can be used to obtain the characteristics of nanoparticles in oil suspensions.

Many previous studies have examined the potential of ultrasound techniques for studying colloids [14,15]. Acoustic methods offer the possibility of non-intrusive, low-cost measurements that can be used in optically opaque, undiluted particulate systems. When a high-frequency sound wave (typically 1–20 MHz) travels through a sample, the measurable parameters (i.e., ultrasound velocity and attenuation) depend on the various properties of the medium. Therefore, ultrasonic measurements can be used to measure the compressibility [16] and the volume fraction [17] of the dispersed phase. By applying the inverse theoretical analysis of ultrasound attenuation spectra obtained in a particulate medium, particle size distribution (PSD) can also be revealed [18], which is vital for practical applications in medicine and industry.

Epstein-Carhart-Allegra-Hawley (ECAH) is the most popular existing ultrasound scattering theory. It assumes that the objects scattered in a continuous medium (e.g., droplets, particles, bubbles, etc.) are spatially separated [19,20]; however, this is idealistic because the high free energy of the system, which is inherent in colloids, as well as the balance of repulsive and attractive forces between interfaces lead to the tendency of the scatterers to form agglomerates [21,22]. In contrast, in media where agglomerations occur, the proper characterization in situ, without special sample preparation prior to measurements, is particularly important for providing reasonable results. The process of dilution can destroy agglomerated structures and change the images of the analyzed system. Therefore, ultrasound experimental techniques supplemented by ultrasound scattering theories can be a powerful tool for showing the tendency toward agglomeration and for providing information about the real appearance of suspensions and PSD [23]. To determine the tendency of agglomeration in suspensions, the zeta potential measurements are commonly utilized [24,25]. However, it should be noted that such measurements also require special sample preparation, mainly the dilution of the colloidal systems studied. That is why techniques that enable direct in situ measurements are needed. Until now, only few studies have used ultrasound to characterize agglomerated systems. The rich literature on two-phase systems of particle suspensions in oil and water focuses on systems with weak acoustic contrast between phases and low-viscous carrier fluids (e.g., polystyrene in water). In the present study, measurements of ultrasound attenuation in a castor oil suspension of magnetite iron oxide NPs were compared with measurements of non-magnetic silica dioxide NPs in suspension. The high viscosity of the carrier fluid, compared to water for example, provided sufficient resistance against particle sedimentation during the experiment. Thus, the analysis of ultrasonic waves as a function of frequency yields reasonable results about the size of suspended particles. The experimental results of ultrasound attenuation were analyzed within the framework of the ECAH theory, which considers contributions to acoustical attenuation due to friction and heat exchange between particles, the surrounding carrier liquid, and the scattering mechanism. The comparison of the ultrasound data with the results of microscopy imaging demonstrated the presence of agglomerated structures of particles dispersed in castor oil.

2. Materials and Methods

2.1. Preparation of Oil Suspensions of Magnetic and Non-Magnetic Particles

Porous silica dioxide nanoparticles (product no. 637246) and iron oxide (iron (II,III) oxide) nanoparticles (product no. 637106) purchased in the form of powder from Sigma-Aldrich Co., St. Louis, MO, USA were used to prepare the oil-based suspensions. The surface of the NP was unmodified, and they were not coated. Castor oil was used as the carrier fluid (MA 220-1, MERLIN, Logrono, Spain). Table 1 provides the basic physical parameters of the continuous phase and the particles, including their viscosity, density, thermal conductivity, and specific heat, as well as the acoustic parameters of ultrasonic velocity and attenuation. The acoustic contrast factors [26] between the castor oil and the silica nanoparticles and between the castor oil and magnetite nanoparticles were 1.59 and

2.11, respectively. For magnetic NPs, the size distribution of particles in the form of powder was calculated based on scanning electron microscopy (SEM) images with 200 nanoparticles. PSD of silica NPs was obtained from transmission electron microscopy (TEM) for particles dispersed in physiological saline solution and calculated with 150 nanoparticles [27]. As the theoretical model requires volume concentration of particles, the PSD was converted to volume distribution by taking into account the densities of particles.

Table 1. The physical parameters of the pure castor oil (continuous phase) and magnetic and non-magnetic particles (dispersed phase) for 25 °C. If the references are not given, the values come from either the measurements or data sheets. For the attenuation coefficient, the frequency, *f*, is expressed in Hz units.

Parameters	Castor Oil	Silica NPs	Magnetite NPs
Viscosity η (Pa·s)	580×10^{-3}	–	–
Density ρ (kg/m^3)	957	1970 [28]	5180 [29]
Thermal conductivity κ (W/mK)	0.180	1.6 [30]	52 [29]
Specific heat C_p (J/kg·K)	1800	728.5 [30]	653 [29]
Thermal expansion β_T (1/K)	7.7×10^{-4} [31]	1.35×10^{-6} [30]	11.8×10^{-6} [29]
Ultrasound velocity c (m/s)	1455	5968 [30]	7157 [29]
Ultrasound atteuation coefficient α (Np/m)	$5.11 \times 10^{-10} f^{1.69}$ [32]	$2.6 \times 10^{-22} f^2$ [33]	$0.01 \times 10^{-15} f^2$ [29]
Shear module μ (N/m^2)	–	2.79×10^{10} [30]	6.03×10^{10} [29]

The suspensions were prepared using an ultrasonic homogenizer (Sonoplus HD 300 equipped with a KE 76 probe; Bandelin, Germany) at a working frequency of 18 kHz and an acoustic intensity estimated at ~17 W/cm^2. The mixture of particles and oil was sonicated for 40 s. The suspensions were tested at two different mass concentrations of particles: 5% and 10%. It is worth noting that the calculations in the ECAH theory required conversion from mass concentration to volume concentration (i.e., volume fraction). Additionally, an optical microscope connected to a camera (UI-3590CP-C-HQ, IDS, Boston, MA, USA) was used to take images of the suspension of magnetite in castor oil in a sample cell (optical path = ~2 mm).

2.2. Experimental Setup

Figure 1 shows the scheme for the ultrasound measurement system used in the experiments. The sample cell was designed using AutoCAD software and printed using a 3D printer. The temperature was maintained at 25 °C and controlled by a thermostat system.

The ultrasonic measurements were carried out using two piezoelectric broadband transducers: a transmitter and a receiver (OLYMPUS, Waltham, MA, USA) driven by an ultrasound generator OPBOX 2.1 (OPTEL, Wrocław, Poland). The ultrasound wave was propagated through the water and sample cells. The signal was recorded at a sampling frequency of 100 MHz.

2.3. Calculation of the Ultrasound Attenuation Coefficient Wave Based on FFT Spectra

The attenuation coefficient of ultrasound in the function of frequency was obtained using the ultrasonic transmission spectroscopy technique. The raw experimental data provided by the setup described in Section 2.3 were analyzed using the well-known reference broadband method [34,35]. The attenuation coefficient was derived from the following equation:

$$\alpha(f) = \alpha(f)_{ref} + \frac{1}{d} \ln \frac{|F_1(f)|}{|F_2(f)|}, \quad (1)$$

where $\alpha(f)$ is the ultrasound attenuation coefficient in Np/m, $\alpha(f)_{ref}$ is the attenuation coefficient of carrier fluid (castor oil), d is the acoustic path inside the sample cell (10 mm), $|F_1(f)|$ is the amplitude of the FFT for the pulse recorded in the castor oil, and $|F_2(f)|$ is

the amplitude of FFT in the pulse recorded in our systems of interest, that is, the magnetic and non-magnetic particle oil suspensions.

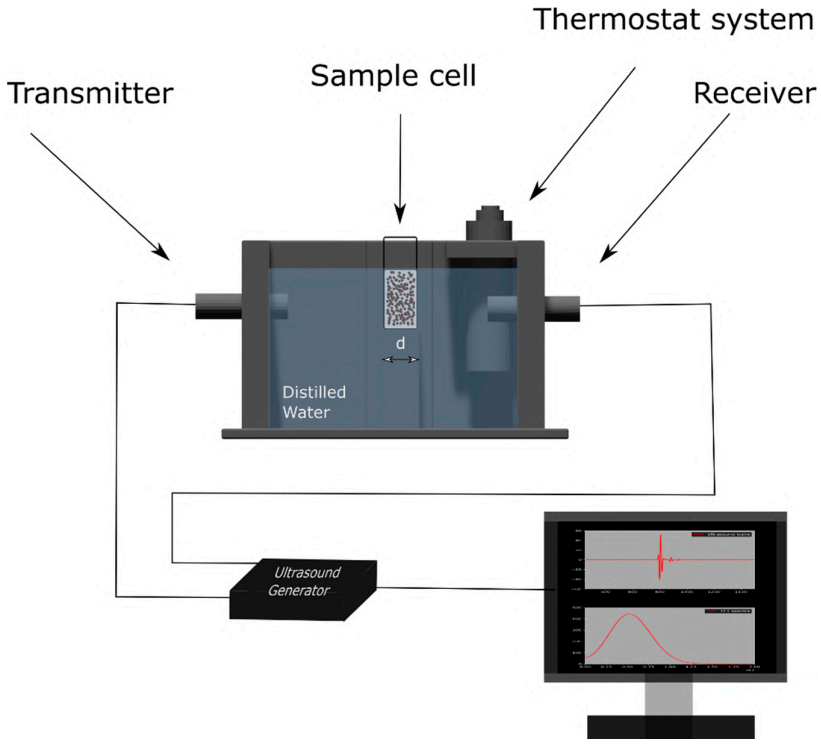

Figure 1. Scheme for an ultrasound measurement system consisting of an ultrasonic testing device with two piezoelectric broadband transducers (transmitter and receiver). Ultrasound wave propagated in the sample at a constant temperature of 25 °C.

Similar to our previous work [12], water was not used as the reference medium because we investigated oil suspensions of magnetic and non-magnetic particles based on castor oil. As the attenuation coefficient of the reference fluid in Equation (1) was expressed as the function of frequency, we expressed $\alpha(f)_{ref}$ as the power-law in the form of $5.11 \times 10^{-10} f^{1.692}$ [19], where f is the frequency in Hz [32].

2.4. Ultrasound Wave Propagation in Two-Phase Systems

Ultrasound attenuation in particle suspension can be conveniently expressed as the sum of four contributions: visco-inertial absorption (α_η), thermal absorption (α_T), scattering losses (α_s), and carrier liquid (α_0) attenuation:

$$a = \alpha_\eta + \alpha_T + \alpha s + \alpha_0. \quad (2)$$

Epstein and Carhart [36] proposed the ultrasound scattering theory for droplets dispersed in liquids, and Allegra and Hawley [37] extended their calculation to solid particles in a liquid continuous phase. The extended theory (ECAH) can be used to characterize the structures of two-phase systems, such as suspensions and emulsions. Based on ultrasound measurements, the scattering of the particle produces three wave modes both inside the particle and in the surrounding fluid: compression mode with the wavenumber k_c, thermal mode with the wavenumber k_T, and shear mode with the wavenumber k_s:

$$k_c = \frac{\omega}{c} + i\alpha \,, \quad (3)$$

$$k_s = (1+i)\left(\frac{\omega\rho}{2\eta}\right)^{\frac{1}{2}}, \tag{4}$$

$$k_T = (1+i)\left(\frac{\omega\rho C_p}{2\kappa}\right)^{\frac{1}{2}}, \tag{5}$$

where c, α, ρ, η, C_p, and κ, ω, are the ultrasound velocity, ultrasound attenuation, density, viscosity, specific heat, the thermal expansion coefficient, and angular frequency, respectively.

In the long wavelength region, where $|k_c R| \ll 1$ and in dilute systems the velocity c_{sol} and attenuation α_{sol} of the scattered ultrasound wave can be calculated by the following equation [28]:

$$\beta = \sqrt{k_c^2 - \frac{3i\phi}{k_c^3 R^3}(A_0 + 3A_1 + 5A_2)}, \tag{6}$$

where $\beta = \frac{\omega}{c_{sol}} + i\alpha_{sol}$ is the complex wave number of the scattered wave, ϕ is the volume fraction of the dispersed phase, and R is the radius of the particle.

The distribution of particle size (PSD) is included in Equation (5) in the form of a histogram with J discrete sizes of particles, R_J using the following formula:

$$\beta = \sqrt{k_c^2 - \sum_{j=1}^{J} \frac{3i\phi_j}{k_c^3 R_j^3}\left(A_{0j} + 3A_{1j} + 5A_{2j}\right)}. \tag{7}$$

The amplitude coefficient, A_0, represents the pulsating motion of the scatterers, which depends on the compressibility difference between the scatterer and the continuous medium, and the difference in the thermal properties of the two media. Coefficient A_1 results from inertial effects due to differences in density between the phases and from the viscous drag of the surrounding fluid. In the long wavelength limit, because the amplitudes of higher order, A_n, decay very rapidly they can be neglected [19].

3. Results and Discussion

3.1. Ultrasound Spectroscopy for Silica NPs Dispersed in Castor Oil

First, the non-magnetic silica NPs were characterized after being dispersed in pure castor oil. Non-magnetic particles dispersed in the continuum phase should exhibit a lower tendency toward clustering compared with magnetic particles. The knowledge of the physical properties of silica particles (Table 1) allowed for the calculation of ultrasound attenuation using the ECAH theory. The theoretical predictions of the ultrasound attenuation coefficient as a function of particle radius are presented in Figure 2a. Figure 2b–d presents the ultrasound attenuation coefficients as a function of frequency.

As shown in Figure 2a, the theoretical results demonstrated the non-monotonous dependence of ultrasonic attenuation on the particle radius (from 1 nm to 10 μm) in a suspension of silica NPs in castor oil. At a constant frequency (10 MHz), the coefficient of attenuation increased in the range of nanoscale from 10–200 nm, and the difference in the attenuation coefficient was approximately 60 Np/m. The increase in attenuation was due to thermal and viscous effects between the two phases, whereas the more significant increase in particle radii above 1 μm was due to Rayleigh scattering. For the frequency range of 1–20 MHz, Figure 2b shows the increase in the attenuation coefficient for the increasing size of the silica NPs from 10–200 nm. It should be noted that castor oil used as the carrier fluid is a high viscous medium that exhibits high ultrasound attenuation. Thus, as shown in Figure 2b, the increase in the attenuation coefficient due to the presence of particles was not high, and there was no significant difference in the theoretical attenuation spectra in the size range between 10 nm and 200 nm. Figure 2c shows the attenuation spectra without the contribution of background attenuation; that is, these results concern only the calculations of the attenuation with the coefficients A_0 and A_1 (see Equation (6)) and the amount of ultrasound attenuation due to particle scattering. The thermal effect A_0,

can be usually neglected when the density contrast between the particles and continuous phase exceeds > 2, when the effect linked to coefficient A_1 tends to dominate [19]. However, this happens mainly when particles are dispersed in low-viscous media, such as water. In contrast, high viscous media, such as castor oil, showed significantly opposite results, in which the contribution of the coefficient A_0 was greater than that of A_1. This surprising result was because the contribution of A_0 involved not only a pure thermal effect but also the so-called material substitution between the silica particles and castor oil [19]. Figure 2d clearly shows that ultrasound attenuation increased as the mass concentration of particles dispersed in the continuous phase increased.

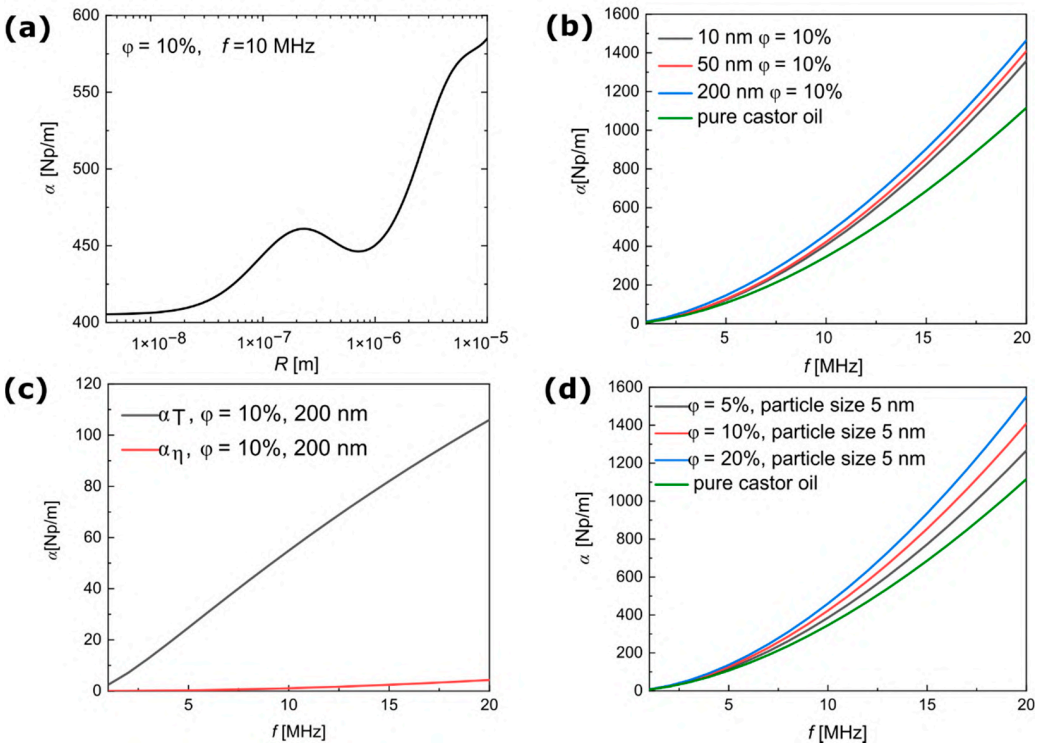

Figure 2. Theoretical results of ultrasound attenuation in dispersions of silica NPs obtained from the ECAH model. (**a**) Ultrasound attenuation coefficient versus particle radius at a constant frequency of 10 MHz. (**b**) Ultrasound attenuation coefficient versus frequency in different particle sizes. (**c**) Contribution of thermal and viscous loss to the ultrasound attenuation coefficient without the influence of background attenuation. (**d**) Ultrasound attenuation coefficient versus frequency in different concentrations of silica NPs. The attenuation spectra of pure castor oil were obtained from [32].

The theoretical predictions presented above were compared with the experimental data. Figure 3a shows the experimental results of ultrasound attenuation as a function of the frequency obtained for a suspension of silica NPs. These results confirmed the expectation that the attenuation coefficient would increase significantly after the nanoparticles were added. Figure 3b shows the SEM image of the powder form of silica NPs. Figure 3c,d presents the TEM image of the silica NPs [27] and the PSD calculated from this image. It is worth noting that to obtain the TEM image, samples of the silica NPs had to be specially prepared; therefore, the optical data used as a reference for the size of particles were not fully based on in situ measurements. In comparison, SEM images taken without sample preparation did not allow for measurement of the PSD as shown in Figure 3b.

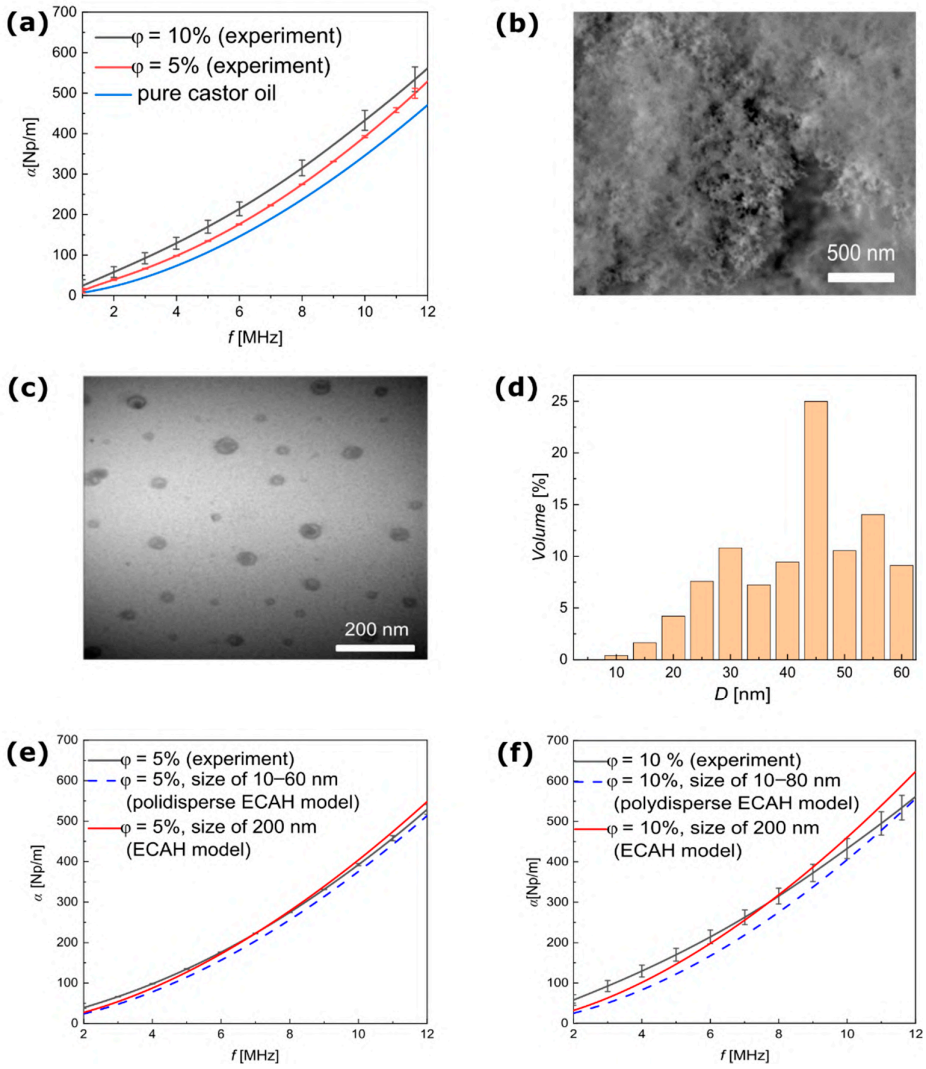

Figure 3. Experimental and theoretical results of ultrasound attenuation of silica NPs dispersed in castor oil. (**a**) Ultrasound attenuation coefficient versus the frequency measured for the mass concentrations of particles at 5% and 10%. (**b**) SEM image of the silica NPs. (**c**) TEM image of the silica NPs [27]. (**d**) PSD of the silica NPs calculated from the TEM image. (**e**) Comparison of the ultrasound attenuation coefficient versus frequency, measured and calculated based on the ECAH model for mass concentration of particles at 5% and (**f**) 10%.

Using the PSD presented in Figure 3d, the ultrasound attenuation was calculated using Equation (7) and directly compared with the experimental results. The results showed a clear discrepancy between particle size in the TEM images and the ultrasound experimental data, shown in Figure 3e,f as a dashed line. The NP mean radius that provided the ultrasound attenuation spectra was comparable to the experimental results at around 200 nm. Therefore, based on the ultrasound spectroscopy results, the non-magnetic silica particles showed little tendency toward the formation of agglomerations in the castor oil, which is in line with Saleh et al., who also showed that silica particles existed in solution as small spherically shaped clusters [38].

3.2. Ultrasound Spectroscopy for Magnetite NPs Dispersed in Castor Oil

The results of the non-magnetic silica NPs were then compared with the results of the magnetic (iron (II,III) oxide) NPs without coating dispersed in pure castor oil. In this

case, the ECAH model was implemented to calculate the ultrasound attenuation coefficient using the physical parameters of castor oil and magnetite, as shown in Table 1.

Figure 4a shows the theoretical dependence of the ultrasonic attenuation coefficient on the particle radii in a range of 1 nm–10 μm at a constant frequency of 10 MHz. The increase in ultrasound attenuation in this case was around 44 Np/m when the values at 10 nm and 100 nm were compared. Similar to the results of the silica NPs, the thermal and viscous effects on the boundaries between phases were responsible for this peak. Regarding the influence of particle size on the attenuation coefficient, Figure 4b shows a monotonous increase in ultrasound attenuation in the range of 2–20 MHz. In the magnetite NP suspensions, the attenuation coefficient was higher than in pure castor oil, but it did not change much between the different sizes. The probable reason is that in the silica and magnetic suspensions, the attenuation of the carrier fluid was much higher than the attenuation of water. Figure 4c presents the attenuation of ultrasound waves without background attenuation in the two phases. The results showed the same behavior as the silica particles, where A_0 tended to dominate the attenuation of ultrasound waves compare with A_1. Figure 4d shows that in a constant particle radius of 10 nm, the ECAH model predicted increased ultrasound attenuation and the mass concentration of particles dispersed in a continuous phase.

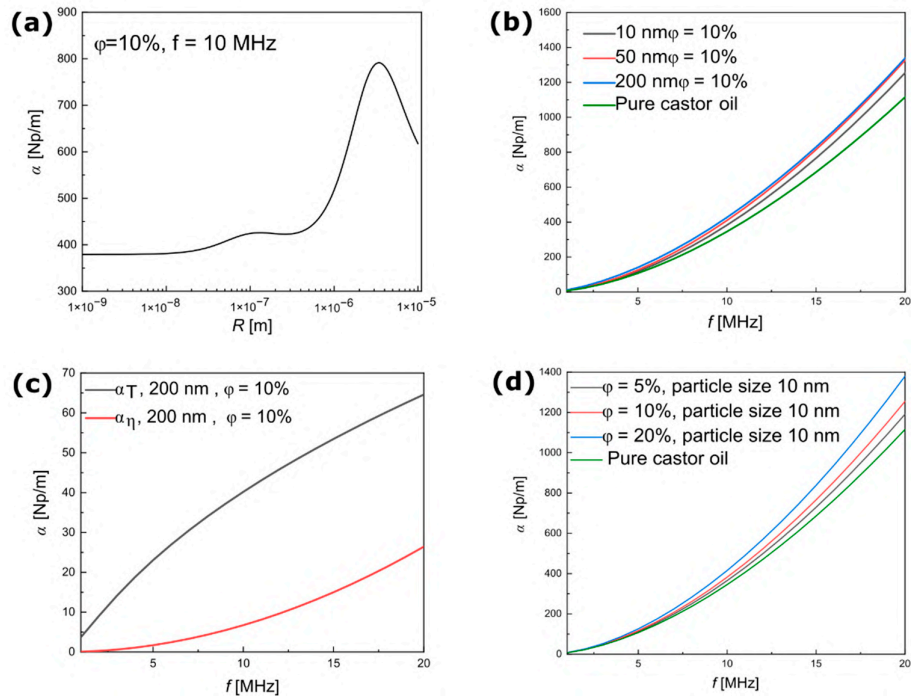

Figure 4. Theoretical results of ultrasound attenuation in dispersions of magnetite NPs obtained from the ECAH model. (**a**) Ultrasound attenuation versus particle radius at a constant frequency of 10 MHz. (**b**) Ultrasound attenuation coefficient versus frequency for different particle sizes. (**c**) Contribution of thermal and viscous loss to the ultrasound attenuation coefficient without the influence of background attenuation. (**d**) Ultrasound attenuation coefficient versus frequency for different concentrations of magnetite NPs. The attenuation spectra for pure castor oil were obtained from [32].

Figure 5a presents the experimental results of the magnetite NPs dispersed in castor oil at the same mass concentration as the silica particles (Figure 4a). The ultrasound spectroscopy results indicated that ultrasound attenuation increased with the mass concentration of magnetic particles, and the attenuation coefficients clearly exceeded the values in pure castor oil. The SEM image (Figure 4b) served to determine the PSD of the magnetite NPs shown in Figure 4c. This distribution was used to reproduce the ultrasound

attenuation coefficient based on the ECAH model. Figure 5d,e shows a comparison of the results of this calculation (Equation (7)) with the experimental results of two mass concentrations: 5% and 10%. One can see the discrepancy in the attenuation coefficient between the experimental results and the theoretical predictions in the range of frequency from 1–12 MHz. The size distribution obtained from the SEM image did not refer to the real size distribution of the particles suspended in castor oil. A possible reason is that the SEM image was taken of the magnetite NPs in the form of powder, so the interaction between the particles in dispersion was neglected. In the carrier fluid, magnetite particles formed much larger structures than those detected by ultrasonic spectroscopy measurements, which was confirmed by the results of further analysis shown in Figure 6.

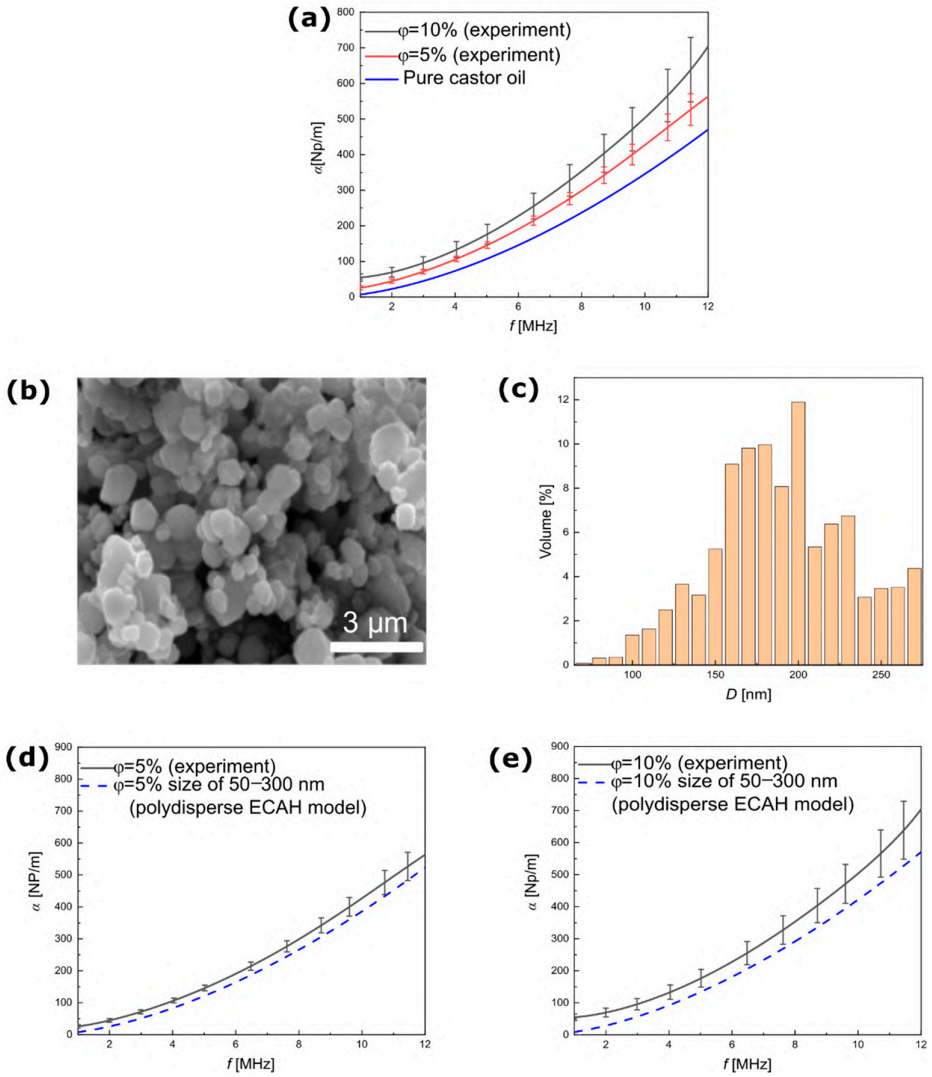

Figure 5. Experimental and theoretical results of ultrasound attenuation of magnetite NPs dispersed in castor oil. (**a**) Ultrasound attenuation coefficient versus the frequency measured for the mass concentrations of particles of 5% and 10%. (**b**) SEM image of the magnetite NPs used. (**c**) PSD for the magnetite NPs calculated from the SEM image. (**d**) Comparison of the ultrasound attenuation coefficient versus the frequency measured and calculated based on the ECAH model for the mass concentration of particles at 5% and (**e**) 10%.

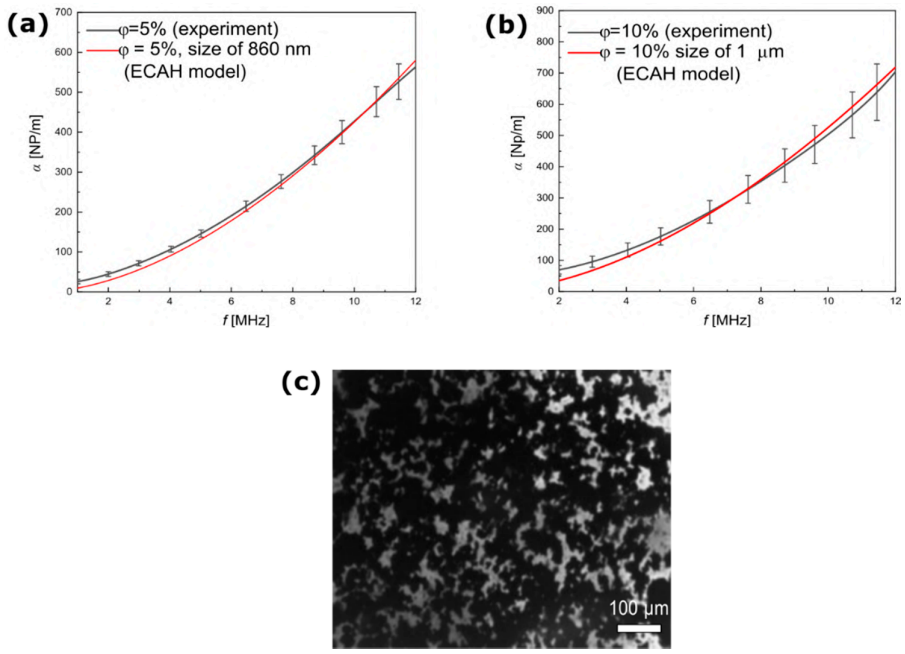

Figure 6. Experimental and theoretical results of the ultrasound attenuation of magnetite NPs dispersed in castor oil at different mass concentrations of particles: (**a**) 5% and (**b**) 10%. The theoretical curves were determined based on Equation (6) for the best-fitted sizes of particle scatterers. (**c**) Optical microscopy image of the dispersion of magnetite NP in castor oil (mass concentration at 10%).

Figure 6a,b presents the results of the ultrasound spectroscopy measurements of the magnetic NPs dispersed in castor oil, as well as the theoretical curves. The best agreement between the theoretical and experimental attenuation spectra was obtained at a particle radius of 860 nm and 1 μm in lower and higher particle concentrations, respectively. This result suggests that clusters of particles were formed in an oil suspension with a high content of magnetite NPs. It is possible that agglomeration increases significantly as concentration increases [39]. This study utilized very low concentrations to fabricate a stable magnetic fluid based on oil. However, the real sizes of the objects dispersed in castor oil were much larger than the microscopy data indicated. Our previous studies on tissue-mimicking phantoms [40,41] showed that bare magnetic NPs, in the form of powder without surface modification, strongly interacted and tended to agglomerate and form larger structures, as shown clearly in the optical microscopy image in Figure 6c. The sizes of the visible clusters were in micrometers, which corresponded well to the size estimated from the comparison between the ECAH theory and the experiment. The cluster of particles in dispersions highly influenced the physical, magnetic, and rheological characteristics as well as their applications in magnetic and ultrasonic heating.

The magnetic and non-magnetic nanoparticles showed different behaviors after being suspended in castor oil. The ultrasound technique facilitated the non-destructive detection of the structure of particles in suspension and permitted determining whether the system was clustered or not. In previous studies in the literature, silica particles have been used to show the influence of different particle sizes and their concentrations in ultrasound attenuation by using the ECAH model [42]. The results showed good agreement between the experimental and theoretical approaches. However, it is worth mentioning that the authors studied silica microparticles in aqueous solutions. In the present study, we used particles of at least two orders of magnitude smaller in size, which were dispersed in a high viscous medium. The difference in the viscosity of the carrier fluid could affect the possibility that silica particles agglomerate according to the range of nanometer sizes.

In the case of the magnetite NPs, magnetic dipole–dipole interactions easily occur, which is responsible for the deteriorated stability of the magnetic fluid and the formation of clusters [22,43]. Such interactions depend strongly on magnetic anisotropy, and the increase in anisotropy constant leads to the stronger agglomeration tendency for smaller, single-domain particles [44]. Additionally, the smaller magnetic and non-magnetic NPs have high free surface energy that generally promotes the tendency of agglomeration [45]. Different approaches may be used to avoid agglomeration in colloidal systems, including sonication of dispersion by ultrasonic bath [46] and particles covered by charged surfactants [47]. The use of the latter can be crucial for altering the affinity of the particles to the emulsion phases in Pickering emulsions.

Knowledge about the real size of particles in situ, rather than the size provided by techniques that require special sample preparation, such as electron microscopy imaging, is important for the further characterization of complex systems that employ nanoparticles. For instance, in Pickering emulsions, the number of particles accumulated at the droplet interface plays an important role in many phenomena, such as magnetic separation and magnetic heating. However, the suspension of nanoparticles must be prepared prior to the production of Pickering droplets. Moreover, the presence or lack of particle clustering at this stage may influence the appearance and properties of final Pickering emulsions.

4. Conclusions

In this study, the ultrasound attenuation spectra were used to determine the size of non-magnetic and magnetic NPs suspended in high viscous media. We implemented the scattering ECAH theory to calculate the ultrasound attenuation spectra with different concentrations and particle sizes using physical properties of the carrier fluid and a dispersed phase. The combination of experimental and theoretical approaches used in this study enabled the detection of particle clusters present in the studied systems. The silica NPs showed a much lower tendency toward clustering compared with the magnetic NPs. In contrast, the measured ultrasound attenuation coefficients of the magnetic NPs were much higher than the theoretical predictions for the sizes obtained from SEM imaging. This discrepancy occurred because SEM images generally show the real size of particles in a dry powder form. This microscopy technique does not take into account the NPs interactions that happen after dispersion, especially in high viscous oils. The change in particle sizes in the theoretical predictions led to better agreement. Therefore, our approach was able to demonstrate the presence of clusters of structures that were micrometers in size in the case of magnetic particles.

The usefulness of the ultrasound method lies in its relative simplicity and non-invasive application. Most importantly, it does not require special sample preparation because the actual suspension is tested. In future research, it will be possible to use this method to study the size of Pickering droplets and their behavior under external magnetic fields.

Author Contributions: B.J.: Investigation, Theoretical analysis, Visualization, Setup design, Writing—original draft, Finalization. T.H.: Methodology, Theoretical analysis, Finalization. R.B.: Methodology, Finalization. A.J.: Conceptualization, Methodology, Supervision, Finalization. All authors have read and agreed to the published version of the manuscript.

Funding: This work was supported by project no. 2019/35/O/ST3/00503 (PRELUDIUM BIS) of the Polish National Science Centre.

Institutional Review Board Statement: Not applicable.

Informed Consent Statement: Not applicable.

Data Availability Statement: Not applicable.

Acknowledgments: The authors would like to thank Rafał Białek for his help with experimental setup design and three-dimension printing.

Conflicts of Interest: The authors declare no conflict of interest.

References

1. Bruce, I.J.; Sen, T. Surface Modification of Magnetic Nanoparticles with Alkoxysilanes and Their Application in Magnetic Bioseparations. *Langmuir* **2005**, *21*, 7029–7035. [CrossRef] [PubMed]
2. Tishkevich, D.I.; Korolkov, I.V.; Kozlovskiy, A.L.; Anisovich, M.; Vinnik, D.A.; Ermekova, A.E.; Vorobjova, A.I.; Shumskaya, E.E.; Zubar, T.I.; Trukhanov, S.V.; et al. Immobilization of boron-rich compound on Fe3O4 nanoparticles: Stability and cytotoxicity. *J. Alloys Compd.* **2019**, *797*, 573–581. [CrossRef]
3. Roca, A.G.; Gutiérrez, L.; Gavilán, H.; Fortes Brollo, M.E.; Veintemillas-Verdaguer, S.; Morales, M.d.P. Design strategies for shape-controlled magnetic iron oxide nanoparticles. *Adv. Drug Deliv. Rev.* **2019**, *138*, 68–104. [CrossRef] [PubMed]
4. Gavilán, H.; Avugadda, S.K.; Fernández-Cabada, T.; Soni, N.; Cassani, M.; Mai, B.T.; Chantrell, R.; Pellegrino, T. Magnetic nanoparticles and clusters for magnetic hyperthermia: Optimizing their heat performance and developing combinatorial therapies to tackle cancer. *Chem. Soc. Rev.* **2021**, *50*, 11614–11667. [CrossRef] [PubMed]
5. Kaczmarek, K.; Mrówczyński, R.; Hornowski, T.; Bielas, R.; Józefczak, A. The Effect of Tissue-Mimicking Phantom Compressibility on Magnetic Hyperthermia. *J. Nanomater.* **2019**, *9*, 803. [CrossRef]
6. Skumiel, A.; Kopcansky, P.; Timko, M.; Molcan, M.; Paulovicova, K.; Wojciechowski, R. The influence of a rotating magnetic field on the thermal effect in magnetic fluid. *Int. J. Therm. Sci.* **2022**, *171*, 107258. [CrossRef]
7. Smolkova, I.S.; Kazantseva, N.E.; Makoveckaya, K.N.; Smolka, P.; Saha, P.; Granov, A.M. Maghemite based silicone composite for arterial embolization hyperthermia. *Mater. Sci. Eng. C Mater. Biol. Appl.* **2015**, *48*, 632–641. [CrossRef]
8. Leong, S.S.; Ahmad, Z.; Low, S.C.; Camacho, J.; Faraudo, J.; Lim, J. Unified View of Magnetic Nanoparticle Separation under Magnetophoresis. *Langmuir* **2020**, *36*, 8033–8055. [CrossRef]
9. Baresel, C.; Schaller, V.; Jonasson, C.; Johansson, C.; Bordes, R.; Chauhan, V.; Sugunan, A.; Sommertune, J.; Welling, S. Functionalized magnetic particles for water treatment. *Heliyon* **2019**, *5*, e02325. [CrossRef]
10. Fatima, H.; Kim, K.-S. Magnetic nanoparticles for bioseparation. *Korean J. Chem. Eng.* **2017**, *34*, 589–599. [CrossRef]
11. Shokrollahi, H.; Khorramdin, A.; Isapour, G. Magnetic resonance imaging by using nano-magnetic particles. *J. Magn. Magn. Mater.* **2014**, *369*, 176–183. [CrossRef]
12. Jameel, B.; Bielas, R.; Hornowski, T.; Józefczak, A. Propagation of ultrasonic wave in magnetic Pickering emulsion under DC magnetic field. *J. Magn. Magn. Mater.* **2022**, *542*, 168590. [CrossRef]
13. Bielas, R.; Hornowski, T.; Paulovičová, K.; Rajňák, M.; Józefczak, A. The effect of magnetic particles covering the droplets on the heating rate of Pickering emulsions in the AC magnetic field. *J. Mol. Liq.* **2020**, *320*, 114388. [CrossRef]
14. Hossein, F.; Materazzi, M.; Lettieri, P.; Angeli, P. Application of acoustic techniques to fluid-particle systems—A review. *Chem. Eng. Res. Des.* **2021**, *176*, 180–193. [CrossRef]
15. Povey, M.J.W. Ultrasound particle sizing: A review. *Particuology* **2013**, *11*, 135–147. [CrossRef]
16. Cushing, K.W.; Garofalo, F.; Magnusson, C.; Ekblad, L.; Bruus, H.; Laurell, T. Ultrasound Characterization of Microbead and Cell Suspensions by Speed of Sound Measurements of Neutrally Buoyant Samples. *Anal. Chem.* **2017**, *89*, 8917–8923. [CrossRef]
17. Su, Q.; Tan, C.; Dong, F. Measurement of Oil–Water Two-Phase Flow Phase Fraction With Ultrasound Attenuation. *IEEE Sens. J.* **2018**, *18*, 1150–1159. [CrossRef]
18. Silva, C.A.M.; Saraiva, S.V.; Bonetti, D.; Higuti, R.T.; Cunha, R.L.; Pereira, L.O.V.; Silva, F.V.; Fileti, A.M.F. Measurements of bimodal droplet size distribution of emulsions using ultrasonic spectroscopy in the long and intermediate wavelength regimes. *Chem. Eng. Sci.* **2021**, *252*, 117274. [CrossRef]
19. Challis, R.E.; Povey, M.J.W.; Mather, M.L.; Holmes, A.K. Ultrasound techniques for characterizing colloidal dispersions. *Rep. Prog. Phys.* **2005**, *68*, 1541–1637. [CrossRef]
20. Mori, H.; Norisuye, T.; Nakanishi, H.; Tran-Cong-Miyata, Q. Ultrasound attenuation and phase velocity of micrometer-sized particle suspensions with viscous and thermal losses. *Ultrasonics* **2018**, *83*, 171–178. [CrossRef]
21. Hotze, E.M.; Phenrat, T.; Lowry, G.V. Nanoparticle Aggregation: Challenges to Understanding Transport and Reactivity in the Environment. *J. Environ. Qual.* **2010**, *39*, 1909–1924. [CrossRef] [PubMed]
22. Yeap, S.P.; Lim, J.; Ooi, B.S.; Ahmad, A.L. Agglomeration, colloidal stability, and magnetic separation of magnetic nanoparticles: Collective influences on environmental engineering applications. *J. Nanopart. Res.* **2017**, *19*, 368. [CrossRef]
23. Yu, H.; Tan, C.; Dong, F. Particle Size Characterization in Liquid–Solid Dispersion With Aggregates by Broadband Ultrasound Attenuation. *IEEE Trans. Instrum. Meas.* **2021**, *70*, 1–11. [CrossRef]
24. Allouni, Z.E.; Cimpan, M.R.; Høl, P.J.; Skodvin, T.; Gjerdet, N.R. Agglomeration and sedimentation of TiO2 nanoparticles in cell culture medium. *Colloids Surf. B* **2009**, *68*, 83–87. [CrossRef] [PubMed]
25. Greenwood, R.; Lapčíková, B.; Surýnek, M.; Waters, K.; Lapčík, L. The zeta potential of kaolin suspensions measured by electrophoresis and electroacoustics. *Chem. Pap.* **2007**, *61*, 83–92. [CrossRef]
26. Ohiri, K.A.; Evans, B.A.; Shields IV, C.W.; Gutiérrez, R.A.; Carroll, N.J.; Yellen, B.B.; López, G.P. Magnetically Responsive Negative Acoustic Contrast Microparticles for Bioanalytical Applications. *ACS Appl. Mater. Interfaces* **2016**, *8*, 25030–25035. [CrossRef]
27. Diao, J.; Xia, Y.; Jiang, X.; Qiu, J.; Cheng, S.; Su, J.; Duan, X.; Gao, M.; Qin, X.; Zhang, J.; et al. Silicon dioxide nanoparticles induced neurobehavioral impairments by disrupting microbiota-gut-brain axis. *J Nanobiotechnol.* **2021**, *19*, 174. [CrossRef]
28. Challis, R.; Tebbutt, J.; Holmes, A. Equivalence between three scattering formulations for ultrasonic wave propagation in particulate mixtures. *J. Phys. D Appl. Phys.* **1998**, *31*, 3481. [CrossRef]
29. Vinogradov, A. Physicochemical and acoustic properties of water-based magnetic colloid. *J. Colloid Sci.* **2004**, *66*, 29–37. [CrossRef]

30. Kaye, G.W.C.; Laby, T. *Tables of Physical and Chemical Constants 16th edn (Harlow)*; NPL (National Physical Laboratory): Teddington, UK, 1995.
31. Patel, V.R.; Dumancas, G.G.; Viswanath, L.C.K.; Maples, R.; Subong, B.J.J. Castor oil: Properties, uses, and optimization of processing parameters in commercial production. *Lipid Insights* **2016**, *9*, S40233. [CrossRef]
32. Tong, J.; Povey, M.J.W. Pulse echo comparison method with FSUPER to measure velocity dispersion in n-tetradecane in water emulsions. *Ultrasonics* **2002**, *40*, 37–41. [CrossRef]
33. Holmes, A.K.; Challis, R.E.; Wedlock, D.J. A wide-bandwidth ultrasonic study of suspensions: The variation of velocity and attenuation with particle size. *J. Colloid Interface Sci.* **1994**, *168*, 339–348. [CrossRef]
34. Strohm, E.M.; Kolios, M.C. Sound velocity and attenuation measurements of perfluorocarbon liquids using photoacoustic methods. In Proceedings of the 2011 IEEE International Ultrasonics Symposium, Orlando, FL, USA, 18–21 October 2011; pp. 2368–2371.
35. Treeby, B.E.; Cox, B.T.; Zhang, E.Z.; Patch, S.K.; Beard, P.C. Measurement of Broadband Temperature-Dependent Ultrasonic Attenuation and Dispersion Using Photoacoustics. *IEEE Trans. Ultrason. Ferroelectr. Freq. Control* **2009**, *56*, 1666–1676. [CrossRef] [PubMed]
36. Epstein, P.S.; Carhart, R.R. The absorption of sound in suspensions and emulsions. I. Water fog in air. *J. Acoust. Soc. Am.* **1953**, *25*, 553–565. [CrossRef]
37. Allegra, J.R.; Hawley, S.A. Attenuation of Sound in Suspensions and Emulsions: Theory and Experiments. *J. Acoust. Soc. Am.* **1972**, *51*, 1545–1564. [CrossRef]
38. Saleh, A.S.; Lee, J.-Y.; Jo, Y.; Yun, J.-I. Uranium(VI) sorption complexes on silica in the presence of calcium and carbonate. *J. Environ. Radioact.* **2018**, *182*, 63–69. [CrossRef]
39. Rajnak, M.; Dolnik, B.; Hodermarsky, P.; Paulovicova, K.; Cimbala, R.; Timko, M.; Kopcansky, P. Dynamic magnetic response of ferrofluids under a static electric field. *Phys. Fluids* **2021**, *33*, 082006. [CrossRef]
40. Kaczmarek, K.; Bielas, R.; Siluk, M.; Hornowski, T.; Józefczak, A. Comparison of magnetic and non-magnetic nanoparticles as sonosensitizers in ultrasonic hyperthermia. *Acta Physica Polonica A* **2020**, *137*, 653–656. [CrossRef]
41. Kaczmarek, K.; Hornowski, T.; Kubovčíková, M.; Timko, M.; Koralewski, M.; Józefczak, A. Heating Induced by Therapeutic Ultrasound in the Presence of Magnetic Nanoparticles. *ACS Appl. Mater. Interfaces* **2018**, *10*, 11554–11564. [CrossRef]
42. Mori, H.; Norisuye, T.; Nakanishi, H.; Tran-Cong-Miyata, Q. Ultrasound attenuation and phase velocity of moderately concentrated silica suspensions. *Ultrasonics* **2019**, *93*, 63–70. [CrossRef]
43. Schwaminger, S.P.; Schwarzenberger, K.; Gatzemeier, J.; Lei, Z.; Eckert, K. Magnetically Induced Aggregation of Iron Oxide Nanoparticles for Carrier Flotation Strategies. *J. Environ. Radioact.* **2021**, *13*, 20830–20844. [CrossRef] [PubMed]
44. Serantes, D.; Baldomir, D. Nanoparticle Size Threshold for Magnetic Agglomeration and Associated Hyperthermia Performance. *Nanomaterials* **2021**, *11*, 2786. [CrossRef] [PubMed]
45. Gambinossi, F.; Mylon, S.E.; Ferri, J.K. Aggregation kinetics and colloidal stability of functionalized nanoparticles. *Adv. Colloid Interface Sci.* **2015**, *222*, 332–349. [CrossRef] [PubMed]
46. Wu, W.; Ichihara, G.; Suzuki, Y.; Izuoka, K.; Oikawa-Tada, S.; Chang, J.; Sakai, K.; Miyazawa, K.; Porter, D.; Castranova, V. Dispersion method for safety research on manufactured nanomaterials. *Ind. Health* **2014**, *52*, 54–65. [CrossRef]
47. Choi, Y.-W.; Lee, H.; Song, Y.; Sohn, D. Colloidal stability of iron oxide nanoparticles with multivalent polymer surfactants. *J. Colloid Interface Sci.* **2015**, *443*, 8–12. [CrossRef]

[Scientific Paper II]

Ultrasound measurements of particle shells in magnetic Pickering emulsions

Jameel, B., Bielas, R., and Józefczak, A.

Measurement 220 (2023) 113409

Measurement 220 (2023) 113409

Contents lists available at ScienceDirect

Measurement

journal homepage: www.elsevier.com/locate/measurement

Ultrasound measurements of particle shells in magnetic Pickering emulsions

Bassam Jameel, Rafał Bielas, Arkadiusz Józefczak *

Chair of Acoustics, Faculty of Physics, Adam Mickiewicz University in Poznań, Uniwersytetu Poznańskiego 2, 61-614 Poznań, Poland

ARTICLE INFO

Keywords:
Ultrasound spectroscopy
Ultrasound scattering theory
Magnetic nanoparticles
Pickering emulsion
Emulsion stability

ABSTRACT

A magnetic Pickering emulsion is an emulsion stabilized by magnetic nanoparticles that accumulate at the droplet interface to form a shell. The physical characterization of a Pickering emulsion, particularly the size of the stabilizing layer and the size of Pickering droplets, is essential for many applications. This report presents the findings of a theoretical and experimental study of ultrasound attenuation involving magnetic Pickering emulsions. Specifically, the ultrasound scattering theory based on the so-called core–shell model was utilized to interpret data obtained from ultrasonic measurements. In this model, the additional phase, i.e., the particle shell covering the oil core of a Pickering droplet, was considered for acoustic wave propagation in emulsions. The attenuation of an ultrasonic wave in the function of wavenumber multiplied by core radius (kb), wavenumber multiplied by shell thickness (kc), and frequency was numerically calculated for different concentrations of the droplets. The theoretical results and measurements were compared using a novel approach based on ultrasound spectroscopy to determine the stability and the size of the magnetic Pickering droplets.

1. Introduction

Emulsions are mixtures of two or more immiscible liquids and can be classified as oil-in-oil, oil-in-water, or water-in-oil emulsions. They are thermodynamically unstable systems that ultimately evolve toward phase separation over time. A molecular surfactant [1,2] or surface-active polymer with low molar mass [3] can be used to decrease the interfacial tension between the phases and thus stabilize emulsion droplets. Micro- and nanoscale colloidal particles can also be used to prepare and stabilize emulsions. These types of stabilized emulsions are known as Pickering emulsions [4]. Rapid technological developments for preparing Pickering emulsions and novel ideas for using Pickering emulsions have become crucial in various fields, including biomedicine [5,6], cosmetics [7], and pharmaceutical industries, among others [8]. Scientific interest in Pickering emulsions has significantly increased, partly because of the rise in nanotechnology and green chemistry [9].

The energy required for stabilizing dispersed droplets using spherical particles depends on the interfacial tension between the dispersed and continuous phases, the radius of the spherical particle [10], and particle wettability, which is characterized by contact angle [11]. Magnetic nanoparticles have attracted great research attention, especially in the biomedical field [12]. Recently, there has been increasing demand for utilizing them also in enhanced oil recovery [13] and water purification [14]. Unmodified magnetite nanoparticles are hydrophilic, and they can be turned into hydrophobic particles through surface modifications. Modified magnetite nanoparticles with increased hydrophobicity exhibit better stabilization behaviors than unmodified ones when considering oil-in-water Pickering emulsions [15]. Moreover, Zhou *et al.* [16] showed that hydrophilic magnetite nanoparticles could weakly stabilize polar oil at a contact angle close to 90°.

Literature on the stability of oil-in-oil magnetic Pickering emulsions (MPEs) is scarce. Therefore, there is a constant need to characterize MPEs by monitoring the preparation process and evaluating the final outcomes. First, droplet size has a strong impact on magnetic behavior under an external magnetic field, as the drag force during magnetic separation is proportional to the radius of the Pickering droplet [17,18]. Additionally, particle size and the solidity of the particle shell around a Pickering droplet influence the rate of magnetic heating and heat transfer during the cooling [19]. Therefore, it is particularly important to obtain reliable, accurate measurements of the sizes of Pickering droplets and their particle shells. While there are various methods for characterizing emulsions, such as laser diffraction [20], dynamic light scattering [21], optical microscope visualization [22], and near-infrared spectroscopy [23], none of these methods can provide information on

* Corresponding author.
E-mail address: arkadiusz.jozefczak@amu.edu.pl (A. Józefczak).

https://doi.org/10.1016/j.measurement.2023.113409
Received 2 June 2023; Received in revised form 18 July 2023; Accepted 2 August 2023
Available online 3 August 2023

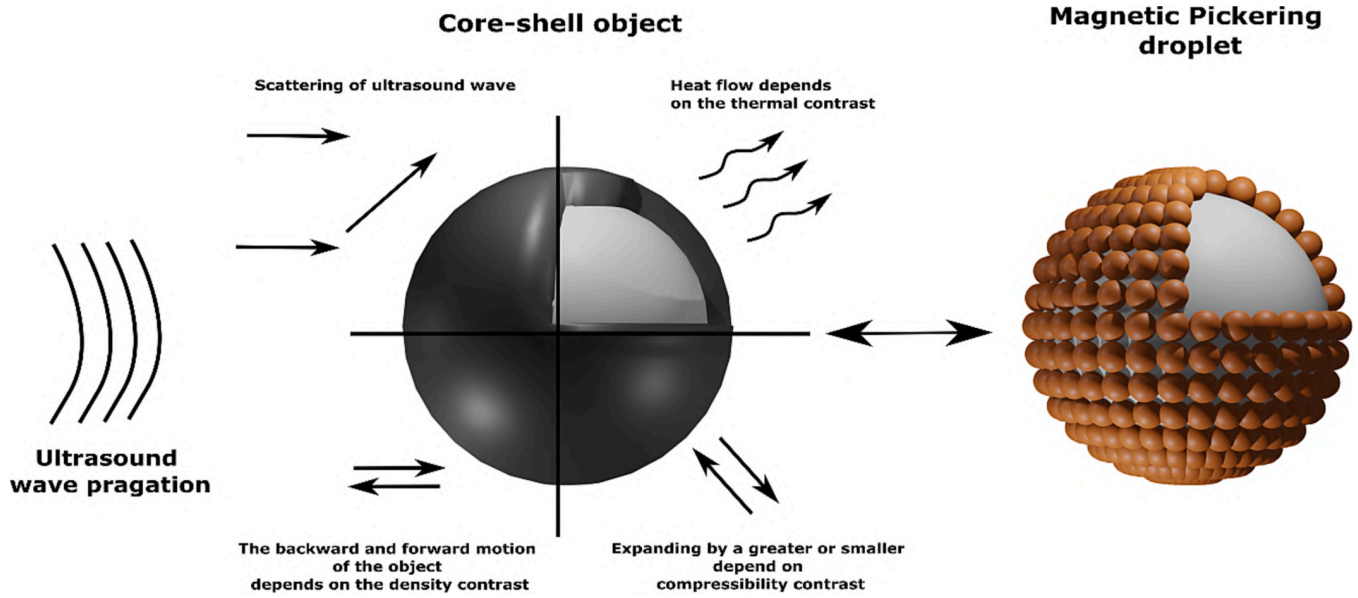

Fig. 1. The ultrasound wave scattering and absorption mechanisms of a core–shell object representing a magnetic Pickering droplet.

the stability of an MPE in a robust, nondestructive way.

Low-intensity ultrasound spectroscopy has been utilized in materials science as in-line measurement technique for calculating the size distributions [24], determining the crystallization [25,26], and monitoring creaming and sedimentation [27]. Also, magnetic systems, such as magnetic fluids, were tested by ultrasound under different magnetic fields [28,29]. The change in ultrasound attenuation has revealed the magnetic interactions in magnetic fluids as important factors influencing their internal structure. Although ultrasound techniques have been broadly used to characterize colloidal systems [30], there are only a few reports on using ultrasound spectroscopy to study particle-stabilized emulsions. A combination of experimental and theoretical descriptions is even less represented in the literature. This may stem from the fact that the commonly used ultrasonic scattering theory based on the works of Epstein and Carhart [31] and Allegra and Hawley [32] does not assume the presence of a particle layer around an emulsion droplet. As we showed in a previous work [33], not considering the contributions of particle shells in the theoretical framework leads to discrepancies between theoretical and experimental results. A possible solution to this issue could be the use of an extended version of the Epstein, Carhart, Allegra, and Hawley (ECAH) theory that describes capsulated emulsions, as proposed by Anson and Chivers [34] known as core–shell model. The practical implementation of Anson and Chivers model was the main goal of this work, following our previous research on magnetic and non-magnetic dispersion using ECAH model [35]. Fig. 1 presents the mechanisms of ultrasound wave scattering and absorption by core–shell object that could be the simplified model of a magnetic Pickering emulsion droplet. Recently, this approach was used to characterize Pickering emulsions by Kanamori *et al.* [36] that utilized the core–shell model to evaluate the stability of an oil-in-water emulsion stabilized by silica particles.

In this study, the droplet radius and magnetic shell thickness of an MPE were investigated using ultrasound spectroscopy. Measuring particle shell size and evaluating Pickering droplet stability are necessary for controlling the formation process of a Pickering emulsion. Here, we used the experimental and theoretical data obtained from ultrasound attenuation spectroscopy as a nondestructive method for determining the important features of the MPE. The formation process of a highly viscous oil-in-oil MPE was influenced by particle concentration, dispersed phase concentration, and electric field application. Ultrasonic waves were employed in the transmission mode at megahertz frequencies, and they matched a range of Pickering droplet sizes, confirming that ultrasound is suitable for characterizing micro-sized Pickering droplets. To interpret the experimental measurements and determine droplet size and shell thickness, the ultrasound scattering theory based on the core–shell model proposed by Anson and Chivers, which has paved the way for better characterizations of MPEs, was applied.

2. Ultrasound scattering theory based on the core–shell model

As the ultrasonic scattering theories have been extended over the past decades, it is necessary to break down the theoretical framework of this study on MPEs. An ultrasonic wave of frequency f that is scattered by an object suspended in a continuous phase can be described by a complex wavenumber β :

$$\beta = \frac{2\pi f}{c} + i\alpha. \tag{1}$$

In **Equation (1)**, the theoretical value of the imaginary part of β represents ultrasound attenuation α, and the real part includes ultrasound velocity c. The ultrasound scattering theory for spherical scatterers was first derived by Epstein, Carhart, Allegra, and Hawley [31,32], taking into account the thermal and shear waves produced during ultrasound propagation in the two phase system. In our previous work [35], the ECAH model was utilized to characterize the solid particles dispersed in a highly viscous medium, resulting in information about the aggregation of magnetic and non-magnetic nanoparticles. The main aim of the present study, in the extension of our previous consideration, was to characterize magnetic Pickering droplets by considering the influence of the third phase in the model (particles). In their work, Anson and Chivers [34] used the core–shell model to analyze the ultrasound scattering induced by a suspended sphere covered with a shell layer made from another material. The present study focused on an oil-in-oil Pickering emulsion covered by magnetic nanoparticles. The scheme in Fig. 2 illustrates the similarities between the core–shell object and the Pickering droplet. In a Pickering droplet, the particle shell stabilizes the droplet interface, which can be approximated with a rigid layer as it is in the core–shell model. This approximation makes the core–shell model useful for characterizing MPEs.

To calculate ultrasound attenuation in the MPE, an additional boundary condition was added to the ECAH model, which influenced the

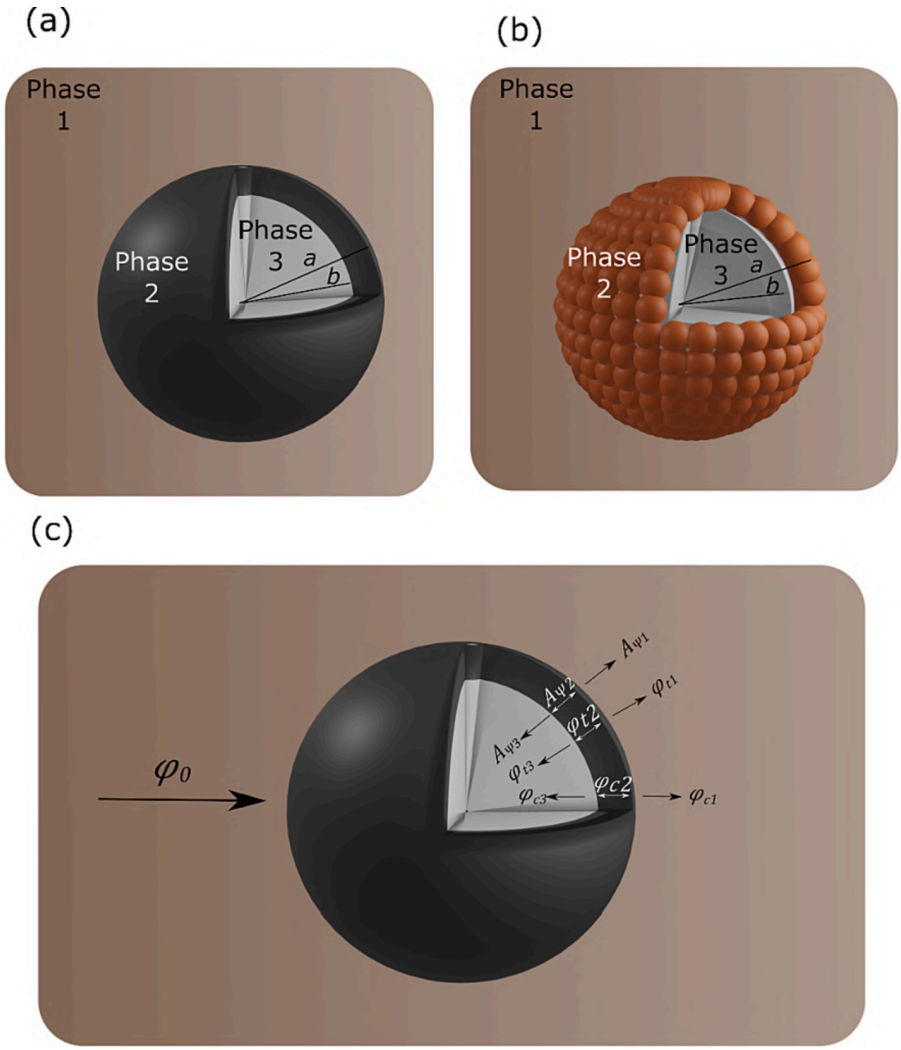

Fig. 2. A schematic representation of three phase object and the difference between (a) a core–shell object and (b) a magnetic Pickering droplet, with a and b indicating the outer and inner radii, respectively; (c) an illustration of the scattering primary compressional wave by the core–shell object into compressional, thermal, and shear waves, represented by their potentials **(Equations (5)–(7)).**

absorption and scattering of the wave after its interaction with the Pickering droplet. As shown in Fig. 2**c**, transmitting a compressional wave into a core–shell object led to the production of compressional, thermal, and shear waves in each interface, with backward and forward propagations to the direction of the incident wave.

In line with the ECAH model, the three wave potentials for three wave modes can be written as follows:

$$\left(\nabla^2 + k_c^2\right)\varphi_c = 0 \tag{2a}$$

$$\left(\nabla^2 + k_t^2\right)\varphi_t = 0 \tag{2b}$$

$$\left(\nabla^2 + k_s^2\right)A_\Psi = 0 \tag{2c}$$

Here, φ_c is the potential of a longitudinal wave of the compressional mode, φ_t is the potential of a longitudinal wave of the thermal mode, and A_Ψ is the potential of a transverse wave of the shear mode. The three modes exist in a carrier fluid (Phase 1), a shell (Phase 2), and a core material (Phase 3), as shown in Fig. 2**c**. Additionally, k_c, k_t, and k_s represent the wavenumbers for the compressional, thermal, and shear modes, respectively.

$$k_c = \frac{\omega}{c} + i\alpha, \tag{3a}$$

$$k_t = (1+i)\left(\frac{\omega\rho C_p}{2\kappa}\right)^{\frac{1}{2}}, \tag{3b}$$

$$k_s = (1+i)\left(\frac{\omega\rho}{2\eta}\right)^{\frac{1}{2}}. \tag{3c}$$

These three wavenumbers depend on the physical properties of the component material that is taken into account for each of the three phases. The physical properties of the material are denoted by c, α, ρ, η, C_p, and κ, which represent ultrasound velocity, ultrasound attenuation, density, viscosity, specific heat, and the thermal conductivity, respectively. Considering that solid magnetic particles would constitute Phase 2, the value of k_s was modified by replacing the shear viscosity η with the parameter $\frac{\mu}{-i\omega}$, where μ is the shear module.

The potential of the longitudinal incident wave in the compressional mode can be expressed using spherical coordinators as follows:

$$\varphi_0 = \sum_{n=0}^{\infty} i^n (2n+1) j_n(k_c r) P_n(cos\Theta) \tag{4}$$

Here,j_n represents the spherical Bessel function, $k_c r$ is the normalized wave number of the compressional mode, r is the sphere radius, P_n is a Legendre polynomial of order n, and Θ is the angle of the spherical coordinator that indicates the angle of propagation direction.

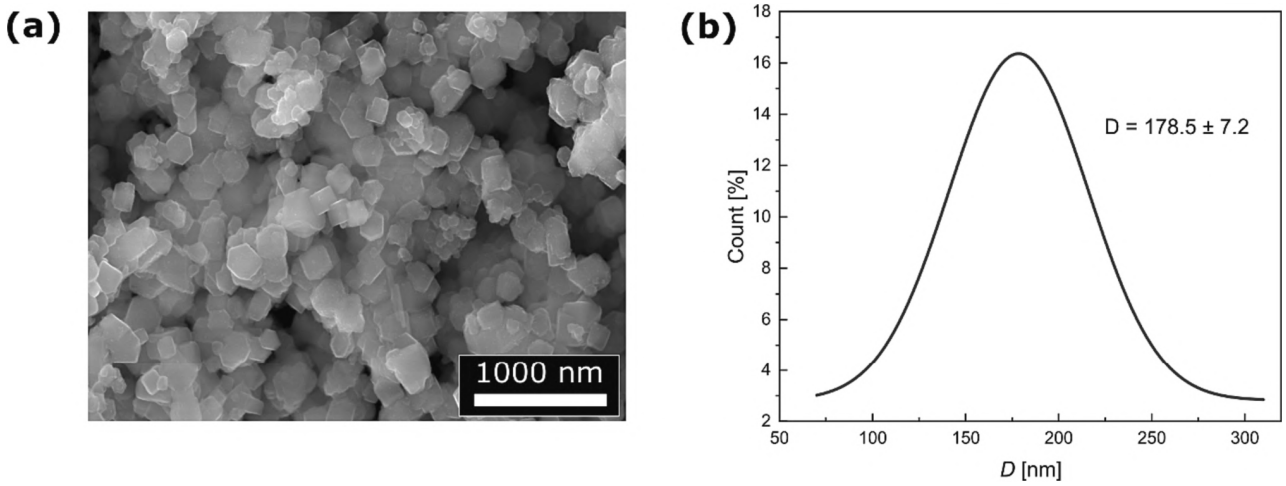

Fig. 3. (a) Scanning electron microscopy image of magnetic nanoparticles; (b) particle size distribution.

After scattering in the continuous phase (Phase 1), as shown in Fig. 2, the waves can be expressed as compressional, thermal, and shear modes, respectively, using the following expressions:

$$\varphi_{c1} = \sum_{n=0}^{\infty} i^n (2n+1) A_n h_n(k_{c1} r) P_n(cos\Theta) \tag{5a}$$

$$\varphi_{t1} = \sum_{n=0}^{\infty} i^n (2n+1) B_n h_n(k_{t1} r) P_n(cos\Theta) \tag{5b}$$

$$A_{\Psi 1} = \sum_{n=0}^{\infty} i^n (2n+1) C_n h_n(k_{s1} r) P_n^1(cos\Theta) \tag{5c}$$

Here, h_n denotes the Hankel function, which represents the forward wave propagation; and A_n, B_n, and C_n are the partial wave amplitudes of the scattered wave in the compressional, thermal, and shear modes, respectively, in a carrier fluid (Phase 1).

Wave scattering in a shell leads to the production of waves in two interfaces—between the core and shell and between the shell and carrier fluid. These waves can be expressed as backward and forward waves based on their potentials as follows:

$$\varphi_{c2} = \sum_{n=0}^{\infty} i^n (2n+1) [D_n j_n(k_{c2} r) + G_n h_n(k_{c2} r)] P_n(cos\Theta) \tag{6a}$$

$$\varphi_{t2} = \sum_{n=0}^{\infty} i^n (2n+1) [E_n j_n(k_{t2} r) + H_n h_n(k_{t2} r)] P_n(cos\Theta) \tag{6b}$$

$$A_{\Psi 2} = \sum_{n=0}^{\infty} i^n (2n+1) [F_n j_n(k_{s2} r) + I_n h_n(k_{s2} r)] P_n^1(cos\Theta) \tag{6c}$$

Here, j_n is the Bessel function, representing the backward wave propagation from the shell to the core; h_n represents the forward wave propagation from the shell to the carrier fluid; D_n, E_n, and F_n are the partial wave amplitudes of the compressional, thermal, and shear modes, respectively, of the backward wave, and G_n, H_n, and I_n are the partial wave amplitudes for the three modes of the forward wave.

The wave potential in the core can be written as a backward wave represented by j_n(Bessel function), with J_n, K_n, and L_n representing the partial amplitudes of the compressional, thermal, and shear waves, respectively (Phase 3).

$$\varphi_{c3} = \sum_{n=0}^{\infty} i^n (2n+1) J_n j_n(k_{c3} r) P_n(cos\Theta) \tag{7a}$$

$$\varphi_{t3} = \sum_{n=0}^{\infty} i^n (2n+1) K_n j_n(k_{t3} r) P_n(cos\Theta) \tag{7b}$$

$$A_{\Psi 3} = \sum_{n=0}^{\infty} i^n (2n+1) L_n j_n(k_{s3} r) P_n^1(cos\Theta) \tag{7c}$$

Equations (5)–(7) were solved for spherical coordinators using series expansions of spherical Hankel and Bessel functions with variable coefficients. The 12 boundary equations and 12 unknown coefficients (A_n, $B_n, C_n, D_n, E_n F_n, G_n, H_n, I_n, J_n, K_n,$ *and* L_n) for the core–shell model were solved using a 12×12 matrix equation [34]. To calculate the ultrasound attenuation coefficient, the partial compression wave amplitude A_n had to be determined.

The calculations could be simplified by assuming that only A_0 and A_1 contribute to the calculated attenuation coefficient in the long wavelength region. A_0 describes the energy loss due to the compressibility difference and thermal contrast between the phases, while A_1 describes the energy loss due to the density contrast between the phases. Partial compression wave amplitudes of higher orders $A_{n>1}$ decay very rapidly at long wavelength limits; therefore, these were neglected.

The attenuation and velocity of an ultrasound wave in the long wavelength region were finally calculated using the following equation for a complex wavenumber [37]:

$$\beta = \sqrt{k_c^2 - \frac{3i\phi_{Si}}{(k_c^3)(a^3)}(A_0 + 3A_1 + 5A_2)}. \tag{8}$$

Here, $\beta = \frac{\omega}{c_{emulsion}} + i\alpha_{emulsion}$ is the complex wavenumber of the scattered wave, ϕ_{Si} is the volume fraction of the dispersed phase $\phi_{Si} = \frac{4}{3}\pi b^3 N$, N is the number of silicone oil droplets (dispersed phase) distributed in the continuous phase, a and b are the outer and inner radii of the Pickering droplet, respectively.

The volume fraction of the dispersed phase (silicone oil) ϕ_{Si} in the continuous phase (castor oil), as seen in **Equation (8)**, was calculated using the following formula:

$$\phi_{Si} = \frac{\phi_m}{\left(\frac{\rho_2}{\rho_1}\right)(1-\phi_m) + \phi_m} \tag{9}$$

Here, ϕ_m is a mass fraction of the dispersed phase, ρ_1 is the density for the dispersed phase (silicone oil), and ρ_2 is the density of the continuous phase (castor oil) used in the experiments.

3. Materials and methods

3.1. Materials

Castor oil (MERLIN, MA220-1, Spain) and silicone oil (Rhodorsil, 47 V 50, USA) constituted the continuous and dispersed phases of the emulsion, respectively. Iron oxide (iron (II, III) oxide) nanoparticles purchased in powder form from Sigma-Aldrich Co., St. Louis, MO, USA (product no. 310069) were used as stabilizers of the emulsion droplets. The magnetic nanoparticles used in this experiment were unmodified and had a polydisperse size distribution, with an average size of around

Table 1
The physical properties of castor oil as the continuous phase, silicone oil as dispersed droplets, and magnetite nanoparticles as stabilizing particles at 25 °C.

Parameters	Castor oil	Silicone oil	Magnetite particles
Viscosity η (Pa • s)	580×10^{-3}(measured)	50×10^{-3}(measured)	–
Density ρ(kg/m^3)	957 (measured)	960 (measured)	5180 [38]
Thermal conductivity κ (W/mK)	0.180 (data sheet)	0.15 (data sheet)	52 [38]
Specific heat c_p (J/kg • K)	1800 (data sheet)	1460 (data sheet)	653 [38]
Thermal expansion β_T (1/K)	7.7×10^{-4} [39]	9.5×10^{-4}(data sheet)	11.8×10^{-6} [38]
Velocity c (m/s)	1455	1004 [40]	7157 [38]
Atteuation α (Np/m)	$2.79 \times 10^{-9} f^{1.56}$(measured)	$3.79 \times 10^{-13} f^{2.02}$(measured)	$0.01 \times 10^{-15} f^2$ [38]
Shear module μ (N/m^2)	–	–	6.03×10^{10} [38]

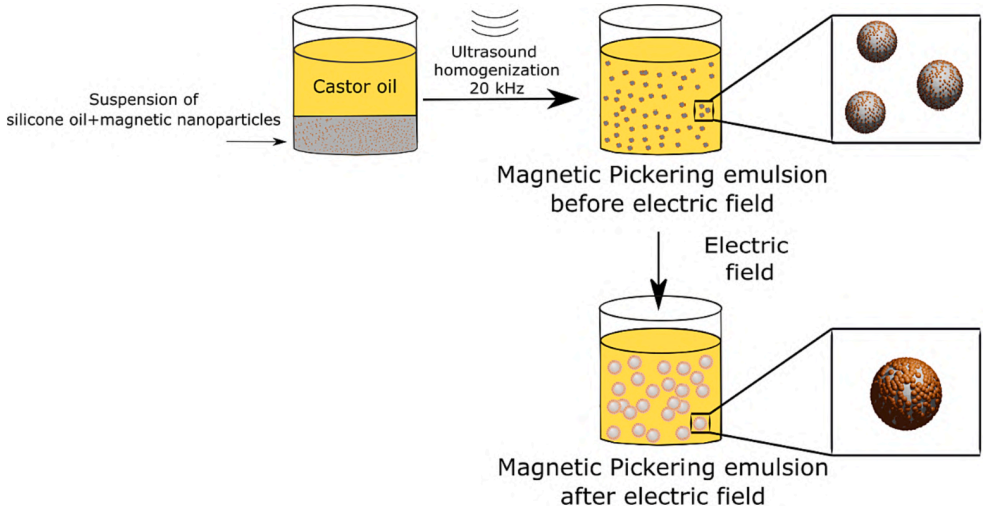

Fig. 4. Schematic illustration of the one-step and two-step methods used to prepare Pickering emulsions stabilized by magnetic nanoparticles.

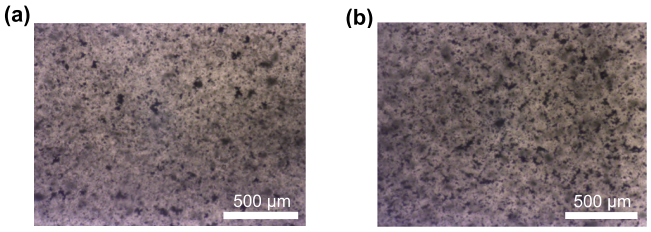

Fig. 5. Optical microscopy images of diluted MPEs prepared using the one-step method for (a) 0.5 % volume fraction of silicone oil and 1:2 ratio of silicone oil to magnetic nanoparticles, and (b) 0.5 % volume fraction of silicone oil and 1:1 ratio of silicone oil to magnetic nanoparticles.

~178 nm; these are shown in the scanning electron microscopy (SEM) images in Fig. 3. The physical properties of the oils and magnetite particles that were considered for the theoretical model are provided in Table 1. The high viscosity of castor oil and the similar densities of castor oil and silicone oil helped maintain the emulsions' stability against sedimentation.

3.2. Magnetic Pickering emulsion preparation

Oil-in-oil Pickering emulsions with droplets covered by magnetite particles were prepared using either a one-step method involving ultrasonic homogenization or a two-step method involving ultrasound homogenization and DC electric field application (see Fig. 4). In the one-step method, a suspension of magnetic nanoparticles in silicone oil was dispersed in castor oil, and after 1 min of ultrasonic homogenization (Sonoplus HD 3100, Bandelin, Germany) with a working frequency of 20 kHz, magnetic Pickering droplets were formed inside the carrier fluid. In the two-step method, a DC electric field was applied after ultrasonic homogenization to increase the number of particles at the droplet interface *via* electrocoalescence [41]. A signal generator (SDG1025, Siglent, Germany), a high-voltage bipolar amplifier (10HVA24-BP1, HVP, Germany), and a digital microscope (AM7115MZTL, Dino-Lite, the Netherlands) were used to produce an electric field with an intensity of ~250 V/mm. The electric field was applied for 20 min.

For the experiment, MPE samples with different volume fractions of silicone oil in relation to castor oil were prepared (0.5 % and 1 %). Different volume ratios of magnetic nanoparticles to silicone were tested (1:1, 1:2, and 1:4). An optical microscope connected to a digital camera (UI-3590CP-C-HQ, IDS, USA) was used to capture images of the MPE in a sample cell (optical path ~2 mm). Fig. 5 shows examples of optical microscopy images. The emulsion structure and numerous droplets were visible in the images after the application of high-intensity ultrasound.

3.3. Ultrasound attenuation measurements

The transmission method was utilized for the ultrasonic measurements of the MPE. A broadband ultrasonic signal was passed through each sample, which caused the pulse of the ultrasonic waveform to change. Further, attenuation in the frequency domain was determined. Two piezoelectric broadband transducers—a transmitter and a receiver (OLYMPUS, Waltham, MA, USA)—driven by an ultrasound generator (OPBOX 2.1 from OPTEL, Poland) were used for this purpose. As the attenuation of an ultrasonic wave in a sample is temperature dependent, all measurements were carried out at a temperature of 25 ± 0.2 °C using a thermostat setup. The ultrasonic wave propagated through the water and the sample as shown in Fig. 6**a**. The signal was recorded at a sampling frequency of 100 MHz.

The signal processing of the ultrasound pulses included two steps.

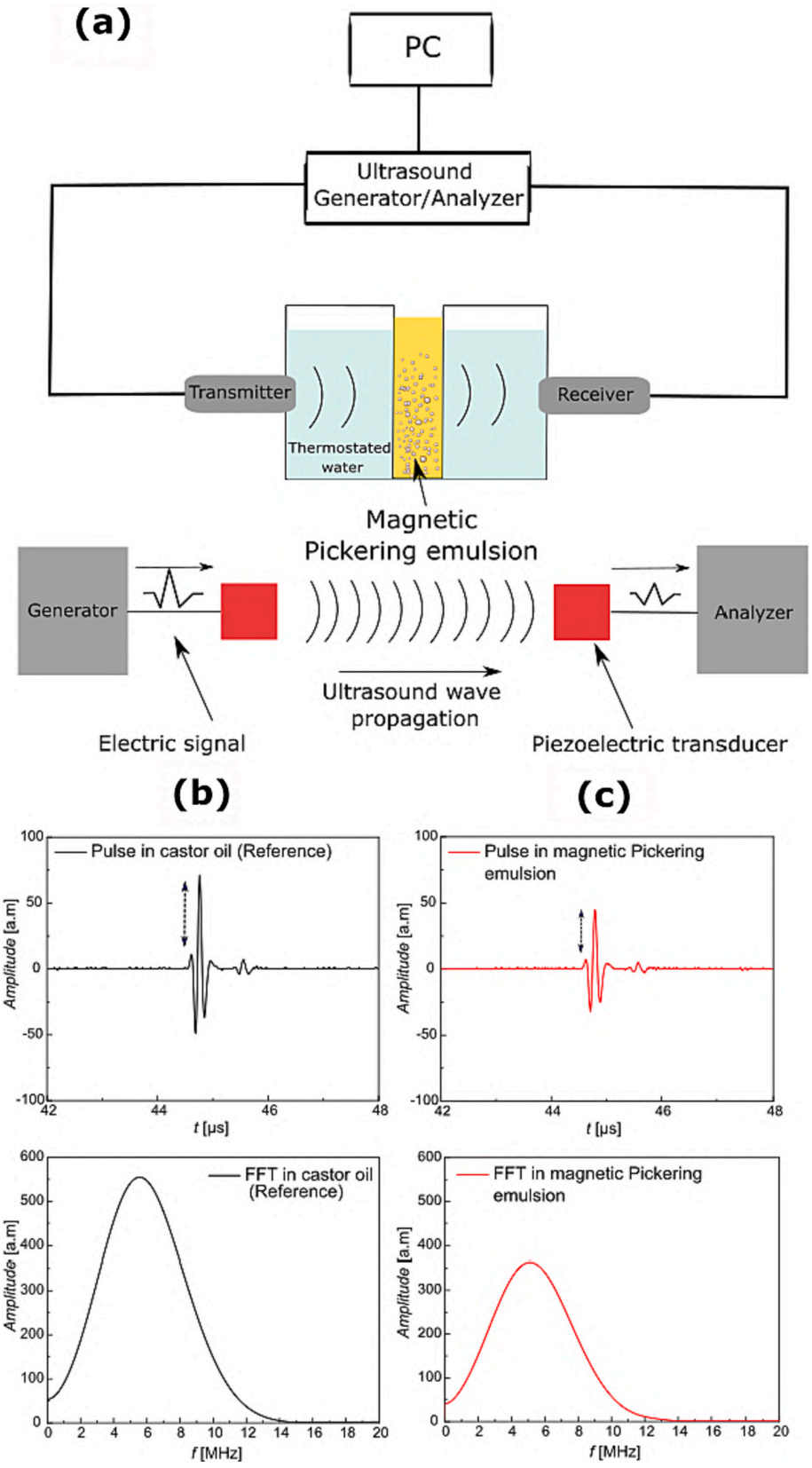

Fig. 6. (a) The experimental setup of the ultrasound measurement system consisting of an OPTEL ultrasonic testing device with two piezoelectric broadband transducers (transmitter and receiver) and a thermostated sample cell for temperature stabilization at 25 °C. Ultrasonic pulses and the fast Fourier transform (FFT) modules for (b) the castor oil (reference) and (c) MPE.

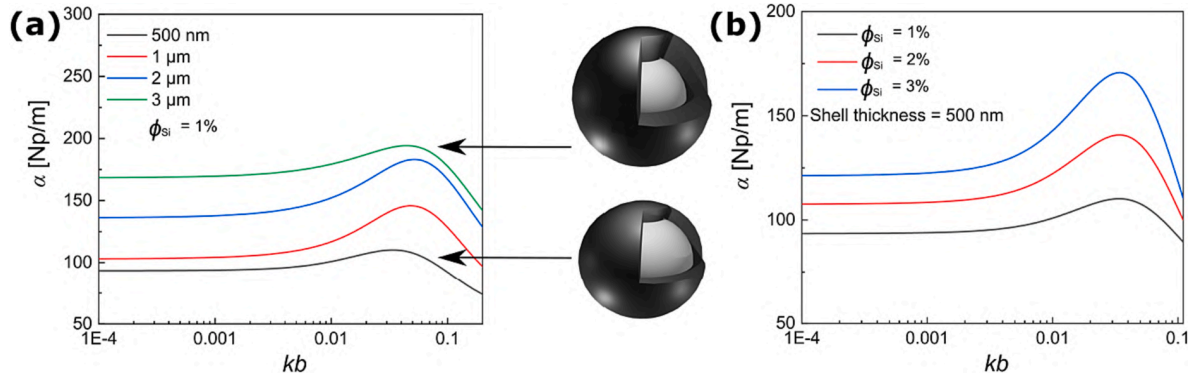

Fig. 7. The theoretical ultrasound attenuation coefficient of droplets at 5 MHz frequency as a *kb* function for (a) various shell sizes at a constant volume fraction of 1 % and (b) various volume fractions at a constant shell size of 500 nm. The schematic representations of the droplets are presented for better understanding the plotted values.

Firstly, pre-processing of ultrasound signals was performed by determining the pulse position, filtering the noise, and applying Hamming window to mitigate spectral leakage. Secondly, we applied a fast Fourier transform (FFT) algorithm to convert the signal from the time domain to the frequency domain. The module of the complex spectrum output represented the amplitude spectra as shown in Fig. 6**b–c** for castor oil and magnetic Pickering emulsions, respectively.

For the experiments, ultrasound attenuation was calculated using the well-known reference method, as given in the following equation:

$$\alpha(f) = \alpha(f)_{ref} + \frac{1}{d}\ln\frac{|F_1(f)|}{|F_2(f)|} \tag{10}$$

Here, $\alpha(f)$ is the ultrasound attenuation coefficient in Np/m, $\alpha(f)_{ref}$ is the attenuation coefficient of the carrier fluid (castor oil) and is frequency dependent, d is the acoustic path inside the sample cell (10 mm), $|F_1(f)|$ is the amplitude of the FFT for the pulse recorded in the castor oil, and $|F_2(f)|$ is the FFT amplitude of the pulse recorded in the MPE.

4. Results and discussion

4.1. Theoretical results of ultrasound attenuation in an oil-in-oil magnetic Pickering emulsion

The theoretical calculations of ultrasound attenuation were presented for oil-in-oil MPE as a function of the core radius (i.e., silicone droplet size) multiplied by wavenumber (*kb*), shell thickness (i.e., magnetic shell size) multiplied by wavenumber (*kc*), and frequency. Based on these calculations, the core–shell model was used to interpret the experimental data obtained from ultrasound spectroscopy measurements.

Fig. 7 provides the theoretical dependence of the ultrasound attenuation coefficient as a function of *kb* based on the core–shell model described in Section 2, where *b* is a silicone droplets radius and *k* is the wavenumber ($k = \frac{2\pi}{\lambda}$) in a range from 0.0001 to 0.2. Fig. 7**a** presents the results of the ultrasound attenuation calculations for different magnetic shell thicknesses at a constant frequency of 5 MHz and a volume concentration of 1 %.

The ultrasound attenuation in the function of *kb* shows negligible changes at lower *kb* values. However, a distinctive peak emerges when droplet radius approaches the micro-size, notably at a *kb* value corresponding to a core radius of 926 nm. The magnitude of the change also depends on the shell thickness of magnetic nanoparticles. A significant increase in the ultrasound attenuation appears as shell thickness increases from 500 nm to 3 μm exceeding the background attenuation of castor oil, which corresponds to 78.8 Np/m for 5 MHz calculated from the power function $6.4 \times f^{1.56}$, where *f* is the frequency in MHz. From an experimental point of view, we focus on the micro-size range due to the expected Pickering droplets radius for used experimental conditions.

Fig. 7**b** shows the theoretical results of ultrasound attenuation as a function of *kb* for different volume concentrations of silicone oil droplets covered by magnetic particle shells of 500 nm thickness. The results indicate that ultrasound attenuation increased as volume concentration increased. For example, ultrasound attenuation at a volume concentration of 1 % and with a droplet radius of 926 nm was around 100 Np/m, while attenuation at a volume concentration of 3 % and with the same droplet radius was around 160 Np/m. The observed increase was due to the increase in the number of scattering objects, which was represented

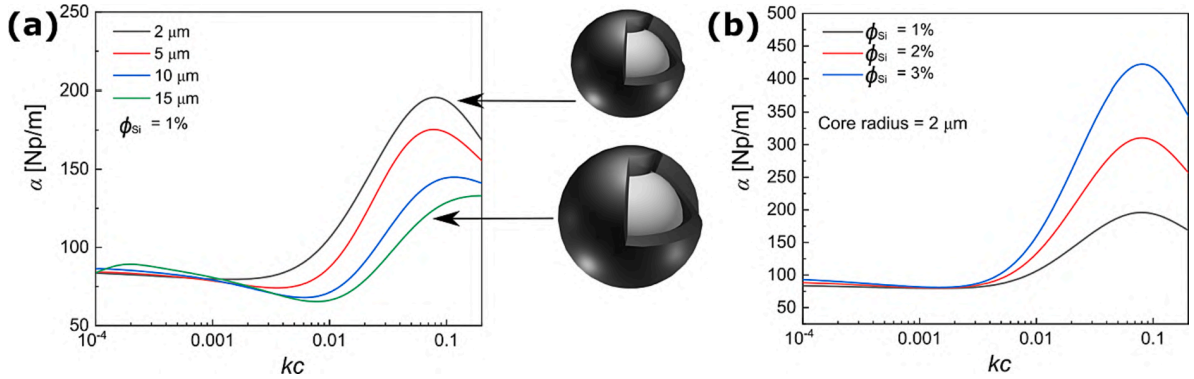

Fig. 8. The theoretical ultrasound attenuation coefficient of droplets at the frequency of 5 MHz as a function of shell thickness for (a) different droplet core sizes at a constant volume fraction of 1 % and (b) different volume fractions at constant droplet core radius of 10 μm. The schematic representations of the droplets are presented for a better understanding of the plotted values.

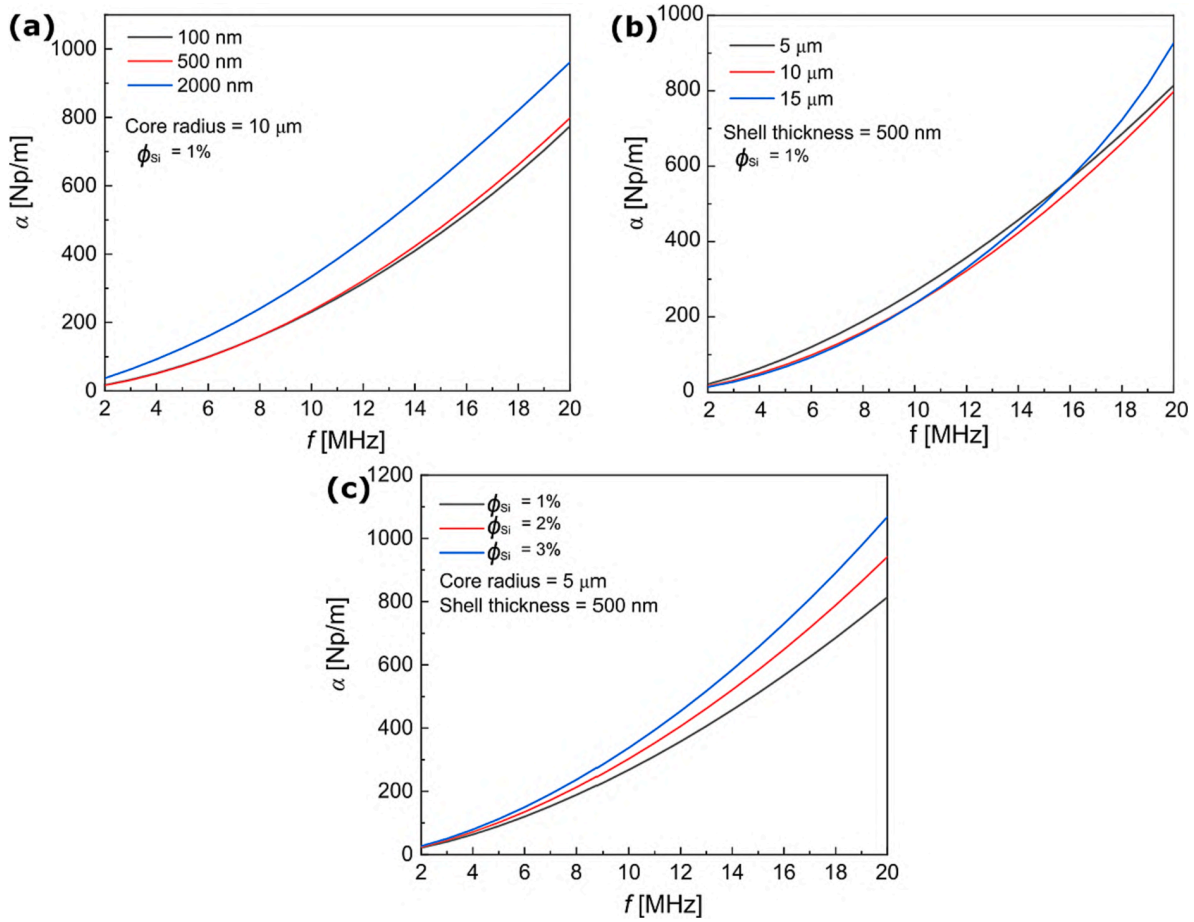

Fig. 9. The theoretical ultrasound attenuation coefficient in the function of frequency. (a) Ultrasound attenuation coefficient versus frequency for different shell radii at constant core radius of 10 μm and volume concentration of 1 %; (b) ultrasound attenuation coefficient *versus* frequency for different core radii at constant shell radius of 500 nm and volume concentration of 1 %; (c) ultrasound attenuation coefficient *versus* frequency for different volume concentrations.

as a concentration and was proportional to the ultrasound attenuation as shown in **Eq. (9)**.

Fig. 8 shows the theoretical dependence of the ultrasound attenuation coefficient as a function of *kc*, where *c* is a shell thickness, in a range of 0.0001 to 0.2, at a constant frequency of 5 MHz. In Fig. 8**a**, the effect of the silicone droplet radius on the ultrasound attenuation at a constant volume concentration of 1 % is presented. These results indicate that ultrasound attenuation decreased as the silicone droplet radius increased from 2 μm to 15 μm, which is consistent with the trend shown in Fig. 7**a**. An increase in attenuation was observed beyond a *kc* value of 0.01, which corresponds to a radius of 463 nm at a frequency of 5 MHz. For micro-sized MPE droplets, a longer wavelength could be used for the characterization process as the ultrasound attenuation value depends on the relation between the wavelength and the object radius, where the wavelength should be smaller than the radius of core–shell object ($ka \ll 1$).

The scattering and viscous mechanism are dominant against the thermal mechanism in the micro-size magnetic Pickering droplet at megahertz frequency. However, thermal loss could be dominant for the nanoscale objects. Fig. 8**b** shows the effect of volume fraction on ultrasound attenuation at a constant silicone droplet size of 2 μm, indicating that ultrasound attenuation increased with every increase in concentration, as expected from **Equation (9)**. This is also comparable to the results related to the function of the core radius.

It was shown theoretically (Figs. 7–8) that ultrasound attenuation in core–shell systems highly depends on the core and shell sizes. This dependence is not monotonous—an increase or decrease in the ultrasound attenuation coefficient value depends on the relation between the core and shell size in a complex way. To determine, from the experimental data collected on the MPE, how many particles reside on the droplet interface and how thick a layer they form, ultrasound attenuation in the frequency domain was calculated.

The theoretical results of ultrasound attenuation (see Fig. 9**a**) revealed the effects of the thickness of the magnetic shell around the silicone droplets when plotted in the function of frequency. Ultrasound attenuation was found to increase with an increase in the thickness of the magnetic shell when considering a constant droplet size of 10 μm and volume fraction of 1 %. This increase in ultrasound attenuation is consistent with the results shown in Fig. 8**a**, where an increase in ultrasound attenuation was observed for shells thicker than 463 nm at a constant frequency of 5 MHz. However, the differences between 100 nm and 500 nm particle shells seemed to diminish.

As shown in Fig. 9**b,** in the low range of frequency, the ultrasound attenuation spectra decreased as the radius of the silicone oil increased from 5 μm to 15 μm when considering a constant shell radius of 500 nm and volume fraction of 1 %. These results are consistent with the findings related to the droplet radius function (Fig. 7**a**), where a reduction in ultrasound attenuation was observed in the micrometer range. It should be noted that, in this case, the differences between the liquid core radii of 10 μm and 15 μm decreased. Furthermore, ultrasound attenuation was found to have a linear dependence on increasing droplet volume fractions, as shown in Fig. 9**c**; ultrasound attenuation increased as volume fraction increased for a shell thickness of 500 nm and core radius of 5 μm.

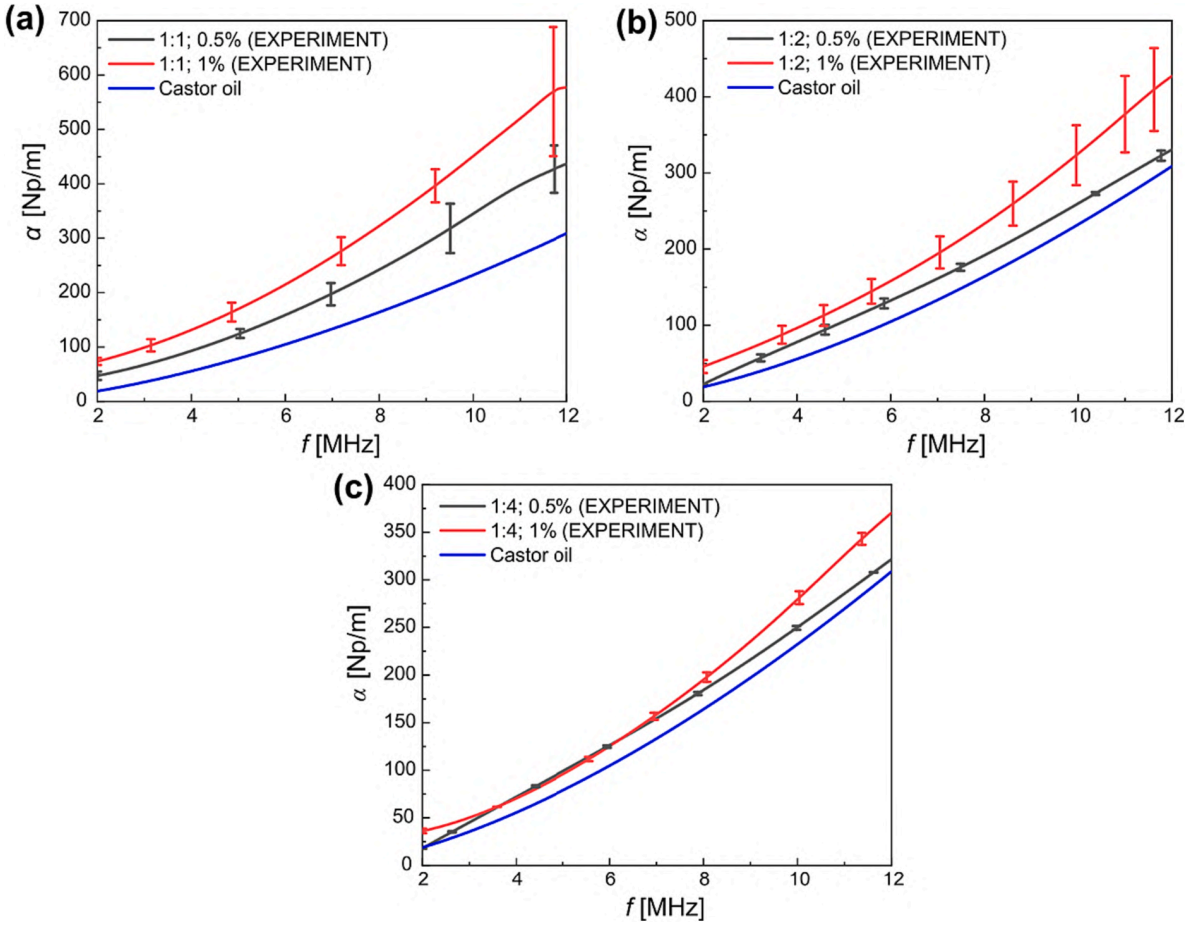

Fig. 10. Experimental results of the ultrasound attenuation coefficient of MPE for the various volume fraction of silicone oil 0.5 % and 1 % for three different magnetic nanoparticles-to-silicone oil volume ratios (a) 1:1, (b) 1:2, and (c) 1:4, respectively. Error bars are standard deviation values from three different measurements.

Since magnetic nanoparticles tend to have a range of sizes, as shown in the SEM images in Fig. 3**,** the shell thicknesses chosen for our calculations were 100 nm, 500 nm, and 2000 nm. The radii of silicone droplets and the concentrations in Fig. 9**b–c** were connected to the experimental conditions, as presented in the next section.

4.2. Ultrasound attenuation measurements of an oil-in-oil magnetic Pickering emulsion

Fig. 10 presents the experimental ultrasound spectroscopy measurements of the MPE, obtained using the one-step ultrasound homogenization method (see Section 3.2). The experiments covered two volume fractions of silicone oil (0.5 % and 1 %), with three different volume ratios of magnetic nanoparticles to silicone oil (1:1, 1:2, and 1:4). The results indicate that ultrasound attenuation decreased with any decrease in the concentration of magnetic nanoparticles at a constant silicone oil concentration (Fig. 10**a–c**). At a 1 % silicone oil concentration and 12 MHz ultrasound frequency, the average ultrasound attenuation value was 576.9 Np/m for the 1:1 volume ratio of magnetic nanoparticles to silicone oil. In contrast, ultrasound attenuation dropped to 427.1 Np/m for the 1:2 volume ratio of magnetic nanoparticles to silicone oil under the same conditions. The statistical analysis based on ANOVA indicated the significant differences between two silicone concentrations (0.5 % and 1 %) for three-volume ratios (1:1, 1:2, and 1:4). Therefore, the volume concentration of magnetic nanoparticles played a key role in ultrasound attenuation, likely due to its higher density particles compared to the liquid phases and its tendency for aggregation [35]. Additionally, for Pickering droplets, the volume concentration of particles determines the droplet size. A high concentration of magnetic nanoparticles leads to fast droplet stabilization, whereas a low concentration results in a relatively slow stabilization process. This, in turn, affects droplet size and the density of particles on the droplet interface [41]. Based on the change in ultrasound attenuation, theoretical calculations were used to interpret the experimental results through ultrasound scattering theory based on the core–shell model. It is important to note that low volume concentrations were used in the experiments to avoid the effects of multiple scattering of ultrasound waves and to minimize the aggregation rate in the system.

4.3. Analysis of the ultrasound attenuation measurements using the core–shell model

Fig. 11 provides a frequency-dependent comparison between the theoretical results and the average value for the attenuation coefficient, obtained from measurements involving three different volume ratios of magnetite nanoparticles to silicone oil (1:1, 1:2, and 1:4) and a constant silicone oil volume concentration of 0.5 %. As shown in Fig. 10, a higher number of particles led to significantly higher ultrasound attenuation. In the core–shell model, the number of particles is controlled by the thickness of the shell—that is, a thicker shell corresponds to a higher concentration or number of magnetic particles at the droplet's interface.

The fitting process was achieved *via* iterations with various shell sizes and core radii that best agreed with experimental data. The results of the fitting process (see Fig. 11**a–c**) suggested that shell thickness

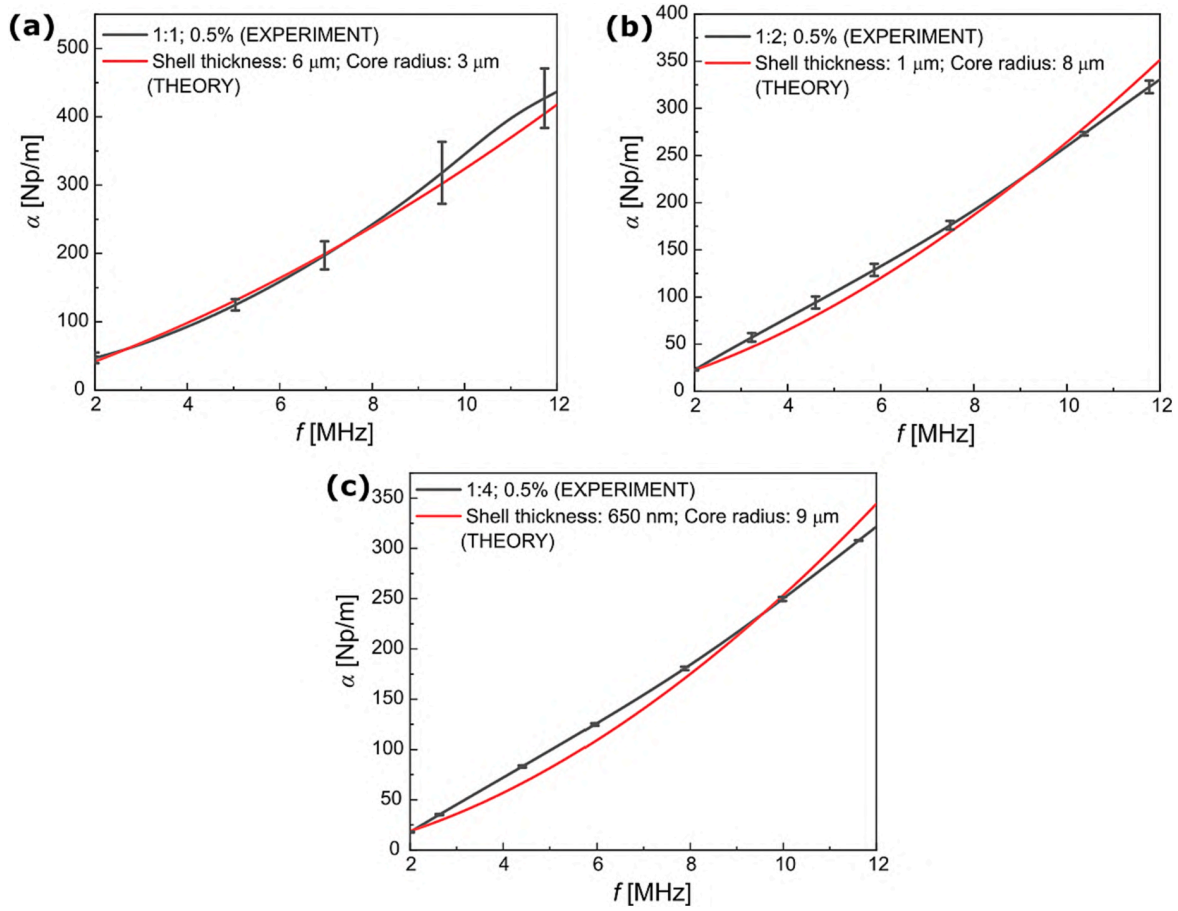

Fig. 11. A comparison of the ultrasound attenuation spectra and theoretical calculations with a constant 0.5 % volume fraction of silicone oil and different magnetic nanoparticle-to-silicone oil volume ratios: (a) 1:1, (b) 1:2, and (c) 1:4. Error bars represent the standard deviation values obtained from three different experiments.

increasing as the magnetic nanoparticle-to-silicone oil ratio increased. Further, the mean radius of the droplets that best fitted the experimental data increased with decreasing number of particles used to stabilize the emulsion from 3 μm to 9 μm. Other studies of MPE have clearly shown that droplet size decreases with increasing magnetic nanoparticle concentration [16,42]; therefore, we concluded that ultrasound spectroscopy is sensitive to changes during emulsion sample preparation.

The volume concentrations of the magnetic nanoparticles in the tested emulsions were lower for the samples considered in Fig. 11**b–c** than those in Fig. 11**a**. The best fit in Fig. 11**b–c** suggests a magnetic shell thickness of around 1 μm or 650 nm, with a core radius of 8 μm and 9 μm, respectively. In fact, the shell thickness was increased compared to the size of the magnetic nanoparticles used in the experiments (~178 nm). This might suggest that our MPE consisted of droplets stabilized by the magnetic nanoparticles aggregated on the droplet interface The precision of measuring the shell thickness may be lower due to the non-capsulated nature of the Pickering emulsion, especially with a low volume ratio of magnetic nanoparticles. The core–shell model could be used to detect capsulated and non-capsulated droplets as well as to study the concentration of particles on the interface of Pickering droplets. The magnetic nanoparticles used in the experiment were unmodified to be able to stabilize the silicone oil – castor oil interface, while ideally separated capsulated droplets were the objects considered in the Anson–Chivers model [34]. When assuming aggregation in the system, the droplets obtained by ultrasound homogenization form large objects that the model can detect as microdroplets with micro-sized shell layers.

The results of a comparison of the ultrasound attenuation measurements and theoretical calculations for a high volume concentration of silicone oil (1 %) with three different volume ratios of magnetic nanoparticles (1:1, 1:2, and 1:4) are presented in Fig. 12. The results showed that the detected droplet radius decreased to ~2 μm when considering the 1:1 volume ratio (Fig. 12**a**). Furthermore, the standard deviations in the experimental measurements were generally higher when higher volume concentrations of droplets were considered, indicating the complexity of the system. This may be evidence of the polydispersity of the system for both droplet radius and shell thickness. The detected magnetic shell sizes associated with the magnetic particle-to-silicone oil ratios of 1:2 (Fig. 12**b**) increased when compared to lower silicone concentration Fig. 11**b**. Interestingly, an increase in the number of silicone oil droplets resulted in a lack of differences with the fitted mean radius of the droplets when the concentration of magnetic nanoparticles was low.

4.4. Analysis of the ultrasound attenuation measurements after DC electric field application

The experimental results obtained from fitting the ultrasound attenuation spectra and the core–shell model revealed a discrepancy between the actual size of the particles and the detected shell thickness. A stable emulsion can be obtained *via* electrocoalescence under DC electric fields [33,41]. Therefore, the core–shell model coupled with ultrasound spectroscopy measurements was tested in monitoring the coalescence process of the Pickering droplets and in estimating changes in the droplet size and particle aggregation at the droplet interface.

Fig. 13 shows how ultrasound attenuation increased after electric field application for two different volume fractions of silicone oil (0.5 % and 1 %) when the volume ratio of magnetic nanoparticle to silicone oil was 1:2. For higher frequency (12 MHz), the difference in the

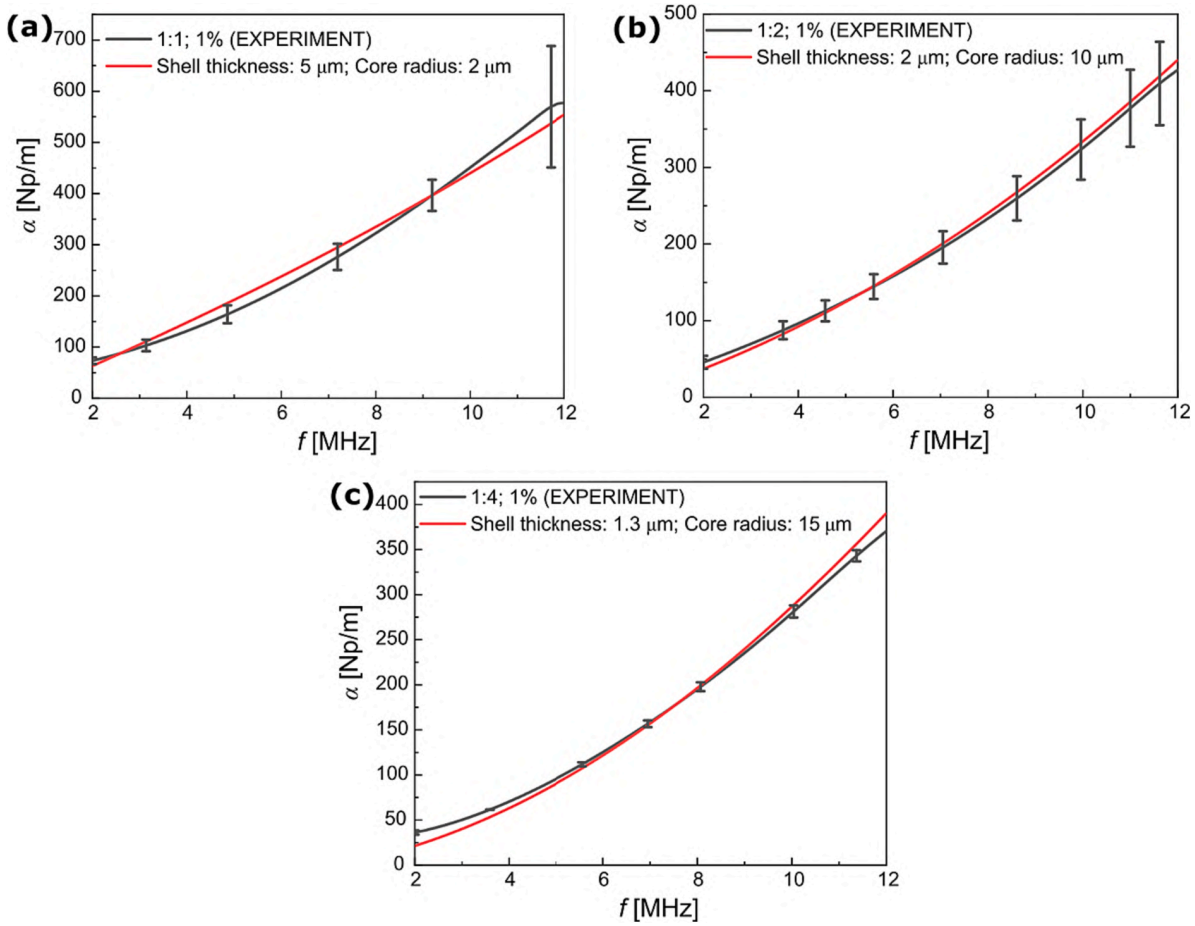

Fig. 12. A comparison of the ultrasound attenuation spectra and theoretical calculations with a constant 1 % volume fraction of silicone oil and different volume ratios of magnetic nanoparticles to silicone oil: (a) 1:1, (b) 1:2, and (c) 1:4. Error bars represent standard deviation values obtained from three different experiments.

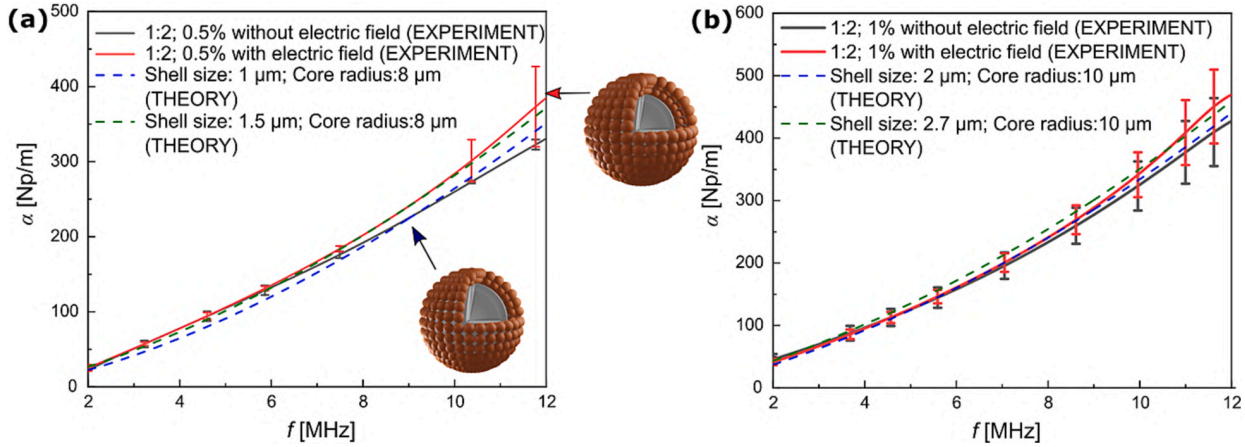

Fig. 13. A comparison of the ultrasound attenuation spectra and theoretical calculations before and after electrical field application with a constant 1:2 volume ratio of magnetic nanoparticle to silicone oil and different volume concentrations of silicone oil: (a) 0.5 % and (b) 1 %. Error bars represent the standard deviation values obtained from three different measurements. Schematic representations of the droplets are presented for a better understanding of the plotted values.

attenuation for average value before and after electric field was 54.1 Np/m and 42.7 Np/m for 0.5 % and 1 %, respectively. This increase was due to changes in the internal structure of the MPE after electro-coalescence events. Following electric field application, ultrasound spectroscopy showed that particle shell stability changed. The fitting of the measurement data to the core–shell model showed that the thickness of the shell increased from 1 μm to 1.5 μm when considering a 0.5 % volume concentration of silicone oil and from 2 μm nm to 2.7 μm when considering a 1 % volume concentration of silicone oil. The increase in the thickness of the shell suggests that the density of the shell or the number of particles on the droplet interface increased because of electrocoalescence. It should be noted that the standard deviation values of the experimental measurements were higher after the electric field application than before. Therefore, ultrasound attenuation after electric

field application may show a wide range of polydispersity of Pickering droplet radius and shell thickness, which can be predicted by changes in ultrasound attenuation as a function of frequency.

The ultrasound attenuation measurements offer an alternative way of characterizing the three-phase system using a nondestructive method and without dilution. Although we tested an MPE prepared in a specific way, the core–shell model can serve as a useful tool for investigating the impacts of various preparation parameters, such as time, amplitude, and working frequency of ultrasound homogenization, on the MPE formation process. Moreover, the time and intensity of electric field application can also affect the MPE formation process, similar to what was recently shown for pH-responsive Pickering emulsions that were more stable at higher pH levels [43]. These can be monitored using real-time ultrasound spectroscopy measurements and the core–shell model.

Besides core–shell model, the different models have been tested for characterizing two-phase emulsions, i.e., without considering the solid phase. In the work of Silva *et al.* [44], such a comparison between the coupled phase model of Evans and Attenborough, elastic scattering, and multiple scattering models of Waterman and Truell were used for water-in-oil emulsion stabilized with polyglycerol polyricinoleate. For the concentration up to 30 %, the adaption of the multiple scattering model showed better agreement with measurements. However, for concentrations higher than 30 %, the combination of the coupled phase and elastic scattering better predicted the experimental data.

Kanamori *et al.* [36] also performed a calculation using both EACH and Anson-Chivers core–shell models. The results indicated the limitation of using the ECAH model to interpret the experimental result of three-phase systems such as Pickering emulsion that is in line with our previous findings [33]. Moreover, the authors used a modified core–-shell model with a neglected thermal effect in the calculation due to the micro-size Pickering droplet. It simplified the complexity of the calculation, which is one of the disadvantages of the core–shell model. Here, we used the core–shell model with thermal effect was utilized to calculate the shell thickness of magnetic Pickering droplets.

With respect to shell thickness, the ultrasonic technique has previously been utilized to monitor the shell elasticity of core–shell objects [45], which is important for drug release and magnetic separation processes. The same core–shell model could also be a useful tool for characterizing multilayer emulsions—that is, emulsions that possess multiple layers at the same time, perhaps with different surface modifications for carrying active substances—and for monitoring the preparation process [46,47]. Monitoring of ultrasound attenuation could lead to revealing a linkage between magnetic properties and magnetic interactions. In our previous work, ultrasound attenuation spectra were used for evaluating the magnetic separation in MPE under a gradient magnetic field [48], where the time of Pickering droplet movement and carrier fluid purification depended on magnetic field intensity and the magnetic properties of the tested system.

This study was conducted to investigate the formation process of an MPE with different volume ratios of magnetic nanoparticles and silicone oil, using ultrasound attenuation spectra. While Pickering droplets can be stabilized with non-full coverage, which still provides efficient stabilization against coalescence [49], knowledge of the concentration of particles on the droplet interface is important for determining the stability of an MPE. Pickering droplet stability and size as well as shell thickness, whether using magnetic or non-magnetic stabilizers, can alter the droplet response to external stimuli.

5. Conclusion

In this study, we characterized Pickering emulsions stabilized by magnetic nanoparticles by ultrasound spectroscopy measurements. The theoretical ultrasound attenuation was calculated based on the core–-shell model by Anson and Chivers in the function of *kb* and *kc* at a constant frequency of 5 MHz. The theoretical calculation indicated that the attenuation coefficient was sensitive to the increasing shell size of the Pickering droplets and the droplet radii. Based on this, the ultrasound attenuation coefficient was calculated as a function of frequency, taking into account the influence of MPE core and shell sizes on ultrasound attenuation. A comparison of the calculations and measurements of ultrasound attenuation indicated an increase in ultrasound attenuation with higher volume ratios of magnetic nanoparticles to silicone oil. Further, the number of particles on the droplet interface increased and the Pickering droplet's radius decreased with higher volume ratios of magnetic nanoparticles. The formation of a Pickering emulsion upon the application of an electric field was also tested. Ultrasound attenuation increased due to changes in the internal structure of the emulsion; the shell thickness predicted by the core–shell model was higher after electric field treatment than before. These findings suggest that ultrasound spectroscopy is a valuable tool for detecting the number of particles at a droplet interface even in optically opaque, multiphase systems such as MPEs.

CRediT authorship contribution statement

Bassam Jameel: Investigation, Visualization, Writing – original draft. **Rafał Bielas:** Methodology, Writing – review & editing. **Arkadiusz Józefczak:** Conceptualization, Methodology, Supervision, Funding acquisition.

Declaration of Competing Interest

The authors declare that they have no known competing financial interests or personal relationships that could have appeared to influence the work reported in this paper.

Data availability

Data will be made available on request.

Acknowledgments

This work was supported by the project no. 2019/35/O/ST3/00503 (PRELUDIUM BIS) of the Polish National Science Centre. The authors wish to thank Prof. Tomasz Hornowski for the valuable discussions and suggestions.

References

[1] J.-C. Baret, F. Kleinschmidt, A. El Harrak, A.D. Griffiths, Kinetic aspects of emulsion stabilization by surfactants: a microfluidic analysis, Langmuir 25 (2009) 6088–6093.
[2] C. Holtze, A. Rowat, J. Agresti, J. Hutchison, F. Angile, C. Schmitz, S. Köster, H. Duan, K. Humphry, R. Scanga, Biocompatible surfactants for water-in-fluorocarbon emulsions, Lab Chip 8 (2008) 1632–1639.
[3] T.F. Tadros, A. Vandamme, B. Levecke, K. Booten, C. Stevens, Stabilization of emulsions using polymeric surfactants based on inulin, Adv. Colloid Interface Sci. 108 (2004) 207–226.
[4] S.U. Pickering, Cxcvi.—emulsions, J. Chem. Soc. Trans. 91 (1907) 2001–2021.
[5] C.L. Harman, M.A. Patel, S. Guldin, G.-L. Davies, Recent developments in Pickering emulsions for biomedical applications, Curr. Opin. Colloid Interface Sci. 39 (2019) 173–189.
[6] J. Wu, G.H. Ma, Recent studies of Pickering emulsions: particles make the difference, Small 12 (2016) 4633–4648.
[7] S. Simovic, N. Ghouchi-Eskandar, C.A. Prestidge, Pickering emulsions for dermal delivery, J. Drug Delivery Sci. Technol. 21 (2011) 123–133.
[8] C. Albert, M. Beladjine, N. Tsapis, E. Fattal, F. Agnely, N. Huang, Pickering emulsions: Preparation processes, key parameters governing their properties and potential for pharmaceutical applications, J. Control. Release 309 (2019) 302–332.
[9] C. Guida, A.C. Aguiar, R.L. Cunha, Green techniques for starch modification to stabilize Pickering emulsions: a current review and future perspectives, Curr. Opin. Food Sci. 38 (2021) 52–61.
[10] B.P. Binks, S. Lumsdon, Influence of particle wettability on the type and stability of surfactant-free emulsions, Langmuir 16 (2000) 8622–8631.
[11] B.P. Binks, Particles as surfactants—similarities and differences, Curr. Opin. Colloid Interface Sci. 7 (2002) 21–41.
[12] C.C. Berry, A.S. Curtis, Functionalisation of magnetic nanoparticles for applications in biomedicine, J. Phys. D Appl. Phys. 36 (2003) R198.

[13] X. Hu, Y. Long, G. Xuan, Y. Wang, X. Huang, Y. Xu, J. Liu, B. Wang, F. Song, Optimized hydrophobic magnetic nanoparticles stabilized Pickering emulsion for enhanced oil recovery in complex porous media of reservoir, Front. Energy Res. 11 (2023) 1212664.
[14] Z. Gricius, G. Øye, Recent advances in the design and use of Pickering emulsions for wastewater treatment applications, Soft Matter 19 (2023) 818–840.
[15] J. Zhou, L. Wang, X. Qiao, B.P. Binks, K. Sun, Pickering emulsions stabilized by surface-modified Fe3O4 nanoparticles, J. Colloid Interface Sci. 367 (2012) 213–224.
[16] J. Zhou, X. Qiao, B.P. Binks, K. Sun, M. Bai, Y. Li, Y. Liu, Magnetic Pickering emulsions stabilized by Fe3O4 nanoparticles, Langmuir 27 (2011) 3308–3316.
[17] S.S. Leong, Z. Ahmad, J. Lim, Magnetophoresis of superparamagnetic nanoparticles at low field gradient: hydrodynamic effect, Soft Matter 11 (2015) 6968–6980.
[18] F.K. Tham, W.M. Ng, S.S. Leong, S.P. Yeap, S.C. Low, H.L. Lee, J. Lim, Magnetophoresis of magnetic Pickering emulsions under low field gradient: macroscopic and microscopic motion, Langmuir 37 (2021) 1811–1822.
[19] R. Bielas, A. Józefczak, The effect of particle shell on cooling rates in oil-in-oil magnetic Pickering emulsions, Materials 13 (2020) 4783.
[20] R. Sijs, S. Kooij, H. Holterman, J. Van De Zande, D. Bonn, Drop size measurement techniques for sprays: Comparison of image analysis, phase Doppler particle analysis, and laser diffraction, AIP Adv. 11 (2021), 015315.
[21] C. Goddeeris, F. Cuppo, H. Reynaers, W.G. Bouwman, G. Van den Mooter, Light scattering measurements on microemulsions: Estimation of droplet sizes, Int. J. Pharm. 312 (2006) 187–195.
[22] L.E. Low, S.P. Siva, Y.K. Ho, E.S. Chan, B.T. Tey, Recent advances of characterization techniques for the formation, physical properties and stability of Pickering emulsion, Adv. Colloid Interface Sci. 277 (2020), 102117.
[23] J. Sjöblom, N. Aske, I. Harald Auflem, Ø. Brandal, T. Erik Havre, Ø. Sæther, A. Westvik, E. Eng Johnsen, H. Kallevik, Our current understanding of water-in-crude oil emulsions.: Recent characterization techniques and high pressure performance, Adv. Colloid Interface Sci. 100–102 (2003) 399–473.
[24] T. Dong, T. Norisuye, H. Nakanishi, Q. Tran-Cong-Miyata, Particle size distribution analysis of oil-in-water emulsions using static and dynamic ultrasound scattering techniques, Ultrasonics 108 (2020), 106117.
[25] A.K. Hipp, B. Walker, M. Mazzotti, M. Morbidelli, In-situ monitoring of batch crystallization by ultrasound spectroscopy, Ind. Eng. Chem. Res. 39 (2000) 783–789.
[26] D.J. McClements, M.J. Povey, E. Dickinson, Absorption and velocity dispersion due to crystallization and melting of emulsion droplets, Ultrasonics 31 (1993) 433–437.
[27] A.M. Howe, A.R. Mackie, M.M. Robins, Technique to measure emulsion creaming by velocity of ultrasound, J. Dispers. Sci. Technol. 7 (1986) 231–243.
[28] A. Józefczak, A. Skumiel, M. Łabowski, Effects of biocompatible coating of nanoparticles on acoustics property of the magnetic fluid, J. Magn. Magn. Mater. 290 (2005) 265–268.
[29] A. Skumiel, T. Hornowski, M. Łabowski, Resonance absorption of the ultrasonic waves in magnetic liquids in DC magnetic field, Ultrasonics 36 (1998) 421–426.
[30] R. Challis, M. Povey, M. Mather, A. Holmes, Ultrasound techniques for characterizing colloidal dispersions, Rep. Prog. Phys. 68 (2005) 1541.
[31] P.S. Epstein, R.R. Carhart, The absorption of sound in suspensions and emulsions. I. Water fog in air, J. Acoust. Soc. Am. 25 (1953) 553–565.
[32] J. Allegra, S. Hawley, Attenuation of sound in suspensions and emulsions: Theory and experiments, J. Acoust. Soc. Am. 51 (1972) 1545–1564.
[33] R. Bielas, Z. Rozynek, T. Hornowski, A. Józefczak, Ultrasound control of oil-in-oil Pickering emulsions preparation, J. Phys. D Appl. Phys. 53 (2019), 085301.
[34] L. Anson, R. Chivers, Ultrasonic scattering from spherical shells including viscous and thermal effects, J. Acoust. Soc. Am. 93 (1993) 1687–1699.
[35] B. Jameel, T. Hornowski, R. Bielas, A. Józefczak, Ultrasound study of magnetic and non-magnetic nanoparticle agglomeration in high viscous media, Materials 15 (2022) 3450.
[36] C. Kanamori, T.T. Nguyen, K. Tsuji, H. Nakanishi, Q. Tran-Cong-Miyata, T. Norisuye, Interfacial structures of particle-stabilized emulsions examined by ultrasonic scattering analysis with a core–shell model, Ultrasonics 116 (2021), 106510.
[37] R.E. Challis, J.S. Tebbutt, A.K. Holmes, Equivalence between three scattering formulations for ultrasonic wave propagation in particulate mixtures, J. Phys. D Appl. Phys. 31 (1993) 3481.
[38] A. Vinogradov, Physicochemical and acoustic properties of water-based magnetic colloid, Colloid J. 66 (2004) 29–37.
[39] V.R. Patel, G.G. Dumancas, L.C.K. Viswanath, R. Maples, B.J.J. Subong, Castor oil: properties, uses, and optimization of processing parameters in commercial production, Lipid Insights 9 (2016). LPI. S40233.
[40] A. Schröder, E. Raphael, Attenuation of ultrasound in silicone-oil-in-water emulsions, EPL (Europhysics Letters) 17 (1992) 565.
[41] Z. Rozynek, R. Bielas, A. Józefczak, Efficient formation of oil-in-oil Pickering emulsions with narrow size distributions by using electric fields, Soft Matter 14 (2018) 5140–5149.
[42] R.R. Raju, F. Liebig, B. Klemke, J. Koetz, pH-responsive magnetic Pickering Janus emulsions, Colloid Polym. Sci. 296 (2018) 1039–1046.
[43] C.S. Sia, H.P. Lim, Y.N. Lin, L.C. Beh, B.T. Tey, B.-H. Goh, L.E. Low, pH-controllable stability of iron oxide@ chitosan nanocomposite-stabilized magnetic Pickering emulsions, Eur. Polym. J. 186 (2023), 111870.
[44] C.A. Silva, S.V. Saraiva, D. Bonetti, R.T. Higuti, R.L. Cunha, L.O. Pereira, F.V. Silva, A.M. Fileti, Measurements of bimodal droplet size distribution of emulsions using ultrasonic spectroscopy in the long and intermediate wavelength regimes, Chem. Eng. Sci. 252 (2022), 117274.
[45] T.N. Tran, D. Shibata, T. Norisuye, H. Nakanishi, Q. Tran-Cong-Miyata, Determination of particle size distribution and elastic properties of silica microcapsules by ultrasound spectroscopy, Jpn. J. Appl. Phys. 55 (2016) 07KC01.
[46] J. Li, H.D.H. Stöver, Pickering emulsion templated layer-by-layer assembly for making microcapsules, Langmuir 26 (2010) 15554–15560.
[47] T. Xia, C. Xue, Z. Wei, Physicochemical characteristics, applications and research trends of edible Pickering emulsions, Trends Food Sci. Technol. 107 (2021) 1–15.
[48] B. Jameel, R. Bielas, T. Hornowski, A. Józefczak, Propagation of ultrasonic wave in magnetic Pickering emulsion under DC magnetic field, J. Magn. Magn. Mater. 542 (2022), 168590.
[49] N. Bizmark, M.A. Ioannidis, Nanoparticle-stabilised emulsions: droplet armouring vs. droplet bridging, Soft Matter 14 (2018) 6404–6408.

[Scientific Paper III]

Magnetorheological characterization of oil-in-oil magnetic Pickering emulsions

Jameel, B., Paulovičová, K., Tóthová, J., Rajňák, M., Molčan, M., Bielas, R., and Józefczak, A.

Journal of Magnetism and Magnetic Materials 588 (2023) 171433

Journal of Magnetism and Magnetic Materials 588 (2023) 171433

Contents lists available at ScienceDirect

Journal of Magnetism and Magnetic Materials

journal homepage: www.elsevier.com/locate/jmmm

Magnetorheological characterization of oil-in-oil magnetic Pickering emulsions

Bassam Jameel [a,*], Katarína Paulovičová [b], Jana Tóthová [c], Michal Rajňák [b,c], Matúš Molčan [b], Rafał Bielas [a], Arkadiusz Józefczak [a]

[a] Chair of Acoustics, Faculty of Physics, Adam Mickiewicz University in Poznań, Uniwersytetu Poznańskiego 2, 61-614 Poznań, Poland
[b] Institute of Experimental Physics, Slovak Academy of Sciences, Watsonova 47, 040 01 Košice, Slovakia
[c] Faculty of Electrical Engineering and Informatics, Technical University of Košice, Letná 9, 042 00 Košice, Slovakia

ARTICLE INFO

Keywords:
Pickering emulsion
Magnetic nanoparticles
Rheology
Magnetorheological effect

ABSTRACT

A magnetic Pickering emulsion is a type of emulsion stabilized by magnetic nanoparticles that accumulate at the droplet interface. This makes the emulsion easy to control using an external magnetic field, which, in turn, makes it useful in many applications. Research and development in this field are ongoing, but regardless of the application, control of the formation process is necessary. Rheological measurements are one of techniques used for evaluating the internal structure and stability of emulsions. The main focus of the current research is to investigate the magnetorheological effect of the rarely tested oil-in-oil (O/O) magnetic Pickering emulsions and compare them with better-characterized oil-based magnetic fluids.

The magnetoviscous effect typically occurs when magnetic nanoparticles or magnetic Pickering emulsions align with the magnetic field, and this effect depends mainly on the internal structure, such as the size and shape of the particles and droplets. The experimental results indicate that the magnetic emulsion fabricated utilizing ultrasound and an additional electric field exhibits higher dynamic yield stress as a function of the magnetic field compared with the partially covered droplets. This suggests that the stable emulsion becomes a more rigid system and is more resistant to deformation when a magnetic field is applied. Besides that, the magnetoviscous effect of the magnetic emulsions was lower compared with that of magnetic suspensions with the same mass fraction of magnetic nanoparticles.

1. Introduction

A magnetorheological (MR) material consists of solid magnetic particles dispersed in a non-magnetic liquid. It can be considered a smart material due to its magnetically responsive behavior, in which the particles arrange themselves into chain-like structures when a magnetic field is applied [1,2]. In MR fluids, when a magnetic field is applied, randomly dispersed particles can rapidly form a solid-like network. These aligned mesoscale structural changes are responsible for an increase in the apparent viscosity of the MR fluids by one order of magnitude in response to a magnetic field [3]. In a few milliseconds, the MR fluid can change from a liquid to a semi-solid state after magnetic field application [2], and requiring higher external forces exceeding to start the flow [4]. In the case of ferrofluids, the size of the dispersed magnetic particles is in the nanoscale range, with a single domain of approximately 10 nm dispersed in a non-magnetic fluid. In contrast, the size of the magnetic particles in MR fluids is in the microscale range [5]. In ferrofluids, Brownian and hydrodynamic forces work to disrupt the formation of chain-like structures [6,7]. Generally, large magnetic particles in MR fluids are more susceptible to creating chain alignment in the magnetic field, leading to an increase in viscosity. The difference between the behavior in the internal structures of ferrofluids and MR fluids makes them appropriate for different technical applications [5]. MR fluids are widely used in mechanical and civil engineering applications, such as MR dampers in automotive suspensions for shock absorption [8], seismic applications [9], and advanced prosthetics in biomedical fields [10,11]. The liquid cores stabilized by magnetic nanoparticles, known as magnetic Pickering emulsions, can also behave as an MR fluid. The micro size of magnetic Pickering droplets, stabilized by nanosized magnetic particles, can form a chain-like structure along with magnetic field lines.

Magnetic Pickering emulsions have been in the scope of scientific

* Corresponding author.
E-mail address: basjam@amu.edu.pl (B. Jameel).

https://doi.org/10.1016/j.jmmm.2023.171433
Received 16 May 2023; Received in revised form 19 October 2023; Accepted 24 October 2023
Available online 28 October 2023

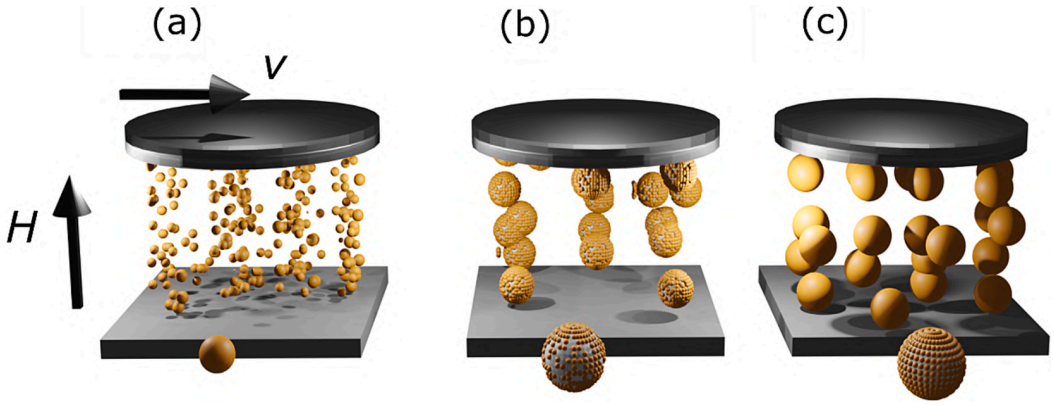

Fig. 1. Illustrations of the structures for (a) oil-based magnetic fluid, (b) pre-emulsion, and (c) stable Pickering emulsion. *H* and *v* represent the magnetic field direction and velocity of spin, respectively.

interest for the last decade, mainly due to their potential applications in oil recovery [12] and biomedicine [13]. There have been numerous reports on the use of magnetic particles to cover either the water [14] or the oil droplets [15] when fabricating emulsions and, in this way, forming magneto-responsive colloidal systems that can be easily separated under the static gradient magnetic field. Furthermore, such particle-covered droplets can be used as sources of heat when placed in an alternating magnetic field [16–18]. Monitoring the processes under magnetic fields is crucial from an application point of view to ensure good stability. This can be performed non-destructively, as demonstrated for magnetic fluids, using optical methods [19,20]. Recently, we showed that ultrasound can also be a powerful tool to obtain good characteristics of magnetic field-induced processes in colloids [17,21]. Pickering emulsion when compared with conventionally used surfactant-stabilized emulsions is believed to be more stable, as the principle of stabilization is the presence of particles attached to the droplet surface by capillary forces [22]. Long-term studies on Pickering emulsion stability have shown that the adsorption of the particles onto the droplets can be treated as irreversible, provided that the wettability of particles related to the three-system contact angle (Young's equation) is carefully chosen [23]. However, the ability to persist against the processes of emulsion aging (coalescence, flocculation, sedimentation, etc.) is not the only important characteristic in the practical applications of magnetic Pickering emulsions. The rheological properties are also needed to accurately predict the behavior of emulsion droplets during industrial [24] or medical process [25].

When magnetic particles have been used as stabilizers, Pickering emulsions exhibit MR responses depending on the intensity of the applied static magnetic field and the Pickering droplet size. There are few reports in the literature on the MR properties of magnetic Pickering emulsions for either oil-in-water or water-in-oil emulsions. For instance, the viscoelastic behaviour of an oil-in-water emulsions stabilized by silane-coated magnetic nanoparticles was shown for polar and non-polar disperse phase [26]. The results indicated there was solid-like behavior, and the change in volume concentration and magnetic field strength were reflected in the shear viscosity and elastic modulus. In contrast, numerous studies have examined the rheological properties of core–shell structures synthesized using the Pickering emulsion polymerization technique [27–29]. However, oil-in-oil (O/O) Pickering emulsions are also possible to prepare and are not yet characterized by rheological techniques. Their rheological properties with and without the application of a magnetic field should also be investigated, as the viscosity of the liquids constituting the dispersed and continuous phase of emulsions is much higher. This viscosity, in turn, is believed to be important, for instance, in MR damper applications.

Fig. 1 illustrates the three different systems that were characterized in this research. The behavior of Pickering emulsions was compared with simpler two-phase systems, specifically oil-based magnetic fluids (Fig. 1a). Additionally, the MR effect of two types of magnetic emulsions was investigated: a partially stable magnetic Pickering emulsion (pre-emulsion, Fig. 1b) and a stable magnetic Pickering emulsion (Fig. 1c). The main aim of the research was to investigate the rheological properties of the O/O magnetic Pickering emulsions by measuring both shear viscosity and dynamic yield stress under the application of a DC magnetic field. In the pre-emulsion, the Pickering droplets were not fully covered by particles, while in the stable emulsion, the Pickering droplets were fully covered after DC electric field application during the fabrication process. Therefore, we also studied the comparison of the Pickering droplet size and rate of aggregation for these two emulsion systems, as well as the examination of the influence of electro-coalescence on the stability of emulsion reflected in rheological data. As the MR effect is one of the important characteristics of the emulsions, the increased magnetic particle density on the Pickering droplets interface after electric treatment led to different MR effects.

2. Materials and methods

2.1. Particles and oils

Iron oxide nanoparticles (Sigma-Aldrich Co., USA) in powder form were used to prepare an oil-based magnetic fluid and stabilize the emulsion droplets. These particles were polydisperse in size, with a median value of approximately 175 nm. Castor oil (MERLIN, MA220-1, Spain) with a viscosity of 700 mPa·s formed the continuous phase, while silicone oil (Rhodorsil, 47 V 50, USA) with a viscosity of 50 mPa·s was used as the dispersed phase. These two types of oils were utilized to prepare an O/O magnetic Pickering emulsion due to their similar densities (around 960 kg/m^3), which was beneficial for the emulsions' stability against sedimentation.

2.2. Method of preparation of oil-based magnetic fluids

Oil-based magnetic fluids were prepared by sonication using a homogenizer (Sonifier Cell Disruptor, Branson Ultrasonics, model 450, USA). The working frequency was 20 kHz, and the acoustic intensity was 9.9 $\frac{W}{cm^2}$. A 10-min application time and an output of 40 W ultrasound power were chosen for the preparation process. Two mass fractions of magnetic nanoparticles were used to prepare the magnetic fluid: 5 % and 10 %.

2.3. Method of magnetic Pickering emulsions preparation

To investigate the differences in rheological behavior between emulsion droplets solely stabilized by magnetic particles and those with

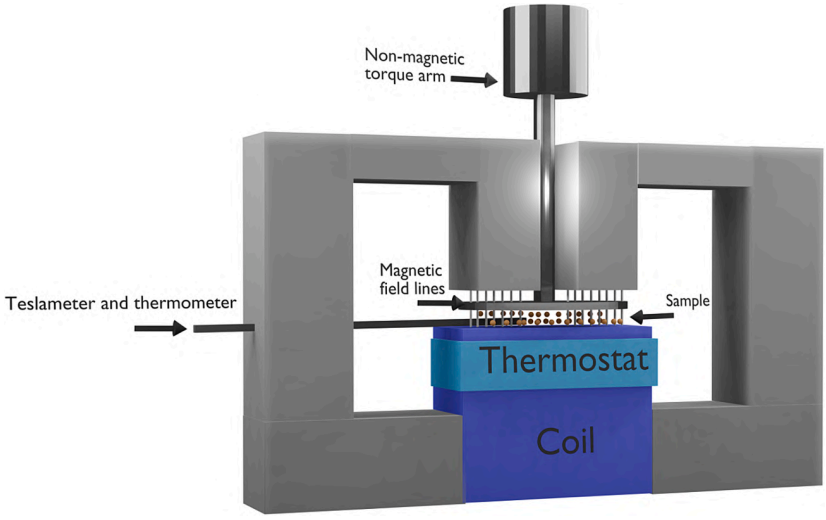

Fig. 2. Schematic of the MR measuring cell.

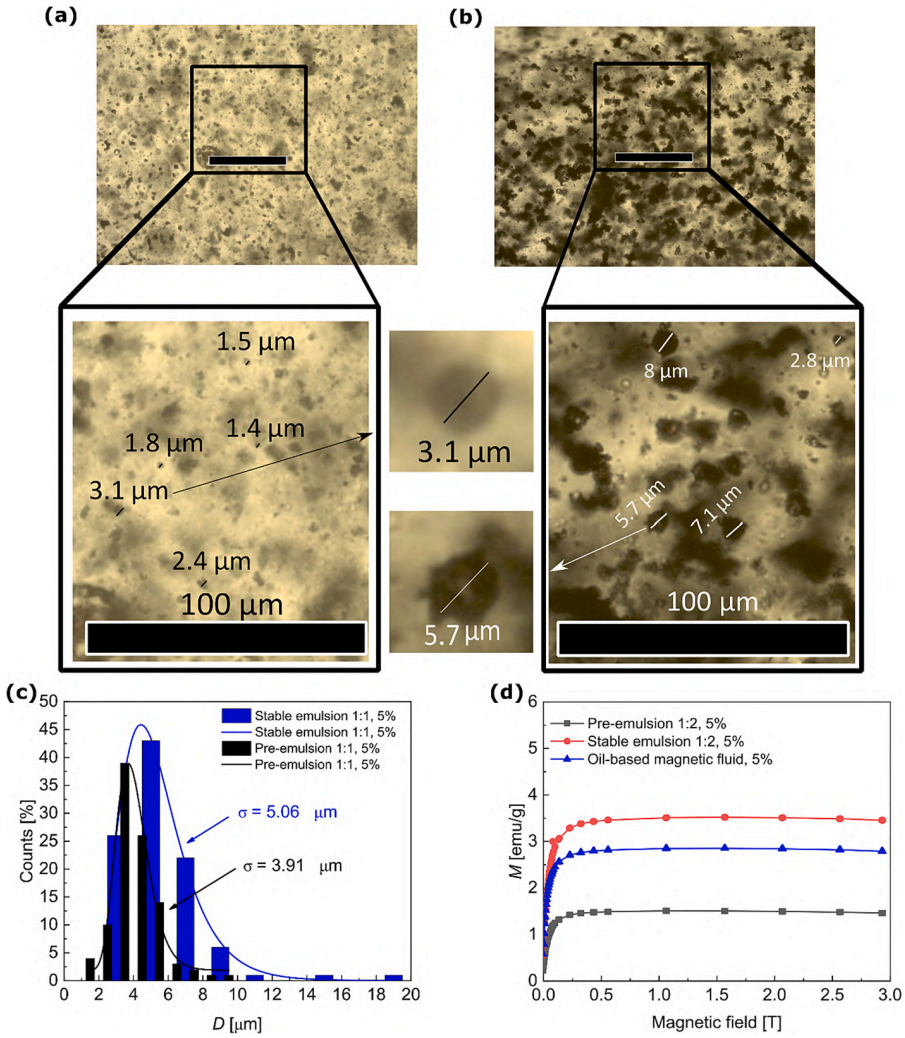

Fig. 3. The optical microscopy images of magnetic Pickering emulsions with 1:1 mass ratio between dispersed and solid phase (a) before and (b) after electric field application. (c) The magnetic Pickering drops distribution, and (d) the magnetization of oil-based magnetic fluid, pre-emulsion, and stable emulsion. The standard deviation of the stable emulsion was ± 3.45 emu/g and for pre-emulsion ± 0.91 emu/g.

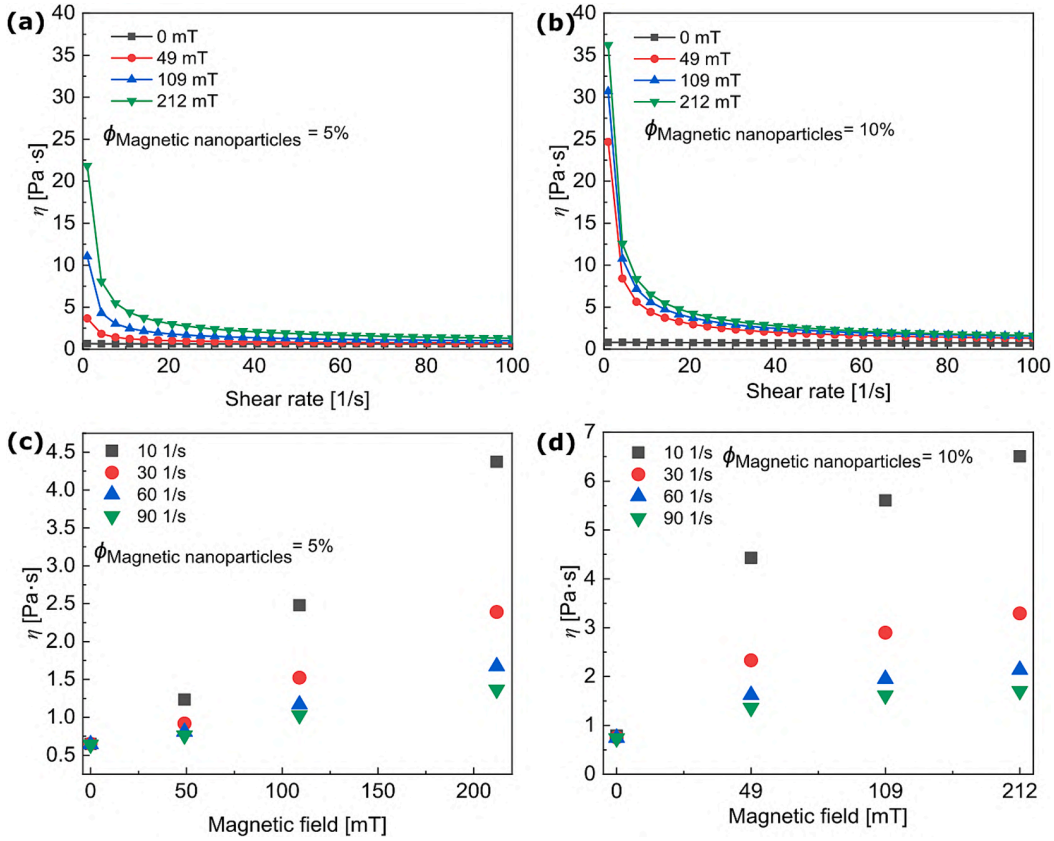

Fig. 4. Rheological properties of an oil-based magnetic fluid. Viscosity as a function of shear rate for (a) 5% and (b) 10% mass concentrations of magnetic nanoparticles at different magnetic field intensities. Viscosity as a function of magnetic field intensity for (c) 5% and (d) 10% mass concentrations of magnetic nanoparticles at different shear rates.

more stable particle shells, we employed a two-step approach to fabricate Pickering emulsions, as developed and described in [30]. First, magnetic Pickering pre-emulsions with droplets barely covered by magnetic nanoparticles were prepared using the Branson homogenizer with the same application time and acoustic intensity as used to prepare the oil-based magnetic fluids. Second, to ensure the stability of the magnetic Pickering emulsion, a DC electric field was applied to the magnetic pre-emulsion for 20 min with an electric field intensity of approximately 250 V/cm. The mass fraction of silicone oil dispersed in castor oil was 5 %, with two different mass ratios of magnetic nanoparticles to silicone oil: 1:2 and 1:1. In particular, a 1:1 mass ratio was chosen for magnetic Pickering emulsion, as it allowed for a direct comparison with the magnetic fluid 5 %, given the same contribution of magnetic nanoparticles to silicone oil in the system with 5 %. The magnetization curves were measured at $T = 298$ K using a vibrating sample magnetometer (VSM) installed on a cryogen free superconducting magnet from Cryogenic Ltd, UK.

2.4. Rheological measurements

The rheological properties of oil-based magnetic fluids and O/O magnetic Pickering emulsions were studied by using a magneto-rheological system with a twin gap rheometer provided by Anton Paar (MCR 502, Austria) with a dedicated MR cell (MRD170/1T) and a measuring system (PP20/MRD/TI). During the measurements, the magnetic field was created by applying an electrical current to a coil located below the sample cell plate. The magnetic field was uniform and oriented perpendicularly to the measuring system gap. The gap distance between the plate was constant (1 mm) in all measurements. The volume of the sample placed between the plates was 0.3 ml. A non-magnetic plate with a diameter of 20 mm was placed on top of MR fluid as shown in Fig. 2. The temperature of the sample cell was maintained during the measurement at ~ 25 °C. A thermocouple sensor from (GMH 3230, Germany) was utilized to monitor the temperature of the MR fluid during the measurement, and a teslameter (FH 54, Germany) was utilized to measure the magnetic field strength. The magnetic flux density gradually increased linearly over time from 0 mT to 212 mT.

3. Results and discussion

3.1. Optical microscopy and magnetization characterization

The optical microscopy images in Fig. 3a, b show the magnetic Pickering droplets, partially aggregated due to the aggregation of magnetic nanoparticles residing at the interface of silicone oil droplets. Additionally, the number of magnetic nanoparticles at the droplet interface was higher in the case of electric field application (Fig. 3b) indicated by a significant black color around the droplets. Apart from the optical imaging limited due to the poor optical transparency of magnetic samples, other techniques could provide information on the stability of Pickering droplets. In one of our research, ultrasound attenuation spectroscopy was used as a tool to measure the droplet size and the shell thickness of the magnetic shell in a magnetic Pickering emulsion [31]. The shell thickness was calculated based on core–shell model, and the experimental results indicated an increase in the ultrasound attenuation, which was attributed to a change in the internal structure of the system after the electric field application. The change in the mean size of 100 droplets estimated from optical microscopy images by ImageJ software is presented in Fig. 3c. For the tested emulsion, the outer radius of the Pickering droplets increased after electrocoalescence

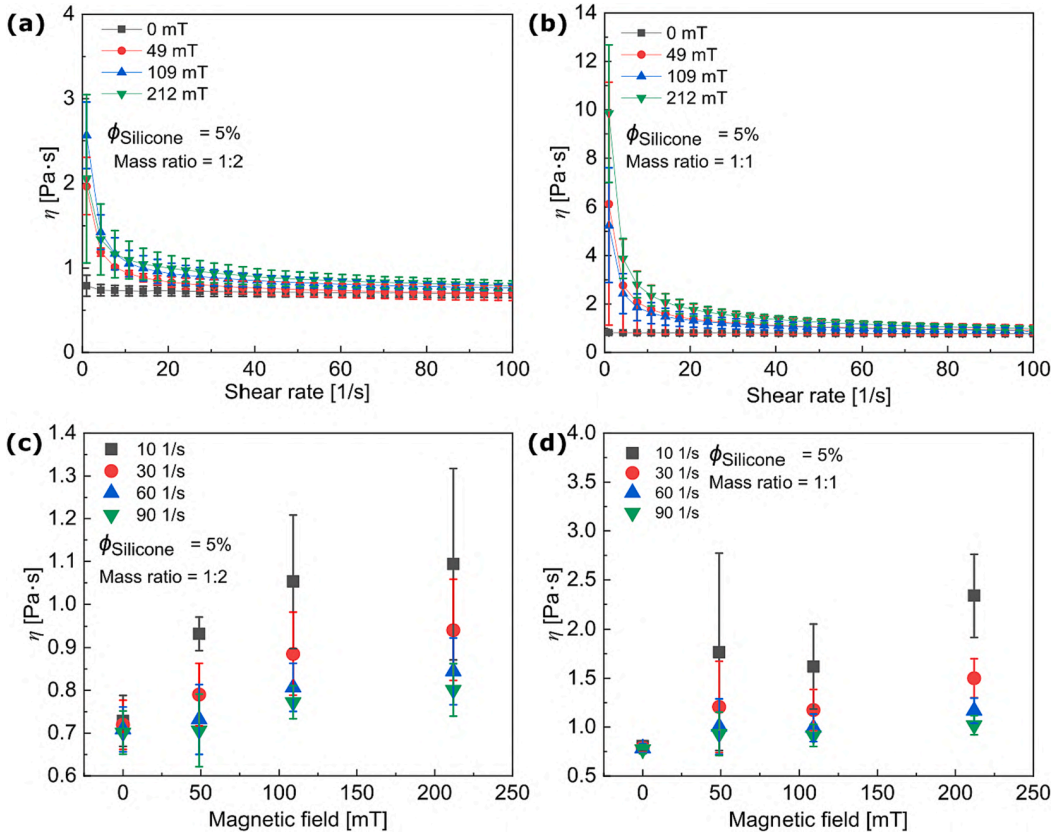

Fig. 5. Rheological properties of O/O magnetic pre-emulsion. Viscosity as a function of shear rate for a 5% silicone oil concentration for (a) 1:2 and (b) 1:1 mass ratios of magnetic nanoparticles to silicone oil at different magnetic field intensities. Viscosity as a function of magnetic field intensity for (c) 1:2 and (d) 1:1 mass ratios of magnetic nanoparticles to silicone oil at different shear rates.

events. As one can see in Fig. 3d, not only the appearance of magnetic Pickering emulsions changed after the electric field application. Despite the same concentration of magnetic nanoparticles, magnetization saturation values varied for various types of emulsion preparation systems that influenced further rheological measurements.

3.2. *Rheological properties of oil-based magnetic fluids*

First, the flow curve of the shear viscosity of an oil-based magnetic fluid was measured for different mass fractions of magnetic nanoparticles: 5 % and 10 %.

Fig. 4a shows the viscosity as a function of shear rate for different magnetic field intensities for a 5 % mass fraction of magnetic nanoparticles. The results indicate that in the absence of a magnetic field, the behavior of a Newtonian fluid appeared, indicating a liquid-like state. However, when a magnetic field was applied, the viscosity increased due to pronounced particle–particle interactions, leading to a change from a liquid state to a semi-solid state by forming a chain-like structure. The particles in an oil-based magnetic fluid exhibited magnetic multidomain behavior, and the application of a magnetic field induced a magnetic dipole in each particle, initiating the formation of chains of particles and/or their aggregates [32]. Furthermore, as the shear rate increased from 10 1/s up to 100 1/s, the influence of the semi-solid state began to disappear due to the deformation of the internal structure, which was evidence of shear thinning behavior as it has been shown for other MR fluid [3]. The results presented in Fig. 4b indicate the influence of a higher mass fraction of magnetic nanoparticles (10 %) on the rheological properties of oil-based magnetic fluid. For higher concentrations, a higher increase in viscosity appeared compared with that shown in Fig. 4a. In fact, increasing the concentration of the system led to higher particle interaction and a greater amount of chain formation compared with lower concentrations. This resulted in changes in the apparent viscosity, which induced a stronger magnetoviscous effect. Based on that, as shown in Fig. 4c, d the viscosity was a function of the magnetic field intensities for different values of shear rates. The viscosity decreased with an increase in the shear rate as the chain-like structure was broken for the higher shear rate due to hydrodynamic force [33]. Additionally, the viscosity was comparable between the 5 % and 10 % concentrations at a higher shear rate range of 100 1/s regardless of the strength of the applied magnetic field. In the literature, a higher content of magnetic material in the sample was not the only factor influencing the MR effect. The stabilized and non-stabilized magnetic fluids also showed different magnetoviscous effects due to the influence of aggregation [34]. Another factor could be the polydispersity of the system that resulted in different magnetoviscous effects [35]. The free rotation of the MR fluid was prevented by counteraction of magnetic and mechanical torque, leading to an increase in viscosity [6].

3.3. *Rheological properties of O/O magnetic Pickering pre-emulsion*

The MR effect for different mass ratios of magnetic nanoparticles to silicone oil (1:2 and 1:1) at a constant mass fraction of silicone oil (5 %) was studied for emulsions. Both pre-emulsions showed similar shear-thinning behavior regardless of the content of nanoparticles. Fig. 5a presents the viscosity as a function of the shear rate for the lower ratio of magnetic nanoparticles (1:2). After magnetic field application, the increase in viscosity appeared similar to the magnetoviscous effect observed in magnetic fluid. However, this increase in viscosity was lower compared with a pre-emulsion with a higher ratio of magnetic nanoparticles to silicone oil (1:1), as shown in Fig. 5b. The mean value of shear viscosity for 49 mT was 1.8 Pa·s for a 1:2 mass ratio and 2.6 Pa·s for a 1:1 mass ratio at zero shear rate. The higher shear rate led to a

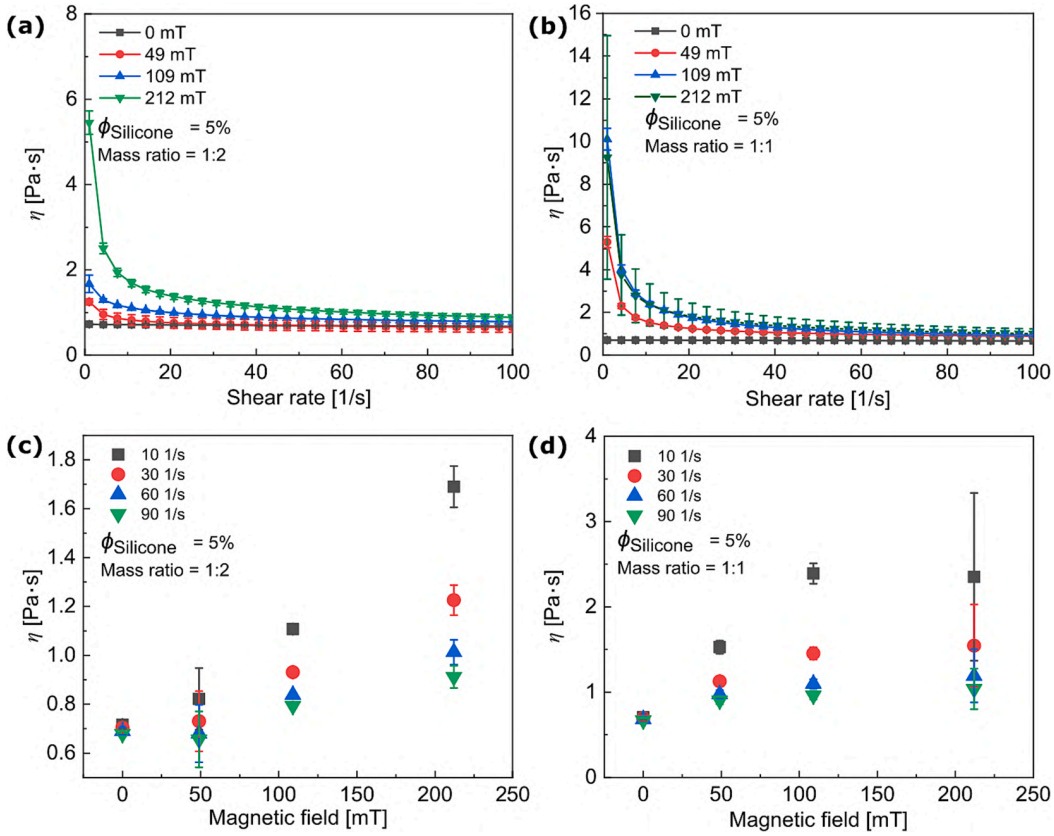

Fig. 6. Rheological properties of the O/O magnetic emulsion after electric field application. Viscosity as a function of shear rate for a 5% silicone oil concentration for (a) 1:2 and (b) 1:1 mass ratios of magnetic nanoparticles to silicone oil at different magnetic field intensities. Viscosity as a function of magnetic field intensity for (c) 1:2 and (d) 1:1 mass ratios of magnetic nanoparticles to silicone oil at different shear rates.

decrease in the value of shear viscosity and became close to the background viscosity of carrier fluid due to the magnetic separation and deformation of the Pickering droplets. Additionally, the increase in the magnetic field intensities from 49 mT and 212 mT does not show a substantial difference. The reason could be the same size of the chain-like structures despite applying different magnetic fields. The concentration of magnetic nanoparticles had a significantly stronger effect on the chain structure behavior.

Generally, the magnetoviscous effect can be influenced by several factors, such as magnetization of magnetic nanoparticles, size of particles or Pickering droplets, aggregation rate, external magnetic field, and concentration. The increase in the ratio of stabilized magnetic nanoparticles helped to improve the stability of magnetic Pickering emulsion and decreased Pickering droplets size [23]. As a result, this change in the internal structure caused different values of the magnetoviscous effect. Dipolar interactions between the magnetic droplets with a mass ratio of 1:1 were higher than for emulsions with 1:2. This could lead to the formation of a network of magnetic droplets and/or agglomerates throughout the emulsion. This led to a greater change from a liquid to a semi-solid state, resulting in an increase in the magnetoviscous effect, as shown in Fig. 5b. Additionally, Fig. 5c, d show typically decreasing viscosity with an increase in the magnitude of the shear rate. The presence of a dispersed liquid phase did not influence the behavior of the hydrodynamic forces that existed for higher shear rates and became large enough for droplets deformation [26].

3.4. Rheology properties of O/O magnetic Pickering emulsion

A stable magnetic Pickering emulsion was prepared after the application of a DC electric field. The new approach for fabricating Pickering emulsion by electric field was first investigated by Rozynek *et al.* [30], where the coalescence of droplets partially covered after electric application resulted in an increase in the surface particle coverage of the droplets. This led to an increase in the stability of the Pickering droplets. Magnetic Pickering emulsions were also studied after AC magnetic field application [16,18]. Then, the results showed different amounts of heat induced between pre-emulsion and stable emulsion.

Fig. 6a–b show the viscosity as a shear rate function for the stable magnetic Pickering emulsion with different magnetic field intensities for two mass ratios of magnetic nanoparticles to silicone oil (1:2 and 1:1, respectively). Generally, the magnetoviscous effect was higher for the sample with a 1:1 mass ratio due to the high concentration of magnetic nanoparticles in the system, and the exposition to a DC electric field did not change this relationship. This increase was found to be even higher than in pre-emulsion (Fig. 5a–b) when comparing the samples with the same magnetic nanoparticle content. This could be evidence of changes in the inner structure of the Pickering emulsion after electric field treatment. The shear viscosity value for the 49 mT magnetic field significantly increased in the case of a 1:1 mass ratio compared to the pre-emulsion. At zero shear rate, the value of shear viscosity was 5.2 Pa·s for stable Pickering emulsion compared to 2.6 Pa·s for pre-emulsion (without electric field application). However, there is no substantial difference for different magnetic field intensities. This is a piece of evidence in the case of stable emulsion there are no influence on the size and the number of chains with different magnetic field application the same as in pre-emulsion. The significant change in magnetoviscous effect has appeared for different preparation methods or different magnetic concentrations rather than magnetic field applications. Fig. 6c–d shows similar behavior as observed in Fig. 5c-d for pre-emulsion. The shear viscosity decreased at a higher shear rate due to the deformation of the droplet and the potential break-up of the chain structure.

Fig. 7 shows a comparison of the flow curves for three systems: oil-

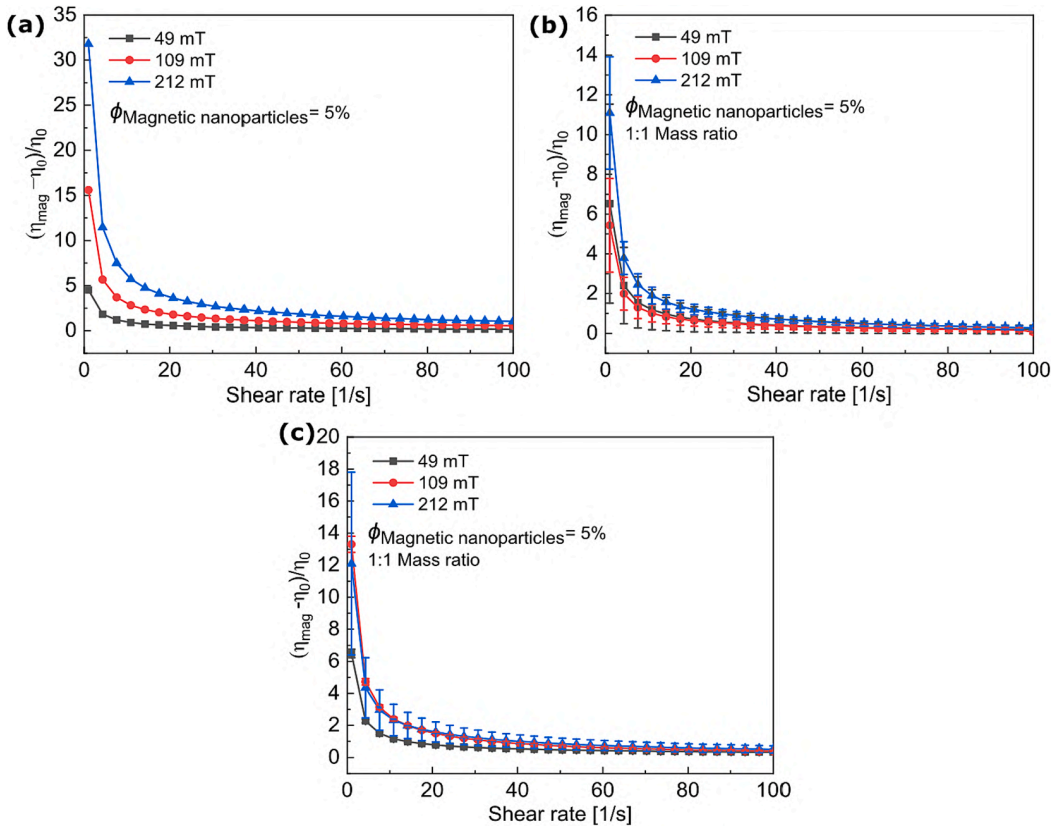

Fig. 7. The relative viscosity as a shear rate function for (a) oil-based magnetic fluid, (b) magnetic Pickering pre-emulsion, and (c) magnetic Pickering stable emulsion.

based magnetic fluid, pre-emulsion, and stable emulsion. The relative change in the viscosity of these systems for different magnetic field intensities (49 mT, 109 mT, and 212 mT) was determined. The relative change can be expressed as: $(\eta_{mag} - \eta_0)/\eta_0$, where η_0 indicates the viscosity with zero magnetic fields and η_{mag} refers to the viscosity of the system under magnetic field application. The magnetic fluid showed a higher increase in viscosity compared with pre-emulsion and emulsion for the same content of magnetic nanoparticles. The magnetic properties also influenced the performance of the MR fluid [36]. The relative change in the viscosity was recorded as 32 for oil-based magnetic fluid and 11, 12 for pre-emulsion and stable emulsion, respectively, for a magnetic field of 212 mT and zero shear rate. According to Kim *et al.*, the higher appearance of the magnetoviscous effect with a series of magnetic field strengths provided evidence of the formation of a chain-like structure and the transition from liquid to solid state [28]. This means that the interaction between the magnetic particles was much higher in the magnetic suspension than in the magnetic emulsion, which led to the faster and easier formation of a chain-like structure aligned with the magnetic field line. Interestingly, a higher change in viscosity, accompanied by higher experimental error, for emulsion with fully covered droplets suggests stronger magnetic droplet interaction than in the case of partially covered droplets in the pre-emulsion. Regardless, there are no substantial differences between the magnetic field intensities. This means that the magnetoviscous effect did not only depend on the magnetic properties of the sample but also on its internal structure. The application of an electric field made the emulsion droplets more stable along with increasing in their size [30]. Larger "hollow magnets" with non-magnetic liquid cores were formed and could interact with the magnetic field.

When describing the rheological properties of a system, the yield point is commonly determined as the point at which a material changes from a solid-like behavior to a liquid-like behavior under shear stress. The Herschel-Bulkley model is a fundamental model used to fit the flow curves and to extract the yield stress from the model parameters of non-Newtonian fluid that required stress to deform such as yield stress. This model is suitable for describing the flow behavior of materials that is more solid-like when the shear rate is below the yield point; after the yield point, the material behaves like a non-linear material [37].

The Herschel-Bulkley model is described by the following equation:

$$\tau = \tau_{dy} + K\dot{\gamma}^n \quad (1)$$

where τ is the shear stress, τ_{dy} is the dynamic yield stress, K is the consistency coefficient, $\dot{\gamma}$ is the shear rate, and n is the flow index.

Fig. 8a–c present the shear stress as a function of the shear rate for the emulsion before and after electric field application, respectively. To measure the yield point, the application of shear rate time was set at 150 s with a shear rate of 0.01 $1/s$, and the time decreased gradually to 1 s at a shear rate of 1,00 $1/s$. A log scale was used to visualize the changes in the low range of shear rate with varying magnetic field strengths.

After fitting the shear stress to the Herschel-Bulkley model (**Eq. (1)**), the dynamic yield stress values were determined. Fig. 8c shows a higher dynamic yield stress of approximately 39.4 % for stable emulsion than for pre-emulsion at magnetic field strength 109 mT. This is consistent with the dependence of the dynamic yield stress on the magnetic field. Fig. 8a.

When the yield stress of a material increases, it means that the material requires a higher level of stress to initiate permanent deformation. This increase in yield stress typically indicates that the material has become more rigid or resistant to deformation, resulting in a more stable emulsion. The application of an electric field to a magnetic emulsion improves the magnetic properties of the shell, leading to an increase in the surface density of Pickering droplets. As demonstrated in one study [27], the magnetically active shell on the polystyrene core with a higher

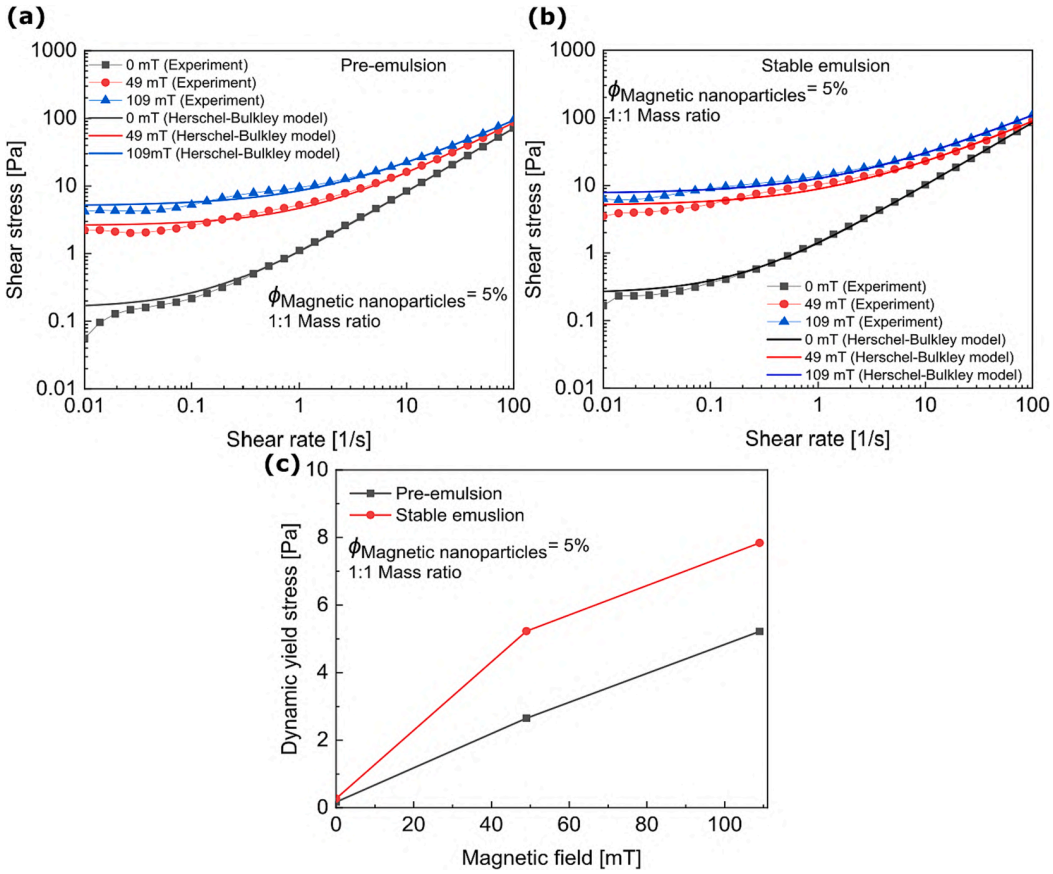

Fig. 8. The experimental results of shear stress as a function of shear rate for (a) magnetic Pickering pre-emulsion and (b) magnetic Pickering stable emulsion. The solid lines represent the relations calculated from the Herschel-Bulkley model. (c) The dynamic yield stress as a function of magnetic field for both emulsion systems.

surface density exhibited higher yield stress. In our work, one of the important differences between the pre-emulsion and stable emulsion was the magnetic particle density on the droplet shell as well as the size of the droplets. In our system, after electrocoalescence, the droplet size increased, as shown, e.g., by non-destructive ultrasound measurement elsewhere [31,38]. Fig. 8d shows that fully-covered droplets exhibited higher yield stress than partially-covered ones, resulting in a different MR effect. This observation further highlights the advantages of using solid particles as stabilizers over traditional surfactants. Beyond the enhanced ability to manipulate emulsion droplets under a magnetic field [21], a dense shell of particles at the interface seems to enhance control over the MR effect that could be crucial for practical applications. However, further investigation of the preparation process of magnetic Pickering emulsion is necessary to identify the dominant factor contributing to the change in MR properties attributed to electric field application: whether it results from better droplet stabilization or the simultaneous formation of complex structures, such as clusters of droplets and particles.

Moreover, the yield stress is also affected by concentration; the transition from a liquid state to a solid state is different with increasing the concentration of magnetic nanoparticles, and the yield stress is one of the ways to investigate this. Therefore, the MR study showed that the O/O magnetic Pickering stable emulsion had a different viscoplastic response than pre-emulsion, and the system became more rigid to deformation after electric field treatment. However, obtaining a viscoelastic response can reflect valuable information about the physical stability of the Pickering droplets. The comparison of different stages of stabilization, that is, the pre-emulsion and stable emulsion, showed that the yield point could be a valuable tool to evaluate the system with different magnetic field strengths. Furthermore, the rheological technique can help to improve the parameters of the formation process of the oil-in-oil magnetic Pickering emulsion, such as the time of sonication, the intensity of electrical field application, and the concentration of stabilizing particles.

4. Conclusion

The study covered the comparison of the MR effect for three systems: oil-based magnetic fluids, magnetic O/O emulsions with partially covered droplets, and stable emulsions. The flow curve and yield stress describing viscoelastic behavior were measured experimentally. The results showed that all three systems exhibited a liquid-like state without a magnetic field application. However, under the magnetic field, the O/O magnetic Pickering emulsion showed a lower magnetoviscous effect compared with the oil-based magnetic fluid for the same content of magnetic particles. Moreover, the emulsions treated with an electric field exhibited a higher magnetoviscous effect due to the change in the internal structure. Also, the values of the dynamic yield stress were higher for the stable emulsion when the magnetic field was applied, which indicates that the viscoelastic behavior of the stable Pickering emulsion exhibited strong solid-like characteristics compared with the partially stable Pickering emulsion. The study findings can be used to improve the formation process of O/O magnetic Pickering emulsions by optimizing sonication time, intensity of electrical field application, and particle concentrations.

CRediT authorship contribution statement

Bassam Jameel: Investigation, Formal analysis, Visualization, Conceptualization, Writing – original draft. **Matúš Molčan:** Writing –

review & editing. **Katarína Paulovičová:** Experimental performance, Finalization. **Jana Tóthová:** Experimental performance, Finalization. **Michal Rajňák:** Experimental performance, Finalization. **Rafał Bielas:** Methodology, Writing – review & editing. **Arkadiusz Józefczak:** Conceptualization, Methodology, Supervision, Funding acquisition.

Declaration of Competing Interest

The authors declare that they have no known competing financial interests or personal relationships that could have appeared to influence the work reported in this paper.

Data availability

Data will be made available on request.

Acknowledgments

This work was supported by project no. 2019/35/O/ST3/00503 (PRELUDIUM BIS) of the Polish National Science Centre, the Polish National Agency for Academic Exchange (NAWA) under grant no. PPN/STA/2021/1/00033/DEC/1, the Slovak Academy of Sciences and Ministry of Education in the framework of project VEGA 2/0011/20, VEGA 1/0353/22, and Slovak Research and Development Agency under the contract No. APVV-18-0160. The authors would also like to thank Katarína Zakuťanská for her help with optical microscopy imaging.

References

[1] J.-P. Lucking Bigué, F. Charron, J.-S. Plante, Understanding the super-strong behavior of magnetorheological fluid in simultaneous squeeze-shear with the Péclet number, J. Intell. Mater. Syst. Struct. 26 (2015) 1844–1855.
[2] R. Tao, Super-strong magnetorheological fluids, J. Phys. Condens. Matter 13 (2001) R979.
[3] H.-X. Wang, Y.-M. Ruan, S. Kong, J. Wang, Experiments and analysis for rheological properties of MRF, J. Cent. South Univ. Technol. 15 (2008) 284–287.
[4] A. Rossi, F. Orsini, A. Scorza, F. Botta, N.P. Belfiore, S.A. Sciuto, A review on parametric dynamic models of magnetorheological dampers and their characterization methods, In: Actuators, MDPI 7 (2018) 16.
[5] J. Salwiński, W. Horak, Measurement of normal force in magnetorheological and ferrofluid lubricated bearings, In: Key Engineering Materials, Trans Tech Publ 490 (2012) 25–32.
[6] L.J. Felicia, S. Vinod, J. Philip, Recent advances in magnetorheology of ferrofluids (magnetic nanofluids)—a critical review, Journal of Nanofluids. 5 (2016) 1–22.
[7] M. Shliomis, Effective viscosity of magnetic suspensions, Zh. Eksp. Teor. Fiz. 61 (1972) 2411–2418.
[8] J. Wang, G. Meng, Magnetorheological fluid devices: principles, characteristics and applications in mechanical engineering, Proceedings of the Institution of Mechanical Engineers, Part l: Journal of Materials: Design and Applications. 215 (2001) 165–174.
[9] S.J. Dyke, B. Spencer Jr, M. Sain, J. Carlson, Modeling and control of magnetorheological dampers for seismic response reduction, Smart Mater. Struct. 5 (1996) 565.
[10] Kim, J.-H., Oh, J.-H. Development of an above knee prosthesis using MR damper and leg simulator. In: Proceedings 2001 ICRA. IEEE International Conference on Robotics and Automation (Cat. No. 01CH37164), IEEE, 2001, Vol. 4, pp. 3686-91.
[11] G. Liu, F. Gao, D. Wang, W.-H. Liao, Medical applications of magnetorheological fluid: A systematic review, Smart Mater. Struct. 31 (2022), 043002.
[12] M.S. Alnarabiji, M.M. Husein, Application of bare nanoparticle-based nanofluids in enhanced oil recovery, Fuel 267 (2020), 117262.
[13] C.L.G. Harman, M.A. Patel, S. Guldin, G.-L. Davies, Recent developments in Pickering emulsions for biomedical applications, Curr. Opin. Colloid Interface Sci. 39 (2019) 173–189.
[14] K.-Y.-A. Lin, H. Yang, C. Petit, Magnetically controllable Pickering emulsion prepared by a reduced graphene oxide-iron oxide composite, J. Colloid Interface Sci. 438 (2015) 296–305.
[15] H. Yang, S. Wang, W. Zhang, J. Wu, S. Yang, D. Yu, et al., Rapid demulsification of pickering emulsions triggered by controllable magnetic field, Sci. Rep. 10 (2020) 16565.
[16] R. Bielas, T. Hornowski, K. Paulovičová, M. Rajňák, A. Józefczak, The effect of magnetic particles covering the droplets on the heating rate of Pickering emulsions in the AC magnetic field, J. Mol. Liq. 320 (2020), 114388.
[17] R. Bielas, B. Jameel, A. Józefczak, Monitoring of Pickering emulsion stability during magnetic heating using ultrasound measurements, Measurement 178 (2021), 109431.
[18] R. Bielas, A. Józefczak, The Effect of Particle Shell on Cooling Rates in Oil-in-Oil Magnetic Pickering Emulsions, Materials. 13 (2020) 4783.
[19] J. Lim, S.P. Yeap, C.H. Leow, P.Y. Toh, S.C. Low, Magnetophoresis of iron oxide nanoparticles at low field gradient: The role of shape anisotropy, J. Colloid Interface Sci. 421 (2014) 170–177.
[20] H. Gavilán, K. Simeonidis, E. Myrovali, E. Mazarío, O. Chubykalo-Fesenko, R. Chantrell, et al., How size, shape and assembly of magnetic nanoparticles give rise to different hyperthermia scenarios, Nanoscale 13 (2021) 15631–15646.
[21] B. Jameel, R. Bielas, T. Hornowski, A. Józefczak, Propagation of ultrasonic wave in magnetic Pickering emulsion under DC magnetic field, J. Magn. Magn. Mater. 542 (2022), 168590.
[22] L.E. Low, S.P. Siva, Y.K. Ho, E.S. Chan, B.T. Tey, Recent advances of characterization techniques for the formation, physical properties and stability of Pickering emulsion, Adv. Colloid Interface Sci. 277 (2020), 102117.
[23] J. Zhou, X. Qiao, B.P. Binks, K. Sun, M. Bai, Y. Li, et al., Magnetic Pickering emulsions stabilized by Fe3O4 nanoparticles, Langmuir 27 (2011) 3308–3316.
[24] M.-F. Li, Z.-Y. He, G.-Y. Li, Q.-Z. Zeng, D.-X. Su, J.-L. Zhang, et al., The formation and characterization of antioxidant pickering emulsions: Effect of the interactions between gliadin and chitosan, Food Hydrocoll. 90 (2019) 482–489.
[25] B.R. Shah, W. Xu, J. Mráz, Fabrication, stability and rheological properties of zein/chitosan particles stabilized Pickering emulsions with antioxidant activities of the encapsulated vit-D3, Int. J. Biol. Macromol. 191 (2021) 803–810.
[26] X. Qiao, J. Zhou, B.P. Binks, X. Gong, K. Sun, Magnetorheological behavior of Pickering emulsions stabilized by surface-modified Fe3O4 nanoparticles, Colloids Surf A Physicochem Eng Asp 412 (2012) 20–28.
[27] S. Han, J. Choi, Y.P. Seo, I.J. Park, H.J. Choi, Y. Seo, High-Performance Magnetorheological Suspensions of Pickering-Emulsion-Polymerized Polystyrene/Fe3O4 Particles with Enhanced Stability, Langmuir 34 (2018) 2807–2814.
[28] J.N. Kim, Y.Z. Dong, H.J. Choi, Pickering Emulsion Polymerized Polyaniline/Zinc-ferrite Composite Particles and Their Dual Electrorheological and Magnetorheological Responses, ACS Omega 5 (2020) 7675–7682.
[29] Q. Lu, H.-J. Jin, H.J. Choi, Pickering emulsion polymerized Fe3O4@ graphene oxide-polystyrene composite particles and their electro/magnetorheological responses, J. Mol. Liq. 365 (2022), 120083.
[30] Z. Rozynek, R. Bielas, A. Józefczak, Efficient formation of oil-in-oil Pickering emulsions with narrow size distributions by using electric fields, Soft Matter 14 (2018) 5140–5149.
[31] B. Jameel, R. Bielas, A. Józefczak, Ultrasound measurements of particle shells in magnetic Pickering emulsions, Measurement 220 (2023), 113409.
[32] M. López-López, P. Kuzhir, S. Lacis, G. Bossis, F. González-Caballero, J.D. Durán, Magnetorheology for suspensions of solid particles dispersed in ferrofluids, J. Phys. Condens. Matter 18 (2006) S2803.
[33] S. Odenbach, H. Störk, Shear dependence of field-induced contributions to the viscosity of magnetic fluids at low shear rates, J. Magn. Magn. Mater. 183 (1998) 188–194.
[34] D.I. Santiago-Quinones, K. Raj, C. Rinaldi, A comparison of the magnetorheology of two ferrofluids with different magnetic field-dependent chaining behavior, Rheol. Acta 52 (2013) 719–726.
[35] S. Chen, D. Li, Control of Magnetic Particle Size in Ferrofluid and Its Effect on Rheological Properties, Chinese Journal of Mechanical Engineering. 35 (2022) 1–9.
[36] C.Y. Gao, S.H. Piao, H.J. Choi, Pickering emulsion polymerized magnetite-poly (methyl methacrylate) composite particles and their magnetorheology, Colloid Polym. Sci. 295 (2017) 959–966.
[37] X. Wang, F. Gordaninejad, Flow analysis of field-controllable, electro-and magneto-rheological fluids using Herschel-Bulkley model, J. Intell. Mater. Syst. Struct. 10 (1999) 601–608.
[38] R. Bielas, Z. Rozynek, T. Hornowski, A. Józefczak, Ultrasound control of oil-in-oil Pickering emulsions preparation, J. Phys. D Appl. Phys. 53 (2019), 085301.

[Scientific Paper IV]

Optimization of ultrasound heating with Pickering droplets using core-shell scattering theory

Jameel, B., Harkavyi, Y., Bielas, R., and Józefczak, A.

Ultrasonics Sonochemistry (2024): *submitted, under review*

Optimization of ultrasound heating with Pickering droplets using core-shell scattering theory

Bassam Jameel, Yaroslav Harkavyi, Rafał Bielas*, and Arkadiusz Józefczak

Chair of Acoustics, Faculty of Physics, Adam Mickiewicz University in Poznań
Uniwersytetu Poznańskiego 2, 61-614 Poznań, Poland
*e-mail: rafal.bielas@amu.edu.pl

Abstract:

Nanoparticles find widespread application in various medical contexts, including targeted nanomedicine and enhancing therapeutic efficacy. Moreover, they are employed to stabilize emulsions, giving rise to stabilized droplets known as Pickering droplets. Among the various methods to improve anti-cancer treatment, ultrasound hyperthermia stands out as an efficient approach. This research proposes Pickering droplets as promising sonosensitizer candidates, to enhance the attenuation of ultrasound with simultaneous potential to act as drug carriers.
The ultrasound scattering theory, based on the core–shell model, was employed to calculate theoretical ultrasound properties such as attenuation and velocity. Additionally, computer simulations, based on a bioheat transfer model, were utilized to compute heat generation in agar-based phantoms of tissues under different ultrasound wave frequencies. Two types of phantoms were simulated: a pure agar phantom and an agar phantom incorporating spherical inclusions. The spherical inclusions, with a diameter of 10 mm, were doped with various sizes of Pickering droplets, considering their core radius and shell thickness. Simulation results present temperature changes for different frequencies, along with heat distribution and ultrasound penetration depth. Notably, spherical inclusions doped with magnetic Pickering droplets exhibited a higher temperature rise compared to non-magnetic counterparts. Furthermore, nanodroplets with a core radius below 400 nm demonstrated better heating performance compared to microdroplets. The enhanced ultrasound energy dissipation could be, therefore, optimized by changing the parameters of Pickering droplets as sonosensitizers. Furthermore, Pickering droplets incorporated into agar phantom could allow obtaining a similar effect of local heating as sophisticated focused ultrasound devices.

Keywords:
Biomaterial; ultrasound heating; ultrasound scattering theory; Pickering emulsion; sonosensitizers; COMSOL simulations.

Highlights

- Ultrasound scattering theory was used to study agar phantoms doped with the Pickering droplets.
- The theoretical ultrasound heating efficiency was affected by the physical properties of Pickering droplets.
- The adjustment of the core radius and shell thickness of the droplets gave improvement to the modeled ultrasound heating.

Graphical abstract

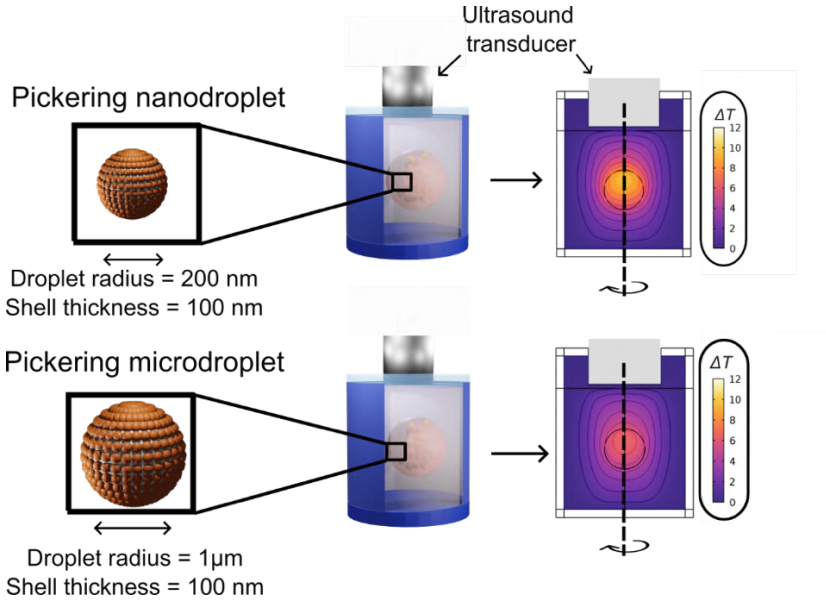

1. Introduction

Hyperthermia is a treatment approach that refers to the procedure of raising tissue temperature to 40 °C – 45 °C for specific medical treatment purposes [1,2]. The effectiveness of thermal enhancement in therapy depends on both the temperature and the duration of exposure within biological cells [3]. Subsequently, hyperthermia exhibits direct cytotoxic effects in microenvironments characterized by low blood supply, hypoxia, and low pH, such as those commonly found in tumor tissues [4]. Clinically, hyperthermia has been used for radiosensitization, enhancing the effectiveness of radiation therapy [5]. Over the past decades, numerous techniques have been employed to perform thermal therapies. Among others, a high-frequency alternative electromagnetic fields [2] as well as the magnetic nanoparticles under an alternating magnetic field [6,7] are used as a source of heat for hyperthermia treatment. Using mechanical ultrasound waves, operating within the frequency range of 1 MHz to 10 MHz, represents an alternative method for inducing heat in biological tissues [8–10].

Ultrasound offers advantages over other treatment techniques, primarily in its non-invasive ability to generate heat in deep-seated tissues. Additionally, the ultrasound technique stands out for its cost-effectiveness, simplicity, and energy efficiency. The direction of ultrasound waves can be controlled through the design of the transducer. Specifically, the application of a focused ultrasound beam, emitted from the curved surface of the transducer, involves converging multiple ultrasound waves onto a single point. The local temperature obtained using ultrasound is crucial in medical processes such as tumor ablation [11–13] and targeted drug delivery [14]. The heat generated by ultrasound waves depends on several parameters, including acoustic intensity, frequency, and the absorption rate of ultrasound waves in the medium. Different wavelengths of the ultrasound wave contribute to distinct relaxation times. Lower frequencies correlate with reduced fluctuations in the medium, featuring longer wavelengths associated with lower

absorption and scattering of the wave. These factors collectively influence heat generation and penetration depth [15].

There are various ways to optimize the value of heating produced by ultrasound waves. For instance, ultrasound wave frequency and intensity have a direct effect on effective treatment plans [16]. The size of the treatment area can be optimized by splitting the ultrasound beam to achieve a larger focal point [17]. On the other hand, the properties of the medium have also an effect on heat value, which might change depending on the human body parts. The medium properties modification such as sonosensitizers, i.e., additional materials incorporated into the medium, offer an alternative means to modify ultrasound absorption, facilitating rapid temperature increases for lower intensity and shorter sonication durations. The ultrasound wave scattered by nanoparticles as sonosensitizers has been used to control the ultrasound attenuation [18,19]. The particle radius is commonly comparable with wavelength, and the physical properties of the nanoparticles provide different scattering and absorption contributions. For instance, the comparison of the magnetite and silica nanoparticles showed different attenuation results theoretically and experimentally, as the physical properties such as density contrast between phases and agglomeration rate had a direct effect on the ultrasound attenuation [20]. This variability extended to different temperature increases observed in the agar phantom enriched with nanoparticles under the ultrasound application [21], where ultrasound velocity and attenuation were affected by the presence of nanoparticles. In general, the addition of magnetic nanoparticles into tissue-mimicking material resulted in a significant increase in the specific absorption rate compared to the pure tissue-mimicking material [22]. Potentially, the Pickering droplet stabilized by nanoparticles can also alter the properties of the tissue phantoms and function as sonosensitizers. Similarly to the nanoparticles, the presence of the Pickering droplets in the system was showed to lead to a change in the attenuation of the medium [23]. The influence of the Pickering droplet on ultrasound hyperthermia was not presented yet in the literature. However, there are studies investigating the thermal effect of the Pickering droplet under the influence of an AC magnetic field [24–26]. In the case of Pickering droplets, we could have many more parameters to control for optimization of the outcome of ultrasound hyperthermia such as the size of the liquid core, the size of the stabilizing particles, their mechanical and thermal properties, and even the shape, as non-spherical particles have been also investigated for Pickering emulsions [27].

In this research, we investigated theoretically the effect of utilizing the Pickering droplets in agar phantom as sonosensitizers. The ultrasound attenuation and velocity of the silicone oil droplet stabilized with magnetite and silica nanoparticles incorporated in pure agar phantom were calculated based on core–shell model proposed by Anson and Chivers [28]. Recently, this model was successfully used to analyze the experimental data of ultrasound spectroscopy in the Pickering emulsion. The output results theoretically and experimentally indicated the changes in the absorption of the medium with different concentrations, Pickering droplet sizes, and other physical properties of the system such as density, specific heat, and thermal conductivity [23,29]. Consequently, in the current research, the difference in physical properties and the resulting different value absorption of the whole system (agar phantom doped with Pickering droplets) led to different amounts of generated heat. The maximum value of the scattering and thermal absorption varied with various wavelengths and object sizes as well as carrier fluid properties. In this research, both a pure agar phantom and an agar phantom with a spherical inclusion were

simulated using COMSOL Multiphysics. Heat transport within the agar phantom was modeled by employing the classic Pennes bioheat equation [30]. The simulation incorporated the physical properties of inclusions doped with either magnetite or silica Pickering emulsion, and examined the impact of varying droplet radius and shell thickness on the final heating effect. This research lays the groundwork for understanding ultrasound wave propagation in agar phantom doped with Pickering droplets, setting the stage for future experimental investigations. The simulation results offer insights into the potential of Pickering nano- and microemulsions, comparing favorably to the current use of nanoparticles, to enhance thermal therapy.

2. Theoretical background

2.1. Ultrasound scattering theory based on core–shell model

The core–shell model is a model proposed by Anson and Chivers that describes the scattering of the ultrasound wave by the core–shell objects that consist of a spherical core (solid or liquid) covered with another type of material as a shell and dispersed in continuous phase [28]. The Pickering droplet has a similarity to such core–shell structure which allows for using the Anson and Chivers model to calculate the ultrasound parameters of the Pickering droplets.

As ultrasound wave travels through emulsion and suspension, it is attenuated. The reason for the attenuation is the absorption and scattering of the wave. The particles and droplets dispersed in continuous phase constituting suspensions or emulsions have a direct effect on the ultrasonic properties and make the ultrasound attenuation and velocity dependent on the size distribution and volume concentration. The Epstein–Carhart–Allegra–Hawley (ECAH) theory [31,32] describes the ultrasound scattering theory by solid or liquid suspension in the continuous phase caused by the viscous-inertial and thermal transport mechanism. The viscous-thermal mechanism occurs the densities are different for both phases. The thermal mechanism occurs due to pressure-temperature coupling due to the thermal contrast between phases. In the core–shell model, the additional physical parameters of the shell material such as its attenuation coefficient are taken into consideration in comparison to ECAH theory [28].

Similarly to the ECAH model, in the core–shell model, the wave equation for the propagation of compressional, shear, and thermal wave are derived as follows:

$$(\nabla^2 + k_c^2)\varphi_c = 0, \quad (1a)$$

$$(\nabla^2 + k_t^2)\varphi_t = 0, \quad (1b)$$

$$(\nabla^2 + k_s^2)A_\Psi = 0. \quad (1c)$$

The main part of our implementation of the core–shell model was to calculate the partial scattering amplitude for the compression wave in the continuous phase, which further was used for the calculation of the ultrasound velocity and the attenuation of the compression wave in the continuous phase The formula below shows the potential of compression ultrasound wave as series expansions that contain the scattering coefficient:

$$\varphi_{c1} = \sum_{n=0}^{\infty} i^n (2n+1) A_n h_n(k_{c1} r) P_n(cos\Theta). \quad (2)$$

φ_{c1} is the potential scattering wave equation for the compression wave in the continuous phase, A_n is the partial scattering amplitude in the continuous phase, h_n is the Hankel function, k_{c1} is the complex wave number of the compression wave, r is the object radius, P_n is the Legendre polynomials of the order *n*, and Θ is the scattering angle. Similarly, the potential of thermal and shear wave were calculated by considering the thermal and shear wavenumbers k_{t1} and k_{s1}. Therefore, in **Equation (3)**, φ_{t1} is related to the potential of the thermal wave, and the B_n is related to the partial amplitude of the thermal wave. In turn, in **Equation (4)**, $A_{\Psi 1}$ is related to the potential of the shear wave in the continuous phase, and C_n is related to the partial wave amplitude of the shear wave.

$$\varphi_{t1} = \sum_{n=0}^{\infty} i^n (2n+1) B_n h_n(k_{t1} r) P_n(cos\Theta), \quad (3)$$
$$A_{\Psi 1} = \sum_{n=0}^{\infty} i^n (2n+1) C_n h_n(k_{s1} r) P_n^1(cos\Theta). \quad (4)$$

The wave scattered forward (the boundary between the droplet shell and agar phantom) and backward (the boundary between the droplet shell and core - silicone oil) can be expressed as the following equations for the compressional, thermal, and shear wave:

$$\varphi_{c2} = \sum_{n=0}^{\infty} i^n (2n+1)[D_n j_n(k_{c2} r) + G_n h_n(k_{c2} r)] P_n(cos\Theta), \quad (5a)$$
$$\varphi_{t2} = \sum_{n=0}^{\infty} i^n (2n+1)[E_n j_n(k_{t2} r) + H_n h_n(k_{t2} r)] P_n(cos\Theta), \quad (5b)$$
$$A_{\Psi 2} = \sum_{n=0}^{\infty} i^n (2n+1)[F_n j_n(k_{s2} r) + I_n h_n(k_{s2} r)] P_n(cos\Theta). \quad (5c)$$

The D_n, E_n, and F_n are the partial wave amplitudes of the backward compressional, thermal, and shear modes, respectively. The G_n, H_n, and I_n are the partial wave amplitudes for the three modes of the forward wave.

The wave scattered in the core (in our implementation in silicone oil droplet) is a backward wave, i.e., the wave propagating back inside the core material, and can be represented as following equations:

$$\varphi_{c3} = \sum_{n=0}^{\infty} i^n (2n+1) J_n j_n(k_{c3} r) P_n(cos\Theta), \quad (6a)$$
$$\varphi_{t3} = \sum_{n=0}^{\infty} i^n (2n+1) K_n j_n(k_{t3} r) P_n(cos\Theta), \quad (6b)$$
$$A_{\Psi 3} = \sum_{n=0}^{\infty} i^n (2n+1) L_n j_n(k_{s3} r) P_n^1(cos\Theta). \quad (6c)$$

The 12 boundary equations and 12 unknown coefficients from the core–shell model ($A_n, B_n, C_n, D_n, E_n\ F_n, G_n, H_n, I_n, J_n, K_n,$ and L_n) were solved using a 12 x 12 matrix equation [28]. This model was recently used for comprehensive theoretical and experimental characterization of oil-in-oil magnetic Pickering emulsions [23]. To calculate the ultrasound attenuation coefficient, the imaginary part of the partial compression wave amplitude A_{n} had to be determined. Furthermore, the real part of the compression wave amplitude A_{n} was used to calculate the ultrasound velocity. In **Table 1**, the physical properties of the phases required for the core–shell model calculation are presented.

The complex wavenumber equation was used to calculate the ultrasound attenuation and velocity of the Pickering droplets when placed in an agar phantom:

$$\beta = \sqrt{k_c^2 - \frac{3i\phi_{Si}}{(k_c^3)(a^3)}(A_0 + 3A_1 + 5A_2)}. \quad (7)$$

Here, $\beta = \frac{\omega}{c_{Agar\ phantom}} + i\alpha_{Agar\ phantom}$ is the complex wavenumber of the scattered wave; the real part, $\frac{\omega}{c_{Agar\ phantom}}$, is related to the ultrasound velocity and $i\alpha_{Agar\ phantom}$ is related to the ultrasound attenuation. ϕ_{Si} is the volume fraction of the dispersed phase, $\phi_{Si} = \frac{4}{3}\pi b^3 N$, where N is the number of silicone oil droplets (dispersed phase) distributed in the continuous phase (agar gel), a and b are the outer and inner radii of the Pickering droplet, respectively. A_0 and A_1 are partial scattering amplitudes that depend on the thermal (monopole effect) and viscous mechanism (dipole effect), respectively. In turn, A_2 is related to the object resonance mechanism (quadrupole effect) that occurred due to the relationship between the wavelength and surface wave that is produced from the interface of compression and shear wave [33]. The mentioned mechanisms occurred due to the different physical properties of the components of core–shell objects.

It is well-known that the shear wave of ultrasound wave has a higher contribution in the solid-state material [34]. However, the existence of shear waves is negligible in soft tissues because soft tissues are approximated and considered liquid [9]. That is the reason why we did not take into account the influence of shear waves propagating in agar phantoms.

Table 1 The physical properties of agar phantom as continuous phase, silicone oil as dispersed droplets, and magnetite nanoparticles as stabilizing particles at 25°C. The frequency (*f*) is expressed in Hz unit.

Parameters	Agar phantom	Silicone oil	Magnetite particles	Silica particles
Viscosity, η (Pa · s)	–	50×10^{-3} (measured)	–	–
Density, ρ (kg/m^3)	1040 [35]	960 (measured)	5180 [36]	1970 [37]
Thermal conductivity, κ (W/ m · K)	0.616 [35]	0.15 (data sheet)	52 [36]	1.6 [37]
Specific heat, c_p (J/kg · K)	3900 [38]	1460 (data sheet)	653 [36]	728 [37]
Thermal expansion, β_T (1/K)	3×10^{-4} [39]	9.5×10^{-4} (data sheet)	11.8×10^{-6} [36]	1.35×10^{-6} [37]
Velocity, *c* (m/s)	1547 [40]	1004 [36]	7157 [36]	5968 [37]
Atteuation, α (Np/m)	$4.6 \times 10^{-6} f + 8.7 \times 10^{-14} f^2$ [40]	$3.79 \times 10^{-13} f^{2.02}$ (measured)	$0.01 \times 10^{-15} f^2$ [36]	$2.6 \times 10^{-22} f^2$ [37]
Shear modulus, μ (N/m^2)	40×10^3 [41]	–	6.03×10^{10} [36]	2.79×10^{10} [37]

The values of ultrasound attenuation coefficient and phase velocity for Pickering emulsions with assumed different core size, shell thickness, and volume concentration in relation to continuous phase (agar gel) were calculated using the Mathematica (13.2). These were then expressed in the

function of frequency for the range of 1 MHz to 12 MHz. These frequencies were chosen based on the requirements for the frequencies used in the ultrasound heating procedures [13,42,43].

2.2. Ultrasound heating model implemented in computer simulation

Theoretical calculations of ultrasound heating were carried out using COMSOL Multiphysics 6.1. Considering the high symmetry of the studied structure, 2-dimensional axisymmetric rotational geometry was used to reduce calculation time. Pressure Acoustics, Frequency Domain together with Bioheat Transfer modules were used to model the ultrasound heating of the samples. In our simulation, we assumed that the inclusion is filled evenly with Pickering emulsion droplets. Ultrasound was generated by the normal displacement of the transducer end with a diameter of 10 mm, providing a dynamic source for the model. The cylindrical phantom (with a diameter of 30 mm and a height of 30 mm) is placed 1 mm away from the transducer. The intervening space between the phantom and the transducer is filled with water, which serves as the coupling medium for the simulation. Additionally, to account for wave reflections and ensure accurate results, the whole system was enclosed by a Perfectly Matched Layer (PML). The scheme of the designed geometry for simulations is shown in **Figure 1**.

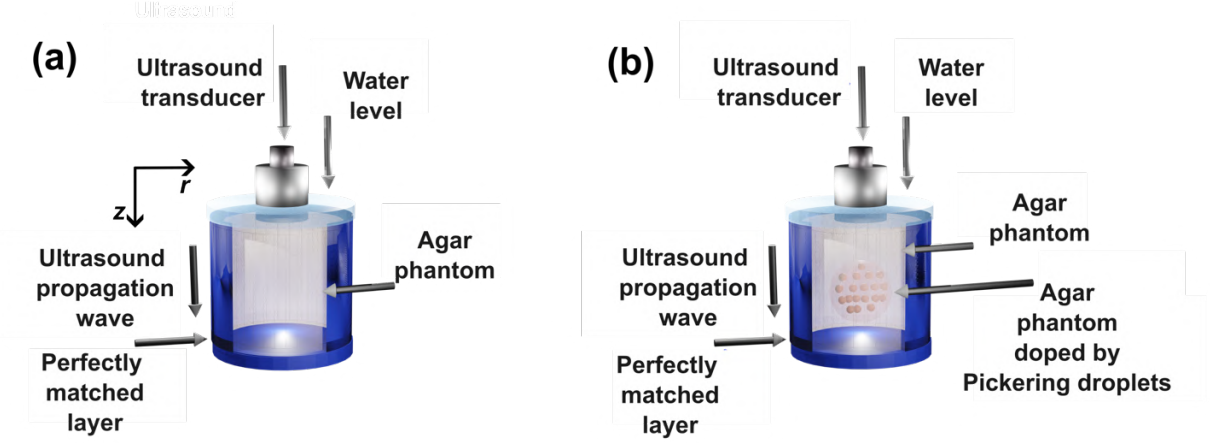

Figure 1 The scheme of the simulation design for (a) pure agar phantom and (b) agar phantom with an inclusion filled with Pickering droplets.

In simulations, the transducer was driven at several frequencies from 1 MHz to 10 MHz with an application time of 180 seconds for each frequency. The output intensity of the ultrasound wave was determined by changing the displacement amplitude of the transducer with different frequencies to achieve the acoustic intensity of 2.5 W/cm^2. This value was chosen to be similar to the intensity that was produced by the ultrasound transducer used commercially for medical purposes and in the research on ultrasound hyperthermia in tissue-mimicking phantoms [30] as well as the ultrasound-triggered release of active substances from Pickering capsules [44]. The acoustic pressure implemented in COMSOL Multiphysics was used for the simulation of ultrasound wave propagation and acoustic pressure change in an agar phantom. The classic Pennes bioheat equation was used in the simulation to model heat transfer in the tissue [30]. This is the mathematical model that describes the heat transfer in the biological tissue, expressed as follows:

$$\rho C_p \frac{\partial T}{\partial t} - k\nabla^2 T - w_b c_b (T_a - T) = Q + Q_m. \quad (8)$$

In the **Equation (8)**, ρ and C_p are the density and the specific heat of the tissue, *T* and *t* are the temperature and the time, respectively. $k\nabla^2 T$ is the thermal conductivity multiplied by the Laplacian operator that represents the spatial temperature gradient. w_b and c_b are the perfusion rate and specific heat of the blood, respectively. In turn, Q and Q_m are the heat source of the absorbed ultrasound energy and heat of the metabolism, respectively. The effect of blood perfusion and metabolic processes on heating effect is omitted ($Q_m = 0$) as the simulation was performed in the agar phantom system where there was no vasculature.
In our simulation, as it was used elsewhere [45,46], the heat is generated by ultrasound waves that propagate perpendicularly through a cylindrical agar phantom. As an axisymmetric cylindrical coordinator, the temperature distribution in the phantom is along the axis of the beam:

$$\rho C_p \frac{\partial T(r,z,t)}{\partial t} - k\left[\frac{\partial}{\partial t} r^2 \frac{\partial T(r,z,t)}{\partial r} + \frac{\partial^2 T(r,z,t)}{\partial z^2}\right] = Q. \quad (9)$$

The *r*, *z*, and *t* represent the distance from the center, the vertical distance from the top, and the application time.
For the initial condition, the time is equal to 0 and then, the temperature in the phantom is T_0:

$$\partial T(r,z,0) = T_0. \quad (10)$$

The following boundary conditions for simulating the experimental conditions:

$$\frac{\partial T(r,z,t)}{\partial r}|_{r=0} = 0, \quad (11a)$$
$$\frac{\partial T(r,z,t)}{\partial r}|_{r=R} = -\frac{h}{k}(T - T_0), \quad (11b)$$
$$\frac{\partial T(r,z,t)}{\partial z}|_{z=0} = -\frac{h}{k}(T - T_0), \quad (11c)$$
$$\frac{\partial T(r,z,t)}{\partial z}|_{z=L} = -\frac{h}{k}(T - T_0). \quad (11d)$$

In **Equations (11a-d)**, *R* and *L* are the cylindrical phantom radius and height respectively and *h* is the connective heat coefficient. The heat map of the temperature distribution of height of the cylindrical agar *L* phantom as well as the different application *T* time was simulated for several frequencies (1 MHz, 2 MHz, 5 MHz, and 10 MHz).

3. Results and discussion

3.1. Attenuation spectra of Pickering droplets stabilized by magnetic nanoparticles in agar phantom

First, we investigated the acoustic properties of the Pickering droplets stabilized by magnetic nanoparticles dispersed in agar phantom. This was further used to optimize ultrasound heating, by determining the ultrasound attenuation and velocity across various radii of silicone oil droplets, magnetic shell thicknesses, and volume concentrations of the dispersed droplets in an agar phantom. The results in **Figure 2** and **Figure 4** show the effect of acoustic properties of Pickering nano- and microdroplets with different shell thicknesses. In one of our previous studies, we showed that this parameter plays a crucial role in attenuation of the Pickering emulsion based on oils [23]. Additionally, **Figure 3** reveals the differences resulting from the use of ultrasound scattering theory based on core–shell model with and without the thermal contribution. For instance, Kanamori et al. [29], provide the calculation details of the core–shell model without thermal contribution. However, the consideration of the contribution of thermal effects to the overall acoustic energy loss in the medium provides important knowledge of the difference in attenuation coefficient and ultrasound velocity between Pickering nano- and microdroplets that we simulated as doped in agar phantom.

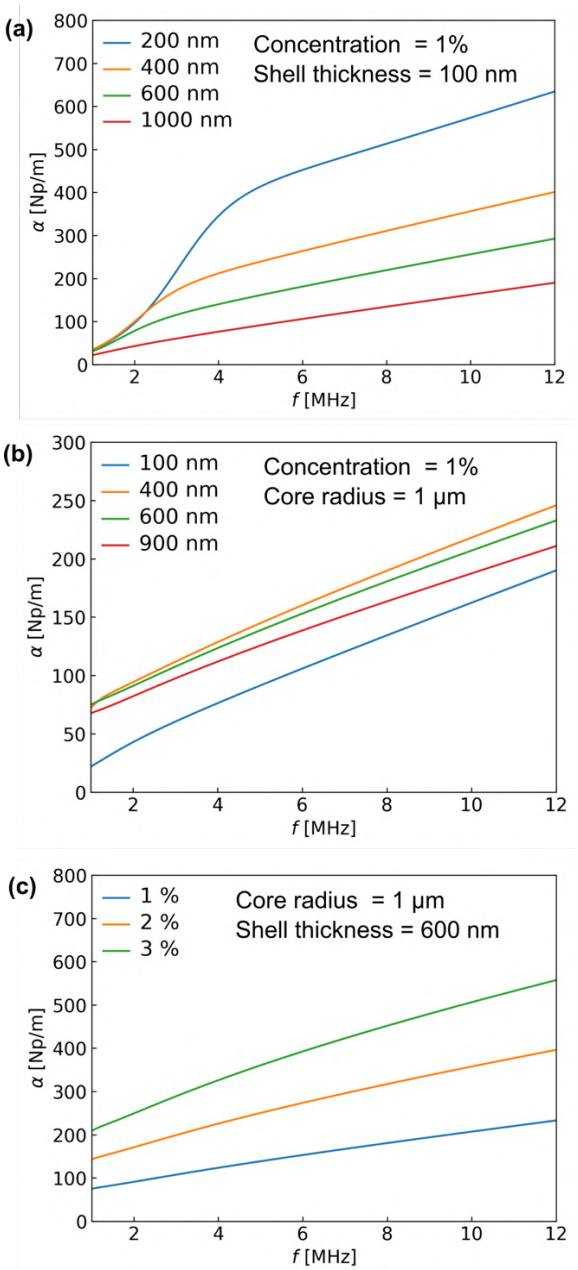

Figure 2 The calculated ultrasound attenuation spectra based on core–shell model for the Pickering droplets stabilized by magnetic nanoparticles and distributed in agar phantom for (a) different liquid core radii, (b) different particle shell thicknesses, and (c) different volume concentrations.

The results in **Figure 2** show the attenuation value strongly depends on the different parameters such as silicone oil droplet radius, particle shell thickness, and concentration. Then, controlling these parameters might optimize the ultrasound heating. Interestingly, the Pickering nanodroplets with a size of 200 nm show higher ultrasound attenuation compared with larger droplets (1 μm) at constant concentration and shell thickness (**Figure 2a**) for frequencies higher than 2.5 MHz. However, the ultrasound scattering theory based on ECAH showed no significant increase in the ultrasound attenuation with different size of silicone droplets when were

dispersed in castor oil [47]. Additionally, the core–shell model for oil-in-oil magnetic Pickering emulsion, when silicone droplets were stabilized with magnetic particles, showed a maximum for ultrasound attenuation increase for 500-nm radius of the droplet [23]. Here, the physical properties of the agar phantom contributed to the calculation as well as the nano-size of the Pickering droplet. We expected that the thermal contrast contribute to ultrasound attenuation higher in the case of nanoscale objects. This is the reason why the non-thermal core–shell model needs to be investigated (**Figure 3**).

The ultrasound attenuation is also affected by the shell thickness of magnetic particles around the silicone droplets. There is a significant increase in the attenuation between 100-nm and 400-nm size of the shell as presented in **Figure 2b**. Additionally, the theoretical result showed no significant differences between the 400-nm and 900-nm shell thicknesses in ultrasound attenuation in this range of frequency from 1 -12 MHz. **Figure 2c** shows the change in the ultrasound attenuation with different ranges of volume concentration. The higher volume concentration had a larger contribution to the ultrasound attenuation, with around 200 Np/m difference between 1% and 2%.

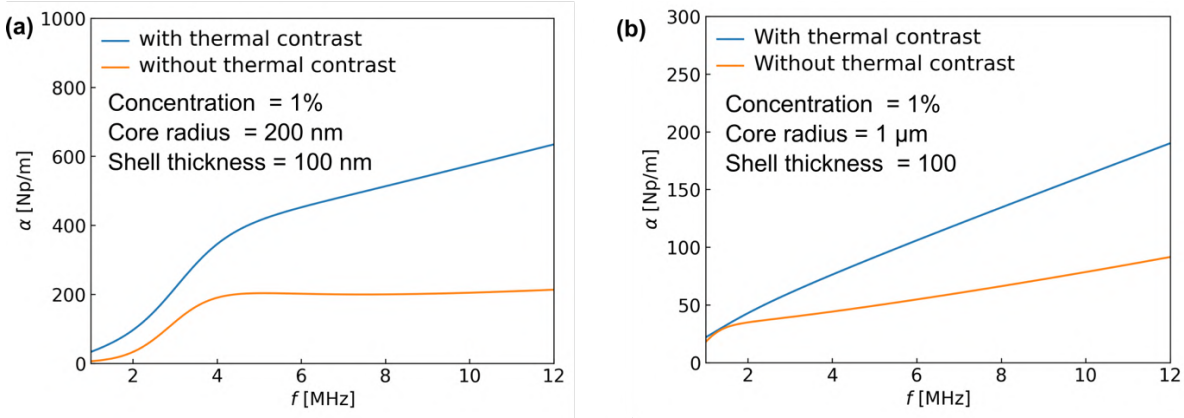

Figure 3 The calculated ultrasound attenuation spectra based on core–shell model including thermal contribution and without including thermal contribution in the core–shell model for Pickering (a) nanoemulsion, and (b) microemulsion.

The results in **Figure 3** show that thermal contribution has a higher impact on ultrasound attenuation for Pickering droplets with a core radius of 200 nm and shell thickness of 100 nm compared with the micro-size Pickering droplets (1 μm droplet radius) when dispersed in an agar gel. For nano-size droplets, the calculations of core-shell model should be done including thermal contrast between phases to provide better accuracy of the results. The thermal and viscous loss did not make linear changes in the ultrasound attenuation to corresponding particles or droplets sizes.

The values of ultrasound velocity in the function of frequency also depended on the Pickering droplet sizes and were required in further COMSOL simulation. The velocity increased with both the increasing radius of droplets and the thickness of the particle shell as shown in **Figure 4a-b**. Interestingly, the velocity of agar phantom doped with Pickering droplets was lower than the ultrasound velocity in pure agar which was 1546 m/s (**Table 1**). The ultrasound velocity was also

influenced by the volume concentration of droplets. The change in the compressibility contrasts with different radii and shell thicknesses influences the velocity value resulting in these differences shown in **Figure 4c**. In a magnetic fluid, the ultrasound velocity also exhibited a similar trend depending on the concentration and temperature [48].

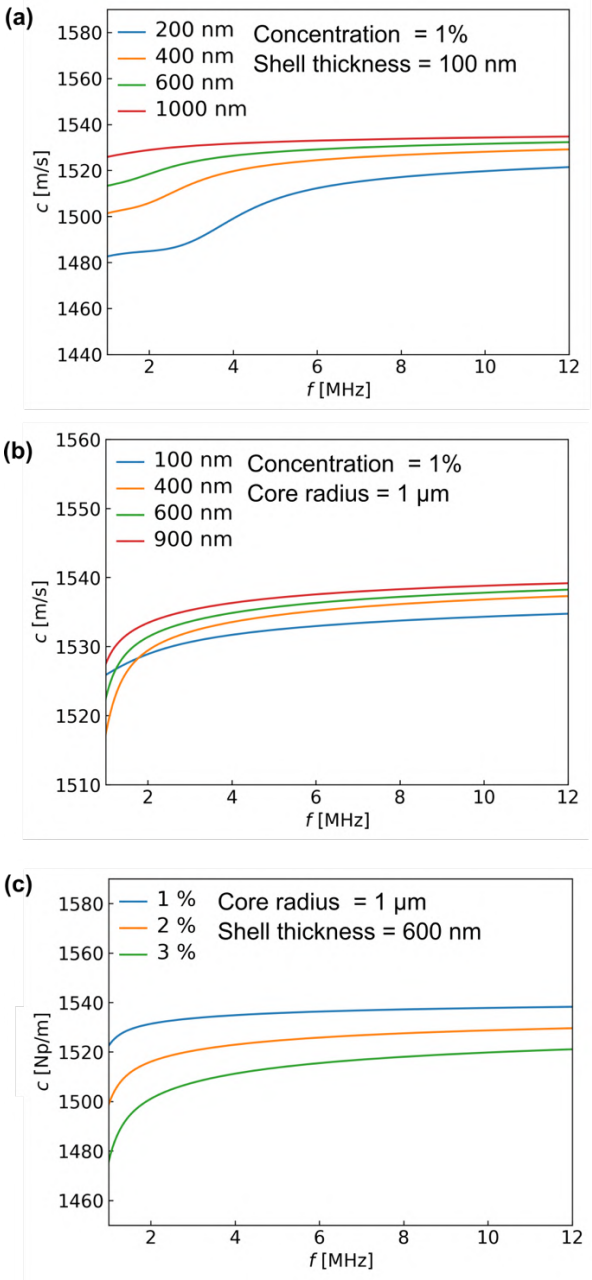

Figure 4 The calculated ultrasound velocity in the function of frequency based on core–shell model for the Pickering droplets stabilized by magnetic nanoparticles and placed in agar phantom for (a) different core radii (b) different shell thicknesses, and (c) different volume concentrations

3.2. Attenuation spectra of Pickering droplets stabilized by silica nanoparticles in an agar phantom

One of the most important feature of the Pickering droplets is that, in practice, they could be prepared with a variety of materials used as particle stabilizers. Here, we provide the comparison between the Pickering droplets stabilized with magnetic (Section 3.1) and non-magnetic (silica) nanoparticles to show how they change the ultrasound attenuation based on core–shell model when distributed in the agar phantom. The formation and functionalization of silica particles are quite well investigated and they have been widely used in medical applications such as drug delivery [49] and bioimaging [50]. Using them as stabilizers could extend the Pickering droplet application [51,52].

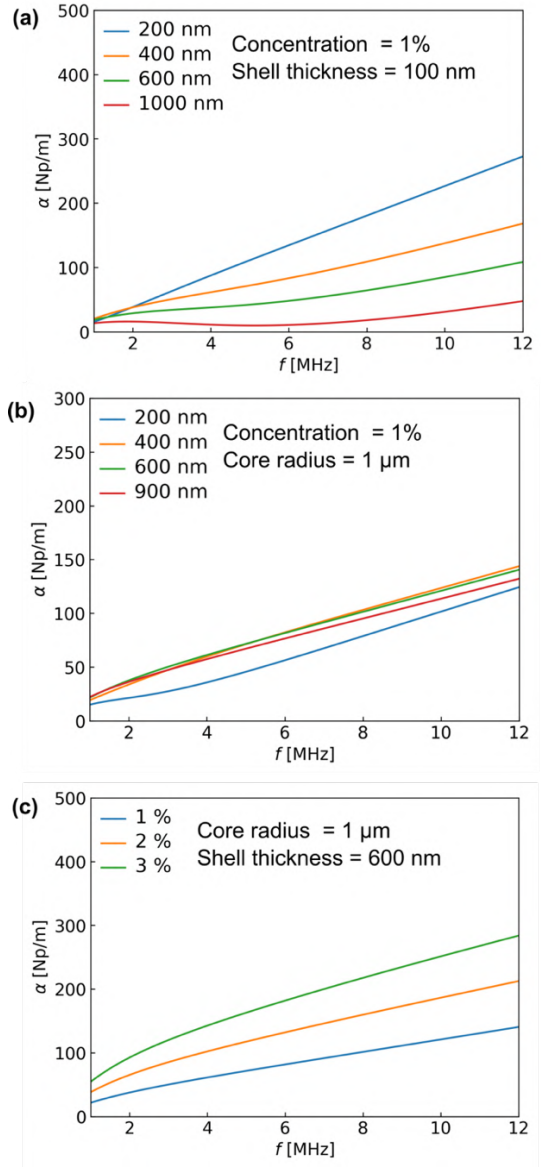

Figure 5 The calculated ultrasound attenuation spectra based on core–shell model for the Pickering droplets stabilized by silica nanoparticles and distributed in agar phantom for (a) different liquid core radii, (b) different particle shell thicknesses, and (c) different volume concentrations.

The ultrasound attenuation value of the Pickering droplets distributed in the agar phantom and stabilized by silica nanoparticles (**Figure 5**) was lower compared to the ultrasound attenuation of Pickering droplets stabilized by magnetite nanoparticles as shown in **Figure 3**. Furthermore, the value of ultrasound attenuation decreased for the micro-droplets (core diameter of 1 μm) when comparing to those with a core of 200 nm as presented in **Figure 5a**. Attenuation coefficient values were generally lower when compared to magnetic nanoparticles with the exact same conditions such as core and shell sizes, volume concentration, and the range of frequencies. The main reason was the difference in physical properties between silica and magnetic nanoparticles such as density and thermal contrast (**Table. 1**). This made Pickering droplets coated by magnetic nanoparticles more attenuating material compared to those stabilized with the silica nanoparticles. That was even more clear in lower range of frequencies (e.g., for 2 MHz), which was important as this range of frequency is used in various medical applications [53].
Additionally, the influence of shell thickness on ultrasound attenuation records significant changes between 200 nm and 400 nm (**Figure 5b**). Interestingly, the values of attenuation coefficient are quite similar for thicknesses of particle layer between 400 nm and 900 nm with constant droplet radius of 1 μm and concentration of 1%. Similarly to the results obtained for magnetic nanoparticles, the increase in the volume concentration also provided higher attenuation in the ultrasound wave as presented in **Figure 5c.**

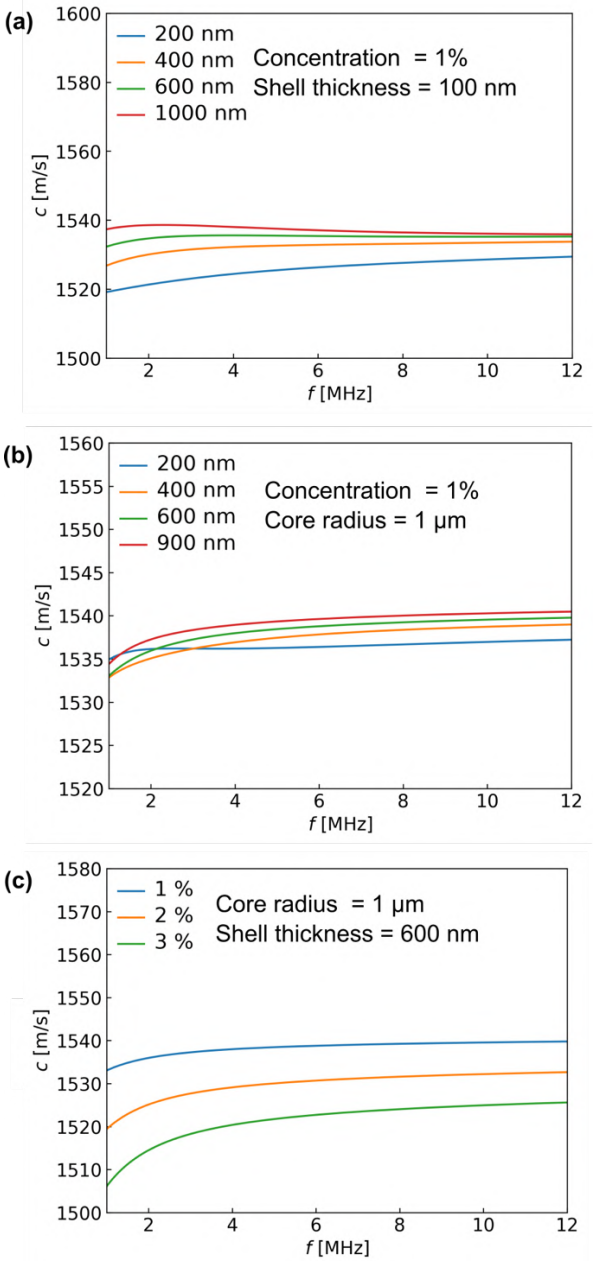

Figure 6 The calculated ultrasound velocity in the function of frequency for the Pickering droplets stabilized by silica nanoparticles and distributed in agar phantom for (a) different core radii (b) different shell thicknesses, and (c) different volume concentrations.

The Pickering emulsions stabilized with silica nanoparticles showed a change in the velocity values for various droplet sizes (**Figure 6a**) and shell thicknesses (**Figure 6b**). These values were higher than those calculated for magnetic nanoparticles stabilizing the droplets due to the difference in the compressibility contrast between phases when these two types of particles were considered (their shear modulus and ultrasound velocity). Furthermore, the higher volume concentrations revealed a lower value of ultrasound velocity in the frequency function (**Figure 6c**), which reflects the same trend as for the results for the magnetic Pickering droplets.

3.3. Computer simulation

3.3.1. Ultrasound heating of the pure agar phantom

In our approach, as shown in the scheme in **Figure 1**, the ultrasound waves generated by the transducer propagate through the water first and then entering the agar phantom. As an entry point, the simulation of ultrasound propagation was performed for pure agar phantom with different frequencies (1, 2, 5, and 10 MHz). The chosen frequencies are within the typical ultrasound diagnostic range (1-15 MHz). It should be noted that the level of accuracy of a wave propagation model is influenced by mesh density or, in other words, the number of elements per wavelength. The result for 5 elements per wavelength was chosen for the acoustic and thermal study [45].

Table 2 The physical properties of the pure agar phantom and water used in the COMSOL simulation.

Parameters	Agar phantom	Water
Density ρ (kg/m^3)	1040 [35]	997 [37]
Thermal conductivity κ (W/m · K)	0.616 [35]	0.5952 [37]
Specific heat c_p (J/KgK)	3900 [38]	4179 [37]
Velocity *c* (m/s)	1547 [40]	1496.7 [37]
Atteuation α (Np/m) (1 MHz)	4.69 [40]	0.025 [54]
Atteuation α (Np/m) (2 MHz)	9.55 [40]	0.22 [54]
Atteuation α (Np/m) (5 MHz)	25.2 [40]	0.63 [54]
Atteuation α (Np/m) (10 MHz)	54.75 [40]	2.5 [54]

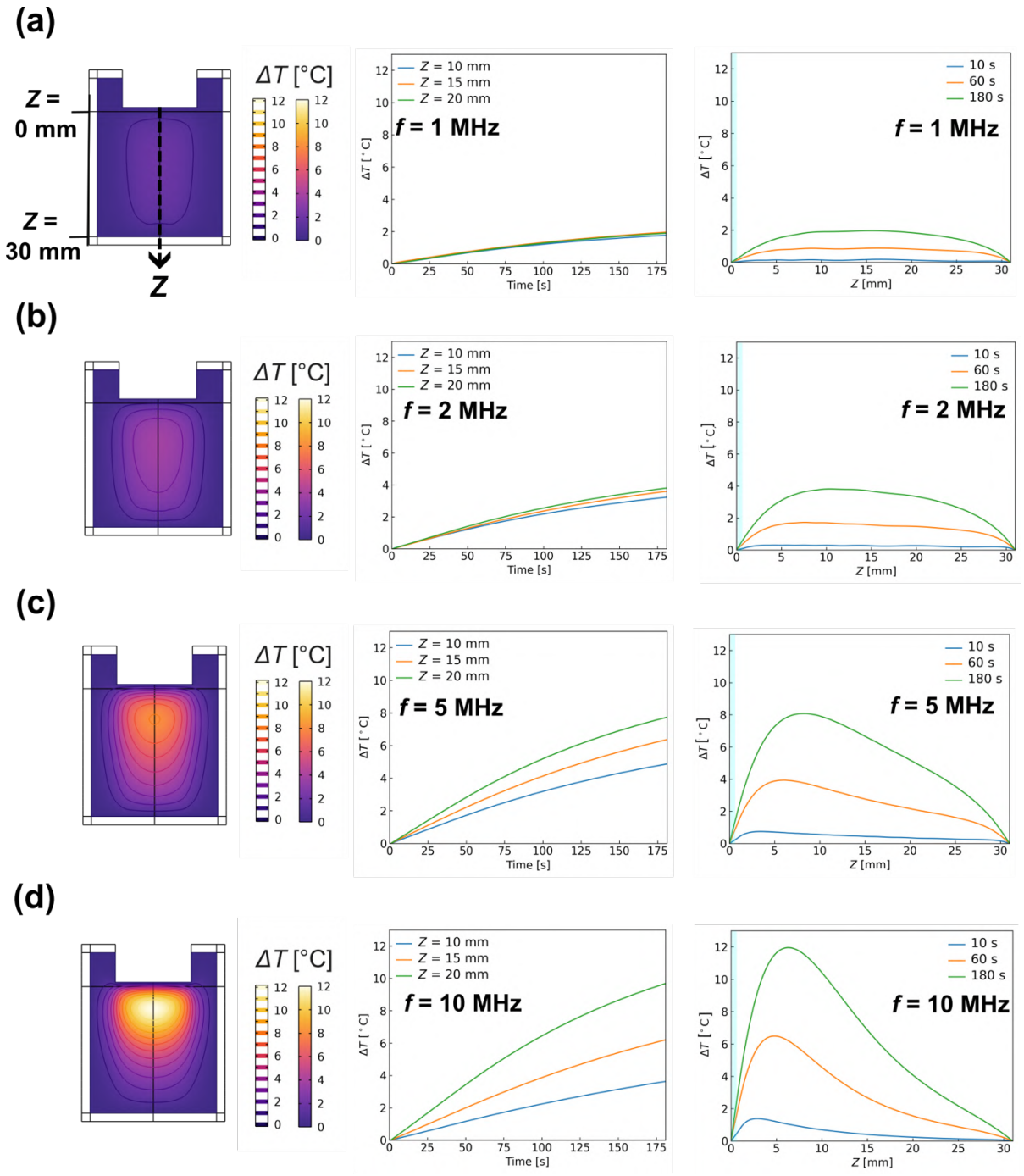

Figure 7 The COMSOL simulation results of ultrasound heating for the pure agar phantom. The heat map illustrates the temperature change in the middle of the cylindrical agar phantom after 180 seconds. Furthermore, the variations in temperature over time are showcased for three distinct *Z* positions (10 mm, 15 mm, and 20 mm), and the temperature changes are presented in relation to *Z* for selected sonication times (10 s, 60 s, and 180 s) at frequencies of (a) 1 MHz, (b) 2 MHz, (c) 5 MHz, and (d) 10 MHz.

Figure 7a-d presents the change in temperature within pure agar phantom for different vertical positions (10 mm, 15 mm, and 20 mm) and different application times (10s, 60s, and 180s) for frequencies of 1 MHz, 2 MHz, 5 MHz, and 10 MHz. Moreover, the heat maps, i.e., the spatial distribution of the temperature elevation, were presented for the 180th second of ultrasound application. In the heat maps, the Z = 0 mm represents the phantom in the transducer side, and Z = 30 mm represents the end of the agar phantom (see, **Figure 1**). The physical properties of the water and agar phantom used for simulation were as listed in **Table 2**. As one can see, the relative temperature (i.e., the temperature rise related to the room temperature of 25 °C) in the center (Z = 15 mm) of the phantom model was higher for higher ultrasound frequency; the temperature increase was of 6 °C for 10 MHz compared to 3.5 °C as shown in **Figure 7d**. Subsequently, temperature distribution was more homogenous for lower frequencies as shown both in temperature versus time and temperature versus height graphs depicted in **Figure 7a-b**. Generally, it indicates higher depth with better temperature homogeneity can be achieved within the lower frequency range (**Figure 7a-b**). One can see that the ultrasound waves of higher frequencies such as 10MHz and 5 MHz can be used to raise the temperature two times more compared with the lower frequencies over a short distance. In general, each frequency range can be used in different applications depending on the penetration depth required. The provided simulation results indicate that using ultrasound of different frequencies improved control of the penetration depth by changing frequency of the ultrasound wave. The range of ultrasound in the tissue can be changed from 1 cm to 12 cm by changing the frequencies from 1 MHz to 10 MHz as well as tissue properties [42]. Nevertheless, as we will demonstrate in the next section, achieving more precise control over the temperature increase in the phantom is feasible when the properties of the sonosensitizers incorporated into the phantom are taken into account.

3.3.2. Ultrasound heating of agar phantom with inclusion agar phantom doped with magnetite Pickering droplets.

The agar phantom with a spherical inclusion doped by magnetic Pickering droplets was simulated using COMSOL. Various physical properties were considered for the spherical inclusion, including thermal and acoustic properties. The ultrasound scattering theory based on the core–shell model provided the ultrasound attenuation and velocity values in the function of frequency for different core radii and shell thicknesses. The 2 MHz frequency and 1% volume concentration of Pickering droplets were set as constant in the simulation. The focus was on evaluating the different droplet radii and shell thickness of Pickering droplets for more efficient heat generation within the inclusion inside agar phantom.

MG 1 and MG 2 were samples of magnetite-stabilized Pickering droplets. They had a consistent shell thickness of 100 nm, but their core radii differed, with MG 1 having a core radius of 200 nm and MG 2 having a core radius of 1 μm. MG 3 and MG 4 were samples with a constant Pickering droplet radius of 1 μm, but with varying shell thicknesses: 400 nm for MG3, and 900 nm for MG4. The physical properties of these samples implemented in the simulation are presented in **Table 3**.

The additional materials dispersed in the phantom change its properties that are need for the simulation of the temperature distribution. Apart from the changed attenuation and velocity depending on frequency determined based on core-shell model (Section 3.1), also the effective

density and the effective specific heat were determined based on a weighted average of respective values for phases. Effective density can be calculated using the formula:

$$\rho_{eff} = (\phi_1 \times \rho_1) + (\phi_2 \times \rho_2) + (\phi_3 \times \rho_3), \quad (12)$$

where ρ_1, ρ_2, and ρ_3 refer to the density of agar phantom, silicone oil, and particle stabilizer, respectively and are multiplied by the volume concentration of each phase ϕ.
Similarly, the weighted average of specific heat in agar phantom with Pickering droplets was calculated as:

$$C_{p1} = (\phi_1 \times C_{p1}) + (\phi_2 \times C_{p2}) + (\phi_3 \times C_{p3}). \quad (13)$$

The C_{p1}, C_{p2}, and C_{p3} are related to the specific heat of agar phantom, silicone oil, and particle stabilizer, respectively and multiplied by the volume concentration of each phase ϕ.
The weighted average of the thermal conductivity of two phases can be calculated from **Equation 14a** (as used in [55] to calculate the thermal conductivity of an oil-in-water emulsion):

$$k_{eff} = k_1 \frac{1+2\phi\chi-2(1-\phi)\xi\chi^2}{1-\phi\chi-2(1-\phi)\xi\chi^2}, \quad (14a)$$

where

$$\chi = \frac{k_2-k_1}{k_2-2k_1}, \quad (14b)$$

$$\xi = 0.21068\phi - 0.04693\phi^2. \quad (14c)$$

Here, *k* and ϕ represent the thermal conductivity and volume concentration, respectively.

Table 3 The physical properties of agar phantom with magnetic Pickering droplets for samples MG 1 and MG 2 (constant shell thickness of 100 nm and core radii 200 nm and 1 μm, respectively) and MG 3 and MG 4 (constant core radius of 1 μm and different shell thicknesses of 400 nm and 900 nm, respectively). The parameters are provided for a constant temperature of 25 °C.

Parameters / Phases	**Density, ρ (kg/m^3)**	**Thermal conductivity, κ (W/mK)**	**Specific heat, C_p (J/kg · K)**	**Velocity, *c* (m/s)**	**Atteuation, α (Np/m)**
Agar phantom	1040 [35]	0.616 [35]	3900 [38]	1547 [40]	9.55 [40]
Water	997 [37]	0.5952 [37]	4179 [37]	1496.7 [37]	0.1 [54]
MG 1	1080.6	0.975	3843.13	1484.8	96.21
MG 2	1080.6	0.975	3843.13	1528.8	42.8
MG 3	1080.6	0.975	3843.13	1529.4	94.28
MG 4	1080.6	0.975	3843.13	1533.4	82,18

In real medical application, the ultrasound wave generated from the transducer must travel through multiple tissue layers such as skin, fat, and muscle. Therefore, controlling low changes in the temperature in these layers is important to leave healthy tissue untouched. A frequency of 2 MHz can be used for this purpose due to the homogeneous temperature change in the system with a longer penetration depth as shown in **Figure 7b.**

Figure 8 shows the dependence of the temperature on the duration of the ultrasound wave application with the different positions in the agar phantom (10 mm, 15 mm, and 20 mm). Additionally, the dependence of the relative temperature at different heights within the agar phantom for different durations of ultrasound exposition (10 seconds, 60 seconds, and 180 seconds) for MG 1 and MG 2 samples. These samples showed the influence of the different core radii 200 nm and 1 μm of magnetic Pickering droplets, at a constant shell thickness of Pickering droplet of 100 nm and volume concentration of 1%.

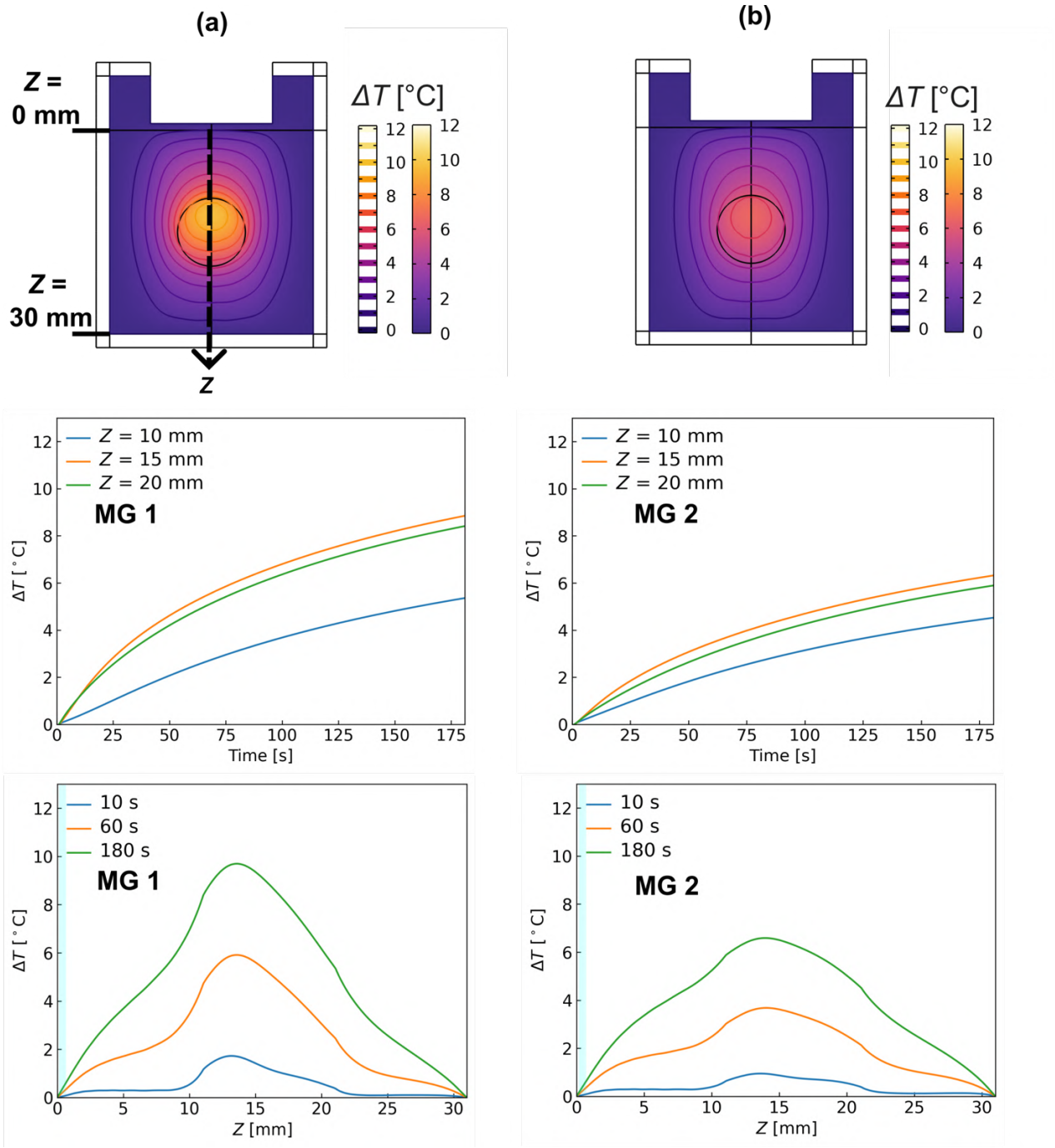

Figure 8 The COMSOL simulation results of ultrasound heating for pure agar phantom with spherical inclusion filled with magnetic Pickering droplets for (a) MG 1 (magnetite–stabilized Pickering droplets with a shell thickness of 100 nm and core radius 200 nm) and (b) MG 2 (magnetite–stabilized Pickering droplets with a shell thickness of 100 nm and core radius 1 μm). The 2 MHz frequency and 1% volume concentration were set as constant in the simulation. The spherical inclusion on the heat map represents a doped agar phantom at 180th seconds from sonication. The blue area represents the coupling medium (water).

Figure 8a presents the results for the agar phantom doped with nano-size of Pickering droplets with a core radius of 200 nm and shell thickness of 100 nm. The part of agar phantom with

distributed Pickering droplets (spherical inclusion) was placed in the center of the pure agar phantom, 10 mm away from the transducer position (see, **Figure 1b**). The temperature change in the agar phantom after 180 seconds above the spherical inclusion (*Z* = 2 mm) was 1.8 °C and below the inclusion (at the position of *Z* = 28 mm) was around 1.4 °C, which corresponded to the temperature rises at 2 MHz frequency. However, as shown in **Figure 7b**, the maximum change in the temperature was around 1.6 °C for *Z* = 2 mm and 1.6 °C for *Z* = 28 mm. Moreover, the insertion of magnetic Pickering droplets in the spherical inclusion resulted in a reduction of the penetration depth below the spherical inclusion and the creation of a shadow effect. The temporal evolution of the heat map between 0 and 180th second of sonication for MG 1 sample is also presented in **Supplementary Materials (Movie S1)**.

Furthermore, at Z = 8 mm (2 mm above the inclusion), there are rising temperature changes (around 5.3 °C) due to the heat transfer from the inclusion itself as shown in **Figure 8a**. Inside the spherical inclusion, the gradient of the temperature change appeared, which was higher at the beginning of spherical inclusion till achieved the maximum at *Z* = 13.5 mm with a change in the temperature of 9.6 °C, and then started to decrease as presented in the change of the temperature in the function of *Z* in **Figure 8a**. In the case of the MG 2 (**Figure 8b**), the temperature increase in spherical inclusion was lower compared to the results for phantom doped with smaller droplets due to the reduction in ultrasound absorption value presented in **Figure 2a**. The highest change in the temperature of 6.5 °C was recorded at *Z*=14 mm. This led to lower heat transfer to the pure agar phantom around the inclusion compared to **Figure 8a**. Therefore, the temperature record at Z = 8 mm was 4.4 °C and for Z = 22 mm was 3.8 °C. As it was for MG 1 sample, the temporal evolution of the heat map between 0 and 180th second of sonication for MG 2 sample is presented in **Supplementary Materials (Movie S2)**. It is also worth noting that, when ultrasound heating efficiency was experimentally investigated for tissue-mimicking materials doped with magnetic micro- and nanoparticles instead of Pickering droplets, nanoparticles exhibited also higher attenuation and a greater temperature rise [56].

The influence of different shell thicknesses in Pickering emulsions stabilized with magnetic particles was also investigated for a constant core radius of 1 μm and concentration of 1%. The simulation results showed no significant changes in the relative temperature when different shell thicknesses were considered for MG 3 (**Figure 9a**) and MG 4 (**Figure 9b**). The Pickering droplets with shell thickness of 900 nm showed a bit lower attenuation compared to those with the 400-nm particle layer as shown before in **Figure 2b**. However, the temperature rise was lower for thinner shells, e.g., when 100-nm 400-nm size were compared, as corresponding to ultrasound attenuation in **Figure 2b**. This is related to the monotonous change in the ultrasound attenuation with the size of scattered objects. Therefore, determining the relation between the object size and wavelength of ultrasound waves could help to improve enhancement of the thermal efficiency during sonication provided by sonosensitizers.

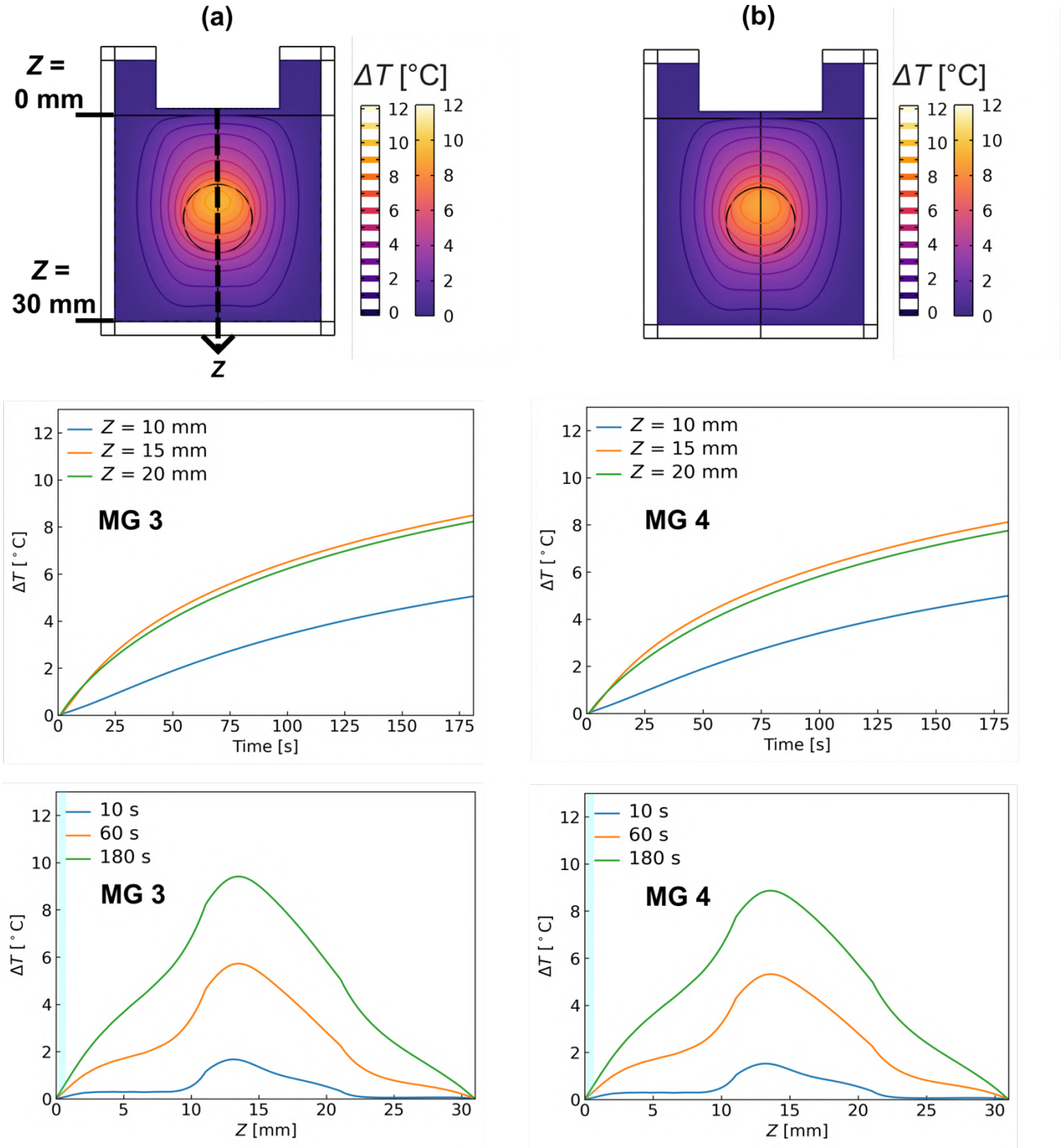

Figure 9 The COMSOL simulation results of ultrasound heating for pure agar phantom with spherical inclusion filled with magnetic Pickering droplets for (a) MG 3 (magnetite–stabilized Pickering droplets with a shell thickness of 400 nm and core radius 1 μm) and (b) MG 4 (magnetite–stabilized Pickering droplets with a shell thickness of 900 nm and core radius 1 μm). The 2 MHz frequency and 1% volume concentration were set as constant in the simulation. The spherical inclusion on the heat map represents a doped agar phantom at 180th seconds from sonication. The blue area represents the coupling medium (water).

3.3.3. Ultrasound heating of agar phantom based on silica Pickering droplet.

As mentioned in Section 3.2, silica nanoparticles are one of the most attractive nanoparticles due to their biocompatible and ease of functionalizing in terms of surface chemistry [57]. That is why, as an example of non-magnetic material, silica nanoparticles were used to stabilize silicone oil Pickering droplets incorporated into the agar phantom with spherical inclusion. The weighted average of the density, specific heat, and thermal conductivity of the doped agar phantom was calculated based on the physical properties of both pure agar and silica nanoparticles using **Equations 12-14**. The ultrasound scattering theory based on the core–shell model was used to calculate ultrasound attenuation and velocity with different core radii and shell thicknesses. As it was for Pickering emulsions stabilized with magnetic nanoparticles, the 2 MHz frequency and 1% volume concentration were set as constant in the simulation.

SI 1 and SI 2 were samples of silica-stabilized Pickering droplets. They had a consistent shell thickness of 100 nm, but their core radii differed, with SI 1 having a core radius of 200 nm and SI 2 having a core radius of 1 μm. In turn, SI 3 and SI 4 were samples of Pickering droplets with constant droplet radius (1 μm) and different shell thicknesses: 400 nm for SI 3, and 900 nm for SI 4. The physical properties of these samples are presented in **Table 4**

Table 4 The physical properties of agar phantom with silica-stabilized Pickering droplets for SI 1 and SI 2 samples (constant shell thickness of 100 nm and core radii 200 nm and 1 μm, respectively) and SI 3 and SI 4 samples (constant core radius of 1 μm and different shell thicknesses of 400 nm and 900 nm, respectively). The parameters were provided for at a constant temperature of 25 °C.

Parameters / Phases	**Density**, ρ **(kg/m^3)**	**Thermal conductivity**, κ **(W/mK)**	**specific heat** , C_p**(J/KgK)**	**Velocity,** c **(m/s)**	**Atteuation**, α **(Np/m)**
Agar phantom	1040 [35]	0.616 [35]	3900 [38]	1547 [40]	9.55 [40]
Water	997 [37]	0.5952 [37]	4179 [37]	1496.7 [37]	0.1 [54]
SI 1	1048.5	0.975	3842.8	1521.3	38.50
SI 2	1048.5	0.975	3842.8	1538,5	15.86
SI 3	1048.5	0.975	3842.8	1535.05	33.79
SI 4	1048.5	0.975	3842.8	1537.25	36.24

The simulation results in **Figure 10** show the effect of inserting nano- and micro-size Pickering droplets with a constant shell thickness of silica nanoparticles and volume concentration of 1%. **Figure 10a** indicates a higher change in the temperature observed for Pickering droplets with a core radius of 200 nm and shell thickness of 100 nm (sample SI 1).

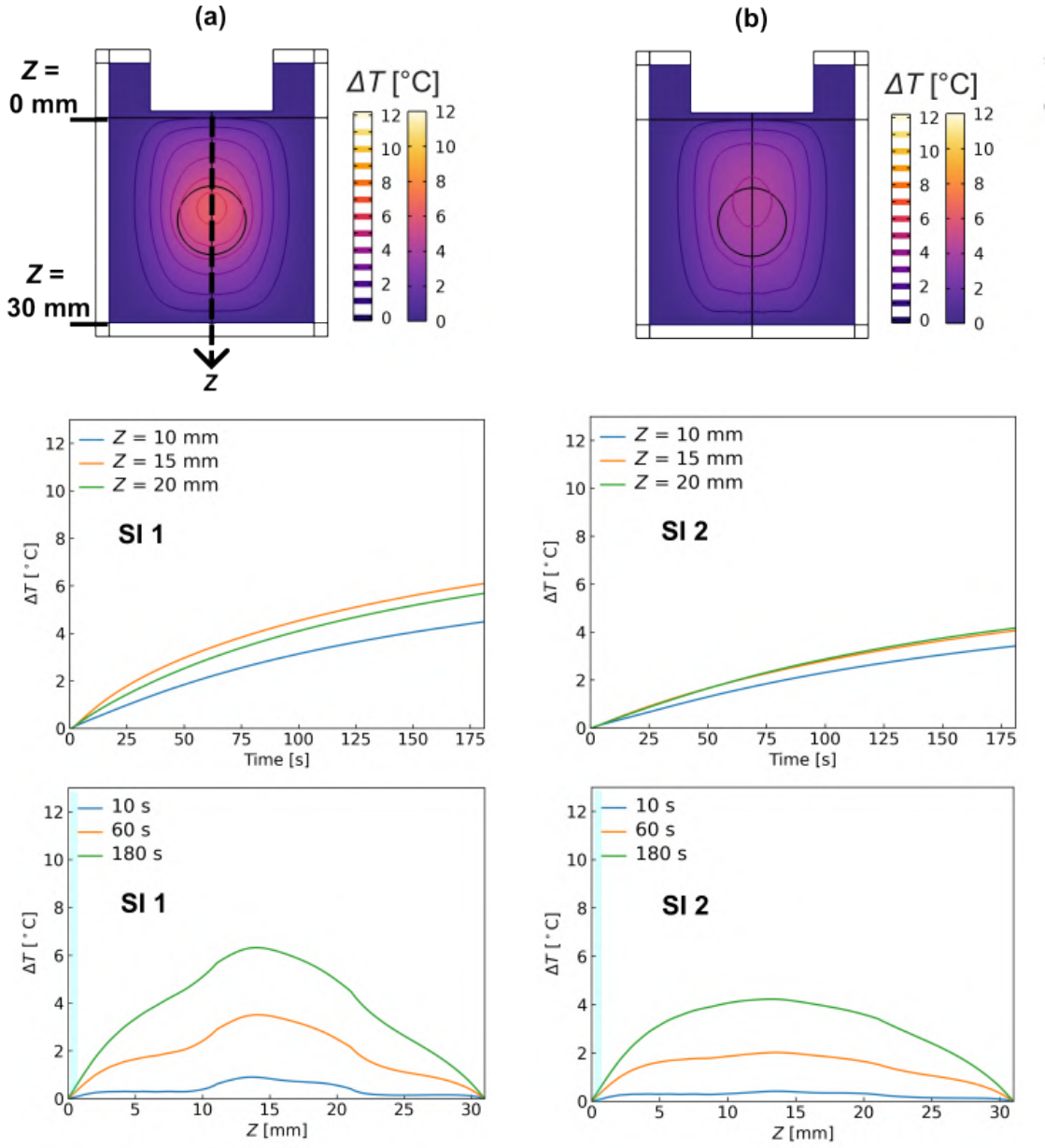

Figure 10 The COMSOL simulation results of ultrasound heating for pure agar phantom with spherical inclusion filled with Pickering droplets for (a) SI 1 (silica–stabilized Pickering droplets with a shell thickness of 100 nm and core radius 200 nm) and (b) SI 2 (silica–stabilized Pickering droplets with a shell thickness of 100 nm and core radius 1 μm). The 2 MHz frequency and 1% volume concentration were set as constant in the simulation. The spherical inclusion on the heat map represents a doped agar phantom at 180th seconds from sonication. The blue area represents the coupling medium (water).

The temperature increased gradually in the spherical inclusion filled with silica-stabilized Pickering droplets. The highest relative temperature of 6.3 °C was recorded close to the center of the inclusion at Z = 14.2 mm. This is correlated with the increase in the ultrasound attenuation of 200 nm core radius and shell thickness of 100 nm (**Figure 5a**). The decreasing

ultrasound attenuation with a core radius of 1 μm and shell thickness of 100 nm (**Figure 5b**) led to the reduction of the temperature elevation in the spherical inclusion as shown for the SI 2 sample in **Figure 10b**. The overall temperature of the SI 2 sample was close to this shown for pure agar phantoms **Figure 7b** as well as the ultrasound attenuation presented of the SI 2 sample in **Table 4 was** close to the ultrasound attenuation of pure agar phantom presented in **Table 1**.

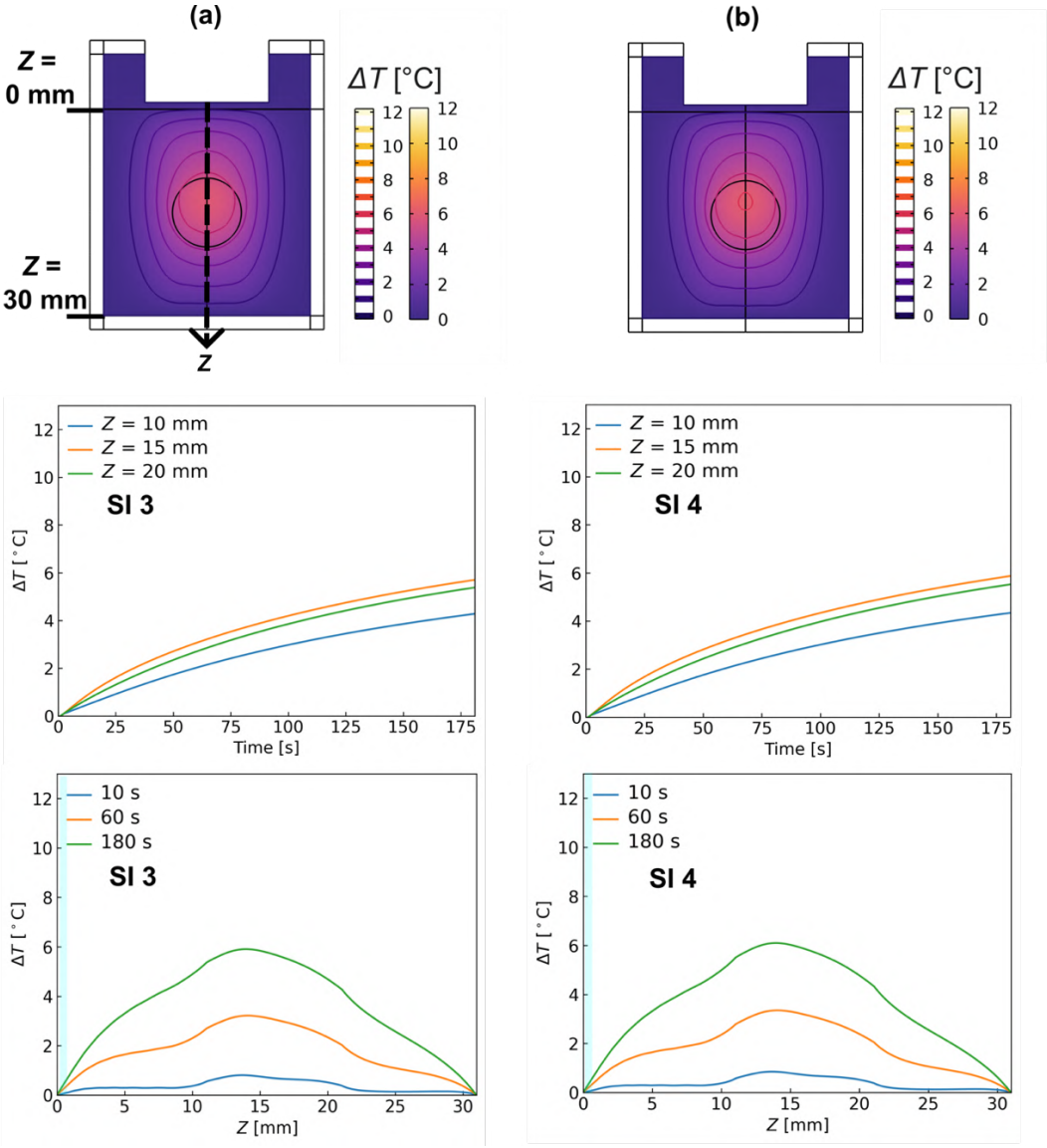

Figure 11 The COMSOL simulation results of ultrasound heating for pure agar phantom with spherical inclusion filled with Pickering droplets for (a) SI 3 (silica–stabilized Pickering droplets with a shell thickness of 400 nm and core radius 1 μm) and (b) SI 4 (silica–stabilized Pickering droplets with a shell thickness of 900 nm and core radius 1 μm). The 2 MHz frequency and 1% volume concentration were set as constant in the simulation. The spherical inclusion on the heat map represents a doped agar phantom at 180th seconds from sonication. The blue area represents the coupling medium (water).

Figure 11 presents the simulation results with different shell thicknesses of silica nanoparticles with a constant droplet core radius of 1 μm at a constant volume concentration of 1%. Both samples SI3 and SI4 show comparable results. The maximum change in the relative temperature for SI 3 was 5.9 °C at Z = 14.2 mm. In contrast, the maximum change in the temperature of SI 4 was 6.09 °C at Z = 14.2 mm. Moreover, there is also no significant change in the ultrasound attenuation between SI 3 and SI 4 samples presented in **Table 4**.

The results show the different object sizes as well as different physical properties of the system have a direct impact on the ultrasound wave scattering and absorption. In the literature, nano-size emulsions with a mean diameter of 260 nm have been used to enhance the bio-effect of high-intensity focused ultrasound [58]. The nano-emulsion also provided efficient and controllable thermal ablation by using short pulses of high-intensity ultrasound wave 19 $\mathrm{W/cm^2}$ tested in vitro [59]. Furthermore, the ultrasound wave application to the system doped with microbubbles was used recently for enhanced ultrasound thermal therapy [60,61]. The heat generation biologically changed the oxidation and the blood flow in the body leading to better treatment performance by following the radiotherapy with lower wave intensity. From practical point of view, one should expect that the penetration of sonosensitizing material will be higher at the nanoscale compared to the microscale. For this reason, the application of the microbubbles in thermal therapy was limited. However, there still remains the path for using nano-sized Pickering droplets that, as we showed, could enhance the thermal effect of applied ultrasound.

The simulation results showed the possibility of using magnetite and silica Pickering droplets as sonosensitizers to enhance the thermal therapy as an alternative to the nanoparticles. The capsulated structure of Pickering droplets can be beneficial to combine two types of treatment when the droplet contains specific medical drugs. As mentioned in the Introduction, the control to release the cargo with additional temperature rise could be achieved by ultrasound wave [14]. The efficiency of such process may be controlled by determining specific Pickering droplet size. Additionally, the localized or general hyperthermia treatment could be achieved using different types of transducers. The local sphere doped by nano- or microdroplets showed an increase in the temperature locally by using a non-focused ultrasound beam with a constant intensity of 2.5 $\mathrm{W/cm^2}$ and a frequency of 2 MHz within penetration depth of 1 cm (**Figure 8, and 9)**. Using specific physical parameters of Pickering emulsions i.e., droplet size distribution that can be obtained by optimization of the process of preparation, for instance, by using different concentrations of stabilizing particles, it is possible to optimize both the maximum temperature elevation and the distribution over the tissue (or tissue-like phantom). Different particle materials provide different contrasts between phases that, along with the size of droplets, contribute mostly to the overall acoustic energy dissipation according to core-shell model of Anson and Chivers.

4. Conclusion

In this study, both the computational approach and the numerical simulation provided a way to effectively investigate the heat generation inside the pure agar phantom including spherical inclusion doped with magnetite and silica-stabilized Pickering droplets induced by ultrasound wave of the intensity of 2.5 W/cm^2. The ultrasound attenuation and velocity of the agar phantom with Pickering droplets were calculated theoretically based on core–shell model. The influence of different radii and shell thicknesses of Pickering droplets on the acoustic properties was investigated. Significantly reduced ultrasound attenuation was observed with silica-based Pickering droplets compared to those stabilized with magnetite from 96.2 Np/m of magnetite (sample MG 1) to 38.5 Np/m of silica (sample SI 1) at the frequency of 2 MHz. The main reason was the varying contribution of density contrast between phases to overall attenuation. Interestingly, the calculation showed the ultrasound attenuation of the nanoemulsion (sample MG 1) was above twice higher than microemulsion (sample MG 2) in the case of magnetite particles used as stabilizers.

Numerical simulations further illustrated the impact of parameters of Pickering droplets on temperature changes within the agar phantom. Both magnetite and silica Pickering droplets dispersed in spherical inclusions exhibited higher ultrasound attenuation compared to the pure agar phantom. Notably, a greater temperature change was recorded for nanodroplets (the highest temperature change of 9.6 °C close to the center of the inclusion) than microdroplets when simulated droplets had a constant shell thickness of 100 nm, volume concentration of 1%, and ultrasound frequency was 2 MHz.

The droplet radius and shell thickness emerged as crucial factors influencing the simulated ultrasound heating efficiency. The precise control of these parameters, aligned with the ultrasound frequency and physical properties of the system, holds the key to enhancing thermal performance. This study emphasizes the importance of tailoring droplet characteristics to optimize the efficiency of ultrasound-induced thermal effects.

CRediT authorship contribution statement

Bassam Jameel: Investigation, Formal analysis, Visualization, Writing – original draft. **Yaroslav Harkavyi**: Investigation, Simulation, Writing–Review & Editing, **Rafał Bielas**: Methodology, Supervision, Writing–Review & Editing **Arkadiusz Józefczak**: Conceptualization, Methodology, Supervision.

Declaration of Competing Interests

There is no conflict of interest to declare.

Acknowledgments

This work was supported by the project no. 2019/35/O/ST3/00503 (PRELUDIUM BIS) and OPUS (Grant No. 2019/33/B/ST5/00935) of the Polish National Science Centre. The authors wish to thank Prof. Tomasz Hornowski for the valuable discussions and suggestions

References

1. Hildebrandt, B. The Cellular and Molecular Basis of Hyperthermia. *Crit. Rev. Oncol. Hematol.* **2002**, *43*, 33–56, doi:10.1016/S1040-8428(01)00179-2.
2. Kok, H.P.; Cressman, E.N.K.; Ceelen, W.; Brace, C.L.; Ivkov, R.; Grüll, H.; Ter Haar, G.; Wust, P.; Crezee, J. Heating Technology for Malignant Tumors: A Review. *Int. J. Hyperthermia* **2020**, *37*, 711–741, doi:10.1080/02656736.2020.1779357.
3. Kroesen, M.; Mulder, H.T.; Van Holthe, J.M.L.; Aangeenbrug, A.A.; Mens, J.W.M.; Van Doorn, H.C.; Paulides, M.M.; Oomen-de Hoop, E.; Vernhout, R.M.; Lutgens, L.C.; et al. Confirmation of Thermal Dose as a Predictor of Local Control in Cervical Carcinoma Patients Treated with State-of-the-Art Radiation Therapy and Hyperthermia. *Radiother. Oncol.* **2019**, *140*, 150–158, doi:10.1016/j.radonc.2019.06.021.
4. Diederich, C.J.; Hynynen, K. Ultrasound Technology for Hyperthermia. *Ultrasound Med. Biol.* **1999**, *25*, 871–887, doi:10.1016/S0301-5629(99)00048-4.
5. Zhu, L.; Altman, M.B.; Laszlo, A.; Straube, W.; Zoberi, I.; Hallahan, D.E.; Chen, H. Ultrasound Hyperthermia Technology for Radiosensitization. *Ultrasound Med. Biol.* **2019**, *45*, 1025–1043, doi:10.1016/j.ultrasmedbio.2018.12.007.
6. Mahmoudi, K.; Bouras, A.; Bozec, D.; Ivkov, R.; Hadjipanayis, C. Magnetic Hyperthermia Therapy for the Treatment of Glioblastoma: A Review of the Therapy's History, Efficacy and Application in Humans. *Int. J. Hyperthermia* **2018**, *34*, 1316–1328, doi:10.1080/02656736.2018.1430867.
7. Dennis, C.L.; Krycka, K.L.; Borchers, J.A.; Desautels, R.D.; Van Lierop, J.; Huls, N.F.; Jackson, A.J.; Gruettner, C.; Ivkov, R. Internal Magnetic Structure of Nanoparticles Dominates Time-Dependent Relaxation Processes in a Magnetic Field. *Adv. Funct. Mater.* **2015**, *25*, 4300–4311, doi:10.1002/adfm.201500405.
8. Filonenko, E.A.; Khokhlova, V.A. Effect of Acoustic Nonlinearity on Heating of Biological Tissue by High-Intensity Focused Ultrasound. *Acoust. Phys.* **2001**, *47*, 468–475, doi:10.1134/1.1385422.
9. O'Brien, W.D. Ultrasound–Biophysics Mechanisms. *Prog. Biophys. Mol. Biol.* **2007**, *93*, 212–255, doi:10.1016/j.pbiomolbio.2006.07.010.
10. Özsoy, Ç.; Lafci, B.; Reiss, M.; Deán-Ben, X.L.; Razansky, D. Real-Time Assessment of High-Intensity Focused Ultrasound Heating and Cavitation with Hybrid Optoacoustic Ultrasound Imaging. *Photoacoustics* **2023**, *31*, 100508, doi:10.1016/j.pacs.2023.100508.
11. Marinova, M.; Rauch, M.; Mücke, M.; Rolke, R.; Gonzalez-Carmona, M.A.; Henseler, J.; Cuhls, H.; Radbruch, L.; Strassburg, C.P.; Zhang, L.; et al. High-Intensity Focused Ultrasound (HIFU) for Pancreatic Carcinoma: Evaluation of Feasibility, Reduction of Tumour Volume and Pain Intensity. *Eur. Radiol.* **2016**, *26*, 4047–4056, doi:10.1007/s00330-016-4239-0.
12. Mauri, G.; Nicosia, L.; Xu, Z.; Di Pietro, S.; Monfardini, L.; Bonomo, G.; Varano, G.M.; Prada, F.; Della Vigna, P.; Orsi, F. Focused Ultrasound: Tumour Ablation and Its Potential to Enhance Immunological Therapy to Cancer. *Br. J. Radiol.* **2018**, 20170641, doi:10.1259/bjr.20170641.
13. Mouratidis, P.X.E.; Ter Haar, G. Latest Advances in the Use of Therapeutic Focused Ultrasound in the Treatment of Pancreatic Cancer. *Cancers* **2022**, *14*, 638, doi:10.3390/cancers14030638.

14. Grüll, H.; Langereis, S. Hyperthermia-Triggered Drug Delivery from Temperature-Sensitive Liposomes Using MRI-Guided High Intensity Focused Ultrasound. *J. Controlled Release* **2012**, *161*, 317–327, doi:10.1016/j.jconrel.2012.04.041.
15. Bamber, J.C. Attenuation and Absorption. In *Physical Principles of Medical Ultrasonics*; Hill, C.R., Bamber, J.C., Ter Haar, G.R., Eds.; Wiley, 2004; pp. 93–166 ISBN 978-0-471-97002-6.
16. Wang, S.; Frenkel, V.; Zderic, V. Optimization of Pulsed Focused Ultrasound Exposures for Hyperthermia Applications. *J. Acoust. Soc. Am.* **2011**, *130*, 599–609, doi:10.1121/1.3598464.
17. Patel, P.R.; Luk, A.; Durrani, A.; Dromi, S.; Cuesta, J.; Angstadt, M.; Dreher, M.R.; Wood, B.J.; Frenkel, V. In Vitro and in Vivo Evaluations of Increased Effective Beam Width for Heat Deposition Using a Split Focus High Intensity Ultrasound (HIFU) Transducer. *Int. J. Hyperthermia* **2008**, *24*, 537–549, doi:10.1080/02656730802064621.
18. Kaczmarek, K.; Hornowski, T.; Dobosz, B.; Józefczak, A. Influence of Magnetic Nanoparticles on the Focused Ultrasound Hyperthermia. *Materials* **2018**, *11*, 1607, doi:10.3390/ma11091607.
19. Józefczak, A.; Kaczmarek, K.; Hornowski, T.; Kubovčíková, M.; Rozynek, Z.; Timko, M.; Skumiel, A. Magnetic Nanoparticles for Enhancing the Effectiveness of Ultrasonic Hyperthermia. *Appl. Phys. Lett.* **2016**, *108*, 263701, doi:10.1063/1.4955130.
20. Jameel, B.; Hornowski, T.; Bielas, R.; Józefczak, A. Ultrasound Study of Magnetic and Non-Magnetic Nanoparticle Agglomeration in High Viscous Media. *Materials* **2022**, *15*, 3450, doi:10.3390/ma15103450.
21. Kaczmarek, K.; Bielas, R.; Siluk, M.; Hornowski, T.; Józefczak, A. Comparison of Magnetic and Non-Magnetic Nanoparticles as Sonosensitizers in Ultrasonic Hyperthermia. *Acta Phys. Pol. A* **2020**, *137*, 653–656, doi:10.12693/APhysPolA.137.653.
22. Gambin, B.; Kruglenko, E. Ultrasonic specific absorption rate in nanoparticle-mediated moderate hyperthermia. *Bull. Pol. Acad. Sci. Tech. Sci.* **2021**, doi:10.24425/bpasts.2021.137053.
23. Jameel, B.; Bielas, R.; Józefczak, A. Ultrasound Measurements of Particle Shells in Magnetic Pickering Emulsions. *Measurement* **2023**, *220*, 113409, doi:10.1016/j.measurement.2023.113409.
24. Kaiser, A.; Liu, T.; Richtering, W.; Schmidt, A.M. Magnetic Capsules and Pickering Emulsions Stabilized by Core−Shell Particles. *Langmuir* **2009**, *25*, 7335–7341, doi:10.1021/la900401f.
25. Bielas, R.; Jameel, B.; Józefczak, A. Monitoring of Pickering Emulsion Stability during Magnetic Heating Using Ultrasound Measurements. *Measurement* **2021**, *178*, 109431, doi:10.1016/j.measurement.2021.109431.
26. Bielas, R.; Hornowski, T.; Paulovičová, K.; Rajňák, M.; Józefczak, A. The Effect of Magnetic Particles Covering the Droplets on the Heating Rate of Pickering Emulsions in the AC Magnetic Field. *J. Mol. Liq.* **2020**, *320*, 114388, doi:10.1016/j.molliq.2020.114388.
27. Li, W.; Suzuki, T.; Minami, H. The Interface Adsorption Behavior in a Pickering Emulsion Stabilized by Cylindrical Polystyrene Particles. *J. Colloid Interface Sci.* **2019**, *552*, 230–235, doi:10.1016/j.jcis.2019.05.058.
28. Anson, L.W.; Chivers, R.C. Ultrasonic Scattering from Spherical Shells Including Viscous and Thermal Effects. *J. Acoust. Soc. Am.* **1993**, *93*, 1687–1699, doi:10.1121/1.406734.
29. Kanamori, C.; Nguyen, T.T.; Tsuji, K.; Nakanishi, H.; Tran-Cong-Miyata, Q.; Norisuye, T. Interfacial Structures of Particle-Stabilized Emulsions Examined by Ultrasonic Scattering

Analysis with a Core–Shell Model. *Ultrasonics* **2021**, *116*, 106510, doi:10.1016/j.ultras.2021.106510.
30. Kaczmarek, K.; Hornowski, T.; Kubovčíková, M.; Timko, M.; Koralewski, M.; Józefczak, A. Heating Induced by Therapeutic Ultrasound in the Presence of Magnetic Nanoparticles. *ACS Appl. Mater. Interfaces* **2018**, *10*, 11554–11564, doi:10.1021/acsami.8b02496.
31. Epstein, P.S.; Carhart, R.R. The Absorption of Sound in Suspensions and Emulsions. I. Water Fog in Air. *J. Acoust. Soc. Am.* **1953**, *25*, 553–565, doi:10.1121/1.1907107.
32. Allegra, J.R.; Hawley, S.A. Attenuation of Sound in Suspensions and Emulsions: Theory and Experiments. *J. Acoust. Soc. Am.* **1972**, *51*, 1545–1564, doi:10.1121/1.1912999.
33. Okura, S.; Tsuji, K.; Norisuye, T. Transition from Liquid Droplet to Solid Particle Investigated by Ultrasonic Spectroscopy. *Ultrasonics* **2023**, *128*, 106879, doi:10.1016/j.ultras.2022.106879.
34. McClements, D.J. Ultrasonic Characterisation of Emulsions and Suspensions. *Adv. Colloid Interface Sci.* **1991**, *37*, 33–72, doi:10.1016/0001-8686(91)80038-L.
35. Bera, C.; Devarakonda, S.B.; Kumar, V.; Ganguli, A.K.; Banerjee, R.K. The Mechanism of Nanoparticle-Mediated Enhanced Energy Transfer during High-Intensity Focused Ultrasound Sonication. *Phys. Chem. Chem. Phys.* **2017**, *19*, 19075–19082, doi:10.1039/C7CP03542J.
36. Vinogradov, A.N. Physicochemical and Acoustic Properties of Water-Based Magnetic Colloid. *Colloid J.* **2004**, *66*, 29–37, doi:10.1023/B:COLL.0000015052.27208.c5.
37. Challis, R.E.; Tebbutt, J.S.; Holmes, A.K. Equivalence between Three Scattering Formulations for Ultrasonic Wave Propagation in Particulate Mixtures. *J. Phys. Appl. Phys.* **1998**, *31*, 3481–3497, doi:10.1088/0022-3727/31/24/012.
38. Sharma, A.; Jangam, A.A.; Yung Shen, J.L.; Ahmad, A.; Arepally, N.; Carlton, H.; Ivkov, R.; Attaluri, A. Design of a Temperature-Feedback Controlled Automated Magnetic Hyperthermia Therapy Device. *Front. Therm. Eng.* **2023**, *3*, 1131262, doi:10.3389/fther.2023.1131262.
39. Li, C.; Li, S.; Guan, G.; Wei, C.; Huang, Z.; Wang, R.K. A Comparison of Laser Ultrasound Measurements and Finite Element Simulations for Evaluating the Elastic Properties of Tissue Mimicking Phantoms. *Opt. Laser Technol.* **2012**, *44*, 866–871, doi:10.1016/j.optlastec.2011.11.017.
40. Sun, C.; Pye, S.D.; Browne, J.E.; Janeczko, A.; Ellis, B.; Butler, M.B.; Sboros, V.; Thomson, A.J.W.; Brewin, M.P.; Earnshaw, C.H.; et al. The Speed of Sound and Attenuation of an IEC Agar-Based Tissue-Mimicking Material for High Frequency Ultrasound Applications. *Ultrasound Med. Biol.* **2012**, *38*, 1262–1270, doi:10.1016/j.ultrasmedbio.2012.02.030.
41. Hamhaber, U.; Grieshaber, F.A.; Nagel, J.H.; Klose, U. Comparison of Quantitative Shear Wave MR-elastography with Mechanical Compression Tests. *Magn. Reson. Med.* **2003**, *49*, 71–77, doi:10.1002/mrm.10343.
42. Ter Haar, >Gail; Coussios, C. High Intensity Focused Ultrasound: Physical Principles and Devices. *Int. J. Hyperthermia* **2007**, *23*, 89–104, doi:10.1080/02656730601186138.
43. Miller, D.L.; Smith, N.B.; Bailey, M.R.; Czarnota, G.J.; Hynynen, K.; Makin, I.R.S.; Bioeffects Committee of the American Institute of Ultrasound in Medicine Overview of Therapeutic Ultrasound Applications and Safety Considerations. *J. Ultrasound Med.* **2012**, *31*, 623–634, doi:10.7863/jum.2012.31.4.623.

44. Kubiak, T.; Zubko, M.; Józefczak, A. The Impact of Ultrasound on Janus Capsules at Gel-Liquid Interface. *Curr. Appl. Phys.* **2022**, *38*, 22–29, doi:10.1016/j.cap.2022.03.008.
45. Focused Ultrasound Induced Heating in Tissue Phantom. *COMSOL Multiphysics 62*, https://www.comsol.com/model/focused-ultrasound-induced-heating-in-tissue-phantom-12659.
46. Focused Ultrasound Induced Heating in Tissue Phantom.
47. Bielas, R.; Rozynek, Z.; Hornowski, T.; Józefczak, A. Ultrasound Control of Oil-in-Oil Pickering Emulsions Preparation. *J. Phys. Appl. Phys.* **2020**, *53*, 085301, doi:10.1088/1361-6463/ab58a7.
48. Dąbek, L.; Hornowski, T.; Józefczak, A.; Skumiel, A. Ultrasonic Properties of Magnetic Nanoparticles with an Additional Biocompatible Dextrane Layer. *Arch. Acoust.* **2013**, *38*, 93–98, doi:10.2478/aoa-2013-0011.
49. Barbé, C.; Bartlett, J.; Kong, L.; Finnie, K.; Lin, H.Q.; Larkin, M.; Calleja, S.; Bush, A.; Calleja, G. Silica Particles: A Novel Drug-Delivery System. *Adv. Mater.* **2004**, *16*, 1959–1966, doi:10.1002/adma.200400771.
50. Tan, W.; Wang, K.; He, X.; Zhao, X.J.; Drake, T.; Wang, L.; Bagwe, R.P. Bionanotechnology Based on Silica Nanoparticles. *Med. Res. Rev.* **2004**, *24*, 621–638, doi:10.1002/med.20003.
51. Zhao, X.; Yu, G.; Li, J.; Feng, Y.; Zhang, L.; Peng, Y.; Tang, Y.; Wang, L. Eco-Friendly Pickering Emulsion Stabilized by Silica Nanoparticles Dispersed with High-Molecular-Weight Amphiphilic Alginate Derivatives. *ACS Sustain. Chem. Eng.* **2018**, *6*, 4105–4114, doi:10.1021/acssuschemeng.7b04508.
52. Arslan Azizoglu, G.; Tuncay Tanriverdi, S.; Aydin Kose, F.; Ballar Kirmizibayrak, P.; Ozer, O. Dual-Prevention for UV-Induced Skin Damage: Incorporation of Melatonin-Loaded Elastic Niosomes into Octyl Methoxycinnamate Pickering Emulsions. *AAPS PharmSciTech* **2017**, *18*, 2987–2998, doi:10.1208/s12249-017-0786-1.
53. Tu, S.J.; Hynynen, K.; Roemer, R.B. Simulation of Bidirectional Ultrasound Hyperthermia Treatments of Neck Tumours. *Int. J. Hyperthermia* **1994**, *10*, 707–722, doi:10.3109/02656739409022449.
54. Strohm, E.M.; Kolios, M.C. Sound Velocity and Attenuation Measurements of Perfluorocarbon Liquids Using Photoacoustic Methods. In Proceedings of the 2011 IEEE International Ultrasonics Symposium; IEEE: Orlando, FL, USA, October 2011; pp. 2368–2371.
55. Reyjal, M.; Tavares, J.R.; Virgilio, N.; Fradette, L. Is the Maxwell–Garnett Continuum Model Valid To Predict the Thermal Conductivity of Particle-Stabilized (Pickering) Emulsions? *Ind. Eng. Chem. Res.* **2013**, *52*, 4962–4966, doi:10.1021/ie303124p.
56. Gambin, B.; Kruglenko, E.; Tymkiewicz, R.; Litniewski, J. Ultrasound Assessment of the Conversion of Sound Energy into Heat in Tissue Phantoms Enriched with Magnetic Micro- and Nanoparticles. *Med. Phys.* **2019**, *46*, 4361–4370, doi:10.1002/mp.13742.
57. Ribeiro, T.P.; Moreira, J.A.; Monteiro, F.J.; Laranjeira, M.S. Nanomaterials in Cancer: Reviewing the Combination of Hyperthermia and Triggered Chemotherapy. *J. Controlled Release* **2022**, *347*, 89–103, doi:10.1016/j.jconrel.2022.04.045.
58. Zhang, P.; Porter, T. An in Vitro Study of a Phase-Shift Nanoemulsion: A Potential Nucleation Agent for Bubble-Enhanced HIFU Tumor Ablation. *Ultrasound Med. Biol.* **2010**, *36*, 1856–1866, doi:10.1016/j.ultrasmedbio.2010.07.001.

59. Chang, N.; Lu, S.; Qin, D.; Xu, T.; Han, M.; Wang, S.; Wan, M. Efficient and Controllable Thermal Ablation Induced by Short-Pulsed HIFU Sequence Assisted with Perfluorohexane Nanodroplets. *Ultrason. Sonochem.* **2018**, *45*, 57–64, doi:10.1016/j.ultsonch.2018.02.033.
60. Leong, K.X.; Sharma, D.; Czarnota, G.J. Focused Ultrasound and Ultrasound Stimulated Microbubbles in Radiotherapy Enhancement for Cancer Treatment. *Technol. Cancer Res. Treat.* **2023**, *22*, 153303382311763, doi:10.1177/15330338231176376.
61. Sharma, D.; McNabb, E.; Law, N.; Cumal, A.; Czarnota, G.J. Ultrasound-Stimulated Microbubbles Enhancement of Fractionated Radiation for Tumor Treatment. *BMC Cancer* **2023**, *23*, 693, doi:10.1186/s12885-023-10981-5.

[Scientific Paper V]

Propagation of ultrasonic wave in magnetic Pickering emulsion under DC magnetic field

Jameel, B., Hornowski, T., Bielas, R., and Józefczak, A.

Journal of Magnetism and Magnetic Materials 542 (2022) 168590

Journal of Magnetism and Magnetic Materials 542 (2022) 168590

Contents lists available at ScienceDirect

Journal of Magnetism and Magnetic Materials

journal homepage: www.elsevier.com/locate/jmmm

Research articles

Propagation of ultrasonic wave in magnetic Pickering emulsion under DC magnetic field

Bassam Jameel, Rafał Bielas, Tomasz Hornowski, Arkadiusz Józefczak *

Chair of Acoustics, Faculty of Physics, Adam Mickiewicz University in Poznań, Uniwersytetu Poznańskiego 2, 61-614 Poznań, Poland

ARTICLE INFO

Keywords:
Static magnetic field
Pickering emulsion
Magnetic particles
Ultrasound wave propagation
Magnetic separation
Ultrasonic spectroscopy

ABSTRACT

A Pickering emulsion is an emulsion stabilized by solid particles accumulated at the surface of droplets. It is also possible to create a stable Pickering emulsion stabilized by ferromagnetic iron oxide nanoparticles to make it susceptible to magnetic fields. This type of emulsion has received great research interest in recent years because it has generated and holds the promise of a variety of practical applications. One interesting application is magnetic separation in the gradient magnetic field. However, the real-time characterization of magnetic Pickering emulsions, especially under external stimuli such as magnetic fields, is generally challenging. We used a convenient method to control the properties of magnetic particle-stabilized emulsions via the ultrasound technique. In the experiments, we investigated the attenuation of ultrasound using ultrasonic spectroscopy as a function of the magnetic particle concentration and magnetic field intensity. The analysis of ultrasonic waves as a function of frequency provided information about the movement of magnetic Pickering droplets during magnetic separation. The results showed much weaker separation for a low magnetic particles concentration as the magnetic force was not sufficient to induce significant droplets movement, whereas for a high concentration the magnetic separation occurred very dynamically.

1. Introduction

Magnetic nanoparticles have been extensively studied as they show unique magnetic properties that lead to useful applications: water purification [1], oil recovery [2], and biomedical applications [3–5]. The ability to control the motion of the particles under an external gradient magnetic field shows considerable promise and gives information about the magnetic separation process [6]. This is based on the phenomenon of magnetophoresis, i.e. the gradual migration of magnetic objects to the place with the highest magnetic field gradient due to the spatial changes of the magnetic field intensity [7]. In fact, the magnetic separation can be further classified into high gradient magnetic separation (HGMS) and low gradient magnetic separation (LGMS), depending on the magnitude of the gradient in the fields applied to the magnetic samples. The setup for HGMS usually consists of a packed bed of magnetically susceptible wires placed inside the sample [8], which produces large field gradients that influence magnetic nanoparticles [9,10]. In the case of LGMS, the permanent magnets are located outside the sample cell and in this way generate a low gradient magnetic field [11]. During LGMS, the magnetic nanoparticles migrate from the lowest to the highest gradient of the magnetic field. During the migration some of magnetic nanoparticles may collide with each other and integrate larger aggregates [12,13]. As a result, the magnetophoretic velocity increases after a large aggregate of particles because the magnetophoretic force that pushes the particles to move is higher for the aggregate than for a single particle [14,15]. The movement of the particle depends therefore not only on the magnetic field intensity and the field gradient, but also on the size of the magnetic objects.

Magnetic nanoparticles can be used as stabilizers in emulsions by accumulation at the surface of droplets. Such emulsions are known as magnetic Pickering emulsions and the presence of magnetic particles makes them both stable and susceptible to the magnetic fields. The emulsion system is considered as thermodynamically unstable due to the high free energy resulting from the existence of two phases [16]. Therefore, it is energetically favorable for solid particles with intermediate wettability to be attached onto the water–oil or oil–oil interface. This particle shell around the droplets makes the emulsions more stable because it constitutes a mechanical barrier against the coalescence [17,18]. Magnetic nanoparticles used as stabilizers can work also as a source of heat when an alternative magnetic field is applied [19]. In

* Corresponding author.
E-mail address: aras@amu.edu.pl (A. Józefczak).

https://doi.org/10.1016/j.jmmm.2021.168590
Received 29 June 2021; Received in revised form 17 September 2021; Accepted 20 September 2021
Available online 24 September 2021

turn, under the effect of the static magnetic field, magnetic separation at the magnetic Pickering emulsion can occur owing to the movement induced by magnetophoretic force, as was stated above for magnetic particles. The droplets' diameter can be controlled via the concentration of particles used under a so-called limited coalescence regime [20]. This can be fulfilled also for magnetic particles.

In the literature, magnetic separation is usually investigated for the dispersion of magnetic particles in liquids. However, magnetic Pickering emulsions have also attracted scientific interest in the last decade. When oil-in-water magnetic Pickering emulsions were exposed to a static magnetic field, the observed separation depended on the oil-to-water mass ratio and the wettability of the particles [21]. Additionally, in other research [22] the velocity of a monodispersed magnetic Pickering emulsion under the influence of different magnetic field gradients for various pH systems was discussed. The results show faster movement of Pickering droplets with velocity proportional to the magnetic field gradient. Destabilization of the Pickering emulsions occurred for a low concentration of magnetic stabilizers, but Pickering emulsions with a high concentration of magnetic particles turned out to be more stable. After longer application of a high-intensity magnetic field, the magnetic nanoparticles were practically torn away from the droplets, which enabled demulsification as the bare droplets are not resistant to coalescence [21].

In this work, we investigated oil-in-oil magnetic Pickering emulsions exposed to DC magnetic fields. We studied how different intensities of the magnetic field and concentrations of magnetite influence the magnetic separation. By using ultrasonic homogenization and DC electric fields, we prepared oil-in-oil emulsions with droplets fully covered by magnetite particles. High-frequency ultrasound was used for non-destructive characterization of the emulsions during magnetic separation. In the literature, there are many reports on using ultrasound attenuation measurements to characterize conventional, surfactant-stabilized emulsion [23–25]. Yet, there are a few works describing ultrasonic propagation in particle-stabilized emulsions, despite the significant difference in their structure in comparison to surfactant-stabilized emulsions, not to mention magnetic emulsions. The analysis was performed both for the time of application of magnetic fields but also in the frequency domain, by obtaining Fourier spectra of the ultrasonic signal. Real-time characterization without special sample preparation, especially under external stimuli (e.g., magnetic and electric fields), is generally challenging. Therefore, this study can offer important information about liquid purification and particles recovery by the magnetic separation technique. These procedures can be monitored by measuring the attenuation coefficient of the ultrasound wave.

2. Materials and methods

2.1. Oils, particles, and magnets

Two types of oils were utilized for the formation of oil-in-oil Pickering emulsion. Castor oil (MERLIN, MA220-1, Spain) with viscosity of 700 mPa·s and silicone oil (Rhodorsil,47 V 50, USA) with viscosity of 50 mPa·s for 25 °C, constituted a continuous and a dispersed phase of the Pickering emulsion, respectively. Their densities were similar (around 960 kg/m^3), which was beneficial for the stability of the emulsions against sedimentation. Magnetic nanoparticles in the powder form (Sigma-Aldrich Co., USA) and with sizes of 50–100 nm were used as stabilizers of the emulsion droplets. Permanent magnets (Roller neodymium magnet, Poland) with a diameter of 20 mm were used as a source of DC magnetic field. The change in the intensity of the magnetic field between different experiments was achieved simply by increasing the number of magnets. A teslameter (RX-21, Resonance Technology, USA) was used for measuring the intensity of the static magnetic field via immersion of the transverse probe inside the sample cell with magnetic Pickering emulsion under the application of magnetic fields of different intensities. The measurements with the teslameter indicated

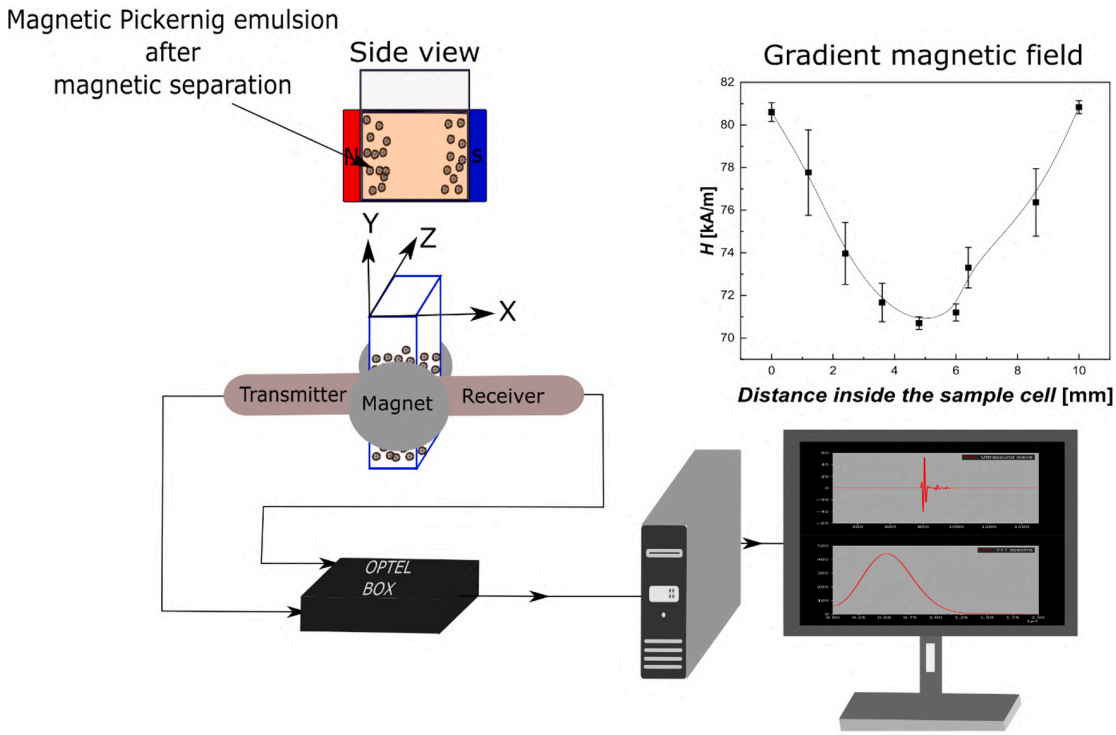

Fig. 1. Scheme of the experimental setup of ultrasound measurement system consisting of OPTEL ultrasonic testing device with two piezoelectric broadband transducers (transmitter and receiver) attached to the wall of the sample cell with a thin layer of gel for better acoustic impedance matching. The inset picture presents the dependence of the magnetic field intensity on the distance inside the sample cell along the Z axis. The diameter of the magnet is 20 mm. The center of the magnet is located in the middle of the sample cell in the Z direction (the edge effect of the magnet is negligible).

the gradient of the magnetic field inside the sample. The characterization of the field is presented as an inset picture in Fig. 1.

2.2. Preparation of magnetic Pickering emulsion

As we showed in the previous works [26], magnetic Pickering emulsions can be efficiently prepared by applying DC electric fields to the pre-emulsions, i.e. emulsions with droplets merely covered by particles prepared via ultrasonic homogenization. In this study, Pickering emulsions with different mass ratios of magnetite particles to silicone oil (1:2, 1:4, 1:10) were prepared, while the mass concentration of silicone oil to castor oil was 5%. To form pre-emulsions we used an ultrasound homogenizer (Sonoplus HD 300, Bandelin, Germany) working at a frequency of 20 kHz with acoustic intensity 17 W/cm^2. The homogenization time was 40 s. Next, stable Pickering emulsions were formed when the DC electric field was applied to the unstable pre-emulsion. The setup for the stabilization under electric fields consisted of the power supply (DF 1730SL, NDN, Poland), signal generator (RSDG 800, Siglent Technologies, USA), and high-voltage amplifier (UltraVolt 1AA12-P4, Advanced Energy, USA). The generated electric field supplied two copper electrodes immersed inside the sample cell with dimensions 10.2 mm × 10.2 mm × 45 mm. A thermometer was used to measure the temperature inside the Pickering emulsion after applying the electric field to ensure the same temperature for all experiments.

2.3. Preparation of single droplet with magnetic particle shell

To show the behavior of the single Pickering droplet under the magnetic field, a silicone oil droplet covered by a magnetite shell was formed in castor oil. Briefly, two sample cells were used. The first sample cell was used for dispersing magnetic nanoparticles into the silicone oil, and the magnetic dispersion was formed with a specific magnetite concentration of 1:10 (magnetic particles to silicone oil). The concentration of magnetic particles into castor oil should be high in order to get better coverage of the Pickering droplets. Sonication was employed for mixing the dispersion at a frequency of 18 kHz working with an acoustic intensity of ~ 17 W cm^{-2}, similarly to the sonication procedure in the formation of stable Pickering emulsions The second sample cell was filled with pure castor oil and placed on an XYZ stage in front of the optical microscopy system for monitoring the changes. Using a mechanical pipette, we took a fixed amount of magnetic dispersion from the first sample cell and injected it into pure castor oil. The magnetic Pickering droplet was formed after application of a DC electric field. When the DC electric field had been applied for several minutes, the induced electrohydrodynamic flows pushed the magnetic particles from the inside of the droplet to its surface [27,28]. All processes were monitored optically using a CMOS camera (UI-3590CP-C-HQ, IDS, USA).

2.4. Experimental setup for ultrasonic monitoring of magnetic separation

Figure 1 presents a schematic illustration of the setup used to study the ultrasonic wave propagation inside the magnetic Pickering emulsion. The setup consisted of a sample cell with dimensions 10.2 mm × 10.2 mm × 45 mm placed on a mechanical XYZ translational stage. An ultrasonic data acquisition system with integrated OPBOX 2.1 (OPTEL, Poland) was used for driving two piezoelectric broadband transducers - transmitter and receiver (OLYMPUS, USA). After traveling through the sample cell, the ultrasonic signal was recorded with the sampling frequency of 100 MHz and the whole ultrasonic system was connected to the PC. The direction of ultrasound propagation was perpendicular to the direction of the magnetic field ($k \perp H$).

2.5. The attenuation of ultrasound based on FFT spectra

In this paper, the reference method was used to measure the attenuation of ultrasonic waves. As castor oil constituted the continuous phase of the tested emulsions, it was used as the reference medium because the acoustic attenuation of castor oil is known at room temperature. The ultrasonic attenuation coefficient in homogeneous media such as pure oils can be expressed by the power law dependence on frequency:

$$\alpha(f) = \alpha_0(f)^y \tag{1}$$

where α_0 is the power law coefficient and y is a power that typically varies in the range $0 < y \leq 2$. The measurement of the attenuation coefficient in castor oil was reported, for instance, by Tong and Povey [29], and for 25 °C, the attenuation coefficient as a function of frequency was expressed as $7.06f^{1.692}$, where f is expressed in MHz. This relation was used in our work as the reference attenuation coefficient, $\alpha(f)_{reference}$.

In the ultrasonic broadband spectroscopy technique, the attenuation coefficient of the emulsion sample can be determined by the following equation:

$$\alpha(f) = \alpha(f)_{reference} + \frac{1}{d}\ln\frac{|F_1(f)|}{|F_2(f)|} \tag{2}$$

where $\alpha(f)$ is the attenuation coefficient as a function of frequency, $\alpha(f)_{reference}$ is the attenuation coefficient for castor oil according to [29], d is the distance between the transmitter and receiver, $|F_1(f)|$ is the absolute number for fast Fourier transform (FFT) for the pulse recorded in the castor oil, and $|F_2(f)|$ is the absolute number for fast Fourier transform (FFT) for the pulse recorded in the Pickering emulsion.

3. Result and discussion

3.1. Single Pickering droplet under influence of DC magnetic field

The optical microscopy results for the single silicone oil droplet coated by a magnetic particle shell and exposed to the DC magnetic field are shown in Fig. 2. To form the stable Pickering droplet, the dispersion of magnetic nanoparticles in silicone oil was injected by a mechanical pipette into the pure castor oil as described in Section 2.3. In Fig. 2**a**, the DC magnetic field was applied to one side of the sample cell to study the influence of the gradient of the magnetic field on the movement of the droplet in the continuous phase (castor oil). Additionally, the DC magnetic field was applied simultaneously to both sides of the sample cell to study the influence of magnetic force on the Pickering droplet in the condition of having two high regions of gradient magnetic field, as presented in Fig. 2**b**. In this case, the magnetic field intensity in the sample cell is as shown in the inset picture in Fig. 1.

The motion and the shape of the Pickering droplet in castor oil can be controlled by external stimuli such as a magnetic field. Fig. 2**a** shows the possibility of Pickering droplet movement in the continuous phase, where the movement time depended on the magnetic force exerted on the particles residing in the droplet interface. Additionally, the shape of larger droplets may be deformed after magnetic field application from two sides of the sample cell (Fig. 2**b**). The pictures show clearly that there was no deformation before the application of the magnetic field. Deformation along the magnetic field gradient happened when the magnetic field was applied. Due to the geometry of the field, the droplet deformed in both directions, as the magnetic particles in two opposite regions of the droplet experienced opposite magnetic forces. At the same time, the droplet not only deformed but also moved to one or the other

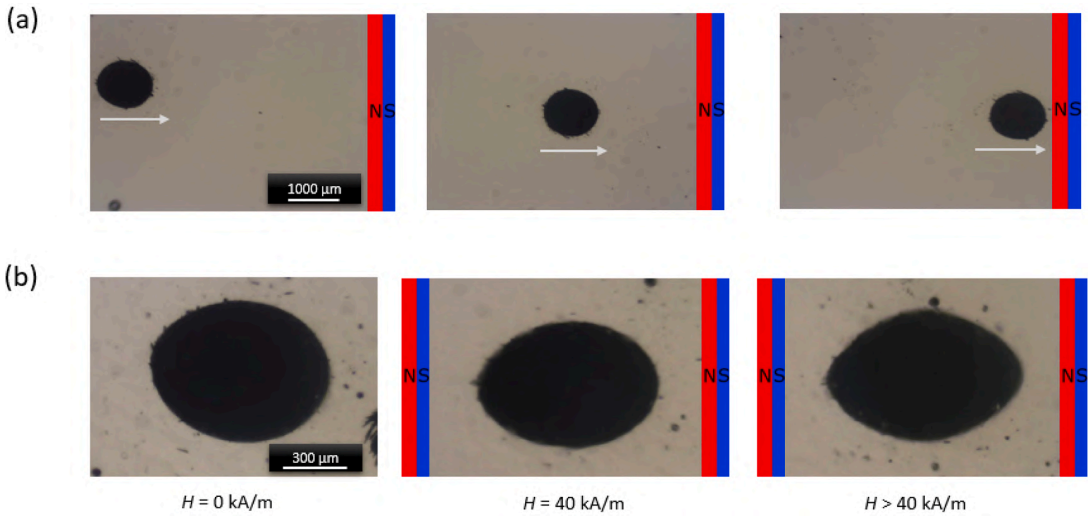

Fig. 2. A silicone oil droplet covered by magnetic nanoparticles after 5 min of application of DC magnetic field of different geometry. (a) Droplet movement from one side to another after the placement of a magnet. The magnetic field intensity was evaluated as 40 kA/m in the center of the sample cell and increasing gradually to ~ 46 kA/m along the x-axis to the sample cell wall. (b) Deformation of the Pickering droplet before and after gradient magnetic field application. The mass ratios of magnetite particles to silicone oil were 1:10.

sample wall, depending on the primary position in relation to the center of the sample cell. In the next section we present the influence of different magnetic field intensities on the magnetic emulsion, i.e., the system consisting of a large number of such particle-stabilized droplets.

3.2. *Ultrasonic spectroscopy analysis for the Pickering emulsion in different concentrations of magnetite*

The magnetic separation in the Pickering emulsion was investigated with ultrasonic spectroscopy. The ultrasonic attenuation coefficients were measured in the magnetic Pickering emulsions based on FFT (**Eq. (2)**). The results for various contents of magnetic particles related to the dispersed phase are presented in Fig. 3 for the magnetic field intensity of ~ 70 kA/m measured in the center of the sample cell with an estimated magnetic field gradient ∇H of 2000kA/m^2. The time of magnetic field application is marked in Fig. 3 **a, b** as a shaded area. The whole measurement lasted 20 min, where 0 min indicates the time before the application of magnetic fields, and from the 3rd to the 20th minute the magnetic field was removed.

As presented in Fig. 3**a**, the highest attenuation of ultrasound waves

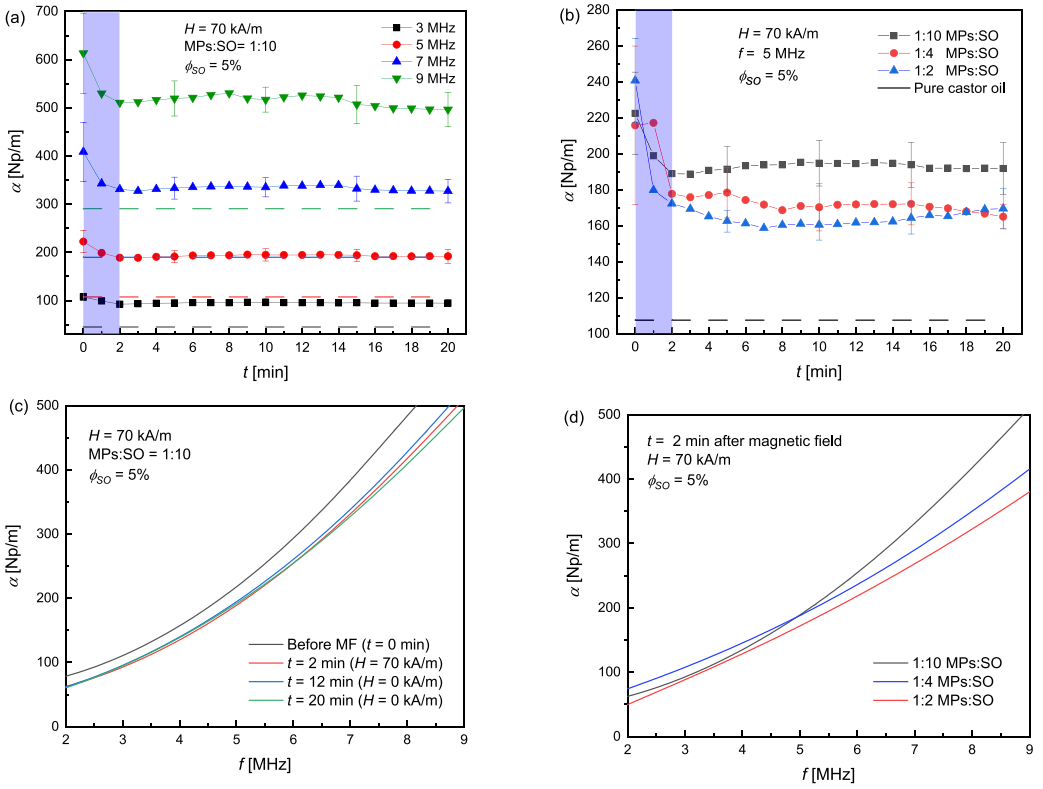

Fig. 3. (a) Ultrasonic attenuation coefficient as a function of time for 3, 5, 7, and 9 MHz at a magnetic particles (MPs) to silicone oil (SO) mass ratio of 1:10 and magnetic field intensity of 70 kA/m. **(b)** Ultrasonic attenuation coefficient for different concentrations of magnetite particles calculated for the center frequency of the transducers, 5 MHz. The dotted lines in (a) and (b) represent the attenuation in castor oil for the corresponding frequency, according to the equation described in section 2.5. **(c)** Ultrasonic attenuation coefficient as a function of frequency for different stages of measurements: before application of magnetic field, 2 min after application of magnetic field, 10 min after removing the magnetic field, and 18 min after removing the magnetic field. **(d)** Ultrasonic attenuation coefficient for different contents of magnetic particles after 2 min of magnetic field application. The error bar in panel (a) and (b) indicates the standard deviation for three independent measurements.

was observed before application of the magnetic fields. During the application of magnetic fields (shaded area) the attenuation decreased significantly, but the decrease of the attenuation was remarkably slower, if any, when the magnetic field was removed. The change in ultrasonic attenuation for a wide range of frequencies reflected how the emulsion changed during the magnetic separation without the need for a special sample treatment such as dilution. The droplets started moving to the magnet side due to the gradient of field inside the sample. Because the intensity of the magnetic field in this experiment was not too high, not all the droplets moved to the magnet side during the application of the magnetic field and some of them stayed simply aligned to the magnetic field line. This explains why the value of attenuation did not attain the values for pure continuous phase, despite the separation of the droplets to the sample cell walls and visible purification of the continuous phase. However, in the case of a higher magnetic particle to silicone oil mass ratio (1:2), the decrease of ultrasonic attenuation (shown for one frequency) was more significant than for emulsions with a lower content of magnetic particles, as shown in Fig. 3**b**. The difference in attenuation between the 1:10 and 1:2 mass ratios was around 30 Np/m when measured after two minutes of magnetic field intensity application. This showed clearly that Pickering emulsions are separated in the same manner as magnetic dispersions [12,14,30,31]. The subtle point is that a larger number of magnetic nanoparticles residing on the droplets leads to a smaller size of droplet due to the so-called limited coalescence regime which can additionally influence the rate of movement of small Pickering droplets to the magnets and change the efficiency of separation.

From Fig. 3**c**, it is clear that, despite the rather significant difference in propagation of ultrasound before and after the application of the magnetic field (Fig. 3**a**), the attenuation spectra did not differ when monitoring the emulsion after application of the magnetic field. Over time, not only the temporal evolution of the attenuation coefficient but also the attenuation spectra seem to be stable. The differences in the shape of the attenuation spectra could suggest further changes in the structure, as the frequency dependence of the ultrasonic attenuation depends on the size of the scattering objects (i.e., droplets and particles, and their agglomerates). The results in Fig. 3**d** indicate such variations for different contents of magnetic particles that, as was stated above, influence not only the dynamics of the separation process but also the size of the Pickering droplets [20]. Nevertheless, the most clear is the influence of the magnetic separation, which explains why for the 1:10 magnetic particle-silicone oil mass ratio the attenuation spectrum is very different and the value of attenuation is the highest.

3.3. *Ultrasonic spectroscopy analysis for the magnetic Pickering emulsion under different intensities of magnetic field*

The influence of different magnetic field intensities on the propagation of ultrasound in magnetic Pickering emulsion is shown in Fig. 4. The magnetic field intensity was controlled by the number of thin bar magnets, so the obtained intensities were proportional to the number of magnets. Similarly to the results in Fig. 3, the magnetic field was applied for 2 min and the ultrasonic attenuation was measured before, during and after application of the field

Figure 4**a** clearly presents the effect of the magnetic field of highest intensity (170 kA/m) measured in the middle of the sample cell on the magnetic Pickering emulsion. The attenuation of ultrasonic waves decreased faster 2 min after application of the magnetic field in comparison to the corresponding results in Fig. 3**a.** What is more, a higher magnetic field caused different dynamics of the change in attenuation for different frequencies of ultrasonic waves. The difference between 3 MHz and 9 MHz in Fig. 4**a** is 284 Np/m, but the difference between 3 MHz and 9 MHz in Fig. 3**a** is 418 Np/m, and these differences can provide information about the purification of the system after magnetic separation.

The efficiency of the magnetic separation and the purification of the system can be tested by comparison with the attenuation of the reference system (castor oil) with magnetic Pickering emulsion after separation. According to the measurements by Tong and Povey [29], the attenuation of the ultrasound wave for 5 MHz was 107.5 Np/m. In Fig. 3**a** and 4**a** the

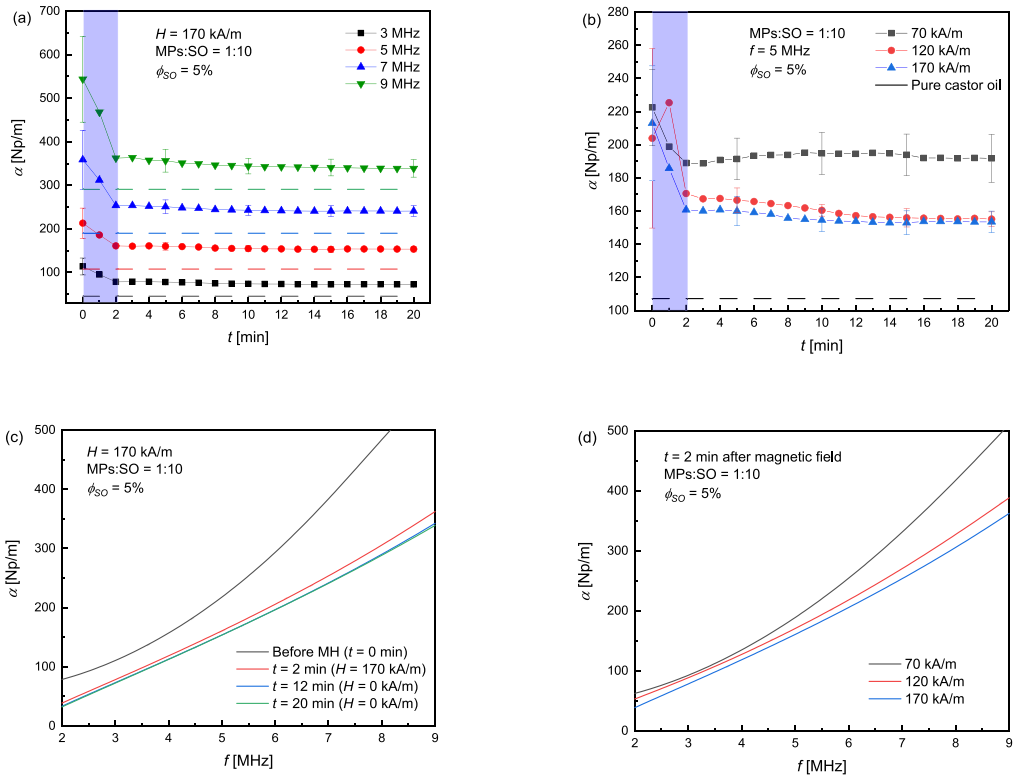

Fig. 4. (a) Ultrasonic attenuation coefficient in a time domain as a function of time for 3, 5, 7, and 9 MHz at a magnetic particles (MPs) to silicone oil (SO) mass ratio of 1:10 and magnetic field intensity of 170 kA/m at the center of the sample cell. **(b)** Ultrasonic attenuation coefficient for different magnetic field intensities calculated for the center frequency of transducers, 5 MHz. The dotted lines in (a) and (b) represent the attenuation in castor oil for the corresponding frequency, according to the equation described in section 2.5 **(c)** Ultrasonic attenuation coefficient as a function of frequency for different stages of measurements: before application of magnetic field, 2 min after application of magnetic field, 10 min after removing the magnetic field, and 18 min after removing the magnetic field. **(d)** Ultrasonic attenuation coefficient for different magnetic field intensities after 2 min of magnetic field application. The error bar in panels (a) and (b) indicates the standard deviation for three independent measurements.

attenuation of the ultrasound wave for 5 MHz was 188.9 Np/m and 160.7 Np/m respectively after 2 min of magnetic field application.

The rate of change in the attenuation coefficient at the intensity and frequency of 170 kA/m and 9 MHz, respectively, in Fig. 4**a 2 min** after application of the magnetic field is 1.56 Np/m·s, whereas the rate of change at the intensity of 70 kA/m in Fig. 3**a** is 0.85 Np/m·s. This indicates clearly that the droplet moved faster to the magnet in the case of higher intensity of the magnetic field and the ultrasound can show that, regardless of the volume of the emulsion and its transparency. However, it may also show that the shape of the droplets changed during the separation process, as the size of scatterers influences the attenuation spectra.

Figure 4**b** provides the results for three different intensities for the center frequency of the transducer of 5 MHz. The ultrasonic results showed clearly the influence of the magnetic field intensity on the dynamics of magnetic separation for the gradient magnetic field after application of the field. However, in the case of the intensity of 170 kA/m, the ultrasound attenuation results indicated that the observed change was comparable with that for 70 kA/m and 120 kA/m. In Fig. 4**c**, the difference in attenuation spectra before application of magnetic field and after 2 min of magnetic field application is clearly observed. But when comparing the results after 2 min and 18 min from removing the magnetic field, there is no such significant difference. This suggests that the magnetic separation, i.e. the migration of Pickering droplets to the magnets, was stopped after removing the magnetic field, despite the high intensity of the applied fields. The difference in the values and the shape of the attenuation spectra before and after the application indicates more structural changes in comparison to the results in Fig. 3**.** Additionally, the result in Fig. 4**d** shows that 2 min of application of the magnetic field in the case of 120 kA/m and 170 kA/m seems to be enough for efficient magnetic separation of a Pickering emulsion with a relatively low content of magnetic particles. In the case of the lower intensities of magnetic field, a longer time (more than 2 min) was required to obtain efficient magnetic separation in the Pickering emulsion.

Other authors [32] studied the magnetic separation by showing the magnetophoresis of iron oxide nanoparticles under a low gradient magnetic field $<$ 100 T/m. Different shapes and concentrations of magnetic nanoparticles were used. Additionally, an optical sensing system was employed to monitor the magnetic separation in the system. After exposure to DC magnetic field, the fastest magnetic separation occurred with a high concentration in around 150 s. In the case of our study, the ultrasound analysis based on FFT provides more information about the behaviour of the Pickering droplets during the application of magnetic field. The ultrasound technique could be especially powerful to study the influence of convection flow and momentum transfer of the magnetic nanoparticles shown in another study [15]. The important factor is that analysis of data with different frequencies can easily show us the rate of change during magnetic field application, as well as the ability to determine the speed of movement, the direction of movement, and the droplet size distribution. And the interesting point for using ultrasound is that it makes it possible to calculate the particles and Pickering droplet distribution theoretically by using the well-known ECAH theory and comparing it with experimental results, which we are planning to investigate in future work.

4. Conclusion

The attenuation of the ultrasonic wave obtained from FFT analysis was employed to monitor the magnetic separation in a Pickering emulsion stabilized by magnetic nanoparticles after exposure to a gradient magnetic field. The attenuation of the ultrasonic wave as a function of frequency provides information about the movement of magnetic Pickering droplets during magnetic separation. The experimental results of the ultrasound attenuation showed weak separation in low magnetite concentrations because the magnetic force was not enough for droplets movement, whereas in a high concentration system magnetic separation occurred and the attenuation analysis as a function of frequency showed the change in the structure. By increasing the value of the magnetic field gradient, the ultrasound analysis shows significant differences before and after application of the magnetic field due to the fast movement of droplets in the direction of the intensity gradient of the magnetic field. Additionally, the study showed that ultrasonic wave FFT spectroscopy is sensitive to the changes occurring in the emulsion under high intensity gradient magnetic fields, which may lead in the future to the development of an ultrasound-based technique for determining the droplet size distribution during the separation process under different magnetic field geometries.

CRediT authorship contribution statement

Bassam Jameel: Investigation, Formal analysis, Visualization, Conceptualization, Writing – original draft. **Rafał Bielas:** Investigation, Visualization, Conceptualization, Writing – original draft. **Tomasz Hornowski:** Writing – review & editing. **Arkadiusz Józefczak:** Conceptualization, Methodology, Supervision, Funding acquisition.

Declaration of Competing Interest

The authors declare that they have no known competing financial interests or personal relationships that could have appeared to influence the work reported in this paper.

Acknowledgment

This work was supported by the project no. 2019/35/O/ST3/00503 (PRELUDIUM BIS) of the Polish National Science Centre.

References

[1] S.P. Yeap, J. Lim, B.S. Ooi, A.L. Ahmad, Agglomeration, colloidal stability, and magnetic separation of magnetic nanoparticles: collective influences on environmental engineering applications, J. Nanopart. Res. 19 (2017) 368.
[2] S.K. Choi, H.A. Son, D. Park, J.W. Kim, Associative polymer-grafted magnetic nanoparticles for stabilization and recovery of pickering emulsions, Bull. Korean Chem. Soc. 39 (6) (2018) 806–811.
[3] S. Khizar, N.M. Ahmad, N. Zine, N. Jaffrezic-Renault, A. Errachid-el-salhi, A. Elaissari, Magnetic nanoparticles: from synthesis to theranostic applications, ACS Appl. Nano Mater. 4 (5) (2021) 4284–4306.
[4] Z.R. Stephen, F.M. Kievit, M. Zhang, Magnetite nanoparticles for medical MR imaging, Mater. Today 14 (7–8) (2011) 330–338.
[5] A. Tufani, A. Qureshi, J.H. Niazi, Iron oxide nanoparticles based magnetic luminescent quantum dots (MQDs) synthesis and biomedical/biological applications: a review, Mater. Sci. Eng. C Mater. Biol. Appl. 118 (2021) 111545.
[6] J. Oberteuffer, Magnetic separation: a review of principles, devices, and applications, IEEE Trans. Magn. 10 (2) (1974) 223–238.
[7] J. Lim, C. Lanni, E.R. Evarts, F. Lanni, R.D. Tilton, S.A. Majetich, Magnetophoresis of nanoparticles, ACS Nano 5 (1) (2011) 217–226.
[8] G.D. Moeser, K.A. Roach, W.H. Green, T. Alan Hatton, P.E. Laibinis, High-gradient magnetic separation of coated magnetic nanoparticles, Aiche J. 50 (11) (2004) 2835–2848.
[9] A. Ditsch, S. Lindenmann, P.E. Laibinis, D.I.C. Wang, T.A. Hatton, High-gradient magnetic separation of magnetic nanoclusters, Ind. Eng. Chem. Res. 44 (17) (2005) 6824–6836.
[10] J. Oberteuffer, High gradient magnetic separation, IEEE Trans. Magn. Mag. 9 (3) (1973) 303–306.
[11] S.S. Leong, S.P. Yeap, J. Lim, Working principle and application of magnetic separation for biomedical diagnostic at high- and low-field gradients, Interface Focus 6 (2016) 20160048.
[12] M. Benelmekki, C. Caparros, A. Montras, R. Gonçalves, S. Lanceros-Mendez, L. M. Martinez, Horizontal low gradient magnetophoresis behaviour of iron oxide nanoclusters at the different steps of the synthesis route, J. Nanopart. Res. 13 (8) (2011) 3199–3206.
[13] J. Lim, S.P. Yeap, S.C. Low, Challenges associated to magnetic separation of nanomaterials at low field gradient, Sep. Purif. Technol. 123 (2014) 171–174.
[14] S.S. Leong, Z. Ahmad, J. Camacho, J. Faraudo, J. Lim, Kinetics of low field gradient magnetophoresis in the presence of magnetically induced convection, J. Phys. Chem. C 121 (9) (2017) 5389–5407.
[15] S.S. Leong, Z. Ahmad, J. Lim, Magnetophoresis of superparamagnetic nanoparticles at low field gradient: hydrodynamic effect, Soft Matter 11 (35) (2015) 6968–6980.

[16] J. Frelichowska, M.-A. Bolzinger, J. Pelletier, J.-P. Valour, Y. Chevalier, Topical delivery of lipophilic drugs from o/w Pickering emulsions, Int. J. Pharm. 371 (1–2) (2009) 56–63.
[17] L.E. Low, S.P. Siva, Y.K. Ho, E.S. Chan, B.T. Tey, Recent advances of characterization techniques for the formation, physical properties and stability of Pickering emulsion, Adv. Colloid Interface Sci. 277 (2020), 102117.
[18] Y. Yang, Z. Liu, D. Wu, M. Wu, Y.E. Tian, Z. Niu, Y. Huang, Edge-modified amphiphilic Laponite nano-discs for stabilizing Pickering emulsions, J. Colloid Interface Sci. 410 (2013) 27–32.
[19] R. Bielas, T. Hornowski, K. Paulovičová, M. Rajňák, A. Józefczak, The effect of magnetic particles covering the droplets on the heating rate of Pickering emulsions in the AC magnetic field, J. Mol. Liq. 320 (2020), 114388.
[20] R. Bielas, Z. Rozynek, T. Hornowski, A. Józefczak, Ultrasound control of oil-in-oil Pickering emulsions preparation, J. Phys. D Appl. Phys. 53 (2020), 085301.
[21] M.J. Hasan, F.A. Petrie, A.E. Johnson, J. Peltan, M. Gannon, R.T. Busch, S. O. Leontsev, E.S. Vasquez, E.E. Urena-Benavides, Magnetically induced demulsification of water and castor oil dispersions stabilized by Fe3O4-coated cellulose nanocrystals, Cellulose 28 (8) (2021) 4807–4823.
[22] F.K. Tham, W.M. Ng, S.S. Leong, S.P. Yeap, S.C. Low, H.L. Lee, J. Lim, Magnetophoresis of magnetic pickering emulsions under low field gradient: macroscopic and microscopic motion, Langmuir 37 (2021) 1811–1822.
[23] D.J. McClements, Ultrasonic characterisation of emulsions and suspensions, Adv. Colloid Interface Sci. 37 (1–2) (1991) 33–72.
[24] D.J. Mcclements, Critical review of techniques and methodologies for characterization of emulsion stability, Crit. Rev. Food Sci. Nutr. 47 (7) (2007) 611–649.
[25] Y. Wang, M.J.W. Povey, A simple and rapid method for the determination of particle size in emulsions from ultrasound data, Colloids Surf. B Biointerfaces 12 (3–6) (1999) 417–427.
[26] Z. Rozynek, R. Bielas, A. Józefczak, Efficient formation of oil-in-oil Pickering emulsions with narrow size distributions by using electric fields, Soft Matter 14 (24) (2018) 5140–5149.
[27] A. Mikkelsen, K. Khobaib, F.K. Eriksen, K.J. Maloy, Z. Rozynek, Particle-covered drops in electric fields: drop deformation and surface particle organization, Soft Matter 14 (2018) 5442–5451.
[28] Z. Rozynek, K. Khobaib, A. Mikkelsen, Opening and closing of particle shells on droplets via electric fields and its applications, ACS Appl. Mater. Interfaces 11 (25) (2019) 22840–22850.
[29] J. Tong, M.J.W. Povey, Pulse echo comparison method with FSUPER to measure velocity dispersion in n-tetradecane in water emulsions, Ultrasonics 40 (1–8) (2002) 37–41.
[30] M. Benelmekki, L.M. Martinez, J.S. Andreu, J. Camacho, J. Faraudo, Magnetophoresis of colloidal particles in a dispersion of superparamagnetic nanoparticles: theory and experiments, Soft Matter 8 (22) (2012) 6039.
[31] P.Y. Toh, S.P. Yeap, L.P. Kong, B.W. Ng, D.J.C. Chan, A.L. Ahmad, J.K. Lim, Magnetophoretic removal of microalgae from fishpond water: Feasibility of high gradient and low gradient magnetic separation, Chem. Eng. J. 211–212 (2012) 22–30.
[32] J. Lim, S.P. Yeap, C.H. Leow, P.Y. Toh, S.C. Low, Magnetophoresis of iron oxide nanoparticles at low field gradient: the role of shape anisotropy, J. Colloid Interface Sci. 421 (2014) 170–177.

[Scientific Paper VI]

Magnetic pickering emulsions heated in a rotating magnetic field

Bielas, R., Jameel, B., Skumiel, A., Timko, M., Kopčanský, P., and Józefczak, A.

Journal of Magnetism and Magnetic Materials 563 (2022) 169946

Journal of Magnetism and Magnetic Materials 563 (2022) 169946

Contents lists available at ScienceDirect

Journal of Magnetism and Magnetic Materials

journal homepage: www.elsevier.com/locate/jmmm

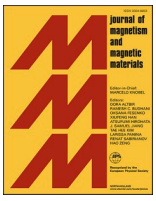

Magnetic pickering emulsions heated in a rotating magnetic field

Rafał Bielas [a], Bassam Jameel [a], Andrzej Skumiel [a], Milan Timko [b], Peter Kopčanský [b], Arkadiusz Józefczak [a,*]

[a] Faculty of Physics, Adam Mickiewicz University in Poznań, Uniwersytetu Poznańskiego 2, 61-614 Poznań, Poland
[b] Institute of Experimental Physics, Slovak Academy of Sciences, Watsonova 47, 040 01 Košice, Slovakia

ARTICLE INFO

Keywords:
Pickering emulsion
Magnetic fluid
Magnetic hyperthermia
Rotating magnetic field

ABSTRACT

Emulsion stabilized by solid particles that accumulate at the surface of droplets is called Pickering emulsion. Depending on the application, solid particles of different properties can be utilized as stabilizers. Magnetic nanoparticles are interesting choice as they can stabilize the emulsion and become heat sources in the presence of external magnetic field. To generate heat, researchers commonly use easily accessible alternating magnetic field, however, the use of rotating magnetic field yields possibility of higher heat output. Our study presents results of calorimetric measurements obtained for oil-in-oil emulsion stabilized by magnetic nanoparticles under the influence of a rotating magnetic field. In our system rotating magnetic field is produced by four separate magnetic fluxes shifted in phase and space by 90°. Results show that the use of rotating magnetic fields efficiently heat Pickering emulsion stabilized by magnetite particles. It also provides improved heating effect comparing to alternating magnetic fields, regardless of shape of the stabilizing particles. The results for magnetic emulsions were also compared to those for magnetic suspensions.

1. Introduction

Emulsions are inherently unstable dispersion systems. Therefore, the use of emulsifiers is indispensable to ensure the stability of the emulsions over time. Surfactants can be used as emulsifiers, however, the emulsion stability strongly depends on conditions such as the temperature, pressure, salinity, etc., which shortens the overall validity period of emulsion [1]. To overcome those issues, Pickering emulsions use solid particles to provide the stability of droplets. This stability depends on two mechanisms: the mechanical barrier mechanism and the three-dimensional viscoelastic particle network mechanism [1–3]. To make sufficient mechanical barrier against droplet coalescence, specific amount of particles with proper wettability is required. The literature presents numerous reports using different types of particles as droplet stabilizers. Kaolin, clay, montmorillonite and graphene oxide are used in the form of flakes and silicon dioxide, zinc oxide, iron oxide, titanium silicate, metal sulfate, polystyrene, Janus microspheres and starch nanocrystals in the form of granules etc. [1–3]. Use of magnetic nanoparticles (MNPs) as droplet stabilizers is very beneficial as well. MNPs thanks to their properties can be used as stabilizers for Pickering emulsions and as a source of heat under an alternating magnetic field. The temperature elevation generated by magnetic particles is used in many applications. The most widespread use of temperature increase applies to magnetic hyperthermia therapy in which the high temperature is utilized in the fight against neoplasms [4]. Although the use of magnetic Pickering droplets in hyperthermia applications has not been reported yet, the high temperature was recently used for the fabrication of Pickering-emulsion-based capsules [5].

In most magnetic hyperthermia experiments, including those with magnetic Pickering emulsions, the alternating magnetic field (AMF) is used to raise the temperature [6,7]. The main reason for this is the simplicity of generating alternating magnetic fields with the commonly accessible single or multilayer solenoids. MNPs exposed to an external AMF undergo magnetization by two main mechanisms which lead to the release of thermal energy to the environment, namely, the delay (relaxation) of the magnetic moment through the oscillation of entire magnetic particle (Brown relaxation) or through the rotation of only magnetic moment itself (Néel relaxation). For larger particles, the movement of the domain walls is the dominant source of energy losses. However, there exists another method for magnetic stimulation of magnetite particles leading to the induction of heat release. This method is based on the application of the rotating magnetic field (RMF). When a magnetic nanoparticle is placed in the RMF it can rotate rather than oscillate in a viscous carrier fluid, and the thermal energy is released due

* Corresponding author.
E-mail address: arkadiusz.jozefczak@amu.edu.pl (A. Józefczak).

https://doi.org/10.1016/j.jmmm.2022.169946
Received 4 July 2022; Received in revised form 26 August 2022; Accepted 7 September 2022
Available online 13 September 2022

to the friction leading to the temperature elevation. By principle, two moments of forces act simultaneously on the nanoparticle: the driving torque and the torque from the resistance forces of the surrounding medium. The presence of two torques leads to a rotation of the spherical MNPs suspended in a carrier fluid [8]. Potentially, the small Pickering droplets stabilized by MNPs can experience such movements as well. Fig. 1 schematically presents the difference in the appearance between MNPs and droplets stabilized with magnetic particles. It should be noted that, like in the case of the AMF application, the processes occurring under the RMF depend on the size of magnetic objects. It means that for larger objects, such as Pickering droplets, the losses of energy from the RMF are caused by the movement of the domain walls rather than the physical rotation of the objects.

Theoretical considerations show that the RMF yields a higher heat output for MNPs dispersion than obtained with the AMF for the same values of the magnetic field intensity H and frequency f [9]. Magnetic fluids based on superparamagnetic iron-oxide nanoparticles placed in the RMF exhibited magnetic heating efficiency (expressed via the rate of temperature increase) more than twice as high as for the AMF [10]. It depended on the size of particles which can be explained by the domination of Brown relaxation, in calorimetric measurements using the RMF, for particles with a diameter greater than 24 nm [11]. Moreover, with the increase of magnetic field intensity, the relaxation losses decreased, while the losses resulting from the movement of domain walls increased [12].

RMF can be used in a variety of applications, e.g., for stimulation of the core–shell droplets. Raju and Koetz [13] showed an inner rotation of the silicone droplet when MNPs were fixed at the inner side of the droplet interface. This is an example of a controlled movement of the interior of complex double emulsions by magnetic manipulation via the interfacially confined magnetic nanoparticles [13]. Zhou *et al.* proposed, in turn, the use of magnetosome particles as nanoscale magnetic stirring bars, that can be encapsulated in micro-droplet and used to stir the solution under an external magnet [14]. In our work, we investigated the heating efficiency of oil-in-oil emulsion stabilized by MNPs under the RMF. It has already been shown [15] that magnetic Pickering emulsions exhibit thermal efficiency under AMF. We additionally compared the temperature increase generated by magnetic materials placed in a rotating and alternating magnetic field. Our results show that the RMF can be effectively used for heating of Pickering emulsion stabilized by magnetite particles, however, the thermal effect in Pickering emulsion depends on the methodology used for the generation a magnetic field.

2. Materials and methods

2.1. Preparation and characterization of magnetic particle suspensions and magnetic Pickering emulsions

Magnetic Pickering emulsions were prepared by applying ultrasound to the mixture of magnetic particles and two types of oil. The castor oil (MA 220–1, MERLIN, Spain) was used as the continuous phase, in which silicone oil (Rhodosil Oils 47 V 50, VWR Chemicals, USA) was dispersed in the form of droplets. The silicone droplets were stabilized by two different types of magnetite nanoparticles purchased from Sigma-Aldrich Co., US, and Nanografi Co., Turkey. Fig. 2**a-b** presents the scanning electron microscopy (SEM) images of MNPs, and Fig. 2**c-d** provides the particle size distributions (PSD) and magnetization curves, respectively. The size distribution of powder magnetite was calculated based on the SEM images containing 100 nanoparticles. The PSD histogram was fitted to a log-normal distribution function to calculate the average particle size as presented elsewhere [16]. The magnetization was measured using the vibrating sample magnetometry (VSM) technique with the VERSALAB commercial device (Quantum Design, USA) in an applied field from −3 T up to 3 T at 300 K with the known weight of the samples.

The emulsions were prepared via the addition of magnetite nanoparticles, silicone oil, and castor oil into the sample cell and mixing them with the ultrasound homogenizer (Sonoplus HD 300; Bandelin, Germany). The mixture was sonicated for 40 s with the ultrasound probe (KE 73) at a working frequency of 18 kHz. The magnetic particle suspensions in castor oil were prepared with the same ultrasound homogenizer for the same length of time, 40 s. In our experiments, four types of samples were evaluated under the influence of the rotating and alternating magnetic field as summarized in Table 1. The mass concentration of MNPs in magnetic Pickering emulsions and magnetic particle suspensions was 10% in the relation to castor oil (10% w/w). The mass ratio of silicone oil to MNPs in magnetic Pickering emulsion was 1:1. To emphasize, both magnetic Pickering emulsions and magnetic suspensions consisted of the same amount of magnetite.

2.2. Methods of calorimetric measurements under rotating and alternating magnetic fields

The system for generating the RMF used a closed magnetic circuit containing a ferrite torus with ferrite cores (Fig. 3). These two pairs of coils together with capacitors in parallel connected to them constitute a

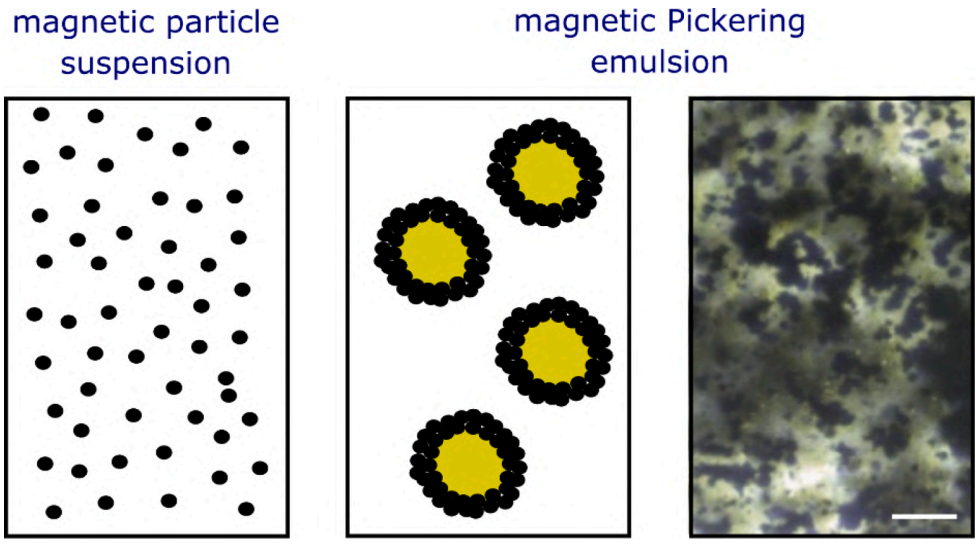

Fig. 1. A schematic illustration of magnetic particle suspension and Pickering emulsion stabilized by magnetic particles. The scale bar is 100 μm.

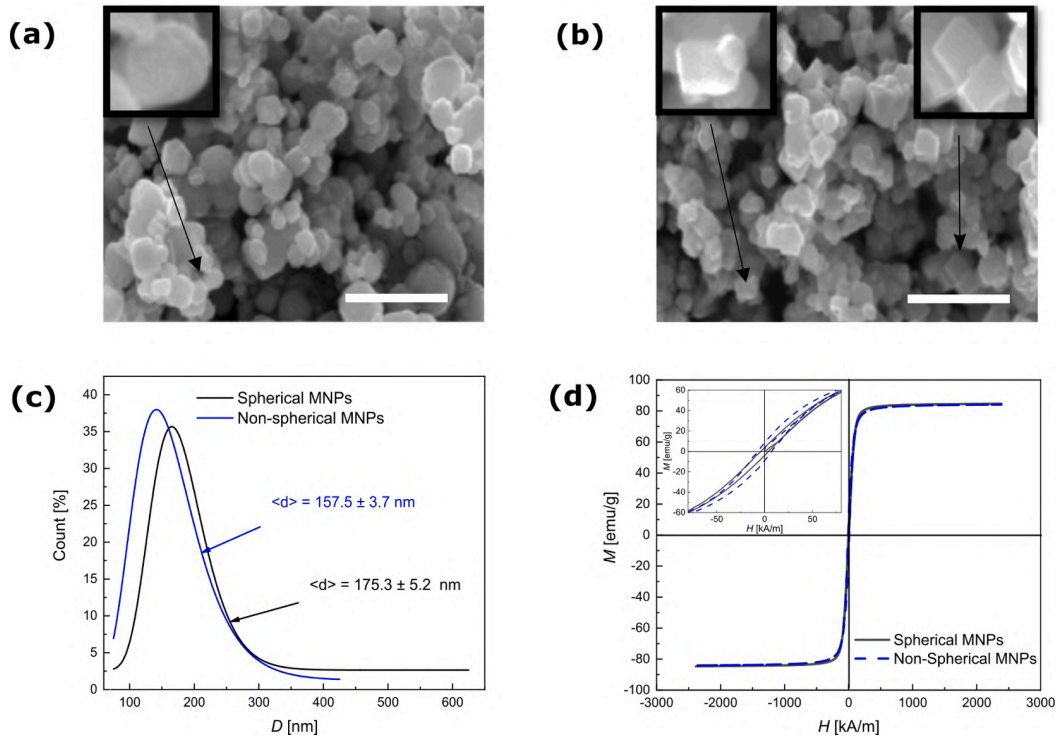

Fig. 2. The scanning electron microscopy images for (a) spherical MNPs and (b) non-spherical MNPs. The scale bar is 1 μm. (c) The particle size distribution for the spherical and non-spherical MNPs. (d) Magnetization curves of magnetic powders consisting of spherical and non-spherical MNPs. The inset graph presents zoomed area for the lowest magnetic field intensities and indicate the presence of a magnetic hysteresis loop.

Table 1
The description of the samples of emulsions and suspensions used in the experiments.

Sample	Description	Magnetic particles
S1	magnetic Pickering emulsion	spherical, 175.3 ± 5.2 nm
S2	magnetic particle suspension	spherical, 175.3 ± 5.2 nm
S3	magnetic Pickering emulsion	non-spherical, 157.5 ± 3.7 nm
S4	magnetic particle suspension	non-spherical, 157.5 ± 3.7 nm

resonant *LC* circuit. They produce two separate magnetic fluxes of equal amplitudes with mutually shifted phases. Since the magnetic fluxes have also shifted in space by the angle of 90°, the RMF is generated in the center of the device as a result of the superposition of both fluxes [12]. The amplitude of the magnetic field intensity was measured with a probe (measuring coil) inserted in the center of the magnetic system. From the oscilloscope reading of the peak-to-peak voltage value induced in the probe, U_p, we obtained the value of the magnetic field intensity H according to the formula:

$$H\left[\frac{\mathrm{A}}{\mathrm{m}}\right] = \frac{U_p\left[V_{pp}\right]}{4\pi S_p f \bullet \mu_0} \tag{1}$$

where S_p [m^2] is the area of all windings for this coil, f [Hz] is the frequency and μ_0 is the magnetic permeability of free space [12]. In our experiments, the intensity of the RMF was in the range from 5.8 to 15.7

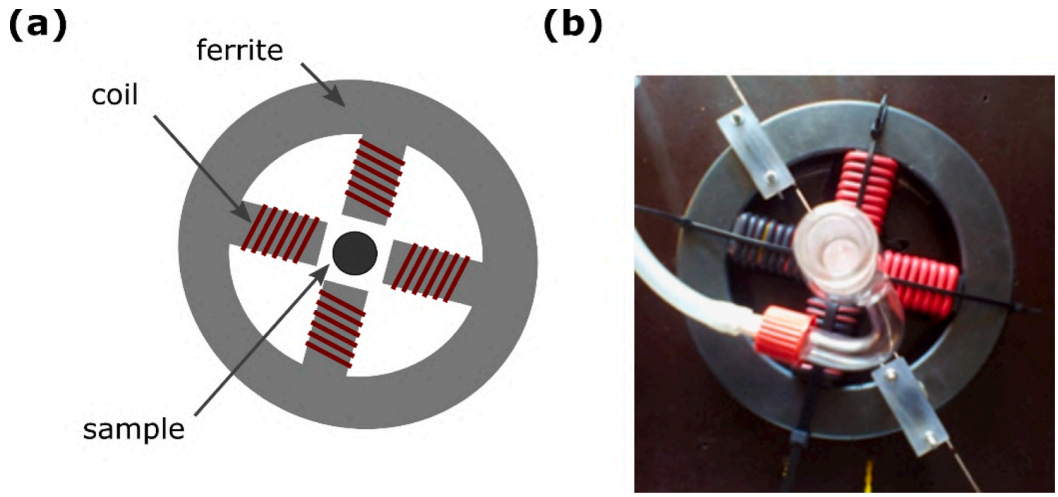

Fig. 3. Experimental setup (magnetic circuits) used for generating a rotating magnetic field (RMF). (a) The scheme and (b) the actual image of the setup with presented cooling system stabilizing the temperature. During measurements with an alternating magnetic field (AMF), only one pair of magnetic coils was turned on.

kA/m for the constant frequency $f = 38.3$ kHz. The same system was used for generating the AMF. To achieve this, only one pair of coils, opposite to each other, is fed with the signal coming from the power amplifier and through a ferrite transformer (the second pair of coils is turned off) [12].

To obtain the temporal evolution of the temperature during magnetic heating, the samples S1-S4 were placed in the glass vials where the temperature was recorded every second using the optical fiber temperature sensor FOT-L-SD (FISO Technology Inc., USA) immersed in the studied sample. The accuracy of the sensor was 0.10 °C and the resolution of 0.01 °C. The temperature elevation of the samples caused by magnetic heating was expressed in relation to the room temperature. To thermostat the samples during measurements, they were placed in a cooler with flowing water as presented in Fig. 3**b**. Before switching on the magnetic field, the temperature of a sample was observed for 30 s. When the mean value of temperature fluctuations was less than around 0.005 °C /s, the magnetic field was turned on. The stabilization of the sample temperature before measurements was crucial for the experiments conducted for the lowest intensity of magnetic fields, as the observed experimental temperature elevations were relatively small.

3. Results and discussion

Fig. 4 presents the optical microscopy images for a single droplet covered by spherical MNPs exposed to the rotating neodymium magnet. The magnet was applied from the top of the transparent sample cell and rotated around it to simulate the low-frequency RMF during calorimetric measurements. It was easily observed that the Pickering droplet followed the movement of the rotating magnet. Even though the rotation of the field in our RMF setup does not come from the motion of the magnets, but the traveling magnetic fluxes, the behavior of the magnetic Pickering droplet was assumed to be similar. Fig. 4**b-d** provide insight into the possible motion of the nanoparticles floating inside the droplet, triggered by the rotating magnetic field. This motion could potentially extend the applicability of the RMF for experiments with droplets containing nanoparticles, as has recently been presented by Zhou *et al.* In their work, magnetotactic bacteria played a role of nanoscale stirring bars entrapped inside the Pickering droplets, causing the chemical reactions to occur at a higher rate [14]. The Pickering droplets obtained from emulsification are much smaller (several micrometers in size) than those presented in Fig. 4, and usually fully covered by at least one layer of MNPs. However, that does not change the fact that the results presented in Fig. 4 prove the magneto-responsiveness of Pickering droplets to time-varying magnetic fields.

To evaluate the thermal efficiency of colloidal systems exposed to magnetic fields generated by our setup, we carried out the calorimetric measurements in the RMF and the AMF mode for samples with two types of MNPs. MNPs used in this study were in the size of hundreds of nanometers (Table 1) but varied in shape. The inset images in Fig. 2**a-b** indicate that nanoparticles used in samples S3 and S4 exhibited higher asphericity compared to samples S2 and S1. For this study, we refer to the MNPs used in samples S3 and S4 as "non-spherical". It was observed that the irregular shape of the particles has an impact on the thermal efficiency achieved during magnetic heating measurements. The results obtained for the samples of Pickering emulsion and magnetic dispersion containing spherical particles are presented in Fig. 5.

In Fig. 5, the time-dependent temperature elevation obtained during magnetic heating followed a well-known trend typical for the measurements under non-adiabatic conditions [17], both for emulsions and dispersions. During the initial seconds of the experiment, when the magnetic field was turned off, the temperature did not change noticeably. After magnetic fields were applied, the monitored temperature increased significantly, but the temperature increase rate was not constant over the whole measurement. The highest temperature increase rate was observed for the highest intensity of the magnetic field. This dependence is consistent with various reports on the heating of magnetic fluids [17,18] and Pickering emulsions [6,15]. Another interesting fact that can be read from Fig. 5 is that the observed temperature increase under the RMF mode (for the highest intensity of magnetic field) was several times higher than the one obtained for the AMF mode, despite both modes having an approximately equal intensity of magnetic field. For sample S2, the temperature increased up to 0.4 °C for the AMF and up to 2 °C for the RMF. Even though in the current study we used large nanoparticles, of a size exceeding the superparamagnetic limit for magnetite which is around 100–160 nm, the presented results are consistent with those previously reported for magnetic fluids [19,20]. It proves that for used frequency and the range of magnetic field intensities the movement of magnetic domain walls, rather than the Brownian

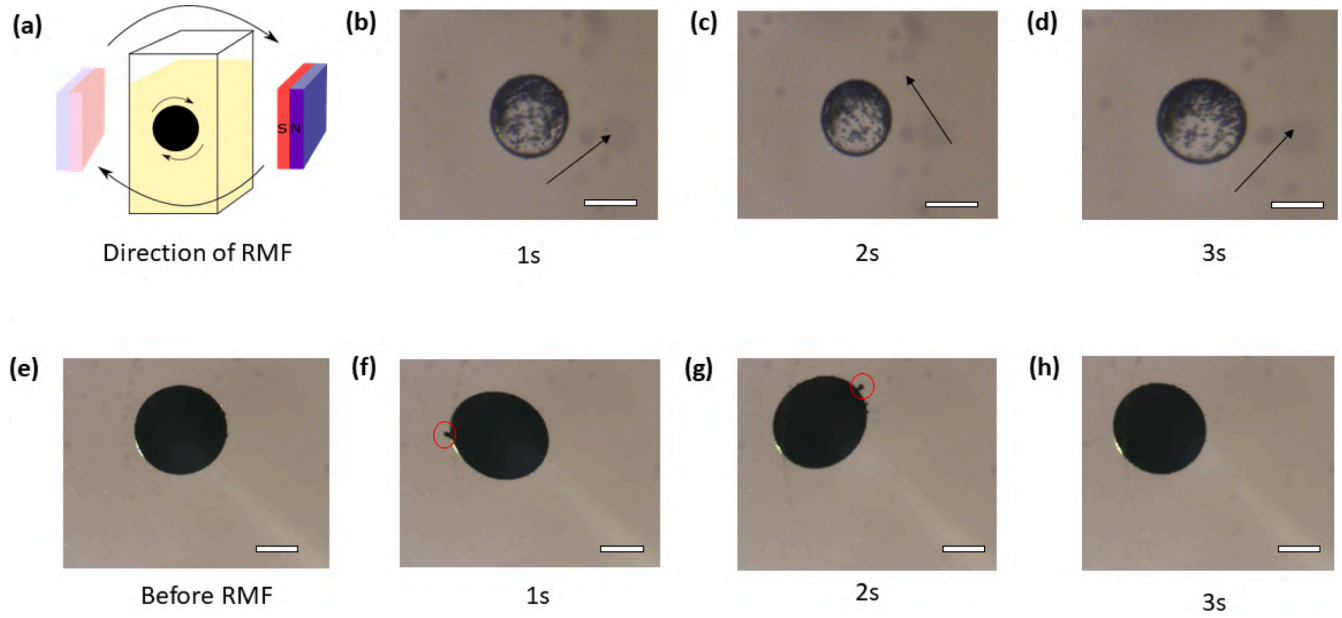

Fig. 4. (a) The schematic illustration of the experimental method for the rotating magnetic field. (b-d) Optical microscopy images of non-fully covered Pickering droplets stabilized with "spherical" MNPs exposed to the rotating magnet. The scale bar is 400 μm. (e-h) Optical microscopy images of fully covered Pickering droplets with spherical MNPs exposed to the rotating magnet. The scale bar is 1000 μm. The change in position of a red circle indicates the movement of a droplet.

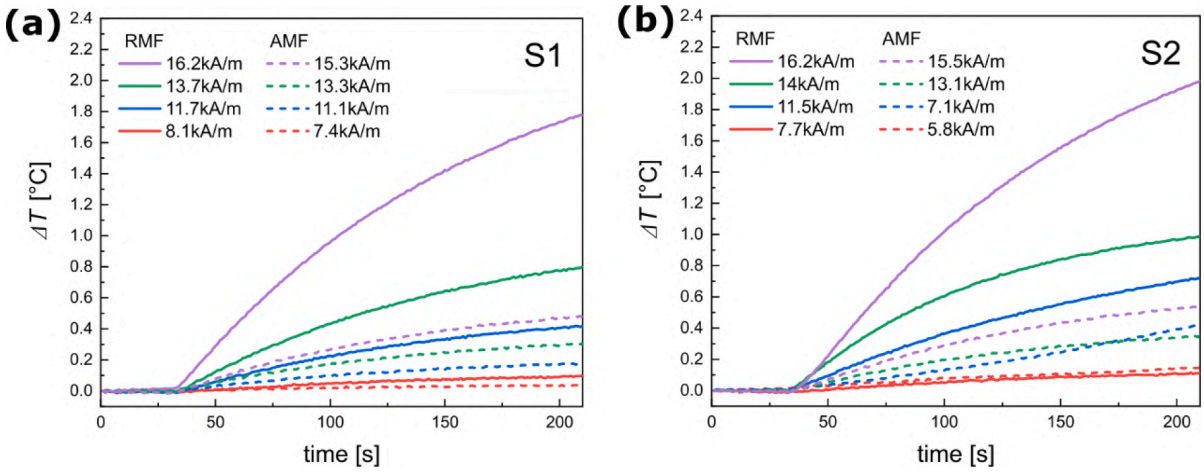

Fig. 5. Temperature increase measured in (a) magnetite-stabilized Pickering emulsions and (b) oil suspension of "spherical" magnetic particles under the rotating (RMF) and alternating (AMF) magnetic fields.

movement of the whole magnetic objects, is a dominant mechanism of heating. Although the droplets covered by nanoparticles are larger than particles and the size of the Pickering droplet generally depends on the number of particles used as stabilizers, the exposition of Pickering emulsions stabilized with spherical particles to the RMF and the AMF provided comparable temperature increase to the ones obtained for magnetic suspension. This provides further evidence that in the proposed experiment the rotation of the magnetic objects cannot be responsible for heating under the RMF. Recently, it also has been shown that the improved magnetic dipolar interactions result in more significant ferromagnetic behavior of particles (hysteresis losses) that also increase with a higher levels of agglomerations [21]. As the magnetic particles used in our study have not been functionalized, the droplets and particles had a tendency to aggregate which could lead to improved contribution from the movement of magnetic domain walls to magnetic heating.

The improved efficiency of heat generation obtained with the RMF compared to the AMF was expected based on the previous works performed on magnetic fluids, where particles were covered with a layer of surfactant. However, the authors used different systems for generating the RMF and the AMF [10]. In our work, the same magnetic arrangement was used for generation of the RMF and the AMF. The observed temperature elevation in Pickering emulsion under the AMF (sample S1, Fig. 5**a**) is much lower than what we have previously reported. The observed temperature elevation was up to 30 °C for a similar concentration of magnetic material [15]. However, in the previous experiments we used a different system for generating the AMF. It consisted of one coil driven by the AC electric field of much higher frequency (around 450 kHz *versus* around 40 kHz in the current paper). Additionally, for magnetic heating measurements, the mass concentration of magnetic material in the tested sample is a crucial parameter that influences the temperature elevation. Numerous works on magnetic fluid hyperthermia using the AMF have reported such dependence [22,23]. However, too high concentration of magnetic material can deteriorate the heating efficiency due to the increased magnetic dipole–dipole interactions [24,25]. Reported limits for the deterioration of the heating under the AMF vary and depend on several parameters such as the intensity and frequency of applied AMF and the size of particles [24,26]. In our experiments, the content of MNPs was the same for all samples (10% w/w).

The temperature increase *versus* time of application of the RMF and the AMF was also investigated for non-spherical MNPs as presented in Fig. 6. Comparing the results presented in Fig. 5**a** and Fig. 6**a**, one can see that the Pickering emulsion stabilized with non-spherical MNPs (S3) exhibited lower temperature increase both under the RMF and the AMF. Surprisingly, the temperature increase in the sample with magnetic suspension was higher when non-spherical MNPs were used, especially for the application of the high-intensity RMF.

According to Fig. 2**d**, both types of particles possessed practically the same magnetization saturation which is the predictor of the responsiveness to the external magnetic fields. The same dependency applies to the hysteresis loops presented in the inset of Fig. 2**d**. The mass concentration of magnetic material in each sample was also equal, therefore, the source of the observed difference in heating performance should be explained in another way. Some authors suggested that the crystal structure of magnetite nanoparticles and their shape influence the critical size for which the transition between single- and multi-domain particles occurs [27]. Others reported that the exquisite heating efficiency of octahedral [28] and cubic [29] nanoparticles exposed to the AMF was caused by the difference in the character of magnetic anisotropy for the non-spherical symmetry. Thus, it is clear that the shape of MNPs influences their behavior under the AMF. However, to our best knowledge, such an impact was not investigated in the context of the RMF. Furthermore, the importance of reported effects is rather negligible for our samples as the mean size of MNPs we used was in the range of 150 – 180 nm. Typically, Pickering droplets are much larger, and their size was estimated to be up to several micrometers [15]. Under the RMF, the packing of particles can influence the results similarly to the situation when MNPs are placed into the tumor, which was shown to deteriorate heating efficiency [30]. In our case, as the surface of particles is unmodified and the tendency of aggregation is high, such a deteriorating effect may occur [31]. On the other hand, as mentioned in the discussion of the results presented in Fig. 5, when the rate of agglomeration in the system increases, the particle–particle interactions increases as well leading to more pronounced hysteresis losses, that contribute to the overall magnetic heating process. Additionally, the Pickering droplet consists of the particle layer (or layers, especially in the case of uncoated MNPs) that can be referred to as "hollow clusters" [32]. Furthermore, it should be noted that for non-spherical MNPs the temperature elevation observed in suspension was comparable to the suspension with spherical MNPs (sample S4 *versus* sample S2). It cannot be explained only by the presence of particle clusters and requires further investigation due to the potential for aggregations. Also, the temperature elevation in emulsions stabilized with "non-spherical" nanoparticles, apart from the results under the RMF for the highest magnetic field intensity, is comparable (Fig. 5**b** *versus* Fig. 6**b**). Nevertheless, improved performance of the RMF compared to the AMF was proved also for the non-spherical particles. It suggests the promising use of the RMF in magnetic heating for a wide range of particle types.

For the potential application of such samples in biomedicine, it is

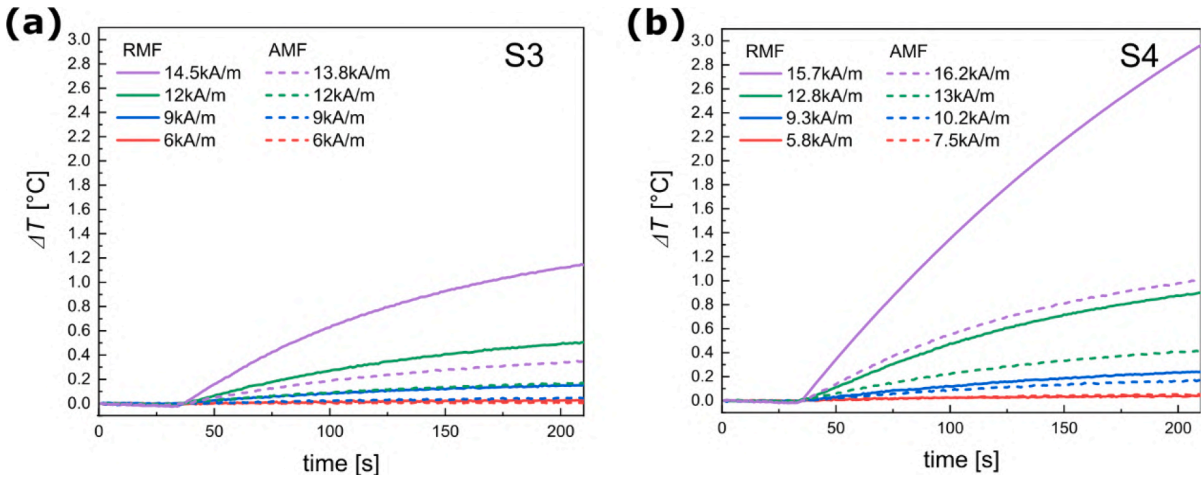

Fig. 6. Temperature increase measured in (a) magnetite-stabilized Pickering emulsions and (b) oil suspension of "non-spherical" magnetic particles under the rotating (RMF) and alternating (AMF) magnetic fields.

crucial to ensure a relatively low concentration of magnetic materials administered to the patient's body [20,33]. For the concentrations that do not exceed several percent w/w, a deteriorating effect of dipole–dipole interactions on heating efficiency due to relaxation losses should be negligible. Therefore, in this range of concentrations, the increased number of particles is expected to provide higher temperature elevation in a sample. Not without significance is also the role of carrier fluid used as a suspension for magnetic materials. In this work, we used castor oil which is several hundred times more viscous than water. On the other hand, the specific limit proposed by Brezovich using the product of magnetic field intensity and frequency of time-varying magnetic fields is fulfilled in our measurements by almost one order of magnitude [33]. It means that the optimization of the parameters of the applied fields rather than the increase of concentration of particles could improve heating efficiency for all types of tested samples.

Measurements of the temperature increase over time are not the only possible method used for evaluation of the heating efficiency in hyperthermia experiments. The rate of temperature elevation is also commonly evaluated. Such a parameter is also present in the expression for the specific absorption rate (SAR) and the specific loss power (SLP). The most common method is based on the calculations of the slope for the linear fitting of the curve to the initial seconds of experiments. For those seconds, the existing conditions are similar to the adiabatic conditions due to the small heat transfer between the sample and the surroundings. For a better understanding of the source of differences in the heating efficiency between Pickering emulsions exposed to the AMF and the RMF, we calculated the temperature increase rate and plotted it in the function of the applied fields. Results are presented in Fig. 7. They were fitted to the power-law equation [34] by using linear fitting procedure. The results in Fig. 7 clearly indicate that not only the temperature increase is higher for the Pickering emulsions stabilized with "spherical" MNPs. Simultaneously, the dynamic of temperature increase for RMF was confirmed to be much higher than for AMF.

For the suspensions of small MNPs exposed to AMF, it has been shown in the literature [35] that the values of exponents derived from the fitting to the power-law formula can deviate from $n = 2$ when heat dissipation from the so-called ferromagnetic regime starts dominating. It was observed even for MNPs with sizes merely exceeding 10 nm. Here, the obtained values of n fall within the range of 1.5–5.5 and show the correlation neither with the applied magnetic field (AMF *vs.* RMF) nor the type of particles. It should be noted Pickering droplets are much larger than single magnetic particles and could form aggregates. This can also determine the observed deviations since, for the increased size of magnetic objects, the intensity of magnetic field that limits the superparamagnetic behavior decreased [35].

Previously, Pickering droplets have been investigated under the RMF mainly in the context of droplet manipulation rather than heat generation [14,36]. According to the results presented in our work, the RMF

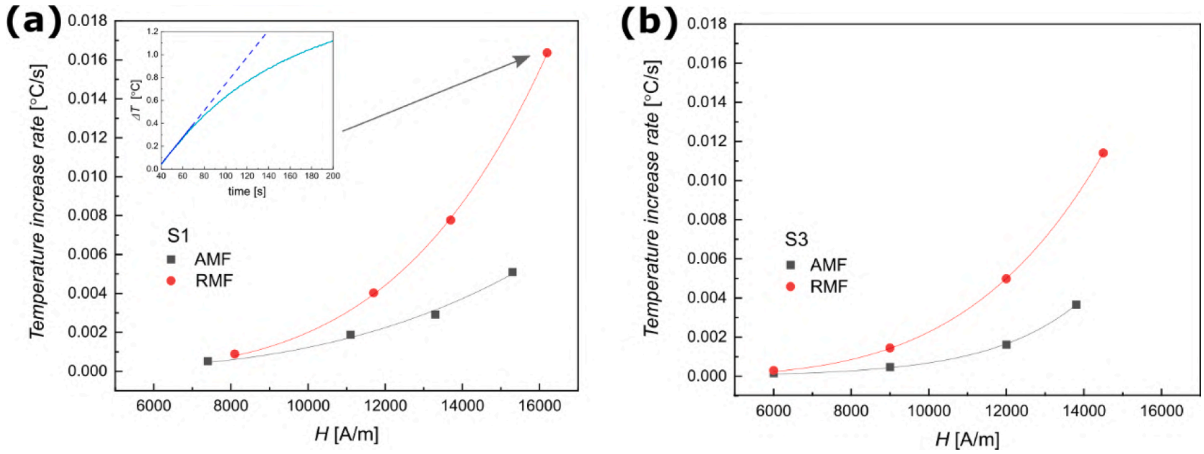

Fig. 7. Temperature elevation rate *versus* intensity of the applied rotating magnetic field (RMF) for Pickering emulsions stabilized with (a) "spherical" and (b) "non-spherical" MNPs (samples S1 and S3, respectively). The inset figure shows the fitting procedure for the point indicated by the grey arrow.

can be also a promising tool to induce a heating in Pickering emulsions. In the future, the observed response of Pickering emulsion droplets to the RMF and the local induction of a higher temperature can be synergistically used, e.g., for the release of substances from the inside of droplets and colloidosomes (i.e., armored emulsion droplets) or even from capsules formed with emulsion droplet precursors. The magnetic Pickering droplets were also shown to be responsive to the static magnetic fields which resulted in their magnetophoresis or deformation [37]. The combined use of static and time-varying magnetic fields could bring new possibilities for limiting the concentration of magnetic materials. What is more, also magnetic fields with different frequencies could be utilized. Recently, Konopacki *et al.* proposed the RMF with a very low frequency of 50 Hz to generate heat in samples of magnetic fluid with MNPs of the size of tens of nm. The heating efficiency clearly decreased with the increasing concentration of magnetic materials [38]. On the other hand, different researchers are working on the so-called frequency mixing magnetic detection for use in bio-sensing [39]. Therefore, the possibility of single setup to generate two different modes of magnetic fields is very important.

The crucial requirement that needs to be fulfilled by magnetic heating procedures applied in biomedicine is their ability to provide repeatable conditions of heating. Recently, Wells *et al.* presented the comparison of various results for calorimetric measurements performed on the same type of magnetic fluids but in different laboratories and reported existing discrepancies. The authors suggested also the urgent need for unification of measurement protocols for magnetic hyperthermia studies. [40]. It is very important for complex systems such as Pickering emulsions, that are not broadly investigated in the literature in the context of magnetic heating. Thus, in the future, drawing definite conclusions on such systems should be done only by providing stable and repeatable experimental conditions.

4. Conclusions

In this work, MNPs were used as a base for magnetic suspensions and as stabilizers for Pickering emulsions. At the same time, magnetic particles acted as a source of heat in the high-frequency rotating magnetic field (RMF). The release of thermal energy was investigated in the alternating magnetic field (AMF) as well. The observed thermal effect depended on the mode of the generated magnetic field: alternating or rotating. For the suspension of MNPs in high-viscous castor oil, the temperature increase during magnetic heating was higher when the RMF was used. Similar results were obtained for Pickering droplets stabilized with the same magnetic nanoparticles. We showed that the heating efficiency under the RMF is also size-dependent and, for magnetic objects with sizes above the superparamagnetic limit, the movement of magnetic domain walls within the particles rather than the movement of the whole objects dominates. Furthermore, the use of MNPs with nearly the same size and magnetization saturation, but more irregular shape resulted in the variation of the temperature increase both in the magnetic suspensions and Pickering emulsions. The reported findings show the promising role of the RMF application for the heating of magnetic Pickering emulsions when the dominating heating mechanism is the movement of magnetic domain walls.

CRediT authorship contribution statement

Rafał Bielas: Conceptualization, Visualization, Writing – original draft. **Bassam Jameel:** Investigation, Visualization, Writing – original draft. **Andrzej Skumiel:** Investigation. **Milan Timko:** Writing – review & editing. **Peter Kopčanský:** Writing – review & editing. **Arkadiusz Józefczak:** Conceptualization, Methodology, Supervision, Funding acquisition.

Declaration of Competing Interest

The authors declare that they have no known competing financial interests or personal relationships that could have appeared to influence the work reported in this paper.

Acknowledgments

This research was supported by the Polish National Science Centre through the projects no. 2019/35/O/ST3/00503 (PRELUDIUM BIS) and no. 2019/35/N/ST5/00402 (PRELUDIUM) and by the projects: MVTS SAV SKTW AMAZON, SAS-MOST JRP 2021/2 (AZCAI) and MVTS SAV FMF-Flexible Magnetic Filaments. The authors wish to thank Dr. Katarzyna Kaczmarek (AMU, Poznań) for the valuable discussions and suggestions.

References

[1] L. Fu, Q. Ma, K. Liao, J. An, J. Bai, Y. He, Application of Pickering emulsion in oil drilling and production, Nanotechnol. Rev. 11 (1) (2022) 26–39.
[2] H. Zhao, Y. Yang, Y. Chen, J. Li, L. Wang, C. Li, A review of multiple Pickering emulsions: solid stabilization, preparation, particle effect, and application, Chem. Eng. Sci. 248 (2022), 117085.
[3] S. Peito, D. Peixoto, I. Ferreira-Faria, A. Margarida Martins, H. Margarida Ribeiro, F. Veiga, J. Marto, A. Cláudia Paiva-Santos, Nano- and microparticle-stabilized Pickering emulsions designed for topical therapeutics and cosmetic applications, Int. J. Pharm. 615 (2022), 121455.
[4] M. Dabaghi, S.M.M. Rasa, E. Cirri, A. Ori, F. Neri, R. Quaas, I. Hilger, Iron oxide nanoparticles carrying 5-fluorouracil in combination with magnetic hyperthermia induce thrombogenic collagen fibers, cellular stress, and immune responses in heterotopic human colon cancer in mice, Pharmaceutics 13 (10) (2021) 1625.
[5] R. Bielas, D. Surdeko, K. Kaczmarek, A. Józefczak, The potential of magnetic heating for fabricating Pickering-emulsion-based capsules, Colloids Surf. B 192 (2020), 111070.
[6] S. Ranoo, B. Lahiri, M. Nandy, J. Philip, Enhanced magnetic heating efficiency at acidic pH for magnetic nanoemulsions stabilized with a weak polyelectrolyte, J. Colloid Interface Sci. 579 (2020) 582–597.
[7] R. Bielas, B. Jameel, A. Józefczak, Monitoring of Pickering emulsion stability during magnetic heating using ultrasound measurements, Measurement 178 (2021), 109431.
[8] S. Andrzej, Influence of high frequency rotating magnetic field on the effect of heating magnetic fluid, Int. J. Phys. Res. Appl. 4 (1) (2021) 015–018.
[9] Y.L. Raikher, V.I. Stepanov, Power losses in a suspension of magnetic dipoles under a rotating field, Phys. Rev. E 83 (2) (2011), 021401.
[10] A. Skumiel, P. Kopcansky, M. Timko, M. Molcan, K. Paulovicova, R. Wojciechowski, The influence of a rotating magnetic field on the thermal effect in magnetic fluid, Int. J. Therm. Sci. 171 (2022), 107258.
[11] A. Skumiel, A new way to generate a rotating magnetic field in the high frequency range, J. Magn. Magn. Mater. 541 (2022), 168529.
[12] A. Skumiel, Generation of a rotating high frequency magnetic field designed for use in magnetic hyperthermia, J. Magn. Magn. Mater. 553 (2022), 169294.
[13] R.R. Raju, J. Koetz, Inner rotation of pickering janus emulsions, Nanomaterials 11 (12) (2021) 3312.
[14] X. Zhou, C. Chen, C. Cao, T. Song, H. Yang, W. Song, Enhancing reaction rate in a Pickering emulsion system with natural magnetotactic bacteria as nanoscale magnetic stirring bars, Chem. Sci. 9 (9) (2018) 2575–2580.
[15] R. Bielas, T. Hornowski, K. Paulovičová, M. Rajňák, A. Józefczak, The effect of magnetic particles covering the droplets on the heating rate of Pickering emulsions in the AC magnetic field, J. Mol. Liq. 320 (2020), 114388.
[16] Z. Rozynek, A. Józefczak, K. Knudsen, A. Skumiel, T. Hornowski, J. Fossum, M. Timko, P. Kopčanský, M. Koneracká, Structuring from nanoparticles in oil-based ferrofluids, Eur. Phys. J. E 34 (3) (2011) 1–8.
[17] B.B. Lahiri, T. Muthukumaran, J. Philip, Magnetic hyperthermia in phosphate coated iron oxide nanofluids, J. Magn. Magn. Mater. 407 (2016) 101–113.
[18] M. Kubovcikova, M. Koneracka, O. Strbak, M. Molcan, V. Zavisova, I. Antal, I. Khmara, D. Lucanska, L. Tomco, M. Barathova, M. Zatovicova, D. Dobrota, S. Pastorekova, P. Kopcansky, Poly-L-lysine designed magnetic nanoparticles for combined hyperthermia, magnetic resonance imaging and cancer cell detection, J. Magn. Magn. Mater. 475 (2019) 316–326.
[19] L.S. Ganapathe, M.A. Mohamed, R. Mohamad Yunus, D.D. Berhanuddin, Magnetite (Fe3O4) nanoparticles in biomedical application: From synthesis to surface functionalisation, Magnetochemistry 6 (4) (2020) 68.
[20] J. Wallyn, N. Anton, T.F. Vandamme, Synthesis, principles, and properties of magnetite nanoparticles for in vivo imaging applications—a review, Pharmaceutics 11 (11) (2019) 601.
[21] U. Engelmann, E.M. Buhl, M. Baumann, T. Schmitz-Rode, I. Slabu, Agglomeration of magnetic nanoparticles and its effects on magnetic hyperthermia, Curr. Directions Biomed. Eng. 3 (2) (2017) 457–460.
[22] A. Rezanezhad, A. Hajalilou, F. Eslami, E. Parvini, E. Abouzari-Lotf, B. Aslibeiki, Superparamagnetic magnetite nanoparticles for cancer cells treatment via

magnetic hyperthermia: effect of natural capping agent, particle size and concentration, J. Mater. Sci.: Mater. Electron. 32 (19) (2021) 24026–24040.
[23] P. Linh, N. Phuc, L. Hong, L. Uyen, N. Chien, P. Nam, N. Quy, H. Nhung, P. Phong, I.-J. Lee, Dextran coated magnetite high susceptibility nanoparticles for hyperthermia applications, J. Magn. Magn. Mater. 460 (2018) 128–136.
[24] V. Pilati, G. Gomide, R.C. Gomes, G.F. Goya, J. Depeyrot, Colloidal stability and concentration effects on nanoparticle heat delivery for magnetic fluid hyperthermia, Langmuir 37 (3) (2021) 1129–1140.
[25] A. Kuncser, N. Iacob, V.E. Kuncser, On the relaxation time of interacting superparamagnetic nanoparticles and implications for magnetic fluid hyperthermia, Beilstein J. Nanotechnol. 10 (2019) 1280–1289.
[26] B.A. Evans, M.D. Bausch, K.D. Sienerth, M.J. Davern, Non-monotonicity in the influence of nanoparticle concentration on SAR in magnetic nanoparticle hyperthermia, J. Magn. Magn. Mater. 465 (2018) 559–565.
[27] Q. Li, C.W. Kartikowati, S. Horie, T. Ogi, T. Iwaki, K. Okuyama, Correlation between particle size/domain structure and magnetic properties of highly crystalline Fe3O4 nanoparticles, Sci. Rep. 7 (1) (2017) 9894.
[28] I. Castellanos-Rubio, I. Rodrigo, R. Munshi, O. Arriortua, J.S. Garitaonandia, A. Martinez-Amesti, F. Plazaola, I. Orue, A. Pralle, M. Insausti, Outstanding heat loss via nano-octahedra above 20 nm in size: from wustite-rich nanoparticles to magnetite single-crystals, Nanoscale 11 (35) (2019) 16635–16649.
[29] K. Parekh, H. Parmar, V. Sharma, R.V. Ramanujan, Heating efficiency dependency on size and morphology of magnetite nanoparticles, AIP Conf. Proc. 1942 (1) (2018), 050022.
[30] S. Dutz, R. Hergt, Magnetic particle hyperthermia—a promising tumour therapy? Nanotechnology 25 (45) (2014), 452001 https://doi.org/10.1088/0957-4484/25/45/452001.
[31] B. Jameel, T. Hornowski, R. Bielas, A. Józefczak, Ultrasound study of magnetic and non-magnetic nanoparticle agglomeration in high viscous media, Materials 15 (10) (2022) 3450.
[32] R. Bielas, A. Józefczak, The effect of particle shell on cooling rates in oil-in-oil magnetic pickering emulsions, Materials 13 (21) (2020) 4783.
[33] S. Dutz, R. Hergt, Magnetic nanoparticle heating and heat transfer on a microscale: basic principles, realities and physical limitations of hyperthermia for tumour therapy, Int. J. Hyperth. 29 (8) (2013) 790–800.
[34] R.M. Wojciechowski, A. Skumiel, M. Kurzawa, A. Demenko, Design, application and investigation of the system for generation of fast changing, rotating magnetic field causing hyperthermic effect in magnetic liquids, Measurement 194 (2022), 111020.
[35] S. Del Sol Fernández, O.F. Odio, P.M. Crespo, E.O. Pérez, G. Salas, L. Gutiérrez, M. d.P. Morales, E. Reguera, Tunable control of the structural features and related physical properties of MnxFe3–xO4 nanoparticles: implication on their heating performance by magnetic hyperthermia, J. Phys. Chem. C 126 (24) (2022) 10110–10128, https://doi.org/10.1021/acs.jpcc.2c01403.
[36] G.-P. Zhu, Q.-Y. Wang, Z.-K. Ma, S.-H. Wu, Y.-P. Guo, Droplet manipulation under a magnetic field: a review, Biosensors (Basel) 12 (3) (2022) 156.
[37] B. Jameel, R. Bielas, T. Hornowski, A. Józefczak, Propagation of ultrasonic wave in magnetic Pickering emulsion under DC magnetic field, J. Magn. Magn. Mater. 542 (2022), 168590.
[38] M. Konopacki, M. Jędrzejczak-Silicka, K. Szymańska, E. Mijowska, R. Rakoczy, Effect of rotating magnetic field on ferromagnetic structures used in hyperthermia, J. Magn. Magn. Mater. 518 (2021), 167418.
[39] U.M. Engelmann, A. Shalaby, C. Shasha, K.M. Krishnan, H.-J. Krause, Comparative modeling of frequency mixing measurements of magnetic nanoparticles using micromagnetic simulations and Langevin theory, Nanomaterials 11 (5) (2021) 1257.
[40] J. Wells, D. Ortega, U. Steinhoff, S. Dutz, E. Garaio, O. Sandre, E. Natividad, M. M. Cruz, F. Brero, P. Southern, Q.A. Pankhurst, S. Spassov, Challenges and recommendations for magnetic hyperthermia characterization measurements, Int. J. Hyperth. 38 (1) (2021) 447–460.

7. Statements of co-authors

ADAM MICKIEWICZ UNIVERSITY, POZNAŃ
Faculty of Physics
Chair of Acoustics

March 22, 2024

Co-author Statement

I declare that I am the co-author of the following publications and my contribution to the presented publications was as follows:

[1] Bassam Jameel, Rafał Bielas, Tomasz Hornowski and Arkadiusz Józefczak, Propagation of ultrasonic wave in magnetic Pickering emulsion under DC magnetic field, J. Magn. Magn. Matter. 542 (2022) 168590.

My contribution: conceptualization, methodology, supervision, funding acquisition.

[2] R. Bielas, B. Jameel, A. Skumiel, M. Timko, P. Kopčanský, A. Józefczak, Magnetic pickering emulsions heated in a rotating magnetic field, J. Magn. Magn. Matter. 563 (2022) 169946.

My contribution: conceptualization, methodology, supervision, funding acquisition.

[3] Bassam Jameel, Tomasz Hornowski, Rafał Bielas and Arkadiusz Józefczak, Ultrasound study of magnetic and non-magnetic nanoparticles agglomeration in high viscous media, Materials, (2022) 15(10) (2022) 3450.

My contribution: conceptualization, methodology, supervision, finalization.

[4] B. Jameel, R. Bielas, A. Józefczak, Ultrasound measurements of particle shells in magnetic Pickering emulsions, Measurement 220 (2023) 113409.

My contribution: conceptualization, methodology, supervision, funding acquisition.

[5] B. Jameel, K. Paulovičová, J. Tóthová, M. Rajňák, M. Molčan, R. Bielas, A. Józefczak, Magnetorheological characterization of oil-in-oil magnetic Pickering emulsions, J. Magn. Magn. Matter. 588 (2023) 171433.

My contribution: conceptualization, methodology, supervision, funding acquisition.

[6] B. Jameel, Y. Harkavyi, R. Bielas, A. Józefczak, Optimization of ultrasound heating by magnetic Pickering emulsions, Ultrasonics Sonochemistry (2024): *submitted, under review.*

My contribution: conceptualization, methodology, supervision.

With best regards,

Arkadiusz Józefczak
arkadiusz.jozefczak@amu.edu.pl

Co-author Statement

I hereby declare my contributions to the following publications:

- Jameel, B., Hornowski, T., Bielas, R., and Józefczak, A., 2022. Ultrasound study of magnetic and non-magnetic nanoparticle agglomeration in high viscous media. Materials, 15(10), 3450.

I contributed to the methodological preparations of the experiments and the finalization of the manuscript.

- Jameel, B., Bielas, R., and Józefczak, A., 2023. Ultrasound measurements of particle shells in magnetic Pickering emulsions. Measurement, 220, p.113409.

I participated in the methodological preparations of the experiments and the final review and editing of the manuscript.

- Jameel, B., Paulovičová, K., Tóthová, J., Rajňák, M., Molčan, M., Bielas, R. and Józefczak, A., 2023. Magnetorheological characterization of oil-in-oil magnetic Pickering emulsions. Journal of Magnetism and Magnetic Materials, 588, p.171433.

I contributed to the methodological preparations of the experiments and the finalization of the manuscript.

- Jameel, B., Harkavyi, Y., Bielas, R., and Józefczak, A., 2024. Optimization of ultrasound heating with Pickering droplets using core-shell scattering theory. *submitted to Ultrasonic Sonochemistry*

I participated in the methodological preparations of the research, as well as the final review and editing of the manuscript. I also supervised the work.

- Jameel, B., Bielas, R., Hornowski, T., and Józefczak, A., 2022. Propagation of ultrasonic wave in magnetic Pickering emulsion under DC magnetic field. Journal of Magnetism and Magnetic Materials, 542, p.168590.

I conceptualized the research, partially prepared the graphics, and participated in writing the original draft of the manuscript.

- Bielas, R., Jameel, B., Skumiel, A., Timko, M., Kopčanský, P. and Józefczak, A., 2022. Magnetic pickering emulsions heated in a rotating magnetic field. Journal of Magnetism and Magnetic Materials, 563, p.169946.

I conceptualized the research, partially prepared the graphics, and participated in writing the original draft of the manuscript.

With best regards,

Dr. Rafał Bielas

Rafał Bielas

Co-author Statement

Due to the death of prof. UAM dr hab. Tomasz Hornowski, I declare his contribution to the following publications:

B. Jameel, T. Hornowski, R. Bielas, A. Józefczak, Ultrasound Study of Magnetic and Non-Magnetic Nanoparticle Agglomeration in High Viscous Media, Materials 15(10) (2022) 3450.

In this publication his contribution:

- Methodology,
- Theoretical analysis,
- Finalization.

B. Jameel, R. Bielas, T. Hornowski, A. Józefczak, Propagation of ultrasonic wave in magnetic Pickering emulsion under DC magnetic field, J. Magn. Magn. Matter. 542 (2022) 168590.

In this publication his contribution:

- Writing – review & editing.

mgr Bassam Jameel

prof. UAM dr hab. Arkadiusz Józefczak

Co-author Statement

I hereby declare that I am a co-author of the following publication:

Bielas, R., Jameel, B., Skumiel, A., Timko, M., Kopčanský, P. and Józefczak, A., 2022. Magnetic pickering emulsions heated in a rotating magnetic field. Journal of Magnetism and Magnetic Materials, 563, p.169946.

My contribution consisted of reviewing and editing the manuscript.

With best regards,

RNDr. Peter Kopčanský, PhD

Co-author Statement

I hereby declare that I am a co-author of the following publication:

Bielas, R., Jameel, B., Skumiel, A., Timko, M., Kopčanský, P. and Józefczak, A., 2022. Magnetic pickering emulsions heated in a rotating magnetic field. Journal of Magnetism and Magnetic Materials, 563, p.169946.

My contribution consisted of reviewing and editing the manuscript.

With best regards,

RNDr. Milan Timko, PhD.

Co-author Statement

I hereby declare that I am a co-author of the following publication:

Bielas, R., Jameel, B., Skumiel, A., Timko, M., Kopčanský, P. and Józefczak, A., 2022. Magnetic pickering emulsions heated in a rotating magnetic field. Journal of Magnetism and Magnetic Materials, 563, p.169946.

My contribution consisted of measurements of the heating of magnetic Pickering emulsions under a rotating magnetic field.

With best regards,

Prof. dr. hab. eng. Andrzej Skumiel

Co-author Statement

I hereby declare that I am a co-author of the following publication:

Jameel, B., Paulovičová, K., Tóthová, J., Rajňák, M., Molčan, M., Bielas, R. and Józefczak, A., 2023. Magnetorheological characterization of oil-in-oil magnetic Pickering emulsions. Journal of Magnetism and Magnetic Materials, 588, p.171433.

My contribution consisted of measurements of the magnetic properties (VSM) of magnetic Pickering emulsions.

Sincerely Yours

RNDr. Michal Rajňák, PhD

Co-author Statement

I hereby declare that I am a co-author of the following publication:

Jameel, B., Paulovičová, K., Tóthová, J., Rajňák, M., Molčan, M., Bielas, R. and Józefczak, A., 2023. Magnetorheological characterization of oil-in-oil magnetic Pickering emulsions. Journal of Magnetism and Magnetic Materials, 588, p.171433.

My contribution consisted of participation in magnetorheological measurements of magnetic Pickering emulsions.

Sincerely Yours

Ing. Katarina Paulovičová, PhD

Co-author Statement

I hereby declare that I am a co-author of the following publication:

Jameel, B., Paulovičová, K., Tóthová, J., Rajňák, M., Molčan, M., Bielas, R. and Józefczak, A., 2023. Magnetorheological characterization of oil-in-oil magnetic Pickering emulsions. Journal of Magnetism and Magnetic Materials, 588, p.171433.

My contribution consisted of participation in magnetorheological measurements of magnetic Pickering emulsions.

Sincerely Yours

Prof. Jana Tóthová, PhD.

Co-author Statement

I hereby declare that I am a co-author of the following publication:

Jameel, B., Paulovičová, K., Tóthová, J., Rajňák, M., Molčan, M., Bielas, R. and Józefczak, A., 2023. Magnetorheological characterization of oil-in-oil magnetic Pickering emulsions. Journal of Magnetism and Magnetic Materials, 588, p.171433.

My contribution consisted of reviewing and editing the manuscript.

Sincerely Yours

Ing. Matúš Molčan, PhD

Co-author Statement

I hereby declare that I am a co-author of the following publication:

Jameel, B., Harkavyi, Y., Bielas, R., and Józefczak, A., 2024. Optimization of ultrasound heating with Pickering droplets using core-shell scattering theory. *submitted to Ultrasonic Sonochemistry*

My contribution consisted of investigation, computer simulation and writing–review and editing of the manuscript.

Sincerely Yours

mgr Yaroslav Harkavyi

Appendix A: Elements of matrix used in ECAH model

d_{11}= ac h'[ac];

d_{12}= $-n(n+1)$ h[as];

d_{13}= acp j'[acp];

d_{14}= $-n(n+1)$ j[asp];

d_{15}= aT h'[aT];

d_{16}= aTp j'[aTp];

d_{21}= h[ac];

d_{22}= $-(h$[as] + as h'[as]);

d_{23}= j[acp];

d_{24}= $-(j$[asp] + asp j'[asp]);

d_{25}= h[aT];

d_{26}= j[aTp];

d_{31}= XX$((\text{as}^2 - 2\text{ac}^2)\ h[\text{ac}] - 2\text{ac}^2\ h''[\text{ac}])$;

d_{32}= XX2 $n(n+1)$(as h'[as] − h[as]);

d_{33}= XXp$((\text{asp}^2 - 2\text{acp}^2)\ j[\text{acp}] - 2\text{acp}^2\ j''[\text{acp}])$;

d_{34}= 2XXp $n(n+1)$(asp j'[asp] − j[asp]);

d_{35}= XX$((\text{as}^2 - 2\text{aT}^2)\ h[\text{aT}] - 2\text{aT}^2\ h''[\text{aT}])$;

d_{36}= XXp $((\text{asp}^2 - 2\text{aTp}^2)\ j[\text{aTp}] - 2\text{aTp}^2\ j''[\text{aTp}])$;

d_{41}= XX(ac h'[ac] − h[ac]);

d_{42}= $-\frac{\text{XX}}{2}(\text{as}^2\ h''[\text{as}] + (n^2 + n - 2)\ h[\text{as}])$;

d_{43}= XXp(acp j'[acp] − j[acp]);

d_{44}= $-\frac{\text{XXp}}{2}(\text{asp}^2 j''[\text{asp}] + (n^2 + n - 2)\ j[\text{asp}])$;

d_{45}= XX(aT h'[aT] − h[aT]);

d_{46}= XXp(aTp j'[aTp] − j[aTp]);

d_{51}= bc h[ac];

d_{52}= 0;

d_{53}= bcp j[acp];

d_{54}= 0;

d_{55}= bT h[aT];

d_{56}= bTp j[aTp];

d_{61}= κ bc ac h'[ac];

d_{62}= 0;

d_{63}= κs bcp acp j'[acp];

d_{64}= 0;

d_{65}= κ bT aT h'[aT];

d_{66}= κs bTp aTp j'[aTp];

Appendix B: Elements of matrix used in core–shell model

$m_{11}= n\, h[\mathrm{xd1}] - \mathrm{xd1}\ \mathrm{h1}[\mathrm{xd1}];$

$m_{12}= (\frac{1}{\mathrm{xt1}^3})(n\, h[\mathrm{xt1}] - \mathrm{xt1}\ \mathrm{h1}[\mathrm{xt1}]);$

$m_{13}= -\left(\frac{1}{\mathrm{xs1}}\right) n(n+1)\, h[\mathrm{xs1}];$

$m_{14}= n\, j[\mathrm{xd2}] - \mathrm{xd2}\ \mathrm{j1}[\mathrm{xd2}];$

$m_{15}= (\frac{1}{\mathrm{xt2}^3})(n\, j[\mathrm{xt2}] - \mathrm{xt2}\ \mathrm{j1}[\mathrm{xt2}]);$

$m_{16}= -\left(\frac{1}{\mathrm{xs2}}\right) n(n+1)\, j[\mathrm{xs2}];$

$m_{17}= n\, h[\mathrm{xd2}] - \mathrm{xd2}\ \mathrm{h1}[\mathrm{xd2}];$

$m_{18}= \left(\frac{1}{\mathrm{xt2}^3}\right) (n\, h[\mathrm{xt2}] - \mathrm{xt2}\ \mathrm{h1}[\mathrm{xt2}]);$

$m_{19}= -\left(\frac{1}{\mathrm{xs2}}\right) n(n+1)\, h[\mathrm{xs2}];$

$m_{1,10}= 0;$

$m_{1,11}= 0;$

$m_{1,12}= 0;$

$m_{21}= h[\mathrm{xd1}];$

$m_{22}= \left(\frac{1}{\mathrm{xt1}^3}\right) h[\mathrm{xt1}];$

$m_{23}= -(\frac{1}{\mathrm{xs1}})((n+1)\, h[\mathrm{xs1}] - \mathrm{xs1}\ \mathrm{h1}[\mathrm{xs1}]);$

$m_{24}= j[\mathrm{xd2}];$

$m_{25}= \left(\frac{1}{\mathrm{xt2}^3}\right) j[\mathrm{xt2}];$

$m_{26}= -(\frac{1}{\mathrm{xs2}})((n+1)\, j[\mathrm{xs2}] - \mathrm{xs2}\ \mathrm{j1}[\mathrm{xs2}]);$

$m_{27}= h[\mathrm{xd2}];$

$m_{28}= \left(\frac{1}{\mathrm{xt2}^3}\right) h[\mathrm{xt2}];$

$m_{29}= -(\frac{1}{\mathrm{xs2}})((n+1)\, h[\mathrm{xs2}] - \mathrm{xs2}\ \mathrm{h1}[\mathrm{xs2}]);$

$m_{2,10}= 0;$

$m_{2,11}= 0;$

$m_{2,12} = 0;$

$m_{31} = \frac{bc1}{bc2}\, h[xd1];$

$m_{32} = \left(\frac{bt1}{bc2}\right)\left(\frac{1}{xt1^3}\right) h[xt1];$

$m_{33} = 0;$

$m_{34} = j[xd2];$

$m_{35} = \left(\frac{bt2}{bc2}\right)\left(\frac{1}{xt2^3}\right) j[xt2];$

$m_{36} = 0;$

$m_{37} = h[xd2];$

$m_{38} = \left(\frac{bt2}{bc2}\right)\left(\frac{1}{xt2^3}\right) h[xt2];$

$m_{39} = 0;$

$m_{3,10} = 0;$

$m_{3,11} = 0;$

$m_{3,12} = 0;$

$m_{41} = \frac{bc1}{bc2}\,(n\, h[xd1] - xd1\ h1[xd1]);$

$m_{42} = \left(\frac{bt1}{bc2}\right)\left(\frac{1}{xt1^3}\right)(n\, h[xt1] - xt1\ h1[xt1]);$

$m_{43} = 0;$

$m_{44} = \left(\frac{\kappa 2}{\kappa 1}\right)(n\, j[xd2] - xd2\ j1[xd2]);$

$m_{45} = \left(\frac{\kappa 2}{\kappa 1}\right)\left(\frac{bt2}{bc2}\right)\left(\frac{n\, j[xt2] - xt2\ j1[xt2]}{xt2^3}\right);$

$m_{46} = 0;$

$m_{47} = \left(\frac{\kappa 2}{\kappa 1}\right)(n\, h[xd2] - xd2\ h1[xd2]);$

$m_{48} = \left(\frac{\kappa 2}{\kappa 1}\right)\left(\frac{bt2}{bc2}\right)\left(\frac{n\, h[xt2] - xt2\ h1[xt2]}{xt2^3}\right);$

$m_{49} = 0;$

$m_{4,10} = 0;$

$m_{4,11} = 0;$

$m_{4c12} = 0;$

$m_{51} = \frac{\rho 1}{\rho 2}\left(Tx1\, h[xd1] - \frac{4xd1\ h1[xd1]}{xs1^2}\right);$

$m_{52}= (\frac{\rho 1}{\rho 2})(\frac{1}{xt1^3})((Tx1\ h[xt1] - \frac{4xt1\ h1[xt1]}{xs1^2}));$

$m_{53}= (\frac{\rho 1}{\rho 2})(\frac{1}{xs1^3})2n(n+1) \times ((n-1)\ h[xs1] - xs1\ h1[xs1]);$

$m_{54}= \frac{((Tx2)j[xd2]) - (4xd2\ j1[xd2])}{xs2^2};$

$m_{55}= (\frac{1}{xt2^3})((Tx2)\ j[xt2] - \frac{4xt2\ j1[xt2]}{xs2^2});$

$m_{56}= (\frac{1}{xs2^3})2n(n+1)((n-1)\ j[xs2] - xs2\ j1[xs2]);$

$m_{57}= \frac{((Tx2)\ h[xd2]) - (4xd2\ h1[xd2])}{xs2^2};$

$m_{58}= (\frac{1}{xt2^3})((Tx2)\ h[xt2] - \frac{(4xt2\ h1[xt2])}{xs2^2});$

$m_{59}= (\frac{1}{xs2^3})2n(n+1)((n-1)\ h[xs2] - xs2\ h1[xs2])$

$m_{5,10}= 0;$

$m_{5,11}= 0;$

$m_{5,12}= 0;$

$m_{61}= (\frac{1}{xs1^2})((n-1)\ h[xd1] - xd1\ h1[xd1])\frac{\rho 1}{\rho 2};$

$m_{62}= (\frac{1}{xt1^3})(\frac{1}{xs1^2})((n-1)\ h[xt1] - xt1\ h1[xt1])(\frac{\rho 1}{\rho 2});$

$m_{63}= -(\frac{1}{xs1^3})((n^2 - 1 - \frac{xs1^2}{2})\ h[xs1] + xs1\ h1[xs1])(\frac{\rho 1}{\rho 2});$

$m_{64}= (\frac{1}{xs2^2})((n-1)\ j[xd2] - xd2\ j1[xd2]);$

$m_{65}= (\frac{1}{xt2^3})(\frac{1}{xs2^2})((n-1)\ j[xt2] - xt2\ j1[xt2]);$

$m_{66}= -(\frac{1}{xs2^3})((n^2 - 1 - \frac{xs2^2}{2})\ j[xs2] + xs2\ j1[xs2]);$

$m_{67}= (\frac{1}{xs2^2})((n-1)\ h[xd2] - xd2\ h1[xd2]);$

$m_{68}= (\frac{1}{xt2^3})(\frac{1}{xs2^2})((n-1)\ h[xt2] - xt2\ h1[xt2]);$

$m_{69}= -(\frac{1}{xs2^3})((n^2 - 1 - \frac{xs2^2}{2})\ h[xs2] + xs2\ h1[xs2]);$

$m_{6,10}= 0;$

$m_{6,11}= 0;$

$m_{6,12}= 0;$

$m_{71}= 0;$

$m_{72}= 0;$

$m_{73}= 0;$

$m_{74}= n\, j[\mathrm{yd2}] - \mathrm{yd2}\ \mathrm{j1}[\mathrm{yd2}];$

$m_{75}= (\frac{1}{\mathrm{xt2}^3})(n\, j[\mathrm{yt2}] - (\frac{b}{a})\mathrm{xt2}\ \mathrm{j1}[\mathrm{yt2}]);$

$m_{76}= -(\frac{1}{\mathrm{xs2}})n(n+1)\, j[\mathrm{ys2}];$

$m_{77}= nh[\mathrm{yd2}] - \mathrm{yd2}\ \mathrm{h1}[\mathrm{yd2}];$

$m_{78}= (\frac{1}{\mathrm{xt2}^3})(n\, h[\mathrm{yt2}] - (\frac{b}{a})\mathrm{xt2}\ \mathrm{h1}[\mathrm{yt2}]);$

$m_{79}= -(\frac{1}{\mathrm{xs2}})n(n+1)\, h[\mathrm{ys2}];$

$m_{7,10}= n\, j[\mathrm{yd3}] - \mathrm{yd3}\ \mathrm{j1}[\mathrm{yd3}];$

$m_{7,11}= (\frac{1}{\mathrm{yt3}^3})(n\, j[\mathrm{yt3}] - \mathrm{yt3}\ \mathrm{j1}[\mathrm{yt3}]);$

$m_{7,12}= -(\frac{1}{\mathrm{ys3}})n(n+1)\, j[\mathrm{ys3}];$

$m_{81}= 0;$

$m_{82}= 0;$

$m_{83}= 0;$

$m_{84}= j[\mathrm{yd2}];$

$m_{85}= (\frac{1}{\mathrm{xt2}^3})\, j[\mathrm{yt2}];$

$m_{86}= -(\frac{1}{\mathrm{xs2}})((n+1)\, j[\mathrm{ys2}] - (\frac{b}{a})\mathrm{xs2}\ \mathrm{j1}[\mathrm{ys2}]);$

$m_{87}= h[\mathrm{yd2}];$

$m_{88}= (\frac{1}{\mathrm{xt2}^3})\, h[\mathrm{yt2}];$

$m_{89}= -(\frac{1}{\mathrm{xs2}})((n+1)\, h[\mathrm{ys2}] - (\frac{b}{a})\mathrm{xs2}\ \mathrm{h1}[\mathrm{ys2}]);$

$m_{8,10}= j[\mathrm{yd3}];$

$m_{8,11}= (\frac{1}{\mathrm{yt3}^3})\, j[\mathrm{yt3}];$

$m_{8,12}= -(\frac{1}{\mathrm{ys3}})(n(n+1)\, j[\mathrm{ys3}] - \mathrm{ys3}\ \mathrm{j1}[\mathrm{ys3}]);$

$m_{91}= 0;$

$m_{92}= 0;$

$m_{93}= 0;$

$m_{94}= j[yd2];$

$m_{95}= (\frac{bt2}{bc2})(\frac{1}{xt2^3})\, j[yt2];$

$m_{96}= 0;$

$m_{97}= h[yd2];$

$m_{98}= (\frac{bt2}{bc2})(\frac{1}{xt2^3})\, h[yt2];$

$m_{99}= 0;$

$m_{9,10}= (\frac{bc3}{bc2})\, j[yd3];$

$m_{9,11}= (\frac{bt3}{bc2})(\frac{1}{yt3^3})\, j[yt3];$

$m_{9,12}= 0;$

$m_{10,1}= 0;$

$m_{10,2}= 0;$

$m_{10,3}= 0;$

$m_{10,4}= (\frac{\kappa 2}{\kappa 3})(n\, j[yd2] - yd2\ j1[yd2]);$

$m_{10,5}= (\frac{\kappa 2}{\kappa 3})(\frac{bt2}{bc2})(\frac{1}{xt2^3})(n\, j[yt2] - (\frac{b}{a})xt2\ j1[yt2]);$

$m_{10,6}= 0;$

$m_{10,7}= \frac{\kappa 2}{\kappa 3}\,(n\, h[yd2] - yd2\ h1[yd2]);$

$m_{10,8}= (\frac{\kappa 2}{\kappa 3})(\frac{bt2}{bc2})(\frac{1}{xt2^3})(n\, h[yt2] - (\frac{b}{a})xt2\ h1[yt2]);$

$m_{10,9}= 0;$

$m_{10,10}= (\frac{bc3}{bc2})(n\, j[yd3] - yd3\ j1[yd3]);$

$m_{10,11}= (\frac{bt3}{bc2})(\frac{1}{yt3^3})(n\, j[yt3] - yt3\ j1[yt3]);$

$m_{10,12}= 0;$

$m_{11,1}= 0;$

$m_{11,2}= 0;$

$m_{11,3}= 0;$

$m_{11,4}= \frac{((Ty2)\ j[yd2]) - (4yd2\ j1[yd2])}{ys2^2};$

$m_{11,5}= (\frac{1}{xt2^3})((Ty2)\, j[yt2] - \frac{4(\frac{b}{a})xt2\ j1[yt2]}{ys2^2})$;

$m_{11,6}= (\frac{1}{xs2})(\frac{1}{ys2^2})2n(n+1)((n-1)\, j[ys2] - ys2\ j1[ys2])$;

$m_{11,7}= \frac{((Ty2)\, h[yd2]) - (4yd2\ h1[yd2])}{ys2^2}$;

$m_{11,8}= (\frac{1}{xt2^3})((Ty2)\, h[yt2] - \frac{4(\frac{b}{a})xt2\ h1[yt2]}{ys2^2})$;

$m_{11,9}= (\frac{1}{xs2})(\frac{1}{ys2^2})2n(n+1)((n-1)\, h[ys2] - ys2\ h1[ys2])$;

$m_{11,10}= (\frac{\rho 3}{\rho 2})((Ty3)\, j[yd3] - \frac{4yd3\ j1[yd3]}{ys3^2})$;

$m_{11,11}= (\frac{\rho 3}{\rho 2})(\frac{1}{yt3^3})((Ty3)\, j[yt3] - \frac{4yt3\ j1[yt3]}{ys3^3})$;

$m_{11,12}= (\frac{\rho 3}{\rho 2})(\frac{1}{ys3^3})2n(n+1)((n-1)\, j[ys3] - ys3\ j1[ys3])$;

$m_{12,1}= 0$;

$m_{12,2}= 0$;

$m_{12,3}= 0$;

$m_{12,4}= (\frac{1}{ys2^2})((n-1)\, j[yd2] - yd2\ j1[yd2])$;

$m_{12,5}= (\frac{1}{xt2^3})(\frac{1}{ys2^2})((n-1)\, j[yt2] - (\frac{b}{a})xt2\ j1[yt2])$;

$m_{12,6}= -(\frac{1}{xs2})(\frac{1}{ys2^2})((n^2 - 1 - \frac{ys2^2}{2})\, j[ys2] + ys2\ j1[ys2])$;

$m_{12,7}= (\frac{1}{ys2^2})((n-1)\, h[yd2] - yd2\ h1[yd2])$;

$m_{12,8}= (\frac{1}{xt2^3})(\frac{1}{ys2^2})((n-1)\, h[yt2] - (\frac{b}{a})xt2\ h1[yt2])$;

$m_{12,9}= -(\frac{1}{xs2})(\frac{1}{ys2^2})((n^2 - 1 - \frac{ys2^2}{2})\, h[ys2] + ys2\ h1[ys2])$;

$m_{12,10}= (\frac{\rho 3}{\rho 2})(\frac{1}{ys3^2})((n-1)\, j[yd3] - yd3\ j1[yd3])$;

$m_{12,11}= (\frac{\rho 3}{\rho 2})(\frac{1}{yt3^3})(\frac{1}{ys3^2})((n-1)\, j[yt3] - yt3\ j1[yt3])$;

$m_{12,12}= -(\frac{\rho 3}{\rho 2})(\frac{1}{ys3^3})((n^2 - 1 - \frac{ys3^2}{2})\, j[ys3] + ys3\ j1[ys3])$;

$C_1= -(n\, j[xd1] - xd1\ j1[xd1])$;

$C_2= -j[xd1]$;

$C_3 = -(\frac{bc1}{bc2})\, j[xd1];$

$C_4 = -(\frac{bc1}{bc2})(n\, j[xd1] - xd1\ j1[xd1]);$

$C_5 = -(\frac{\rho 1}{\rho 2})(Tx1\, j[xd1] - \frac{4xd1}{xs1^2}\ j1[xd1]);$

$C_6 = -(\frac{\rho 1}{\rho 2})(\frac{1}{xs1^2})((n-1)\, j[xd1] - xd1\ j1[xd1]);$